POPULATION BALANCE MODELING OF CRYSTALLIZATION FOR MONITORING AND OPTIMAL CONTROL

Caio Felippe Curitiba Marcellos

Tese de Doutorado apresentada ao Programa de Pós-graduação em Engenharia Química, COPPE, da Universidade Federal do Rio de Janeiro, como parte dos requisitos necessários à obtenção do título de Doutor em Engenharia Química.

Orientadores: Argimiro Resende Secchi
Maurício Bezerra de Souza Jr.
Paulo Laranjeira da Cunha Lage

Rio de Janeiro
Agosto de 2018

POPULATION BALANCE MODELING OF CRYSTALLIZATION FOR MONITORING AND OPTIMAL CONTROL

Caio Felippe Curitiba Marcellos

TESE SUBMETIDA AO CORPO DOCENTE DO INSTITUTO ALBERTO LUIZ COIMBRA DE PÓS-GRADUAÇÃO E PESQUISA DE ENGENHARIA (COPPE) DA UNIVERSIDADE FEDERAL DO RIO DE JANEIRO COMO PARTE DOS REQUISITOS NECESSÁRIOS PARA A OBTENÇÃO DO GRAU DE DOUTOR EM CIÊNCIAS EM ENGENHARIA QUÍMICA.

Examinada por:

Prof. Argimiro Resende Secchi, D.Sc.

Prof. Paulo Laranjeira da Cunha Lage, D.Sc.

Prof. Luis Américo Calçada, D.Sc.

Prof. Luiz Augusto da Cruz Meleiro, D.Sc.

Prof. Marcio Nele de Souza, D.Sc.

Prof. Tânia Suaiden Klein, Ph.D.

RIO DE JANEIRO, RJ – BRASIL
AGOSTO DE 2018

Marcellos, Caio Felippe Curitiba

Population Balance Modeling of Crystallization for Monitoring and Optimal Control/Caio Felippe Curitiba Marcellos. – Rio de Janeiro: UFRJ/COPPE, 2018.

XXII, 167 p.: il.; 29, 7cm.

Orientadores: Argimiro Resende Secchi
Maurício Bezerra de Souza Jr.
Paulo Laranjeira da Cunha Lage

Tese (doutorado) – UFRJ/COPPE/Programa de Engenharia Química, 2018.

Referências Bibliográficas: p. 132 – 143.

1. crystallization. 2. enantiomers. 3. modeling. 4. control. 5. parameter estimation. I. Secchi, Argimiro Resende *et al.* II. Universidade Federal do Rio de Janeiro, COPPE, Programa de Engenharia Química. III. Título.

To my daughter Alice.

Agradecimentos

Agradeço aos meus orientadores pelos conselhos e ensinamentos.
Agradeço à minha família e amigos pelo suporte nesta jornada.
Agradeço a Deus.
À CAPES e FAPERJ pelo apoio financeiro.

Resumo da Tese apresentada à COPPE/UFRJ como parte dos requisitos necessários para a obtenção do grau de Doutor em Ciências (D.Sc.)

MODELAGEM DE CRISTALIZAÇÃO POR BALANÇO POPULACIONAL PARA MONITORAMENTO E CONTROLE ÓTIMO

Caio Felippe Curitiba Marcellos

Agosto/2018

Orientadores: Argimiro Resende Secchi
Maurício Bezerra de Souza Jr.
Paulo Laranjeira da Cunha Lage

Programa: Engenharia Química

A Equação do Balanço da População (PBE) descreve a mudança na distribuição do tamanho de partícula. Este estudo avalia a PBE com nucleação, crescimento e dissolução. Processos com nucleação e crescimento são conhecidos por serem problemáticos devido aos perfis descontínuos que causam. A dissolução requer o conhecimento do número de partículas no tamanho estável mínimo, de modo que as partículas instáveis sejam removidas da fase particulada. Essas condições requerem o uso de métodos numéricos especializados para sua modelagem matemática. Nesta tese, é dada ênfase ao *Moving Section Method* (MSM) que combina o método das classes com o método das características para mitigar erros de difusão numérica. O trabalho concentrou-se na aplicação do PBE para a cristalização enantiosseletiva de sistemas formadores de compostos racêmicos. Inicialmente, a conservação dos momentos da distribuição foi analisada para o MSM com mecanismos de crescimento e nucleação e propôs-se métodos para a adição de novos elementos da malha do tamanho de partículas. A estimação de parâmetros cinéticos foi abordada para a dissolução de NaCl em soluções de monoetilenoglicol (MEG) a partir de dados de padrões de cores (RGB), o que pode ser obtido por aparato experimental de baixo custo. Um método para determinar as condições de operação para o cristalizador em batelada com base no diagrama ternário é descrito. Posteriormente, mostram-se que as informações obtidas no diagrama ternário, como o rendimento máximo obtido pelo processo devido à termodinâmica, podem ser usadas para formular restrições para um método de controle baseado em otimização não linear para obter as características desejadas do produto.

Abstract of Thesis presented to COPPE/UFRJ as a partial fulfillment of the requirements for the degree of Doctor of Science (D.Sc.)

POPULATION BALANCE MODELING OF CRYSTALLIZATION FOR MONITORING AND OPTIMAL CONTROL

Caio Felippe Curitiba Marcellos

August/2018

Advisors: Argimiro Resende Secchi
Maurício Bezerra de Souza Jr.
Paulo Laranjeira da Cunha Lage

Department: Chemical Engineering

The Population Balance Equation (PBE) describe the change in the particle size distribution occasioned by a variety of mechanisms. This study evaluate the PBE with nucleation, growth and dissolution. The nucleation with growth process is known to be problematic due to the sharp profiles that it causes. The dissolution process requires the knowledge of the number of particles at the minimal stable size, such that unstable particles are removed from the particulate phase. These conditions require the use of specialized numerical method for mathematical modeling. In this thesis, an emphasis is given in the *Moving Sectional Method*, which combines the method of classes with the method of characteristics to mitigate numerical diffusion errors. The work focused on the PBE application for the enantioselective crystallization of racemic compounding forming systems. Initially, the conservation of the moments of the distribution was analyzed for the MSM with growth and nucleation mechanisms and methods were proposed for the addition of new elements of the particle size mesh. The estimation of kinetic parameters was approached for the dissolution of NaCl in solutions of monoethyleneglycol (MEG) from data of color patterns (RGB), which can be obtained by experimental apparatus of low cost. A method for determining the operating conditions for the batch crystallizer based on the ternary diagram is described. Subsequently, it is shown that the information obtained in the ternary diagram, such as the maximum yield obtained by the process due to thermodynamics, can be used to formulate constraints for a control method based on non-linear optimization to obtain the desired characteristics of the product.

Contents

List of Figures

List of Tables

List of Symbols

A	Heat exchange area $[m^2]$, p. 105
B_0	Nucleation rate $[1/s]$, p. 15
$C_{NaCl,L}$	NaCl liquid concentration $[kg/m^3]$, p. 68
$C_{NaCl,S}$	NaCl solid concentration $[kg/m^3]$, p. 68
C_{fines}	Fine particles mass based composition [-], p. 106
$D(t)$	Dissolution rate $[\mu m/s]$, p. 65
E_a	Activation energy $[J/mol]$, p. 66
E_b	Activation energy for the nucleation rate $[J/mol]$, p. 111
E_g	Activation energy for the growth rate $[J/mol]$, p. 111
G	Particle growth rate $[m/s]$, p. 14
GS	Grayscale [-], p. 62
K_{eq}	Equilibrium constant [-], p. 66
M_T	Ratio of crystal mass to solvent mass [-], p. 111
M_{tot}	Total mass in the crystallizer $[kg]$, p. 105
N	Number of particles [-], p. 11
P	Enantiomeric purity [-], p. 94
R	Universal gas constant $[J/(molK)]$, p. 8
S	Fundamental supersaturation [-], p. 8
T	Temperature $[K]$, p. 8
T_{jkt}	Jacket temperature $[K]$, p. 105

U	Overall heat transfer coefficient of the crystallizer surface $[Js^{-1}K^{-1}m^{-2}]$, p. 105
V	Volume $[m^3]$, p. 13
Y_c	Crystal yield [-], p. 93
$\Delta\overline{G}$	Change in molar free-energy of reaction $[J/mol]$, p. 66
Ξ	Property of interesse to be monitored in the first bin, p. 50
β_j	Parameters for GS correlation, p. 68
χ	Solution molar fraction [-], p. 8
χ_{sat}	Saturation molar fraction [-], p. 8
$\dot{V}_k$	Volumetric flow rate of input and output streams $[m^3/s]$, p. 14
γ	Activity coefficient [-], p. 8
γ_{sat}	Saturation activity coefficient [-], p. 8
λ	Factor for non elementary reaction of dissolution [-], p. 66
$\hat{\mathbf{n}}$	Normal vector, p. 13
$\mathbf{n_A}$	Mass flux of a specie A $[kg/(m^2s)]$, p. 15
$\mathbf{v}$	Advective velocity of the particle in its coordinates, p. 11
$\mathbf{x}$	particle space coordinates, p. 11
$\mathcal{B}$	Overall rate of particle birth, p. 12
$\mathcal{D}$	Overall rate of particle death, p. 12
$\mathcal{S}$	Contour surface $[m^2]$, p. 13
R	Particle coordinate space domain, p. 11
μ_j	j-th order moment, p. 18
$\overline{\mu}$	Chemical potential $[J/mol]$, p. 8
ρ_A	Density of a specie A $[m^3/kg]$, p. 15
ρ_l	Liquid density $[kg/m^3]$, p. 105
ρ_{mix}	Mixture density $[kg/m^3]$, p. 68

τ	Activity coefficient correction factor due to co-solvent presence [-], p. 67
ζ	MEG contribution exponent for the dissolution rate [-], p. 67
a	Chemical activity [-], p. 8
a_0	Factor for initial mass of crystals, p. 104
a_{sat}	Saturation chemical activity [-], p. 8
b	Supersaturation exponent for the nucleation rate [-], p. 111
c_j	Molality of specie j $[mol/kg]$, p. 67
c_p	Specific heat capacity of the suspension $[Jkg^{-1}K^{-1}]$, p. 105
e_j	Unit vector along a particle coordinate j, p. 11
g	Supersaturation exponent for the growth rate [-], p. 111
k_V	Particle shape factor [-], p. 16
k_{b0}	Pre-exponential factor for the nucleation rate $[kg^{-1}s^{-1}]$, p. 111
$k_{d,0}$	Arrhenius pre-exponential constant for the dissolution rate $[\mu m/s]$, p. 66
k_{g0}	Pre-exponential factor for the growth rate $[m/s]$, p. 111
l	Particle characteristic size $[m]$, p. 14
l_{min}	Nuclei critical size $[m]$, p. 15
m_A	Mass of component A $[kg]$, p. 17
$m_{NaCl,L}$	mass of NaCl in the liquid phase $[kg]$, p. 65
$m_{NaCl,S}$	mass of NaCl in the solid phase $[kg]$, p. 68
n	Particle size distribution $[1/(m^3 m)]$, p. 11
r_A	Mass production rate of A per unit of volume $[kg/(m^3 s)]$, p. 15
$r_{add,k}$	Number of additions for the experiment k, p. 64
t	time $[s]$, p. 11
w	Mass fraction [-], p. 63

x	Discretized size pivot [m], p. 22
w	Mass composition [-], p. 147

List of Abbreviations

RGB	Red-green-blue color pattern, p. 4
ATR-FTIR	Total Reflectance Fourier Transform Infrared, p. 26
DQMOM	Direct Quadrature Method of Moments, p. 17
FBRM	Focused Beam Reflectance Measurement, p. 27
MEG	Monoethylene Glycol, p. 60
MSM	Moving Sectional Method, p. 4
NRTL	Non Random Two Liquids, p. 150
ODE	Ordinary Differential Equation, p. 18
PBE	Population Balance Equation, p. 1
PSD	Particle Size Distribution, p. 1
QMOM	Quadrature Method of Moments, p. 17
RGB	Red, green and blue, p. 60
SMB	Simulated Moving Bed, p. 2
SMOM	Standard Method of Moments, p. 17

Chapter 1

Introduction

1.1 Contextualization

The Population Balance Equation (PBE) is a conservation law used to account for the number of particles in a system and has applications in several fields, as precipitation, polymerization, crystallization, food processes, pharmaceutical manufacture, pollutant formation in flames, particle size distribution (PSD) of crushed material and rain drops, dispersed phase distributions in multiphase flows, and growth of microbial and cell populations (Qamar, 2008). The PBE can account for different mechanisms capable of modifying the particles distribution, such as particle growth and dissolution, nucleation, agglomeration, breakage and disappearing. The mathematical description of particulate processes using the PBE results in a system of hyperbolic partial integro-differential equations, which pose a numerical complexity and leveraged studies in specialized methods for it solution.

Crystallization is the main technological process for forming particles in the pharmaceutical industry and has a fundamental role in drugs stability and bioavailability properties. These properties are associated with the purity, morphology and size distribution. Myerson (2002) indicated that the bioavailability is associated with the PSD, for example, it can be decreased if the crystals are too large. On the other hand, small size crystals are more subject to degradation during processing and storage.

According to Rentsch (2002) 56% of the drugs in use are chiral compounds, and approximately 88% of those are marketed in the form of racemates. Even though these drugs are made of substances of similar chemical structure, in many cases the isomers have differences in biological activity, such as pharmacology, toxicology, pharmacokinetics and metabolism. Thus, the chiral separation of undesired isomer has great appeal in research and development of technologies (Nguyen et al., 2006).

One example of such chiral pharmaceutical is the praziquantel. The

R-praziquantel has a anthelmintic activity and is used to treat parasitic worm infections, such as schistosomiasis. The comercial formulation is the racemate, since it is synthesized as a racemic mixture by a low cost procedure when compared to the enantioselective synthesis (Novaes et al., 1999). However, its stereoisomer S-praziquantel is responsible for the medication's bitter taste. Additionally, it presents higher toxicity and is associated with the side effects of the drug. Thus, the purification of R-praziquantel can lead to a more efficient formulation and with reduced collaterals effects.

In recent years, the use of liquid chromatography for the separation of enantiomers has gained great importance due to advances in the development of increasingly efficient and selective stationary phases. In addition, the advent of simulated moving bed (SMB) chromatography allows the more efficient and economical production of enriched solution of the preferred enantiomer. On the other hand, obtaining high purity product reduces the productivity of SMB (Gedicke et al., 2005). This scenario led to the strategy of coupled SMB chromatography with direct crystallization. This approach allowed the crystallization of pure solid enantiomer associated with the use of chromatography at an optimum productivity region, i.e. without requiring high purities, to be obtained. One of the pioneers of this approach was Lim et al. (1995). (1995) to obtain purified R-praziquantel.

The monitoring and control of particulate systems can be viewed in three different levels (Chianese and Kramer, 2012) accordingly with the measurement capability. The lower level corresponds to analyzing the process based on basic process variables, as temperature, flow rates and pressure. In the intermediary level, the supersaturation tracking requires the solute composition measurement and saturation condition prediction. Lastly, the third level corresponds to the analysis of properties associated with the overall solid phase or even with the complete particle size distribution, which is considered to be difficult to be measured online but gives a detailed understanding of the process.

1.2 Goals and Contributions

The enantioselective crystallization of racemic compound forming system is analyzed in this thesis. Such application can be studied and improved by different approaches. For instance, in a physicochemical scope when the interaction of the enantiomers with other compounds are investigated for a enhanced separation, such as optically active solvents or by formation of diastereomers. On the other hand, the separation can be analyzed by a plant-wide viewpoint, in this case the goal is to provided optimal conditions for the operation. This is the approach investigated in this work.

The study of optimal operation conditions envolves the definition of a performance index, that represents the effectiveness of the ongoing operation. In a general manner, the process conditions and operation patterns that can be manipulated are evaluated to provide the optimal performance index under the process constraints. A mathematical model of the system provides predictions for the actual process behavior and for the performance index. Moreover, measurements of key variables are necessary for establishing the mathematical model and for process monitoring.

The analyze of optimal operation of the enantioselective crystallization of racemic compound forming system was the main goal of this thesis. The preliminary motivation was the separation of praziquantel enantiomers. However, the investigation of optimal operation conditions requires knowledge of the crystallization kinetic parameters for the model definition, which were not available for the praziquantel system. Thus, a general approach for racemic compound forming system was considered, but using data from the mandelic acid enantiomers in water system (Zhang et al., 2010). The process is a batch operation in a vessel with a termal jacket and with fines dissolution loop. Only the particle mechanisms of nucleation and growth were included.

The contributions given on this application were:

- Operation design to achieve maximum separation yield: a diagram showing the initial composition and its relation to the working temperature range and final yield was proposed.
- Structured optimal control operation: a methodology for the definition of an optimization-based control scheme was developed using the information from the ternary diagram for maximizing the mass of crystal from the seeded particles and reducing nucleation.
- A demonstration of the proposed methods was shown for the mandelic acid enantiomers with the additional evaluation of the use of fine dissolution loop.
- An efficient implementation of a model predictive controller using the PBE distributed model was presented.

Furthermore, the numerical method of Kumar and Ramkrishna (1997) (denoted as Moving Sectional Method - MSM) for nucleation and growth was analyzed in respect to the error introduced by the nucleated particles. In short, in this method the size coordinate was discretized in bins and, accordingly with their size, particles are assigned to the corresponding size in the discretized grid. The size grid moves accordingly with the characteristic velocity of the system (growth rate). However,

nucleated particles continuously appear in the solid phase at certain minimal stable size, which is often close to zero and negligible compared with the working size range. Hence, as particles grow, the size grid moves and the newly nucleated particles are not correctly accounted by the method. To overcome this issue, Kumar and Ramkrishna (1997) proposed the periodic addition of new bins at small time intervals at the minimal stable size. The following contributions were addressed:

- The growth rate of the first bin, which is the one receiving the nucleated particles, was analyzed under different simplification hypotheses and compared with reported equations found in the literature.
- The addition of multiple bins for the representation of nucleated particle were examined for the preservation of moment of orders higher than one.
- Numerical schemes were proposed for controlled bin addition for efficiently representing the nucleation in which more bins are added on the time intervals of higher nucleation and growth rate.

The monitoring of the particulate system is crucial for a enhanced process operation. A method of inferring the amount of solid in suspension was proposed by Caciano de Sena et al. (2011) using a Charge Coupled Device camera that captures the red-green-blue color pattern (RGB) from a predefined area of the system under analysis. Silva et al. (2013) used the method for determining solubilities curves. Figueiredo (2016) also used this method for study the dissolution kinetics of NaCl particles in glycol aqueous solution. In this thesis, a continuation of Figueiredo (2016) work was evaluated. The dissolution data were used to estimate kinetic parameters using the population balance to model the particulate system for the first time. The goal of this work was to define a suitable dynamic model capable of describing the dissolution of NaCl crystals ranging from a solution free of solute up to a close to equilibrium condition. The main contributions regarding to this application are the following:

- A dissolution model using the PBE was defined using a dissolution rate equation capable of describing the dynamic behavior of a wide range of undersaturation, including the dissolution plateau. The model was able to describe classified particle addition and the disappearance due to dissolution.
- A methodology for determining the kinetic parameters of the dissolution was presented using the RGB color pattern measurements under different MEG and temperature condition.

All the contributions of this thesis are related with the main goal of optimal operation of enantioselective crystallization of racemic compound forming system. The MSM contributions assisted in the numerical solution of the system by identifying possible source of errors. However, the proposed schemes of bins additions were not necessary in the optimal control study. The periodic bin addition scheme was sufficient to provide acceptable errors in the moments conservation due to the nucleated particles. The contributions related with the monitoring of the particulate system, although analyzed for dissolution only, could be used as an low-cost alternative for estimating growth and nucleation kinetics. Since the experimental data acquisition was not in the scope of this work, the proposed methodology for kinetic parameters estimation were not applied for the enantioselective crystallization.

1.3 Thesis Structure

A brief introduction for the following chapters is:

- **Chapter 2 — Bibliographic Review:** a pertinent introduction of particulate process with focus on crystallization and recent developments in the literature for numerical solution of the PBE is given.
- **Chapter 3 — First Bin Analysis for the Moving Sectional Method:** A detailed analyze on the Moving Sectional Method is presented in respect to the moment errors due to the growth of nucleated particles. Simplification hypotheses were addressed to define the first bin growth rate, which receives newly nucleated particles. Controlled schemes for the addition of new bins are proposed for efficiently reduce moment conservation errors.
- **Chapter 4 — Inferring kinetic dissolution of NaCl in aqueous glycol solution using a low-cost apparatus and population balance model:** In this chapter the dissolution of NaCl in glycol solution is addressed. Data from the work of Figueiredo (2016) were used for the development of a methodology to determine kinetic parameters of the dissolution process. The influence of temperature and glycol composition were evaluated.
- **Chapter 5 — Optimal operation of batch enantiomer crystallization: From ternary diagrams to predictive control:** The separation of enantiomers for racemic compound forming system using crystallization is addressed. A methodology was proposed for determining operational conditions. Furthermore, a method for maximizing the growth of seeds while

keeping a maximum yield was proposed using a model predictive controller designed based on information from the ternary diagram.

- **Chapter 6 — Conclusion:** This chapter summarizes the main results presented in this thesis.

Chapter 2

Bibliographic Review

2.1 Convencional Crystallization

Crystallization is denoted as the process of forming solid crystals in a homogeneous solution and, essentially, can be considered as a solid-liquid separation. Its main applications are in the pharmaceutical, chemical and food industry.

The driving force for the process of transforming a substance in solution into a solid state (crystal), the crystallization process, is the difference between the chemical potential of the substance between these states. It can be written as:

$$\Delta\overline{\mu} = \overline{\mu}_{\text{crystal}} - \overline{\mu}_{\text{solution}} \tag{2.1}$$

The chemical potential $\overline{\mu}$ is a function of chemical activity (a) according to Eq. 2.2. The fundamental driving force is defined in Mullin (2001) as in Eq. 2.3 and is related with the saturation activity a_{sat}.

$$\overline{\mu} = \overline{\mu}_0 + RT \ln a \tag{2.2}$$

$$\frac{\Delta\overline{\mu}}{RT} = \ln \frac{a}{a_{sat}} = \ln S \tag{2.3}$$

where S is the fundamental supersaturation. Thus, isolating S from Eq. 2.3, a definition for S (Eq. 2.4) is obtained:

$$S = \exp\left[\frac{\Delta\overline{\mu}}{RT}\right] = \frac{a}{a_{sat}} \tag{2.4}$$

By the chemical activity definition $a = \gamma\chi$, where γ is the activity coefficient and χ the molar fraction of the crystallizing substance in the liquid phase, the fundamental supersaturation can be written as Eq. 2.5. The saturation activity coefficient and molar fraction is given by γ_{sat} and χ_{sat}, respectively.

$$S = \frac{\gamma\chi}{\gamma_{sat}\chi_{sat}} \tag{2.5}$$

The solubility of a substance in a solvent is the maximum concentration that can be in equilibrium at a given operating condition. There is usually an increase in solubility with increasing temperature. The understanding of the process can be obtained by evaluating a graph of solute concentration as function of temperature, according to Figure 2.1 (Mullin, 2001), which shows tree important regions:

- Undersaturated: region in which crystals are dissolved;
- Metastable: region of supersaturation in which there is crystal growth;
- Labile: region in which the solution tends to spontaneous nucleation.

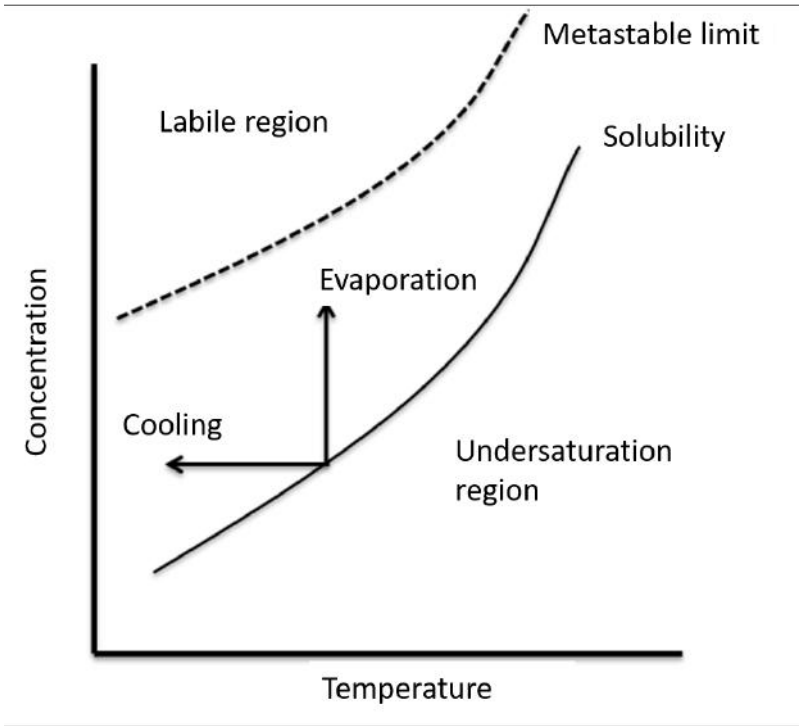

Figure 2.1: Solubility diagram: solute concentration *vs* temperature. Adapted from Mullin (2001).

Crystallization processes are typically described and studied based on the number of particles with a certain property of interest. This property is usually related with the particle size, but can also be other quantities, such as crystal purity, temperature, bio-activity, etc. In this work the focus is given to the crystal size distribution.

The number of particles at certain particle size is described based on the particle size distribution (PSD). The PSD is important since it provides an understanding of the dynamics of crystallization. In addition, it has a high influence in the product quality and in downstream processing (Chianese and Kramer, 2012).

The main mechanisms involved in the change of particles size and number are schematized in Figure 2.2 and described as (Jones, 2002):

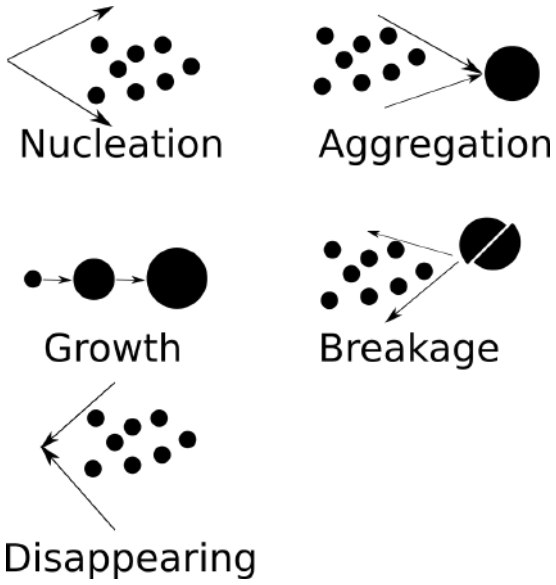

Figure 2.2: Representative scheme for pertinent particle mechanisms in crystallization. Adapted from Jones (2002).

- Nucleation: dispersed solute molecules bind to generate new small particles denoted as nuclei.
- Growth: correspond to the increasing of the crystal size and is dependent on the supersaturation and can also be a function of crystal size. The dissolution can be seem as the opposite of the growth process.
- Aggregation: is the merging of smaller particles into a single one.
- Breakage: it represents the formation of new particles from the breakage of larger ones.
- Disappearing: particles with size smaller than the critical size vanish from the solid phase.

In the nucleation process, solute molecules dispersed in the solvent bind to give aggregates called nuclei. Mullin (2001) highlighted that there is no general agreement on the nomenclature used for the classification of types of nucleation, mentioning the primary and homogeneous nucleation for cases when nuclei are formed but without the influence of crystalline matter. The primary and heterogeneous nucleation occur due to the presence of impurities. The secondary nucleation is refereed to the cases in which the nuclei are formed in the vicinity of crystals. All of this mechanisms have as driving force the supersaturation.

Particle aggregation and breakage are not treated in this thesis and the reader is referred to Randolph and Larson (1988) for more theorethical details and to Silva et al. (2010) for a discussion on numerical methods for it mathematical modeling.

The growth of the crystals corresponds to the increase in their size. The growth is dependent on supersaturation and may be dependent on crystal size. It occurs in supersaturated conditions and involves two major processes: (i) the mass transport from the solution to the crystal surface by diffusion and convection and (ii) the incorporation of material into the crystal lattice in a surface reaction process. The former step is subdivided in the following stages (Jones, 2002):

1. Adsorption of the incoming material to the crystal lattice;
2. Release of portion of the solvation shell;
3. The diffusion of the growth unit into the adsorption layer up to its incorporation or its release to the solution;
4. If the incoming material reaches a favorable site (usually edges or kinks) it can adhere to the lattice and loses the remaining of the solvation shell.

Dissolution process follows the reverse process delineated for the growth (Lasaga, 1998) in undersaturated conditions. However, the dissolution usually occurs at a fast pace than the growth (Mullin, 2001). Particles in an undersaturated solution loose matter to the dispersed phase reducing their size until a minimal stable size is reached. At this point the remaining aggregate is no longer stable and vanishes from the particulate phase. The dissolution will be discussed in Chapter 4.

2.2 Population Balance Mathematical Modeling

2.2.1 Population Balance Formulation

The phase space of the particle consists of a number of independent coordinates of its distribution that allows the complete description of its properties. In the analysis of the particle phase space a division is made between the internal and external coordinates. The external ones refer to the spatial distribution, however they are not evaluated in the majority of the studies of crystallization, because perfectly agitated tank process is usually considered (Ramkrishna, 2000). The internal coordinates are linked to the properties of each particle individually and provide quantitative measurements of its state, regardless of its spatial position. The main internal coordinate is the particle size, other examples are: particle composition, energy, age and chemical activity. The following is the population balance formulation based on Randolph and Larson (1988).

Generally, one can consider the particle distribution function $n(\mathbf{x}, t)$ defined on a domain R consisting of the three spatial coordinates plus m independent internal properties, which compose the particle space $\mathbf{x}$. According to the definition of particle distribution, the number of particles (dN) existing in a given time t in a volume of its infinitesimal phase space $d\mathsf{R}$ is given by:

$$dN(\mathbf{x}, t) = n(\mathbf{x}, t)d\mathsf{R} \tag{2.6}$$

Thus, the number of particles in a sub region $\mathsf{R_1}$ is obtained by the integral:

$$N(\mathsf{R_1}) = \int_{\mathsf{R_1}} nd\mathsf{R} \tag{2.7}$$

In particulate processes there are continuous changes in the positions of the phase space, that is, each particle moves along the internal and external coordinates. When these changes are gradual and continuous, it refers to the movement as advection along the respective coordinate of the phase space. The rate of change in a coordinate is then called the advective velocity of the particle under this coordinate. One can then define this velocity ($\mathbf{v}$):

$$\mathbf{v} = \mathsf{v_x}e_\mathsf{x} + \mathsf{v_y}e_\mathsf{y} + \mathsf{v_z}e_\mathsf{z} + \mathsf{v_1}e_1 + \mathsf{v_2}e_2 + \ldots + \mathsf{v_m}e_\mathsf{m} \tag{2.8}$$

or:

$$\mathbf{v} = \mathbf{v_e} + \mathbf{v_i} \tag{2.9}$$

In this case, $\mathsf{v_j}$ corresponds to the velocity component in the coordinate j and e_j are the unit vectors along this coordinate. The terms $\mathbf{v_e}$ and $\mathbf{v_i}$ are the velocities in the external and internal coordinates, respectively. The velocity in the external coordinate in well-stirred media has stochastic characteristics that tend to homogenize its effects, and its evaluation are often of little practical importance. The internal velocity of the particles $\mathbf{v_i}$ are functions only of the state of the particles.

The population balance in a given region of the particle phase space using the Lagrangian viewpoint, i.e. the subregion $\mathsf{R_1}$ moving with the phase-space velocity, is written as:

$$\frac{d}{dt}N(\mathsf{R_1}) = \text{Rate of net particle generation} \tag{2.10}$$

in which the net particle generation is due to birth and death events, such as nucleation, breakage and agglomeration. Considering $\mathcal{B}$ and $\mathcal{D}$ the rates of particle birth and death, respectively, the quantity of new particles arising in the system is

given by:

$$\text{Rate of net particle generation} = (\mathcal{B} - \mathcal{D}) d\mathsf{R} \tag{2.11}$$

Eq. 2.11 and 2.7 can be substituted in Eq. 2.10:

$$\frac{d}{dt}\int_{\mathsf{R}_1} n(\mathbf{x}, t) d\mathsf{R} = \int_{\mathsf{R}_1} (\mathcal{B} - \mathcal{D})\, d\mathsf{R} \tag{2.12}$$

According to the Leibniz integrals differentiation rule and considering the space $\mathsf{R_1}$ dependent on t, that is, $\mathsf{R_1} = \mathsf{R_1}(t)$ (or basing on the Reynolds transport theorem), the left side of Eq. 2.12 becomes:

$$\frac{d}{dt}\int_{\mathsf{R}_1} n(\mathbf{x}, t) d\mathsf{R} = \int_{\mathsf{R}_1} \left[\frac{\partial n}{\partial t} + \nabla \cdot \left(n \frac{d\mathbf{x}}{dt}\right)\right] d\mathsf{R} \tag{2.13}$$

The advective velocity of the particles is: $\mathbf{v} = \mathbf{v_e} + \mathbf{v_i}$ e $d\mathbf{x}/dt = \mathbf{v}$. The formulation is then:

$$\int_{\mathsf{R}_1} \left[\frac{\partial n}{\partial t} + \nabla_{\mathbf{e}} \cdot (n\mathbf{v_e}) + \nabla_{\mathbf{i}} \cdot (n\mathbf{v_i}) + \mathcal{D} - \mathcal{B}\right] d\mathsf{R} = 0 \tag{2.14}$$

in which $\nabla_{\mathbf{i}}$ and $\nabla_{\mathbf{e}}$ are the $\nabla[\cdot]$ operator in respect to the internal and external coordinates, respectively.

Since the subregion $\mathsf{R_1}$ has been chosen arbitrarily, equality is only true when the integrand is everywhere null in the space. Thus, the population balance is given by:

$$\frac{\partial n}{\partial t} + \nabla_{\mathbf{e}} \cdot (n\mathbf{v_e}) + \nabla_{\mathbf{i}} \cdot (n\mathbf{v_i}) + \mathcal{D} - \mathcal{B} = 0 \tag{2.15}$$

The population balance equation corresponds to the continuity of the number of particles in the phase space considered. The solution of this equation together with the mass and energy balances, the formation and disappearance kinetics of particles and the conditions of entry and exit in the region of interest, determine the dynamics of the multidimensional distribution of particles.

In the evaluation of practical problems of particulate processes, the main interest is in the monitoring of internal coordinates, such as the characteristic particle size. In several applications, information about the distribution at external coordinates is not of paramount importance. Thus, Eq. 2.15 can be rewritten in order to consider average properties in the external coordinate domain. Considering a control physical volume $V(t)$ one can apply the operator $\int_{V(t)} \dot{dV}$ to Eq. 2.15:

$$\int_{V(t)} \frac{\partial n}{\partial t} dV + \int_{V(t)} \left[\nabla_{\mathbf{e}} \cdot (n\mathbf{v_e})\right] dV + \int_{V(t)} \left[\nabla_{\mathbf{i}} \cdot (n\mathbf{v_i})\right] dV + \int_{V(t)} (\mathcal{D} - \mathcal{B}) dV = 0 \quad (2.16)$$

The physical volume $V(t)$ is considered to have a contour surface $\mathcal{S}(t)$ that moves with a certain velocity $\mathbf{v_S}$ and with normal vector $\hat{\mathbf{n}}$. The transport theorem for the quantity n allows to write the first term in Eq. 2.16 as:

$$\int_{V(t)} \frac{\partial n}{\partial t} dV = \frac{d}{dt}\left[\int_{V(t)} n dV\right] - \oint n\mathbf{v}_{\mathcal{S}} \cdot \hat{\mathbf{n}} d\mathcal{S} \quad (2.17)$$

The second term in 2.16 can be rewritten using the Gauss Theorem yielding Eq. 2.18

$$\int_{V(t)} \left[\nabla_{\mathbf{e}} \cdot (n\mathbf{v_e})\right] dV = \oint_{\mathcal{S}(t)} n\mathbf{v_e} \cdot d\mathcal{S} \quad (2.18)$$

The former two equations are substituted in Eq. 2.16 resulting in 2.19, in which the divergent operator $\nabla_{\mathbf{i}}$ was removed from the integral, since it is related to the internal coordinates whereas the integral is for the spatial coordinates.

$$\frac{d}{dt}\left[\int_{V(t)} n dV\right] - \oint n\mathbf{v}_{\mathcal{S}} \cdot \hat{\mathbf{n}} d\mathcal{S} + \oint_{S(t)} n\mathbf{v_e} \cdot d\mathcal{S} + \nabla_{\mathbf{i}} \cdot \left[\int_{V(t)} (n\mathbf{v_i})\, dV\right] + \int_{V(t)} (\mathcal{D} - \mathcal{B}) dV = 0 \quad (2.19)$$

The goal of the PBE application in this study is to evaluate averaged values for the size distribution in the physical volume of interest. In such case: $\int_{V(t)} n dV = \bar{n} V(t)$, $\int_{V(t)} (\mathcal{D} - \mathcal{B}) dV = (\bar{\mathcal{D}} - \bar{\mathcal{B}}) V(t)$ and $\int_{V(t)} n\mathbf{v_i} dV = V(t)\bar{n}\mathbf{v_i}$, where the overline notation refers to the averaged value of a quantity. Eq. 2.19 is then:

$$\frac{d}{dt}\left[\bar{n} V(t)\right] - \oint_{\mathcal{S}(t)} n\mathbf{v}_{\mathcal{S}} \cdot \hat{\mathbf{n}} d\mathcal{S} + \oint_{\mathcal{S}(t)} n\mathbf{v_e} \cdot d\mathcal{S} + \nabla_{\mathbf{i}} \cdot \left[V(t)\bar{n}\mathbf{v_i}\right] + (\bar{\mathcal{D}} - \bar{\mathcal{B}}) V(t) = 0 \quad (2.20)$$

Applying the chain rule to the first term in Eq. 2.20 and rearranging it:

$$V(t)\left[\frac{d\bar{n}}{dt} + \nabla_{\mathbf{i}} \cdot (\bar{n}\mathbf{v_i}) + (\bar{\mathcal{D}} - \bar{\mathcal{B}})\right] + \bar{n}\frac{dV}{dt} + \oint_{\mathcal{S}(t)} n(\mathbf{v_e} - \mathbf{v}_{\mathcal{S}}) \cdot \hat{\mathbf{n}} d\mathcal{S} = 0 \quad (2.21)$$

To evaluate the last term in the left hand side of Eq. 2.21 the surface of the system is decomposed into three components:

- $\mathcal{S}_k$: representing fixed surface but open to input and output material streams
- $\mathcal{S}_S$: impenetrable and fixed surface

- $\mathcal{S}_m$: moving surface but impenetrable (no particulate crossing)

such that $\mathcal{S} = \mathcal{S}_k + \mathcal{S}_S + \mathcal{S}_m$

For the first component $\mathbf{v}_\mathcal{S} = 0$, since the surface is fixed. Thus, considering that all the material stream crossing the surface $\mathcal{S}_k$ in the system can be represented by a k-th volumetric inlet or outlet flows $\dot{V}_k$ (entries with positive sign) and with averaged population density n_k:

$$\oint_{\mathcal{S}_k} n(\mathbf{v_e} - \mathbf{v}_\mathcal{S}) \cdot \hat{\mathbf{n}} d\mathcal{S} = \oint_{\mathcal{S}_k} n\mathbf{v_e} \cdot \hat{\mathbf{n}} d\mathcal{S} = -\sum_k \dot{V}_k n_k \tag{2.22}$$

For the second component $\mathbf{v}_\mathcal{S} \cdot \hat{\mathbf{n}} = 0$ and $\mathbf{v_e} \cdot \hat{\mathbf{n}} = 0$. The last component has $\mathbf{v}_\mathcal{S} = \mathbf{v_e}$. Hence:

$$\oint_{\mathcal{S}_S \cup \mathcal{S}_m} n(\mathbf{v_e} - \mathbf{v}_\mathcal{S}) \cdot \hat{\mathbf{n}} d\mathcal{S} = 0 \tag{2.23}$$

Thus, substituting Eq. 2.22 into Eq. 2.21 and dividing all the terms by $V(t)$ results in Eq. 2.24

$$\frac{d\bar{n}}{dt} + \nabla_\mathbf{i} \cdot (\bar{n}\mathbf{v_i}) + (\bar{\mathcal{D}} - \bar{\mathcal{B}}) + \bar{n}\frac{d\ln V}{dt} - \sum_k \frac{\dot{V}_k}{V(t)} n_k = 0 \tag{2.24}$$

Eq. 2.24 is called the macroscopic population balance, being distributed in the internal coordinates and grouped in the outer phase space. This formulation is of great use in the description and prediction of particulate processes.

The solution of Eq. 2.24 to crystallizers often considers some simplifications, for example, the consideration of the internal coordinate only as the characteristic particle size l, i.e. $\mathbf{v_i} = v_l$. Thus, the term $\nabla_\mathbf{i} \cdot (n\mathbf{v_i})$ can be written as $\dfrac{\partial}{\partial l}[v_i n]$. The velocity v_i is denoted as particle growth rate and represents the advective velocity of a particle along the coordinate l (Eq. 2.25).

$$G = \frac{dl}{dt} \tag{2.25}$$

A further common simplification in the crystallization modelling is the assumption of only nucleation as relevant in the appearance and disappearance term, in which new particles are born with a minimal stable size l_{min}. Thus, $\bar{\mathcal{B}} - \bar{\mathcal{D}} = B_0\delta(l - l_{min})$ and Eq. 2.24 reduces to:

$$\frac{\partial \bar{n}}{\partial t} + \frac{\partial}{\partial l}(G\bar{n}) + \bar{n}\frac{d\ln V}{dt} = \sum_k \frac{\dot{V}_k}{V} n_k + B_0\delta(l - l_{min}) \tag{2.26}$$

, where B_0 represents the rate of appearance of particles due to nucleation. For

simplification sake, the overline notation is not included hereinafter for the averaged number density.

Formulation of the Crystallizer Mass Balance

The rates involved in the population balance (growth and nucleation) are dependent on the supersaturation of the medium. In turn, the supersaturation is a function of composition. Thus, a crystallizer mathematical simulation requires the inclusion of the mass balance. Considering ρ_A as the mass density of a component A in the liquid phase, the continuity equation for A in a mixture is:

$$\int_{V(t)} \left[\frac{\partial \rho_A}{\partial t} + \nabla \cdot \mathbf{n_A} - r_A \right] dV = 0 \tag{2.27}$$

where $\mathbf{n_A}$ is the mass flux for component A in the liquid phase, such that $\mathbf{n_A} = \rho_A \mathbf{v_A}$, in which $\mathbf{v_A}$ is the velocity of specie A. The quantity r_A corresponds to the mass production rate of A per unit of volume as a result of the particulate process. By the Gauss divergent theorem and considering $\hat{\mathbf{n}}$ as the normal unit vector in relation to the infinitesimal surface $d\mathcal{S}$, Eq. 2.27 becomes:

$$\int_{V(t)} \frac{\partial \rho_A}{\partial t} dV + \oint_{\mathcal{S}} \mathbf{n}_A \cdot \hat{\mathbf{n}} d\mathcal{S} - \int_V r_A dV = 0 \tag{2.28}$$

As in the previous section, the transport theorem can be used to rewrite the first term in Eq. 2.28:

$$\int_{V(t)} \frac{\partial \rho_A}{\partial t} dV = \frac{d}{dt} \left[\int_{V(t)} \rho_A dV \right] - \oint_{\mathcal{S}} \rho_A \mathbf{v}_{\mathcal{S}} \cdot \hat{\mathbf{n}} d\mathcal{S} \tag{2.29}$$

Inserting Eq. 2.29 into Eq. 2.28 and using the definition $\mathbf{n_A} = \rho_A \mathbf{v_A}$ yields:

$$\frac{d}{dt} \left[\int_{V(t)} \rho_A dV \right] - \oint_{\mathcal{S}} \rho_A \mathbf{v}_{\mathcal{S}} \cdot \hat{\mathbf{n}} d\mathcal{S} + \oint_{\mathcal{S}} \rho_A \mathbf{v_A} \cdot \hat{\mathbf{n}} d\mathcal{S} - \int_V r_A dV = 0 \tag{2.30}$$

or:

$$\frac{d}{dt} \left[\int_{V(t)} \rho_A dV \right] + \oint_{\mathcal{S}} \rho_A (\mathbf{v_A} - \mathbf{v}_{\mathcal{S}}) \cdot \hat{\mathbf{n}} d\mathcal{S} - \int_V r_A dV = 0 \tag{2.31}$$

In practice, for many crystallization studies, is sufficient to represent the involved quantities as volume averaged values. With $\bar{\rho}_A$ and $\bar{r}_A$ as the averaged values for ρ_A and r_A, Eq. 2.31 becomes:

$$\frac{d}{dt} \left[\bar{\rho}_A V(t) \right] + \oint_{\mathcal{S}} \rho_A (\mathbf{v_A} - \mathbf{v}_{\mathcal{S}}) \cdot \hat{\mathbf{n}} d\mathcal{S} - \bar{r}_A V(t) = 0 \tag{2.32}$$

Analogously to the previous section derivation, the second term can be rewritten as:

$$\oint_{\mathcal{S}} \rho_A(\mathbf{v_A} - \mathbf{v}_{\mathcal{S}}) \cdot \hat{\mathbf{n}} d\mathcal{S} = -\sum_k \dot{V}_k \rho_{A,k} \tag{2.33}$$

in which $\rho_{A,k}$ is the volume averaged density of specie A in an input or output k-th material stream. Thus, Eq. 2.32 becomes:

$$\frac{d}{dt}\left[\bar{\rho}_A V(t)\right] - \sum_k \dot{V}_k \rho_{A,k} - \bar{r}_A V(t) = 0 \tag{2.34}$$

The term $\bar{r}_A$ in crystallization is related with the consumption of solute mass by crystals. Considering the volume of a particle V_{1c} given by:

$$V_{1c}(t) = k_V l(t)^3 \tag{2.35}$$

where $l(t)$ is the characteristic size of a particle and k_V the form factor of a particle, the mass of the particle will be $m_{1c} = \rho_c V_{1c}$ and the variation of the mass of a crystal in time is given by:

$$\frac{dm_{1c}}{dt} = \rho_c \frac{dV_{1c}}{dt} \tag{2.36}$$

Substituting Eq. 2.35 into 2.36 and applying the chain rule:

$$\frac{dm_{1c}}{dt} = 3\rho_c k_V l^2 \frac{dl}{dt} \tag{2.37}$$

and by the definition of Eq. 2.25, Eq. 2.37 becomes:

$$\frac{dm_{1c}}{dt} = 3\rho_c k_V l^2 G \tag{2.38}$$

Therefore, the rate of change of the mass of all the crystals in the system in volumetric basis (r_c) is:

$$r_c = \int_0^\infty \frac{dm_{1c}}{dt} n(l,t) dl = 3\rho_c k_V \int_0^\infty l^2 G n(l,t) dl \tag{2.39}$$

For a particular application in which the solute only loses mass via crystallization: $r_c = -\bar{r}_A$. Thus, Eq. 2.41 is rewritten as follows:

$$\frac{d}{dt}\left[\bar{\rho}_A V(t)\right] - \sum_k \dot{V}_k \rho_{A,k} + \left[3\rho_c k_V \int_0^\infty l^2 G n(l,t) dl\right] V(t) = 0 \tag{2.40}$$

Rearranging and substituting $\bar{\rho}_A V$ by the mass of solute A (m_A):

$$\frac{dm_A}{dt} = -3V(t)\rho_c k_V \int_0^\infty l^2 Gn(l,t)dl + \sum_k \dot{V}_k \rho_{A,k} = 0 \tag{2.41}$$

2.2.2 Numerical Methods for Solving the PBE

The use of the population balance (PBE - Population Balance Equation) represents a well-established approach as the mathematical tool for predicting particulate systems. However, its application results in a system of hyperbolic partial integro-differential equations to describe changes in particle size distribution (Christofides et al., 2007). The population balance is intrinsically linked to the mass, energy and moment balances to predict the rates of variation of the state variables. In addition, certain applications require fast and robust solutions, such as real-time application in predictive controllers, optimization methods or parameter estimation. These characteristics motivated extensive research for the development of adequate numerical methods for the system solution.

According to Silva et al. (2010) there are several numerical techniques available for PBE solution: Monte Carlo methods, methods based on weighted residues, method of classes and method of moments. The application and assumed hypotheses direct the choice of the most appropriate technique.

The method of moments was one of the first adopted methods and is based on the reformulation of the system to replace the particle size distribution by the moments of the distribution (Randolph and Larson, 1988). When growth is independent of the particle size and aggregation and breakage effects are negligible, for instance, the Standard Method of Moments (SMOM) is used.

According to Silva et al. (2010), the transformation by the method of the moments can lead to a closing problem due to the dependence of the moments differential equations of low order with moments of higher orders. Extensions of the method of moments such as QMOM (Quadrature Method of Moments) and DQMOM (Direct Quadrature Method of Moments) were developed in order to solve the closure problem. A disadvantage of the method is that the reconstruction of the distribution may be numerically unstable and may lead to numerical difficulties. The main advantage is its fast convergence, being the most common technique for coupling with computer fluid dynamics simulations.

The methods based on discretization divide the domain of the independent variable into intervals and transform the continuous PBE into a set of equations in terms of sectional moments of zero order. Among these methods are the finite difference method and the method of classes (Kumar and Ramkrishna, 1996a).

The weighted residue methods have extensive application in the solution of

partial differential equations and are based on the approximation of the number distribution by a series of trial functions whose coefficients are determined so that the approximation satisfies the population balance. These methods can be global, when the approximation seeks to represent the entire distribution, or in finite elements, in which the method is applied for each discretization element of the independent variable. The approximation coefficients result from the application of the approximation to the differential equation and from the imposition that the function of the approximation residue is orthogonal to a set of weighting functions. The choice of these functions results in the class of the weighted residues method, such as orthogonal collocation or Galerkin method (Lemos et al., 2014).

The method of the characteristics has extensive application for hyperbolic partial differential equations. The technique reduces the partial differential equation in a set of ODE (Ordinary Differential Equation) when determining the characteristic curves. Hounslow and Reynolds (2006) used this method for solving problems with nucleation and particle size independent growth. Aamir (2010) extended the application for cases where growth rate is dependent on size and nucleation rate dependent on the third order moment by combining the method of the characteristics with the QMOM.

Method of Moments

The application of the method of moments transforms the mathematical system of partial differential equations into ordinary differential equations by introducing a change of variable based on the j-th moment of the size distribution. The method reduces the numerical complexity of the system. However, extra numerical techniques are necessary to restore the size distribution of crystals. The j-th moment is given by Eq. 2.42:

$$\mu_j = \int_0^\infty l^j n(l,t) dl \tag{2.42}$$

In the following, the formulation of the method of moments is derived. Multiplying Eq. 2.26 by l^j and integrating into dl, it is obtained Eq. 2.43:

$$\int_0^\infty \left[\frac{\partial n}{\partial t} + \frac{\partial}{\partial l}(Gn) + n\frac{d\ln V}{dt} - \sum_k \frac{\dot{V}_k}{V} n_k - B_0 \delta(l - l_{min}) \right] l^j dl = 0 \tag{2.43}$$

Evaluating Eq. 2.43 term by term it is possible to formulate the method of

moments. Differentiating Eq. 2.42 in respect to t Eq. 2.44 is achieved: µ

$$\frac{d\mu_j}{dt} = \int_0^\infty l^j \frac{\partial n}{\partial t} dl \tag{2.44}$$

Eq. 2.44 corresponds to the first term of Eq. 2.43. Applying the integration by parts method to the second term:

$$\int_0^\infty \frac{\partial}{\partial l} \left[n(l,t) G \right] l^j dl = |l^j n G|_0^\infty - \int_0^\infty n G j l^{j-1} dl \tag{2.45}$$

where the term $|l^j n G|_0^\infty$ is defined as:

$$|l^j n G|_0^\infty = \left[\lim_{l \to \infty} \left(l^j n(l,t) G \right) - \lim_{l \to 0} \left(l^j n(l,t) G \right) \right] \tag{2.46}$$

and by the condition of compatibility, which refers to $\lim_{l\to\infty}[l^j n(l,t)]=0 \ \forall j$, Eq. 2.46 becomes:

$$|l^j n G|_0^\infty = 0 \tag{2.47}$$

Replacing Eq. 2.47 in Eq. 2.45:

$$\int_0^\infty \frac{\partial}{\partial l} \left[n(l,t) G \right] l^j dl = - \int_0^\infty n G j l^{j-1} dl \tag{2.48}$$

For the fifth term of the integral in Eq. 2.43 it is obtained:

$$\int_0^\infty -\delta(l - l_{min}) B_0 l^j dl = -l_{min}^j B_0 \tag{2.49}$$

The third and fourth terms of Eq. 2.43 become:

$$\int_0^\infty n \frac{d(\ln V)}{dt} l^j dl = \frac{d(\ln V)}{dt} \mu_j \tag{2.50}$$

$$\int_0^\infty \sum_k \frac{\dot{V}_k}{V} n_k(l,t) l^j dl = \sum_k \frac{\dot{V}_k}{V} \mu_{j,k} \tag{2.51}$$

In this way, replacing all the terms in Eq. 2.43, it is finally achieved the PSD moments equation:

$$\frac{d\mu_j}{dt} - \int_0^\infty n G j l^{j-1} dl - l_{min}^j B_0 + \frac{d(\ln V)}{dt} \mu_j - \sum_k \frac{\dot{V}_k}{V} \mu_{j,k} = 0 \tag{2.52}$$

Method of Classes coupled to the Method of the Characteristics

The Method of Classes was first proposed by Marchal et al. (1988) with the subdivision into discrete and contiguous intervals of the characteristic particle size. Such ranges are called bins and use macroscopic balances to describe their

populations. In this regard, the partial integro-differential formulation becomes an ordinary differential equation system of first order (Kumar and Ramkrishna, 1997).

Kumar and Ramkrishna (1997) introduced a method for the solution of the population balance that combines the method of *Moving Pivot (MP)*, formulated by the own authors (Kumar and Ramkrishna, 1996b) and which is an extension of the Method of Classes, with the method of characteristics to include growth and nucleation mechanisms. The proposed method allows the solution of the PBE with nucleation, growth and aggregation. In addition, it avoids problems of numerical instabilities common to the Method of Classes, as it is demonstrated in their article by examples that combine different mechanisms.

In the following, the formulation of the Kumar and Ramkrishna (1997) method, hereinafter referenced as Moving Sectional Method (MSM), is presented. Because the present work considers only growth (or dissolution) and nucleation, the terms related to aggregation (or breakage) will not be considered. The internal phase space of the particle is given only by its characteristic size.

On the basis of the population balance, Eq. 2.26, the method of the characteristics can be used to describe the variation of the numerical density. The differentiation of the second term provides:

$$\frac{\partial n}{\partial t} + G\frac{\partial}{\partial l}n(l,t) + n(l,t)\frac{dG}{dl} - \sum_k \frac{\dot{V}_k}{V}n_k - B_0\delta(l-l_{min}) + n\frac{d\ln V}{dt} = 0 \qquad (2.53)$$

Substituting $G = \dfrac{dl}{dt}$:

$$\frac{\partial n(l,t)}{\partial t} + \frac{dl}{dt}\frac{\partial}{\partial l}n(l,t) + n(l,t)\frac{dG}{dl} - \sum_k \frac{\dot{V}_k}{V}n_k - B_0\delta(l-l_{min}) + n\frac{d\ln V}{dt} = 0 \quad (2.54)$$

Defining the total derivative for the numerical density:

$$\frac{dn(l,t)}{dt} = \frac{\partial n(l,t)}{\partial t} + \frac{\partial n(l,t)}{\partial l}\frac{dl}{dt} \qquad (2.55)$$

Applying to Eq. 2.54:

$$\frac{dn(l,t)}{dt} + n(l,t)\frac{dG}{dl} - \sum_k \frac{\dot{V}_k}{V}n_k - B_0\delta(l-l_{min}) + n\frac{d\ln V}{dt} = 0 \qquad (2.56)$$

From Eq. 2.56, Method of Classes concepts are applyed to discretize the particle size in the region of interest. Assuming that each subdivision i (bin) is limited by l_i and l_{i+1}, its total number of particles rate can be obtained by integrating Eq. 2.56 with lower limit l_i and upper l_{i+1}:

$$\int_{l(t)_i}^{l(t)_{i+1}} \frac{dn(l,t)}{dt} dl + \int_{l(t)_i}^{l(t)_{i+1}} n(l,t) \frac{dG}{dl} dl + \\ - \int_{l(t)_i}^{l(t)_{i+1}} \left[\sum_k \frac{\dot{V}_k}{V} n_k + B_0 \delta(l - l_{min}) + n \frac{d \ln V}{dt} \right] dl = 0 \tag{2.57}$$

The integration by parts applied to the second integral results in:

$$\int_{l(t)_i}^{l(t)_{i+1}} \frac{dn(l,t)}{dt} dl + |n(l,t)G|_{l(t)_i}^{l(t)^{i+1}} - \int_{l(t)_i}^{l(t)_{i+1}} G \frac{\partial n(l,t)}{\partial l} dl + \\ - \int_{l(t)_i}^{l(t)_{i+1}} \left[\sum_k \frac{\dot{V}_k}{V} n_k + B_0 \delta(l - l_{min}) + n \frac{d \ln V}{dt} \right] dl = 0 \tag{2.58}$$

Rearranging:

$$\int_{l(t)_i}^{l(t)_{i+1}} \left[\frac{dn(l,t)}{dt} - G \frac{\partial n(l,t)}{\partial l} \right] dl + |n(l,t)G|_{l(t)_i}^{l(t)^{i+1}} + \\ - \int_{l(t)_i}^{l(t)_{i+1}} \left[\sum_k \frac{\dot{V}_k}{V} n_k + B_0 \delta(l - l_{min}) + n \frac{d \ln V}{dt} \right] dl = 0 \tag{2.59}$$

Using Eq. 2.55 and replacing it in the integrand of the first term:

$$\int_{l(t)_i}^{l(t)_{i+1}} \left[\frac{\partial n(l,t)}{\partial t} \right] dl + |n(l,t)G|_{l(t)_i}^{l(t)^{i+1}} + \\ - \int_{l(t)_i}^{l(t)_{i+1}} \left[\sum_k \frac{\dot{V}_k}{V} n_k + B_0 \delta(l - l_{min}) + n \frac{d \ln V}{dt} \right] dl = 0 \tag{2.60}$$

By means of the Leibniz integral differentiation rule, Eq. 2.60 becomes:

$$\frac{d}{dt} \left[\int_{l(t)_i}^{l(t)_{i+1}} n(l,t) dl \right] - \int_{l(t)_i}^{l(t)_{i+1}} \left[\sum_k \frac{\dot{V}_k}{V} n_k + B_0 \delta(l - l_{min}) + n \frac{d \ln V}{dt} \right] dl = 0 \tag{2.61}$$

By the definition of growth rate, the temporal variation of the bins boundaries is given by:

$$\frac{dl_i}{dt} = G(l_i) \tag{2.62}$$

The application of the method of the characteristics causes the discretized mesh to move with the characteristic velocity, treating the advection accurately. This approach reduces numerical diffusion in the solution when compared to other

discretization methods that approximate the advection term (Qamar, 2008).

Each bin has a particle number (population), given by:

$$N_i(t) = \int_{l_i}^{l_{i+1}} n(l,t)dl \tag{2.63}$$

Considering that it is possible to approximate the properties of the population using the discrete numerical density function:

$$n(l,t) = \sum_{i=1}^{M} [N_i(t)\delta(l - x_i)] \tag{2.64}$$

where x_i is the representative size of each bin, called as pivot (Kumar and Ramkrishna, 1997), and M is the total number of bins. Like the boundaries of the bins, the pivots also vary according to:

$$\frac{dx_i}{dt} = G(x_i) \tag{2.65}$$

Finally, by substituting Eq. 2.63 into Eq. 2.61 and integrating the term with the nucleation rate, ensuring that l_{min} is between l_0 and l_1, it is obtained:

$$\frac{d}{dt}N_i(t) - \sum_k \frac{\dot{V}_k}{V}N_{i,k} + N_i\frac{d\ln V}{dt} = \begin{cases} B_0 & \text{if } i = 0 \\ 0 & \text{if } i = 1, \ldots, M-1 \end{cases} \tag{2.66}$$

According to Kumar and Ramkrishna (1997) the method of the characteristics combined with the concepts of the Method of Classes prevents the discretization of the advection term to avoid problems of numerical instabilities. However, the nucleation term requires a special treatment. The difficulty lies in the fact that the new particles arising from nucleation must be added in some bin, but as these move with time there is a possibility that the new particles are smaller in size than the smaller size represented by the set of bins.

The solution adopted by Kumar and Ramkrishna (1997) is the addition of new bins successively at regular time intervals at the nuclei size, that is, with the properties: $l_0 = l_1 = x_0 = l_{min}$ and $N_1 = 0$ as initial values for the next simulation between $[t, t + \Delta t]$. The remaining bins must be renumbered. While the temporal variations of the other bins are given by the above-mentioned equation, for the new one it is:

$$\frac{dl_0}{dt} = 0 \tag{2.67}$$

$$\frac{dx_0}{dt} = \frac{1}{2}\left(\frac{dl_0}{dt} + \frac{dl_1}{dt}\right) \tag{2.68}$$

The Kumar and Ramkrishna (1997) formulation correctly quantifies the number of particles due to the nucleation. For a detailed analysis of moment conservation in the presence of nucleation see Chapter 3.

Eq. 2.66 in conjunction with Eqs. 2.65, 2.62, 2.67 and 2.68 form the population balance equation system. This set of equation is solved successively during a small time interval Δt, where at the end of each iteration a new bin is introduced into the system and the rest are renumbered. The interval Δt is given by the time required for the new bin to increase its boundaries to a size according to the desired resolution. Kumar and Ramkrishna (1997) point out that such approach allows the simulation of different events, such as the dissolution of all or a set of particles and simultaneous growth and dissolution.

After integration in several Δt's the amount of bins in the equation set can increase dramatically, making the technique computationally expensive. Kumar and Ramkrishna (1997) indicated that the bins that need to be eliminated are assimilated to their neighbors so that the desired population properties are preserved. Thus, needing to relocate the population of a bin with pivot x_i to its neighbors $i-1$ and $i+1$ the fractions relative to each of them, respectively η_{i-1} and η_{i+1} for the preservation of the moments of orders ϖ and ς are:

$$\eta_{i+1} = \frac{x_i^{\varpi} x_{i-1}^{\varsigma} - x_{i-1}^{\varsigma} x_{i-1}^{\varpi}}{x_{i+1}^{\varpi} x_{i-1}^{\varsigma} - x_{i+1}^{\varsigma} x_{i-1}^{\varpi}} \tag{2.69}$$

$$\eta_{i-1} = \frac{x_i^{\varpi} x_{i+1}^{\varsigma} - x_{i-1}^{\varsigma} x_{i+1}^{\varpi}}{x_{i+1}^{\varsigma} x_{i-1}^{\varpi} - x_{i+1}^{\varpi} x_{i-1}^{\varsigma}} \tag{2.70}$$

In their paper the authors suggest the collapse of any pivot in the case that $\frac{x_{i+1}}{x_{i-1}} < r_{critical}$, while preserving the properties of interest, which usually are the number and mass ($r_{critical}$ being a predefined value). Lee et al. (2001) suggest an approach to mesh readjustment. The adaptation criterion conserves mass and number of the distribution and is based on the variation of the PSD, in order to leave more sparsely spaced regions and maintain refined mesh for regions of significant variations.

Others numerical methods applied for the PBE solution

In addition to the numerical methods mentioned in the previous section, the crystallization literature uses several others for the PBE solution. In Costa et al. (2007) and Ramkrishna (2000) different methods are discussed. Three discretization methods are compared in Nopens et al. (2005), and Silva et al. (2010) performed a comparative study of moment-based techniques. Some of these techniques with expressive application in crystallizers are presented below.

The Finite Differences Method is widely used for the solution of partial differential equations, however, for the PBE solution it is not indicated due to its hyperbolic character. In this technique, the differential equations are approximated using finite difference schemes for the derivatives. Usually, nucleation is considered as a boundary condition. For example, in Eq. 2.26, the partial derivative with respect to the characteristic size can be approximated by a second order backward type:

$$\frac{\partial n(l,t)}{\partial l} \approx \begin{cases} \dfrac{1}{2\Delta l}\left(3n(l_i,t) - 4n(l_{i-1},t) + n(l_{i-2},t)\right) \text{ for } i > 2 \\ \dfrac{1}{\Delta l}\left(-\dfrac{3}{2}n(l_1,t) + 2n(l_2,t) - \dfrac{1}{2}n(l_3,t)\right) \text{ for } i = 1 \\ \dfrac{1}{2\Delta l}\left(n(l_3,t) - n(l_1,t)\right) \text{ for } i = 2 \end{cases} \tag{2.71}$$

Another technique used is the so-called finite-volume semi-discrete high-resolution method (Koren, 1993). In this method, the size domain l is discretized in M cells of size Δl and the points l_i refer to its centers and $l_{i\pm\frac{1}{2}}$ to its borders. It is defined $\mathcal{F}_i = G(l_i,t)n(l_i,t)$ as the rate of particles entering or leaving a cell and with approximation as in Eq. 2.72.

$$\mathcal{F}_{i+\frac{1}{2}} = \mathcal{F}_i + \frac{1+\kappa}{4}(\mathcal{F}_{i+1} - \mathcal{F}_i) + \frac{1-\kappa}{4}(\mathcal{F}_i - \mathcal{F}_{i-1}) \tag{2.72}$$

where κ is a parameter in the range $[-1,1]$. At the lower limit it represents a second order fully one-sided upwind scheme and at $\kappa = 1$ it is a standard second order central scheme. In the homogeneous case, the temporal variation of the size distribution evaluated in each centroid (n_i) is:

$$\frac{\partial n_i}{\partial t} = -\frac{\mathcal{F}_{i+\frac{1}{2}} - \mathcal{F}_{i-\frac{1}{2}}}{\Delta l}, \text{ para } i = 1,2,\ldots,M \tag{2.73}$$

Qamar et al. (2008) formulate it for the crystallization process with homogeneous nucleation and in supersaturated or undersaturated condition for $\kappa = 1/3$:

$$\text{If } G_{i+\frac{1}{2}} \geqslant 0 \begin{cases} \mathcal{F}_{\frac{1}{2}} = \mathcal{F}_{in} \text{ for } i = 0 \\ \mathcal{F}_{i+\frac{1}{2}} = \mathcal{F}_i \text{ for } i = 1, M-1 \text{ and } M \\ \mathcal{F}_{i+\frac{1}{2}} = \mathcal{F}_i + \frac{1}{2}\phi'(\mathfrak{r}_{i+\frac{1}{2}})\left(\mathcal{F}_i - \mathcal{F}_{i-1}\right) \text{ for } i = 2, ..., M-2 \end{cases} \tag{2.74}$$

with:

$$\mathfrak{r}_{i+\frac{1}{2}} = \frac{\mathcal{F}_{i+1} - \mathcal{F}_i + \varepsilon_m}{\mathcal{F}_i - \mathcal{F}_{i-1} + \varepsilon_m} \tag{2.75}$$

$$\text{If } G_{i+\frac{1}{2}} < 0 \begin{cases} \mathcal{F}_{M+\frac{1}{2}} = \mathcal{F}_{in} \text{ for } i = M \\ \mathcal{F}_{i+\frac{1}{2}} = \mathcal{F}_{i+1} \text{ for } i = 0, 1 \text{ and } M-1 \\ \mathcal{F}_{i+\frac{1}{2}} = \mathcal{F}_{i+1} + \frac{1}{2}\phi'(\mathfrak{r}_{i+\frac{1}{2}})\left(\mathcal{F}_{i+1} - \mathcal{F}_{i+2}\right) \text{ for } i = 2 \text{ to } M-2 \end{cases} \tag{2.76}$$

with:

$$\mathfrak{r}_{i+\frac{1}{2}} = \frac{\mathcal{F}_i - \mathcal{F}_{i+1} + \varepsilon_m}{\mathcal{F}_{i+1} - \mathcal{F}_{i+2} + \varepsilon_m} \tag{2.77}$$

and

$$\phi'(\mathfrak{r}_{i+\frac{1}{2}}) = \max\left(0, \min\left(2\mathfrak{r}_{i+\frac{1}{2}}, \min\left(\frac{1}{3}, \frac{2}{3}\mathfrak{r}_{i+\frac{1}{2}}, 2\right)\right)\right) \tag{2.78}$$

where ε_m is a small number to avoid division by zero.

Weighted residue methods correspond to the approximation of the solution with a series of tentative functions, whose coefficients must be determined. Solsvik and Jakobsen (2013) compare methods such as orthogonal collocation, Galerkin, Tau, and least squares. The studied system was a bubble column reactor. For the evaluated system, the authors found that the orthogonal collocation method provides the greatest efficiency in terms of computational time without losing accuracy in the prediction of PSD.

The approximation considers the expansion of the PSD function into an infinite set of orthogonal bases functions $\phi_k(l)$: $n(l,t) = \sum_{k=0}^{\infty} c_k(t)\phi_k(l)$. The coefficients $c_k(t)$ characterize the system. This approximation is replaced in the population balance equation in order to define the residuals $\mathcal{R}(l,t)$. These are forced to be orthogonal to a set of weighting functions $w_i(l)$, that is:

$$\int_0^{\infty} w_i(l)\mathcal{R}(l,t)dl = 0 \tag{2.79}$$

For example, defining the functions $w_i(l)$ as the Dirac delta functional, the orthogonal collocation method is obtained. These methods can also be applied in finite elements.

2.3 Instrumentation used in Crystallizers

One of the major challenges and obstacles of the development of the crystallization process corresponds to the difficulty of estimating the states since it is necessary to characterize the liquid phase and the solid phase.

In the liquid phase, the properties of interest are temperature and composition. In the solid phase it is desired to obtain the PSD and, in some cases, the morphology of the crystals.

The measurement of these variables is necessary for better understanding of the dominant mechanisms in the process; design of experiments and data acquisition to estimate kinetic parameters or identification of models and establishment of control schemes to maximize product quality and minimize operational costs. A discussion of the development of technologies for monitoring crystallization is presented by Nagy et al. (2013).

The concentration measurement can be performed by instruments such as refractometer and densimeters for binary systems (solute-solvent). Total Reflectance Fourier Transform Infrared (ATR-FTIR) is also used. A monitoring and control study for the crystallization of a drug was carried out by Liotta and Sabesan (2004) using in *in-situ* measurements of ATR-FTIR. Worlitschek and Mazzotti (2004) used an experimental scheme in which measurements of paracetamol concentration were performed by densimeter, but for this it was necessary to pump the process sample to the analyzer.

In ternary systems, such as enantioselective crystallization, specific instrumentation is required. Elsner et al. (2005) utilize an operating configuration of a racemic solid-forming enantioselective crystallizer by pumping samples of the liquid to a polarimeter and a densimeter.

An advance in the particle size distribution measurement technology that allowed *in situ* characterization, which can be applied without dilution, is the *Focused Beam Reflectance Measurement* (FBRM). However, this apparatus measures the chord length distribution (CLD), which differs from the particle size distribution. Thus, reconstruction is necessary to obtain an estimation of the PSD (Worlitschek and Mazzotti, 2004). Many works are being carried out to provide techniques for transforming CLD into PSD. These works use the three-dimensional morphology of the crystal and evaluate methods for its two-dimensional projection (Kail et al., 2007).

The FBRM measurement principle is based on the backward light scattering. A probe immersed in the fluid emits a rotating laser at a constant speed. When there is an intersection by a particle, the light scattering occurs, a fraction of this is collected by a detector in the opposite direction of the emission. Due to the

rotation of the emission, the laser tends to travel through the particle constantly dispersing light to the detector. Due to irregularities or movements this signal is noisy and requires low frequency filtering. After traversing the entire particle, there is a reduction in scattered light. At this moment there is the measurement of the time elapsed to cross the particle. Since the velocity is known, one can get the chord length (Chianese and Kramer, 2012).

2.4 Control Methods Applied to Batch Crystallizer

The term control for batch crystallizers is used in the literature in two main configurations: open-loop optimal control and closed-loop control.

In the first case, the intention is to find the profile of the manipulated variables that leads to the optimal operational condition before starting the process. The optimal condition to be achieved is based on one or more performance indexes of interest associated with PSD of the final time of operation. On the second configuration, the closed-loop batch crystallizer control consists of the manipulation of certain variables in order to guarantee the operation as desired.

2.4.1 Open Loop Control

Mullin and Nỳvlt (1971) called as programmed cooling the open loop control of cooling crystallizers. The proposal was that nucleation could be maintained at a constant rate by using programmed cooling curves. The model adopted is based on a supersaturation balance. Jones (1974) using the population balance formulation arrived at a similar but more generic model for the supersaturation balance. Using the method of moments, the author determined the optimal cooling profile using optimal control concepts. Both works have shown theoretically and experimentally that for a greater growth of the crystals the temperature must reduce slowly at the beginning and more quickly at the end of the process.

Several other studies are found in the literature that aim to obtain the optimal trajectory to be implemented in the crystallization. Ajinkya and Ray (1974) evaluated the optimization to provide maximum average size and minimum PSD variance. Chang and Epstein (1982) compared the use of the model via moments with model using the method of the characteristics for different indexes of performance. The results showed agreement on the use of both types of model. Myerson (2002) formulated the optimal control problem generically based on nonlinear programming.

Worlitschek and Mazzotti (2004) evaluated the crystallization of paracetamol in ethanol. A PBE model with solution by the Galerkin method and saturation given by the Schroder Van-Laar equation was used. Before the application of non-linear optimization techniques, the modeling, parameter estimation and online PSD monitoring were discussed. An important focus was given to the difficulties related to the instrumentation of the crystallization process, especially in relation to the size distribution measurements. The authors used the FBRM to obtain the CLD and restored the PSD through the projection method in convex sets. In the optimization adopted, the intention was to obtain a PSD with imposed shape. Mathematically, it corresponds to the minimization of the objective function given by the least squares of the errors between the calculated distribution in each cell with the desired distribution. The manipulated variable was discretized over time and linearly interpolated for the dynamic simulations.

Angelov et al. (2008) formulated the open loop optimization for preferential crystallization of the enantiomeric solid conglomerate system. The manipulated variable, the internal temperature of the crystallizer, was parameterized using B-spline. With the method of moments, the authors calculated the optimal temperature trajectory. A low initial variation profile with pronounced final variation was obtained by considering the third order momentum maximization of the preferred enantiomer and 95% purity constraint.

One of the first works to assess the inclusion of fine removal in open loop optimization was Jones et al. (1984), which addressed the batch crystallization of potassium sulfate in aqueous solution. The crystallizer configuration consisted of classified removal of fine particles, pumping the fines stream to an external heat exchanger, and cooling to the operating temperature before recycling the stream. The experiment demonstrated that the removal of fines reduces the amount of crystals formed by secondary nucleation, increases the average size of the crystals and decreases the coefficient of variation of the PSD.

Stoller et al. (2008) (apud Chianese and Kramer (2012)) experimentally analyzed the dissolution of fines in an external heating system similar to Jones et al. (1984). The analysis utilized potassium sulfate with stream recycle with fines of less than 300 μm and a 2 mm inner diameter tube. The service fluid was oil at 130 and 150℃. Using a residence time of 3 s, the authors have showed that the dissolution is not completely affected, being dissolved from 60 to 80% of the initial mass. With a mathematical model using computational fluid dynamics it was found that 90% of the dissolved mass occurs in the vicinity of the tube wall.

A methodology for the open-loop optimization of crystal size distribution considering growth, nucleation and dissolution for crystallization with cooling is presented in Nagy et al. (2011). The optimal temperature trajectory was obtained

by the joint solution of the PBE by the method of moments with the method of the characteristics. The approach was evaluated experimentally for crystallization of potassium aluminum in water. Kinetic parameters of the model were determined based on laboratory and pilot plant data. The approach considers *in situ* dissolution, e.g, undersaturation is forced inside the crystallizer. According to the authors, the methodology allowed for greater flexibility in the final PSD shape, since the dissolution eliminates nucleated crystals in case of accidental sowing, besides not requiring extra equipment for the recycling of fines.

2.4.2 Closed Loop Control

The optimal control in open loop is of great importance to guide the operation of the crystallizer. However, in the presence of disturbances, modeling errors and deviation in the trajectory of the manipulated variables, the operation will not occur according to the optimal obtained offline.

Rawlings et al. (1993) indicated that the open loop operational path is not enough to control the PSD. The use of this approach solely will not allow a reproducible operation, and there may be a discrepancy from the expected optimal. The reason lies mainly in the difficulties of characterizing the kinetics of crystals.

The crystallization operation is benefited by the use of the optimal control in closed loop, which can be based on models or not. This approach promotes the interaction of the control system with the process by using feedback from the measurements of process variables.

Model-based control can use process data to identify models. However, in the control of particulate processes it is common to use models based on the first principles, that is, mass, energy and population balances, with empirical kinetics. The formulation of reduced models from a most complete phenomenological model is also used. (Chianese and Kramer, 2012).

In the closed-loop control approach without using dynamic models, strategies based on the process knowledge and heuristics are employed. For example, there is the so-called direct nucleation control approach, whose concept is to keep the number of particles constant. Another method is the concentration feedback control that aims to maintain supersaturation in an ideal range for the operation (Nagy and Braatz, 2012).

Model-based predictive control (MPC) corresponds to a methodology capable of providing high-performance operation by considering desired performance indexes in the formulation of the objective function and by including constraints of the manipulated and process variables. MPC is also able to handle interactions of multivariate systems. According to Shi et al. (2005), the MPC method calculates

the control action by the online solution of the optimization problem with constraint at each sampling instant. Therefore, the method suppresses influence of external disturbances and tolerates model errors.

Eek (1995) used a linear MPC strategy considering two ways of obtaining the models: reduced order of the phenomenological model and models based on input and output data. The results obtained in the predictive control of a pilot plant showed a better performance when using the model identified by process data. A possible explanation for this refers to the hypotheses adopted for the formulation of the model based on fundamental principles.

Rohani et al. (1999) evaluated the multivariable control of crystallizers. They compared the linear control based on the ARX model (Autoregressive with eXogenous Input) with the nonlinear neuronal networks based model. In their analyzes, linear predictive control was used for MISO (Multi-Input Single-Output) models. In addition, to deal with process constraints, the Feasible Sequential Quadratic Programming (FSQP) optimizer was used. The authors reported problems in the optimization method for large control horizons, so most of the considered results used a control horizon with a single sampling time. The authors concluded that the nonlinear control had better performance.

Eaton and Rawlings (1990) extended the application used by Witkowski and Rawlings (1987) for continuous operation of nonlinear predictive control to batch crystallizer. The model used is based on PBE and makes a segregation of the distribution due to the nucleation from the distribution corresponding to the seeded crystals. The overall distribution was the sum between these two. The controller was formulated to minimize the ratio between the third order moment of the nucleation distribution part and the PSD of the seeded crystals. A constraint was adopted to ensure desired productivity. The solution of the nonlinear optimization problem was performed after the application of the orthogonal collocation method and used the successive quadratic programming to solve the optimization problem. According to the authors, the method is feasible to be applied in real time, but its complexity may be hindering for industrial applications.

According to Christofides (2002a) the difficulty of developing model based control for crystallizers is due to the system characteristics (distributed parameters, integral and hyperbolic). The PBE solution methods can result in a system of high order ordinary differential equations, being impractical to implement in real time for predictive control. The authors presented methods for the order reduction of the model based on population balance using weighted residue method. They also addressed several issues related to model-based controllers, such as parameter uncertainty, non modeled actuator and sensor dynamics, robust and fault tolerant control.

Zhang and Rohani (2003) considered the closed-loop control with an extended Kalman filter to estimate seven unmeasured variables based on three-variable measurements: temperature, concentration, and temperature of the thermal jacket. A cooling trajectory was obtained offline and the implementation during operation used a conventional PI controller. A numerical implementation showed that the approach allowed a PSD with lower coefficient of variation and larger average size when compared with natural or linear cooling.

Shen et al. (1999) (apud Chianese and Kramer (2012)) evaluated the use of model-based predictive control in order to track the optimal trajectory obtained offline. It was demonstrated that MPC via global linearization methodologies, generic models and multi-linear models provides superior performance to the use of conventional PI controllers.

Shi et al. (2005) developed a methodology for predictive control using a model based on the method of moments. The approach considered the separation of the nucleation moments and the seeding crystals. The objective function adopted is to minimize the third order moment of the nucleation part while adopting a constraint for the third order moment of the seeded distribution range. Simulation results, which used PBE solution through discretization in second order finite differences as a plant, showed that the strategy was able to reduce the amount of fines generated in relation to linear cooling. The effect of modeling errors on the controller performance were also evaluated, showing that the control acts more severely on the manipulated variable, but achieves a final PSD similar to the case of coincident model and plant.

Mesbah et al. (2012) presented a non-linear control based on output feedback type models for the optimal operation of industrial semi-batch crystallizers. The control strategy was formulated to solve an optimal control problem. The authors also studied the efficiency of the methodology in the presence of model imperfections.

Kwon et al. (2013) compared different morphology control strategies for batch crystallization of proteins. Predictive control and conventional methods were evaluated, such as constant temperature control and constant supersaturation. The predictive controller was able to regulate the desired morphology at the end of the batch, in addition to reducing undesirable effects of nucleation.

Gamez-Garci et al. (2012) obtained the optimal open loop trajectory of a cooling crystallizer using method of moments and supersaturation given by a polynomial equation with respect to temperature. During the operation a robust controller was applied to the optimal trajectory tracking. Two robust control approaches were also evaluated: modeling error compensation and integral high order sliding mode control. Good robustness properties were reported.

A nonlinear model predictive controller was applied by de Moraes et al. (2018) for a continuous evaporative crystallizer of potassium sulphate. The objective was the

regulatory control for disturbances on the feed solute and flowrate by manipulating temperature and steam outflow rate. The MPC formulation was compared to PI controllers and showed better performance.

2.5 Literature Critical Review

The literature on crystallizers may be considered rather extensive for the evaluation of numerical methods and PSD control techniques. Studies concerning the application of crystallization methods for the separation of enantiomers are more restricted. Most of the work in this topic deals with the separation of conglomerate-forming enantiomeric compounds. For this case, there are works that aim at mathematical modeling to evaluate the dynamics of crystallization (Elsner et al., 2005; Lorenz et al., 2006a). An evaluation of the optimal control in open loop was performed by Angelov et al. (2008).

Enantioselective crystallization for racemic compounding systems is not much explored in the literature regarding the mathematical modeling of crystallization dynamics. Yinghong (2009) experimentally evaluates the kinetics of growth and nucleation and uses models of moments and Laplace transform considering only the preferential enantiomer. Lorenz et al. (2006b) discusses the application of preferential crystallization to this system and demonstrates its viability experimentally.

Regarding the separation of enantiomers by crystallization, the present work contributes with the theoretical evaluation of mathematical model that allows the study of the dynamics of the PSD incorporating in a more rigorous form the constraints of the phase diagram. Another contribution refers to the closed-loop control of these systems including the dissolution of fine particles.

Chapter 3

First Bin Analysis for the Moving Sectional Method

As shown by Kumar and Ramkrishna (1997) the incorporation of nucleation phenomena by the Moving Sectional Method requires the workaround of successively adding new bins at minimal size, thus it is an approximation and a source of errors in the particle size distribution properties. The added bin occupies the first position in the grid with pivot as $x_0 = l_{min}$ and at the time of addition it is initialized with $N_0 = 0$, which is refereed here as a collapsed bin.

The nuclei size usually is very smaller compared to the working particle size range, because of that in the mathematical modeling a minimal size of zero is often considered. At a first glance, the introduction of nucleated particles could be treated as it is considered by Kumar and Ramkrishna (1997) for dealing with aggregation of particles, which uses neighbors pivots both to the left and to the right of a pivot to conserve two arbitrary moment orders. However, because of the very small size of the incoming nuclei, posing a pivot smaller than the minimal size would subject the dynamic integration to very small time steps and would be unsuitable for some applications.

In this section, the strategy of adding bins at minimal size l_{min} at periodic times is analyzed in respected to the conservation of a k-th moment of the distribution. The focus is in the nucleation and growth mechanisms and, since the MSM can adequately preserve the growth of seeded particles, only the nucleation size range is used in the analysis. The analysis is performed for the case of size independent growth.

Firstly, the preservation of a k-th moment when using the MSM for only a single bin added at initial time is evaluated. Some simplifications are considered in the definition of the added bin growth rate G_0 and the calculated moments using the MSM are confronted with the expected moments for test cases. It is shown that when the desired moment to be conserved is of order $k > 1$, there is additional

difficult since G_0 is dependent on the expected moment.

Later, the case with multiple added bins to describe the nucleated particles is addressed, which is the scheme suggested by Kumar and Ramkrishna (1997) to minimize the overall moment conservation error. It is shown that if the order to be preserved is $k = 1$, the equation for G_0 can be stated as in the case with single bin addition with the other bins moving accordingly with the computed system growth rate G. However, such condition does not hold true for the case with $k > 1$. In this case, a different pivot movement scheme is defined and test cases are reported comparing the expected moments to the calculated by the method.

Finally, strategies for defining proper times for adding bins during the simulation are discussed. Ideally, new bins should be added at very small time intervals in order to preserve most of the distribution properties. However, this corresponds to high computational cost and in practice a commitment between the addition of bins and the simulation performance is required. The bin addition based solely on a predefined time interval is not suitable when the growth and nucleation varies along the simulation, since it causes more errors when those variables are at high values, whereas it may result in unnecessary bins additions. Thus, controlled bins addition schemes based on the current values of the growth and nucleation rate are presented.

3.1 MSM with nucleation and growth and single added bin at initial time

3.1.1 Sectional Moment at a bin

Each bin i has a k-th moment defined as Eq. 3.1 with the boundaries l_i and l_{1+1}.

$$\mu_k^{(i)} = \int_{l_i}^{l_{i+1}} l^k n(l,t) dl \tag{3.1}$$

Applying Leibnitz theorem on the moment definition Eq. 3.1, in order to get its time derivative $\frac{d\mu_k^{(i)}}{dt}$, results in Eq. 3.2. The notation for the dependence of $n(l,t)$ and $G(l,t)$ on l and t is not included for convenience.

$$\frac{d\mu_k^{(i)}}{dt} = \frac{d}{dt}\left[\int_{l_i}^{l_{i+1}} l^k n dl\right] = \int_{l_i}^{l_{i+1}} \frac{\partial(l^k n)}{\partial t} dl + \left[l^k n G\right]_{l_i}^{l_{i+1}} \tag{3.2}$$

It is considered the PBE with growth mechanism and with a source of new particles $\dot{n}_{new}(l)$ included inside the bin i ($l_i \leq l \leq l_{i+1}$):

$$\frac{\partial n}{\partial t} + \frac{\partial}{\partial l}(Gn) = \dot{n}_{new}(l) \tag{3.3}$$

Applying the integral operator $\int_{l_i}^{l_{i+1}} l^k(\cdot)dl$ on both sides it is obtained Eq. 3.4

$$\int_{l_i}^{l_{i+1}} \frac{\partial(l^k n)}{\partial t}dl + \int_{l_i}^{l_{i+1}} l^k \frac{\partial}{\partial l}(Gn)dl = \int_{l_i}^{l_{i+1}} l^k[\dot{n}_{new}(l)]dl \tag{3.4}$$

Integrating by parts the second term ($u = l^k$, $du = kl^{k-1}dl$):

$$\int_{l_i}^{l_{i+1}} l^k \frac{\partial}{\partial l}(Gn)dl = \left[l^k nG\right]_{l_i}^{l_{i+1}} - \int_{l_i}^{l_{i+1}} Gnkl^{k-1}dl \tag{3.5}$$

Then, substituting the second term in Eq. 3.4 by Eq. 3.5 it is obtained:

$$\int_{l_i}^{l_{i+1}} \frac{\partial(l^k n)}{\partial t}dl + \left[l^k nG\right]_{l_i}^{l_{i+1}} = \int_{l_i}^{l_{i+1}} Gnkl^{k-1}dl + \int_{l_i}^{l_{i+1}} l^k[\dot{n}_{new}(l)]dl \tag{3.6}$$

The left hand side of Eq. 3.6 can be substituted by Eq. 3.2 to obtain the sectional moment at a given bin i:

$$\frac{d\mu_k^{(i)}}{dt} = \int_{l_i}^{l_{i+1}} Gnkl^{k-1}dl + \int_{l_i}^{l_{i+1}} l^k[\dot{n}_{new}(l)]dl \tag{3.7}$$

3.1.2 Including Nucleation for the expected process: nuclei always added at l_{min}

In this case the nuclei are added at the nuclei size l_{min}, which is considered to be constant, and is a conventional nucleation definition (Eq. 3.8) found in the literature (Randolph and Larson, 1988).

$$\dot{n}_{new}(l) = B_0\delta(l - l_{min}) \tag{3.8}$$

Because the lower boundary l_0 in the MSM is fixed constant at l_{min} the first bin is supposed to receive the nucleated particles, since $l_{min} \in [l_0, l_1] \quad \forall \quad t \geqslant 0$.

Using the derived equation for the sectional moment rate Eq. 3.7 at first bin $i = 0$ and substituting the boundary $l_0 = l_{min}$ and also $\dot{n}_{new}(l)$ using Eq. 3.8 it is obtained Eq. 3.9.

$$\frac{d\mu_k^{(0)}}{dt} = \int_{l_{min}}^{l_1} Gnkl^{k-1}dl + \int_{l_{min}}^{l_1} l^k[B_0\delta(l - l_{min})]dl \tag{3.9}$$

Integrating the last term results in Eq. 3.10, which gives the rate of change of the first bin sectional moment order k for the expected nucleation occurring at the minimal size.

$$\frac{d\mu_k^{(0)}}{dt} = \int_{l_{min}}^{l_1} Gnkl^{k-1}dl + B_0 l_{min}^k \tag{3.10}$$

3.1.3 Sectional first bin moment when using the MSM

Because the distribution is considered to occur at the representative size (the pivots), new particles entering in the system due to nucleation will have a size greater than expected as the particle grow, since the pivot is greater than the nuclei size for $t > 0$. The sectional moment for the first bin ($i = 0$) calculated by the moving sectional method is denoted as $\mu^{(0)}_{k,msm}$.

Considering the definition for the sectional moment (Eq. 3.1) for the first bin $i = 0$:

$$\mu^{(0)}_k = \int_{l_0}^{l_1} l^k n(l,t) dl \tag{3.11}$$

Using the definition from Kumar and Ramkrishna (1997) for the MSM $n(l,t) = \sum_i N_i \delta(l - x_i)$, and substituting into Eq. 3.11, Eq. 3.12 is achieved. Because of the MSM approximation, the nomenclature for the sectional moment $\mu^{(i)}_k$ is replaced to $\mu^{(i)}_{k,msm}$.

$$\mu^{(0)}_{k,msm} = \int_{l_0}^{l_1} l^k \sum_i N_i \delta(l - x_0) dl \tag{3.12}$$

The integration of the right hand side results in:

$$\mu^{(0)}_{k,msm} = x_0^k N_0 \tag{3.13}$$

Differentiating Eq. 3.13 with respect to time gives:

$$\frac{d\mu^{(0)}_{k,msm}}{dt} = \frac{d}{dt}[N_0 x_0^k] \tag{3.14}$$

Thus:

$$\frac{d\mu^{(0)}_{k,msm}}{dt} = \frac{dN_0}{dt} x_0^k + N_0 \frac{dx_0^k}{dt} = \frac{dN_0}{dt} x_0^k + N_0 k x_0^{k-1} \frac{dx_0}{dt} \tag{3.15}$$

From Kumar and Ramkrishna (1997) MSM equation set with nucleation and growth, the following definitions are used:

$$\frac{dN_0}{dt} = B_0 \tag{3.16}$$

$$\frac{dx_0}{dt} = G_0 \tag{3.17}$$

In Eq. 3.17, G_0 corresponds to the first bin growth rate when using the MSM. Substituting these two equations into Eq. 3.15 gives:

$$\frac{d\mu_{k,msm}^{(0)}}{dt} = B_0 x_0^k + N_0 k x_0^{k-1} G_0 \tag{3.18}$$

3.1.4 Equating the moment calculated from the moving pivot

The previous derivations provided the first bin sectional moment for the following cases:

- For the source of particles at the nuclei size l_{min} yielding the expected first bin sectional moment - Eq. 3.10
- For the source of particles at the first pivot size because of the use of the MSM - Eq. 3.18

These two approaches are then compared. Equating Eq. 3.10 to Eq. 3.18 provides:

$$\frac{d\mu_{k,ex}^{(0)}}{dt} = \frac{d\mu_{k,msm}^{0}}{dt} \tag{3.19}$$

which gives:

$$l_{min}^k B_0 + \int_{l_{min}}^{l_1} Gnkl^{k-1} dl = B_0 x_0^k + N_0 k x_0^{k-1} G_0 \tag{3.20}$$

Solving for the first pivot growth rate G_0:

$$G_0 = \frac{1}{N_0 k x_0^{k-1}} \left\{ B_0 (l_{min}^k - x_0^k) + \left[\int_{l_{min}}^{l_1} Gnkl^{k-1} dl \right] \right\} \tag{3.21}$$

This equation relates the first bin growth rate G_0, which can be a function of l and t, when applying the MSM with the actual process growth rate $G(t)$ and nucleation rate $B_0(t)$. Thus the first bin growth rate can be adjusted in order to preserve a desired k-th moment. Note that by the definition from Eq. 3.16 the zero order moment is inherently preserved by the MSM.

Although Eq. 3.21 provides the adjustment of G_0 for preserving a moment of order $k > 0$ and $k = 0$ for the generic case with size dependent and time varying growth rate and time varying nucleation rate, it is not of practical use since the integral in Eq. 3.21 requires specialized numerical methods. Thus, in the following, Eq. 3.21 is evaluated for particular cases that are common in the literature.

3.1.5 Particular cases for first bin moment conservation

In this section simplifications are applied to Eq. 3.21 providing relations for the first bin growth rate using the MSM. The following cases are evaluated:

1. Size independent growth rate;
2. Size independent growth rate preserving order $k = 1$;
3. Constant nucleation and growth rate preserving order $k = 1$ with $N_0(0) = 0$;
4. Constant nucleation and growth rate with $N_0(0) \geqslant 0$ and $l_{min} \geqslant 0$;
5. Constant nucleation and growth rate with $N_0(0) = 0$ and $l_{min} = 0$.

Figure 3.1 schematize the simplifications for the first bin growth rate based on Eq 3.21 for a better overview of the above considerations. The refereed equations in the diagram will be discussed in the following.

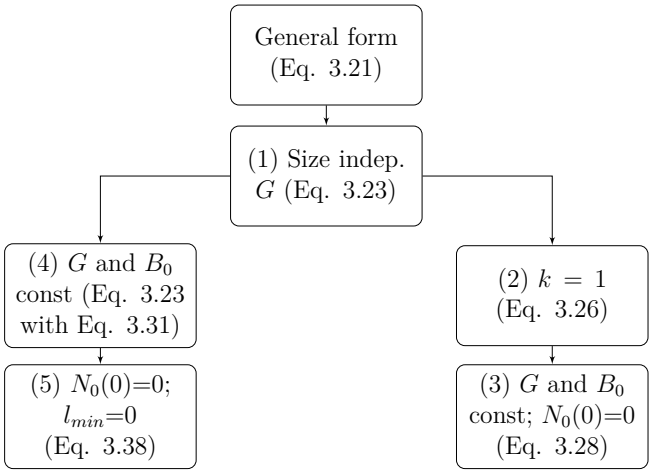

Figure 3.1: Schematic overview of G_0 simplifications.

Size independent growth rate

For this case the integral in the last term of Eq. 3.21 is simplified as:

$$\int_{l_{min}}^{l_1} Gnkl^{k-1}dl = Gk\int_{l_{min}}^{l_1} nl^{k-1}dl = kG\mu_{k-1,ex}^{(0)} \tag{3.22}$$

Eq. 3.21 is then:

$$G_0 = \frac{1}{N_0 k x_0^{k-1}}\left[B_0(l_{min}^k - x_0^k) + kG\mu_{k-1,ex}^{(0)}\right] \tag{3.23}$$

where $\mu_{k,ex}^{(0)}$ is the expected value of the k-th moment for the first bin.

This equation indicates that some desired k-th moment can be conserved if the growth rate for the first bin is adjusted using Eq. 3.23. For that, $\mu_{k,ex}^{(0)}$ can be obtained solving the expected sectional moment equation for bin $i = 0$ (Eq. 3.10). This can be accomplished by coupling the MSM equation set to the k differential equations for the expected sectional moment at the first bin. Thus, the use of Eq. 3.23 is only possible if the expected moment $\mu_{k,ex}^{(0)}$ can be determined. However, if $k = 1$, Eq. 3.23 will not depend on the expected moment, as described in the following.

Size independent growth rate preserving order $k = 1$

Substituting $k = 1$ in Eq. 3.23:

$$G_0(t) = \frac{1}{N_0}\left[B_0(l_{min} - x_0) + G\mu_{0,ex}^{(0)}\right] \tag{3.24}$$

Because of definition in Eq. 3.16, the expected moment order zero for the first bin $\mu_{0,ex}^{(0)}$ is represented by N_0 when using the MSM. Thus:

$$G_0 = \frac{1}{N_0}\left[B_0(l_{min} - x_0) + GN_0\right] \tag{3.25}$$

Rearranging:

$$G_0 = \frac{B_0}{N_0}(l_{min} - x_0) + G \tag{3.26}$$

Eq. 3.26 was obtained by Spicer et al. (2002). It indicates that for preserving the moments of order 0 and 1, the first bin rate with the MSM can be adjusted by adding to the system growth rate G a portion proportional to the distance of the zero pivot to the critical size $(l_{min} - x_0)$ and with the number of particles N_0 acting as an inertia term.

Constant nucleation and growth rate preserving order $k = 1$

Even thought those assumptions are not realistic for practical application, since both growth and nucleation varies according to the system supersaturation level, it provides good insights on the first bin size dynamics.

When G is constant it is also assumed that the first pivot growth rate is also constant, thus: $x_0(t) = l_{min} + G_0 t$. Moreover, with nucleation rate constant, the number of particles in the first bin is: $N_0(t) = B_0 t$ when considering the collapsed added bin ($N_0(t = 0) = 0$). With those simplifications Eq. 3.26 is then:

$$G_0 = \frac{B_0}{B_0 t}(l_{min} - l_{min} - G_0 t) + G = -\frac{1}{t}(G_0 t) + G \tag{3.27}$$

Thus, G_0 assumes the form:

$$G_0 = \frac{1}{2}G \tag{3.28}$$

as it is used by Kumar and Ramkrishna (1997) and indicates that the moments of orders $k = 1$ and $k = 0$, when both nucleation and growth are constant, are preserved if the first bin growth rate is half of the calculated system growth rate.

Constant nucleation and growth rate with $l_{min} \geqslant 0$ and $N_0(t = 0) \geqslant 0$

The expected moment of order k for the first bin ($\mu^{(0)}_{k,ex}$) can be obtained in the condition of constant nucleation and growth rate using Eq. 3.10:

$$\frac{d\mu^{(0)}_k}{dt} = kG\mu^{(0)}_{k-1,ex} + B_0 l^k_{min} \tag{3.29}$$

Eq. 3.29 can be rewritten for the aforementioned condition of G and B constant, in which $\mu^{(0)}_k(0)$ is the initial value of the k-th moment (for the bin $i = 0$):

$$\mu^{(0)}_{k,ex}(t) = kG\int_{t_0}^{t} \mu^{(0)}_{k-1,ex}dt + B_0 l^k_{min}t + \mu^{(0)}_k(0) \tag{3.30}$$

By recursively integrating Eq. 3.30 using $k = [0, 1, 2, 3, \ldots]$ it is possible to obtain Eq. 3.31, which relates the expected first bin moment k for constant growth and nucleation with the simulation time t, nucleation rate B_0, growth rate G, minimal size l_{min} and initial value of moments $\mu^{(0)}_j(0)$.

$$\mu^{(0)}_{k,ex}(t) = B_0 \sum_{j=0}^{k} \left[l^{k-j}_{min} G^j t^{j+1} \frac{k!}{(k-j)!} \frac{1}{(j+1)!} \right] + \sum_{j=0}^{k} \left[G^j t^j \mu^{(0)}_{k-j}(0) \frac{k!}{(k-j)!} \frac{1}{j!} \right] \tag{3.31}$$

Thus, it is possible to use $\mu^{(0)}_{k-1,ex}(t)$ from Eq. 3.31 into Eq. 3.23 to define the first bin growth rate G_0 under the simplification of constant growth and nucleation rate, which for small simulation time interval can be acceptable.

Constant nucleation and growth rate with $l_{min} = 0$ and $N_0(t = 0) = 0$

In this case, using $l_{min} = 0$ turns Eq. 3.23 into:

$$G_0 = \frac{1}{N_0 k x_0^{k-1}} \left[-B_0 x_0^k + kG\mu^{(0)}_{k-1,ex} \right] \tag{3.32}$$

The expected first bin moment, Eq. 3.31, with further simplifications of $l_{min} = 0$ and $N_0(t{=}0) = 0$, which occurs for the condition of an added collapsed bin at zero size, is rewritten as in Eq. 3.33. Note that for $N_0(t{=}0) = 0$, the initial moments

$\mu_k^{(0)}(0)$ are also zero. Moreover, it is used the definition of $l_{min}^{(k-j)}$ as 1 for $j = k$ and 0 otherwise if $l_{min} = 0$.

$$\mu_{k,ex}^{(0)}(t) = \frac{G^k B_0 t^{k+1}}{k+1} \tag{3.33}$$

Using the definitions for constant growth and nucleation: $N_0 = B_0 t$ and $x_0 = G_0 t$ when $l_{min} = 0$ together with Eq 3.33 into Eq. 3.32 it is obtained:

$$G_0 = \frac{1}{B_0 t k G_0^{k-1} t^{k-1}} \left[-B_0 G_0^k t^k + kG \frac{G^{k-1} B_0 t^k}{k} \right] \tag{3.34}$$

Rearranging:

$$G_0 = \frac{-B_0 G_0^k t^k}{B_0 t k G_0^{k-1} t^{k-1}} + \frac{kG \frac{G^{k-1} B_0 t^k}{k}}{B_0 t k G_0^{k-1} t^{k-1}} \tag{3.35}$$

which is simplified to:

$$G_0 = \frac{-G_0}{k} + \frac{G^k B_0}{k G_0^{k-1}} \tag{3.36}$$

Isolating G_0 in Eq. 3.36 gives:

$$(1 + 1/k) G_0 = \frac{G^k}{k} \tag{3.37}$$

$$G_0 = (k+1)^{\frac{-1}{k}} G \tag{3.38}$$

Eq. 3.38 relates G_0 to the system growth rate G by the proportional constant $(k+1)^{\frac{-1}{k}}$, which for $k = 1$ yields $G_0 = 0.5G$ as in Eq. 3.28 and for $k = 3$ $G_0 \approx 0.63G$. Eq. 3.38 serves as a guidance on how to define the first bin movement in respect to the growth rate.

3.1.6 Simple test cases for illustrating the particular cases

In the next, some simple test cases are presented in order to exemplify and compare the particular cases described earlier. All test scenarios are given from an initial time $t = 0$ to a final time $t = 10$ and without intermediary bin additions. The following cases are evaluated:

1. Constant G and B_0 with $l_{min} = 0$
2. Constant G and B_0 with $l_{min} > 0$
3. Constant B_0 and time varying $G = G(t)$ with $l_{min} = 0$
4. Constant G and time varying $B_0 = B_0(t)$ with $l_{min} = 0$

5. $G = G(t)$ and $B_0 = B_0(t)$ with $l_{min} > 0$

6. Constant G and B_0 with $l_{min} > 0$ and $N_0(t{=}0) > 0$

All the examples are performed without seeds, except for the last test case. Without including seeds all particles entering in the system is due to the nucleation, thus the error on the moment calculations are related solely with the first bin, since all particles are created in it. For these cases, it is considered that the first bin at initial time is collapsed, e.g. $N_0(0) = 0$, $l_0 = l_1 = x_0 = l_{min}$. The last test case consider that particles are presented in the first bin at initial time, thus it is not used the collapsed first bin condition.

For all cases the first four expected moments are calculated by the standard method of moments for comparison with the MSM using different first bin growth rate G_0 equations. Moreover, when using Eq. 3.23, the expected sectional moment $\mu^{(0)}_{k-1,ex}$ is calculated by augmenting the differential equation set with Eq. 3.10 for the sectional first bin moment, except for the last case, in which $\mu^{(0)}_{k-1,ex}$ is obtained directly from Eq. 3.31.

Constant G and B_0 with $l_{min} = 0$

This is the case with the most simplifications and is in conformity with the derivation of Eq. 3.38. In this case, the first pivot movement rate G_0 (Eq. 2.68) is defined as $G_0 = \dfrac{dx_0}{dt} = (k+1)^{\frac{-1}{k}} G$. Table 3.1 compares the MSM with the exact moment calculation for the first 4 moments. The expected moments are calculated using Eq. 3.10 after the simplifications. The table shows that the expected moment is obtained using $k = 1$ to $k = 3$.

Table 3.1: Simple test case with constant $G = 1$ and $B_0 = 1$ with $l_{min} = 0$

Case	μ_0	μ_1	μ_2	μ_3
Expected	**10.00**	**50.00**	**333.33**	**2500.00**
Eq. 3.38 with k=1	10.00	**50.00**	250.00	1250.00
Eq. 3.38 with k=2	10.00	57.73	**333.33**	1924.50
Eq. 3.38 with k=3	10.00	63.00	396.85	**2500.00**

Constant G and B_0 with $l_{min} > 0$

This case is similar to the former but using $l_{min} = 5$ and the obtained moments are presented in Table 3.2. Such conditions are in accordance with the derivation of Eq. 3.28 for preserving moment order $k = 1$. However, does not satisfy conditions for Eq. 3.38, thus fails when using this equation with arbitrary order k. Hence, when $l_{min} > 0$ and the order to preserve is $k > 1$ it is necessary to use a more generic equation (Eq. 3.23).

Table 3.2: Simple test case with constant $G = 1$ and $B_0 = 1$ with $l_{min} = 5$

Case	μ_0	μ_1	μ_2	μ_3
Expected	**10.00**	**100.00**	**1083.33**	**12500.00**
Eq. 3.38 with k=1	10.00	**100.00**	1000.00	10000.00
Eq. 3.38 with k=2	10.00	107.73	1160.68	12504.63
Eq. 3.38 with k=3	10.00	113.00	1276.81	14427.46
Eq. 3.23 with k=1	10.00	**100.00**	1000.00	10000.00
Eq. 3.23 with k=2	10.00	104.08	**1083.33**	11275.69
Eq. 3.23 with k=3	10.00	107.72	1160.40	**12500.00**

Time varying $G = G(t)$ and B_0 constant with $l_{min} = 0$

Table 3.3 presents the comparison for the case using a time varying growth rate $G = 0.1t$, constant nucleation rate $B_0 = 1$ and zero critical size simulating up to $t = 10$. The table includes the Kumar and Ramkrishna (1997) cited first bin movement scheme and also G_0 using Eq. 3.23 for three scenarios conserving moments of order 1 to 3. It can be noted that using the simple form $G_0 = \frac{1}{2}G$ fails to preserved order $k = 1$, but when applying Eq. 3.23 with the corresponding k the moment is conserved.

Table 3.3: Simple test case with constant $G = 0.1t$ and $B_0 = 1$ with $l_{min} = 0$

Case	μ_0	μ_1	μ_2	μ_3
Expected	**10.00**	**33.33**	**133.33**	**571.43**
Eq. 3.38 with k=1	10.00	25.00	62.50	156.25
Eq. 3.23 with k=1	10.00	**33.33**	111.11	370.37
Eq. 3.23 with k=2	10.00	36.52	**133.33**	486.86
Eq. 3.23 with k=3	10.00	38.52	148.36	**571.43**

Time varying $B_0 = B_0(t)$ and G constant with $l_{min} = 0$

This case consider a nucleation rate dependent on time as $B_0 = 0.1t$ and $G = 1$ with zero minimal size and with final time as 10. The same comparisons are performed as in the previous test case and Table 3.4 shows that the Eq. 3.23 can preserve the chosen moment order.

Table 3.4: Simple test case with constant $G = 1$ and $B_0 = 0.1t$ with $l_{min} = 0$

Case	μ_0	μ_1	μ_2	μ_3
Expected	**5.00**	**16.67**	**83.33**	**500.00**
Eq. 3.38 with k=1	5.00	25.00	125.00	625.00
Eq. 3.23 with k=1	5.00	**16.67**	55.56	185.19
Eq. 3.23 with k=2	5.00	20.41	**83.33**	340.21
Eq. 3.23 with k=3	5.00	23.21	107.72	**500.00**

Time varying $B_0 = B_0(t)$ and $G = G(t)$ with $l_{min} > 0$

In this scenario, both nucleation rate and growth rate are time dependent: $B_0 = 0.1t$ and $G = 0.1t + 0.5$ with $l_{min} = 5$ and with final time as 10. Table 3.5 shows that the Eq. 3.23 can conserve defined moment order.

Table 3.5: Time varying $B_0 = 0.1t$ and $G = 0.1t + 0.5$ $l_{min} = 5$

Case	μ_0	μ_1	μ_2	μ_3
Expected	**10.00**	**91.67**	**908.33**	**9616.07**
Eq. 3.38 with k=1	10.00	100.00	1000.00	10000.00
Eq. 3.23 with k=1	10.00	**91.67**	840.28	7702.55
Eq. 3.23 with k=2	10.00	95.31	**908.33**	8657.01
Eq. 3.23 with k=3	10.00	98.70	974.24	**9616.07**

Constant G and B_0 with $l_{min} > 0$ and $N_0(0) > 0$

This case differ from the former since at initial time it is considered that particles are present in the first bin with $N_0(0) = 10$. It is also considered that all those particles have a size of 6 and it is used a non collapsed first bin pivot $x_0(0)$ at the same size. Thus, the initial first bin sectional moment of order k is obtained as $N_0(0)x_0(0)^k$. New particles are nucleated at a constant rate of $B_0 = 1$ at minimal size $l_{min} = 5$ and the growth rate is constant $G = 1$. Table 3.6 shows the comparison for the expected moment with the MSM using Eq. 3.23, but with the expect moment obtained direct from Eq. 3.31. Again, the simple form $G_0 = \frac{1}{2}G$ did not conserve any moment order for the first bin, using Eq. 3.23 with 3.31, on the other hand, it was capable of preserving desirable moment orders.

Table 3.6: Test case with constant $G = 1$ and $B_0 = 1$ with $l_{min} = 5$ and $N_0(0) = 10$

Case	μ_0	μ_1	μ_2	μ_3
Expected	**20.00**	**260.00**	**3643.33**	**53460.00**
Eq. 3.38 with k=1	20.00	220.00	2420.00	26620.00
Eq. 3.23 with k=1 $\mu_{k-1,ex}^{(i=0)}$ from Eq. 3.31	20.00	**260.00**	3380.00	43940.00
Eq. 3.23 with k=2 $\mu_{k-1,ex}^{(i=0)}$ from Eq. 3.31	20.00	269.94	**3643.33**	49173.75
Eq. 3.23 with k=3 $\mu_{k-1,ex}^{(i=0)}$ from Eq. 3.31	20.00	277.56	3852.09	**53460.00**

3.2 Multiple added bins for nucleation handling

Firstly, the same equations derived for single bin addition are applied for multiple bin addition, which corresponded to define a particular first bin growth rate by Eq. 3.23 and considering all other pivots to grow according to G. The second case

enumerated in Section 3.1.6 is used for this comparison and the obtained moments are reported in Table 3.7.

Table 3.7: Test case with constant $G = 1$ and $B_0 = 1$ with $l_{min} = 5$ using single bin addition equations but adding 3 bins from $t = 0$ to $t = 10$

Case	μ_0	μ_1	μ_2	μ_3
Expected	**10.00**	**100.00**	**1083.33**	**12500.00**
Eq. 3.38 with k=1	10.00	**100.00**	1074.07	12222.22
Eq. 3.38 with k=2	10.00	102.58	1126.31	13073.14
Eq. 3.38 with k=3	10.00	104.33	1162.59	13675.21
Eq. 3.23 with k=1	10.00	**100.00**	1074.07	12222.22
Eq. 3.23 with k=2	10.00	100.69	1087.94	12446.27
Eq. 3.23 with k=3	10.00	101.36	1101.48	12666.32

It can be noted that using this approach, only the $k = 1$ moment order was preserved. Hence, in the following, a modified approach is delineated for preserving higher moment order when growth and nucleation are occurring.

When multiple bins are added to represent the nucleation phenomena using the MSM, after the second bin addition, there is a situation in which nucleated particles are represented not only by the first bin, but also by the former added bins. At a certain bin addition time instant t_{add} there will be the new pivot x_0 at the minimal size l_{min} and the previously added bins with pivot $x_i > l_{min}$.

It is possible to separate the expect moment after the bin addition time t_{add} in the following portions to be analyzed: the moment from the newly formed nuclei $\mu_{k,ex}^{(fresh)}$, the moment from the previously nucleated particles $\mu_{k,ex}^{(former)}$ and the moment from the seeded particles $\mu_{k,ex}^{(seed)}$. Thus, the overall expected moment is defined as Eq. 3.39. Since the seeded moment is not the source of error in this analyze, it can be removed from this analysis.

$$\mu_{k,ex} = \mu_{k,ex}^{(fresh)} + \mu_{k,ex}^{(former)} + \mu_{k,ex}^{(seed)} \tag{3.39}$$

Analogously, the MSM moment can also be separated using the same criteria. In this case, the newly formed nuclei are to be represented by the first bin $\mu_{k,msm}^{(0)}$ and the former nucleated particles up to the new bin addition time instant t_{add} are defined as $\sum_{i=1}^{n_b} \mu_{k,msm}^{(i)}$, in which n_b represents the total number of added bins.

The newly nucleated particles from t_{add} to the next bin addition time instant are thus defined as in the previous section. The rate of change of a moment $\mu_{k,ex}^{(fresh)}$ is defined as in Eq. 3.10 and the rate of change for the moment from the MSM at the first bin $\mu_{k,msm}^{(0)}$ as in Eq. 3.18. Thus, equating these moments, a similar equation for the first bin growth rate as achieved in the single bin addition section, Eq. 3.23, is obtained.

$$G_0 = \frac{1}{N_0 k x_0^{k-1}} \left[B_0 (l_{min}^k - x_0^k) + kG\mu_{k-1,ex}^{(fresh)} \right] \tag{3.40}$$

The rate of change of the expected moment $\mu_{k,ex}^{(former)}$ from t_{add} to the next added bin time instant can be defined by Eq. 3.41 from Eq. 3.7 with G constant. At t_{add} the initial condition for $\mu_{k,ex}^{(former)}$ is reinitialized as the sum of $\mu_{k,ex}^{(former)}$ with $\mu_{k,ex}^{(fresh)}$ at t_{add} before the introduction of the new bin, which represents all nucleated bins up to t_{add}.

$$\frac{d\mu_{k,ex}^{(former)}}{dt} = kG\mu_{k-1,ex}^{(former)} \tag{3.41}$$

The moment $\mu_{k,ex}^{(former)}$ is represented using the MSM by the portion $\sum_{i=1}^{n_b} \mu_{k,msm}^{(i)}$. The rate of change of $\mu_{k,msm}^{(i)}$ for $i > 0$ to $i \leq n_b$ can be defined based on Eq. 3.7, but removing the nucleation term, since those bins do not receive nucleated particles (Eq. 3.42) and constant G with the MSM approximation:

$$\sum_{i=1}^{n_b} \frac{d\mu_{k,msm}^{(i)}}{dt} = k \sum_{i=1}^{n_b} N_i x_i^{k-1} G_i \tag{3.42}$$

in which G_i represents the growth rate at a pivot i. A further consideration is assumed that the growth rate of the bins with $i > 0$ up to $i \leq n_b$ are all equal to G^{former}. Equating Eq. 3.42 to Eq. 3.41 yields Eq. 3.43.

$$kG\mu_{k-1,ex}^{(former)} = kG^{former} \sum_{i=1}^{n_b} N_i x_i^{k-1} \tag{3.43}$$

Thus, Eq. 3.43 can be rewritten to get Eq. 3.44 that represents the defined growth rate for the previously nucleated particles from t_{add} to the next added bin.

$$G^{former} = \frac{\mu_{k-1,ex}^{(former)}}{\sum_{i=1}^{n_b} N_i x_i^{k-1}} G \tag{3.44}$$

Thus, the definition of a G^{former} requires the determination of $\mu_{k-1,ex}^{(former)}$ during the simulation, which is not possible in a variety of applications.

3.2.1 Multiple bins addition with $k = 1$

The MSM is capable of preserving the number of particles, thus: $\mu_{0,ex}^{(former)} = \sum_{i=1}^{n_b} N_i$. Hence, Eq. 3.45 is found when applying $k = 1$ to Eq. 3.44. Note that the so-called G^{former} equals to the system growth rate G. Therefore, it is possible to preserve the moment order $k = 1$ adding multiple bins using the previously obtained equation for the first bin growth rate (Eq. 3.40) and with all other pivot moving according to the system growth rate G, as shown in Table 3.7.

$$G^{former} = \frac{\mu_{0,ex}^{(former)}}{\sum_{i=1}^{n_b} N_i} G = G \tag{3.45}$$

3.2.2 Simple test cases applied to the multiple bin addition scheme

In this section, former test cases applied to the single bin addition are evaluated using the provided multiple bin addition scheme.

Constant G and B_0 with $l_{min} > 0$

The G^{former} approach is implemented for the condition with constant G and B_0 and with $l_{min} = 5$. Table 3.8 reports the obtained moment values. Confronting it with Table 3.7, which applied the G_0 for the first bin and all other bins growing by rate G with 3 bin additions, can be noted that using a new value for the growth rate of the nucleated particle as G^{former} it was possible to preserve orders with $k > 1$.

Table 3.8: Test case with constant $G = 1$ and $B_0 = 1$ with $l_{min} = 5$ using multiple bin addition equations adding 3 bins from $t = 0$ to $t = 10$

Case	μ_0	μ_1	μ_2	μ_3
Expected	**10.00**	**100.00**	**1083.33**	**12500.00**
Eq. 3.38 with k=1	10.00	**100.00**	1074.07	12222.22
Eq. 3.38 with k=2	10.00	102.58	1126.31	13073.14
Eq. 3.38 with k=3	10.00	104.33	1162.59	13675.21
Eq. 3.44/Eq. 3.40 with k=1	10.00	**100.00**	1074.07	12222.22
Eq. 3.44/Eq. 3.40 with k=2	10.00	100.50	**1083.33**	12359.29
Eq. 3.44/Eq. 3.40 with k=3	10.00	101.01	1092.71	**12500.00**

Time varying $G = G(t)$ and B_0 constant with $l_{min} = 0$

Table 3.9 presents the results using Eq. 3.44 with Eq. 3.40 for the definition of the nucleated particles growth rate. The moment of orders $k = 1$, $k = 2$ and $k = 3$ were accurately preserved using nucleated particles growth rate according to Eqs. 3.40-3.44. The case with multiple bins addition but only the first bin growth rate adjusted as G_0 is also included for comparison, which failed on preserving moments of orders $k > 1$.

Time varying $B_0 = B_0(t)$ and G constant with $l_{min} = 0$

This example has time varying birth rate and the moments using the aforementioned bins growth rate scheme are reported in Table 3.10. The values applying multiple bins addition, but using only the first bin growth rate Eq. 3.23

Table 3.9: Simple test case with constant $G = 0.1t$ and $B_0 = 1$ with $l_{min} = 0$ using multiple bin addition equations adding 3 bins from $t = 0$ to $t = 10$

Case	μ_0	μ_1	μ_2	μ_3
Expected	**10.00**	**33.33**	**133.33**	**571.43**
Eq. 3.38 with k=1	10.00	32.41	124.23	516.90
Eq. 3.23 with k=1	10.00	**33.33**	130.32	552.25
Eq. 3.23 with k=2	10.00	34.52	136.57	582.38
Eq. 3.23 with k=3	10.00	35.32	140.91	603.56
Eq. 3.44/Eq. 3.40 with k=1	10.00	**33.33**	130.32	552.25
Eq. 3.44/Eq. 3.40 with k=2	10.00	34.16	**133.33**	560.54
Eq. 3.44/Eq. 3.40 with k=3	10.00	34.79	136.18	**571.43**

and the others bins growth rate as G, are also included. As previously, for $k > 1$ the cases using only Eq. 3.23 did not conserved the moments.

Table 3.10: Simple test case with constant $G = 1$ and $B_0 = 0.1t$ with $l_{min} = 0$ using multiple bin addition equations adding 3 bins from $t = 0$ to $t = 10$

Case	μ_0	μ_1	μ_2	μ_3
Expected	**5.00**	1**6.67**	8**3.33**	50**0.00**
Eq. 3.38 with k=1	5.00	17.59	87.96	542.70
Eq. 3.23 with k=1	5.00	1**6.67**	78.97	457.88
Eq. 3.23 with k=2	5.00	18.02	88.24	524.10
Eq. 3.23 with k=3	5.00	18.96	95.24	576.21
Eq. 3.44/Eq. 3.40 with k=1	5.00	1**6.67**	78.97	457.88
Eq. 3.44/Eq. 3.40 with k=2	5.00	17.62	8**3.33**	475.46
Eq. 3.44/Eq. 3.40 with k=3	5.00	18.38	87.75	50**0.00**

Time varying $B_0 = B_0(t)$ and $G = G(t)$ with $l_{min} > 0$

Table 3.11 reports the case with both nucleation rate and growth rate time dependent: $B_0 = 0.1t$ and $G = 0.1t + 0.5$ with $l_{min} = 5$ and with final time as 10. It shows that adapting only the first bin growth rate by Eq. 3.23 did not conserve the moments of orders $k > 1$. When using Eqs. 3.40-3.44 it was possible to conserve such moments.

3.3 Approaches for defining bin addition time instants

As discussed in the previous sections, the MSM under nucleation and growth possess the hindrance to preserve higher order moments due to the nucleation at minimal size. Schemes for conserving moments with $k > 1$ were evaluated, however,

Table 3.11: Time varying $B_0 = 0.1t$ and $G = 0.1t + 0.5$ $l_{min} = 5$

Case	μ_0	μ_1	μ_2	μ_3
Expected	**10.00**	**91.67**	**908.33**	**9616.07**
Eq. 3.38 with k=1	10.00	92.59	915.64	9642.20
Eq. 3.23 with k=1	10.00	**91.67**	895.88	9305.85
Eq. 3.23 with k=2	10.00	92.55	910.82	9504.28
Eq. 3.23 with k=3	10.00	93.41	925.47	9701.35
Eq. 3.44/Eq. 3.40 with k=1	10.00	**91.67**	895.88	9305.85
Eq. 3.44/Eq. 3.40 with k=2	10.00	92.45	**908.33**	9459.52
Eq. 3.44/Eq. 3.40 with k=3	10.00	93.22	920.76	**9616.07**

they are not of practical implementation for general particulate processes, since the obtained formulation is dependent on the expected moment values. Furthermore, they are designed to preserve a chosen moment, but not all. Thus, in situations in which the nucleation and growth rate are dependent on the PSD properties it will lead to errors, since the chosen moment order may differ from the one G or B_0 depends on. For instance, this occurs for growth rate dependent on supersaturation, which is often dependent on the second order moment (area).

In this context, frequently adding new bins at minimal size is still necessary in order to minimize errors in the simulated particle distribution. Thus, in the following approaches are discussed to efficiently define proper time instants for adding a new bin depending on the system state.

Two approaches were evaluated for controlled bin addition. One uses the current value of the growth rate and nucleation rate to predict a time interval for the next bin addition based on a predefined maximum property of interest. The second approach is to use an event based time integrator solver to stop the simulation at the time in which a chosen property of the first bin reaches a certain value.

3.3.1 Determination of time interval for controlled bin addition based on current particle rates

In crystallization processes studies, it is common to evaluate the dynamic behavior of the system by manipulating input variables and observing the dynamic profiles up to equilibrium. Thus, it will present situations with higher driving force and, closer to saturation, it can be relatively smaller. In this context, it is necessary to concentrate the mesh grid at nucleation size during the time intervals of higher driving force, while when closer to equilibrium the mesh grid resolution to treat the nucleation can be more coarse.

This behavior can be accomplished by analyzing the calculated nucleation rate and growth rate at a given time. When using the MSM, higher growth rate leads to

more prediction errors since nucleated particles are considered to be formed at the zero pivot and not at the minimal size. Moreover, higher nucleation rate generates more particles at the zero pivot and thus amplifies the moment errors for the MSM approximation.

In this section, it is proposed to use the nucleation and growth rate at a certain time t to predict a property of interest for the first bin to be maintained under a predefined maximum value. Such property can be a moment of order k or a property that depends on the moment, such as mass or volume of particles in the first bin. Based on this prediction and comparing it to the predefined reference value, a time interval Δt_{add} for simulating up to the next bin addition can be obtained.

It can be considered a given property Ξ to be monitored during the bin addition scheme. It is supposed that such a property is a function of the first bin moments: $\Xi = \Xi(\mu_0(\Delta t), \mu_1(\Delta t), \ldots, \mu_k(\Delta t))$. As mentioned Ξ can be a property such as mass or volume, e.g. $\Xi = \rho_c k_v \mu_3(\Delta t)$ or $\Xi = k_v \mu_3(\Delta t)$ or a property function of two moments such as the volume-mean size or the area-mean size: $\Xi = \frac{\mu_4(\Delta t)}{\mu_3(\Delta t)}$ and $\Xi = \frac{\mu_3(\Delta t)}{\mu_2(\Delta t)}$. Additionally, it is defined a reference value of this property Ξ^{ref} to be used as a condition for the determination of the time interval for adding a new bin Δt_{add}.

It is proposed to use the hypothesis of constant nucleation and growth rate at a time t. Doing so, the obtained Eq. 3.31 can be used for the prediction of the first bin moment order k at a time interval Δt. With the aid of this simplification, $\Xi(\Delta t)$ can be directly calculated.

The time interval to simulate up to the next bin addition Δt_{add}^{pred} can be obtained by solving the equation Eq. 3.46, which can be performed by iterative methods such as Newton-Raphson. The derivative of Eq. 3.31 in respect to t is shown by Eq. 3.47.

$$\Xi(\Delta t) - \Xi^{ref} = 0 \tag{3.46}$$

$$\frac{d}{dt}[\mu_{k,ex}^{(0)}(t)] = B_0 \sum_{j=0}^{k} \left[l_{min}^{k-j} G^j t^j \frac{k!}{(k-j)!} \frac{1}{(j)!} \right] + \sum_{j=0}^{k} \left[G^j t^{j-1} \mu_{(k-j)}^{(0)}(0) \frac{k!}{(k-j)!} \frac{1}{(j-1)!} \right] \tag{3.47}$$

Note that if the calculation of Δt_{add}^{pred} is performed right after a bin addition, the initial condition $(\mu_k^{(0)}(0))$ for Eq. 3.31 and 3.47 are zero. However, if such calculation is to be performed with $N_0(0) > 0$, $\mu_k^{(0)}(0)$ can be obtained using the MSM approximation: $\mu_k^{(0)}(0) = x_0(0)^k N_0(0)$.

This approach to determine Δt_{add}^{pred} is based on the simplification of G and B_0 constant, thus the reference value of the property can be ether over or under

estimated when simulating using the MSM. To avoid errors of not introducing a new bin, it is proposed the use of a limiting time interval representing the maximum interval to add a new bin.

A possible algorithm to implement the bin addition based on constant G and B_0 is depicted in Algorithm 1. It is considered that a time vector t with a total of r_t samples is given and at each t_j for $j \in [0, r_t - 1]$ a new bin should be added. The limiting time interval is $\Delta t_{lim} = t_{j+1} - t_j$. It is considered that the property of interest is a moment of order k of the first bin ($\Xi = \mu_k$). In line 5 of Algorithm 1 the value of the property is computed from Eq. 3.31 for the limiting time interval Δt_{lim}. Only if the obtained value is higher than the reference property value μ_k^{max} it should solve Eq. 3.46 for obtaining a Δt_{add}. Otherwise, the time interval to simulate up to the next bin addition is Δt_{lim}.

Algorithm 1 Algorithm for controlled bin addition based on constant G and B_0 predictions

1: $t_{now} = t_0$
2: $j = 0$
3: **while** ($j < r_t - 1$) **do**
4: Δt_{lim}=$t_{j+1} - t_{now}$
5: $\mu_{k,ex}^{lim} = \mu_k^{ex,i=0}(\Delta t_{lim})$ (Eq. 3.31)
6: **if** ($\mu_{k,ex}^{lim} \leq \mu_k^{max}$) **then**
7: $\Delta t_{add} = \Delta t_{lim}$
8: **else**
9: Δt_{add} = solution of Eq. 3.46
10: **end if**
11: Integrate system with the MSM from t_{now} up to Δt_{add}
12: Add new bin to the dynamic system
13: $t_{now} = t_{now} + \Delta t_{add}$
14: **if** ($t_{now} \geqslant t_{j+1}$) **then**
15: $j = j + 1$
16: **end if**
17: **end while**

3.3.2 Event based integration for controlled bin addition

This scheme for controlled bin addition uses a selected property to be maintained under control during the simulation using the MSM. A reference value for this property is also assigned as in the previous scheme.

Differential equation solution with root-finding, also denoted as event location, attempt to determine the time instant of an event represented by a function $g_{ev}(t, y) = 0$. Many studies were published addressing this topic: Kahaner et al. (1989); Shampine and Thompson (2000) and references therein.

Modern numerical packages provides this functionality for ODE solvers, such as the *ode* function family from *Matlab* software, the *solve_ivp* from the *Scipy* package (Jones et al., 2001) and the CVODE solver from the Sundials suite (Hindmarsh et al., 2005).

In this work the *Scipy* package was used for the event handling using Eq. 3.46 to stop the solver at the time instant in which the selected property reaches the reference value. After stopping the integration a new bin is added to the system and the solver is reinitialized for the next iteration.

3.3.3 Numerical examples

This section provides two examples to evaluate and compare the aforementioned numerical methods for controlled bin additions.

Test Case 1

This numerical case was used by Shi et al. (2006) and reported by Rawlings et al. (1993). It comprises of a crystallizer of potassium sulfate modeled using the driving force as in Eq. 3.49. The population balance based on solvent mass ($n(l,t)$) can be written as Eq. 3.48 and includes growth $G(t)$ and nucleation mechanism $B_0(t)$, in which nuclei particles are formed with negligible size ($l_{min} = 0$). The mass balance is necessary for the determination of the supersaturation and it is defined based on the concentration $C(t)$ by Eq. 3.50.

$$\frac{\partial n(l,t)}{\partial t} + G(t)\frac{\partial n(l,t)}{\partial l} = B_0(t)\delta(l) \tag{3.48}$$

$$S = \frac{C - C_{sat}}{C_{sat}} \tag{3.49}$$

$$\frac{dC}{dt} = -3\rho_c k_v G(t)\mu_2(t) \tag{3.50}$$

The kinetic rates $G(t)$ and $B_0(t)$ are defined by Eqs. 3.51 and 3.52. The required parameters are listed in Table 3.12. The initial condition for $C(0)$ is 0.1681 and, at this value, the temperature for saturation is approximately $50°C$. However, the temperature was set to $20°C$, such that the supersaturation was maximum at initial time. The saturation composition is temperature dependent and defined by Eq. 3.53. The seeded distribution was discretized using 200 bins.

$$G(t) = k_g \exp\left[\frac{-E_g}{RT}\right] S^g \tag{3.51}$$

$$B_0(t) = k_b \exp\left[\frac{-E_b}{RT}\right] \mu_3(t) S^b \tag{3.52}$$

$$C_{sat} = 6.29 \cdot 10^{-2} + 2.46 \cdot 10^{-3} T - 7.14 \cdot 10^{-6} T^2 \tag{3.53}$$

Table 3.12: Parameters for batch crystallization model from Shi et al. (2006).

Parameter	Symbol	Value	Unit
Nucleation exponent	b	1.45	-
Growth exponent	g	1.5	-
Nucleation coefficient	k_b	285.01	$1 s^{-1} \mu m^{-1}$
Growth coefficient	k_g	1.44e8	$\mu m s^{-1}$
Nucleation Activation Energy	E_b/R	7517.0	K
Growth Activation Energy	E_g/R	4859.0	K
Total solvent mass	m_{slv}	27	kg
Crystal density	ρ_c	2.66e-12	$g \mu m^{-3}$
Volume shape factor	k_v	1.5	-

The process starts with seeds defined as a parabolic distribution from 250 to 300 μm as follows: $n(l, 0) = 0.0032(300 - l)(l - 250)$ for $250 \leq l \leq 300$ and zero otherwise.

This example was solved using the MSM with Eq. 3.26 for the first pivot growth rate and applying $G(t)$ for all other pivot growth. This example does not have an analytical solution (Qamar, 2008), thus it was solved with 1000 bins addition for establishing a referential solution. The final time was set to 15 min.

The bin addition scheme from section 3.3.1 and from section 3.3.2 were implemented using the crystal mass at first bin as controlled property with a reference value of $0.01g$. These implementations were compared with a periodic bin addition scheme. The Runge-Kutta 5(4) method was used to integrate the dynamic system.

The bin addition scheme based on the prediction of Δt_{add} using constant G and B_0 was applied using a limiting time interval of 90 s. The number of added bins after completing the simulation was 24. Hence, for comparison, the regular bin addition scheme was implemented using 25 sample times, which corresponds to the same number of added bin at final time.

Table 3.13 reports the obtained zero order moment and the mass ($m_c^{nucl} = m_{slv} \rho_c k_v \mu_3^{nucl}$) for the nucleated crystals portion. The absolute value and the relative error (in percentage) based on the reference solution are shown for those moments. Δt_{add}^{pred} refers to the scheme using constant G and B_0 for the determination of a bin addition time interval.

Inspecting the table it can be notice that all cases provide relative small deviation

Table 3.13: The number of added bins during simulation, the zero and third calculated moment and relative errors percentage using the proposed bin addition schemes for the test case 1.

Scheme	**Added bins**	$\boldsymbol{\mu_0^{nucl}}$	$\boldsymbol{m_c^{nucl}}$(g)	$\boldsymbol{\mu_0^{nucl-rel}}$(%)	$\boldsymbol{\mu_3^{nucl-rel}}$(%)
Reference	1000	528.882	194.960	-	-
Periodic addition	24	529.852	186.878	0.183	-4.145
Δt_{add}^{pred}	24	528.987	194.387	0.020	-0.294
Event based	12	529.058	194.014	0.033	-0.485

from the reference solution. For the periodic bin addition, the relative error for the zero order moment is in an order of 9 times greater than the others controlled bin addition schemes. The third order moment error was also greater for the period bin addition. The event based scheme had slightly higher relative error than the Δt_{add}^{pred} case, but the number of added bins were only 12, compared to the others case with 24 added bins.

Figure 3.2 present the particle distribution at final time using the aforementioned schemes for bin addition. The labels are: *ref* for the reference solution; *iter* for the case with regular bin addition; Δt_{add}^{pred} for the case with the hypothesis of constant G and B_0 for the prediction of the property of interest and, lastly, *event* representing the case using the event based scheme. The nucleated particles portion is in the range of $0 \leq l < 325\mu m$.

The profile of the number of added bins by simulation time is depicted in Figure 3.3, which also presents the growth and nucleation rate profiles computed for the reference solution. The *iter* case provides linearly added number of bins. The Δt_{add}^{pred} case had 10 bins added in the first 1.5 min, region with higher nucleation and growth rate, and because of the limiting $\Delta t = 90$ s it was added new bins even when G and B_0 were almost zero. The *event* based approach also had most of the added bins occurring at the earlier stage and after the nucleation and growth rate getting to smaller values no bin were added, since the bin addition condition of 0.01 g at the first bin was not satisfied after around 5 min of simulation.

Test Case 2

This example was taken from Qamar (2008) and is a batch crystallization model with population balance, mass balance and supersaturation as in the previous example (Eqs 3.48, 3.50 and 3.49). The kinetic equations for growth and nucleation are defined by Eqs 3.54 and 3.55.

$$G(t) = k_g S(t) \tag{3.54}$$

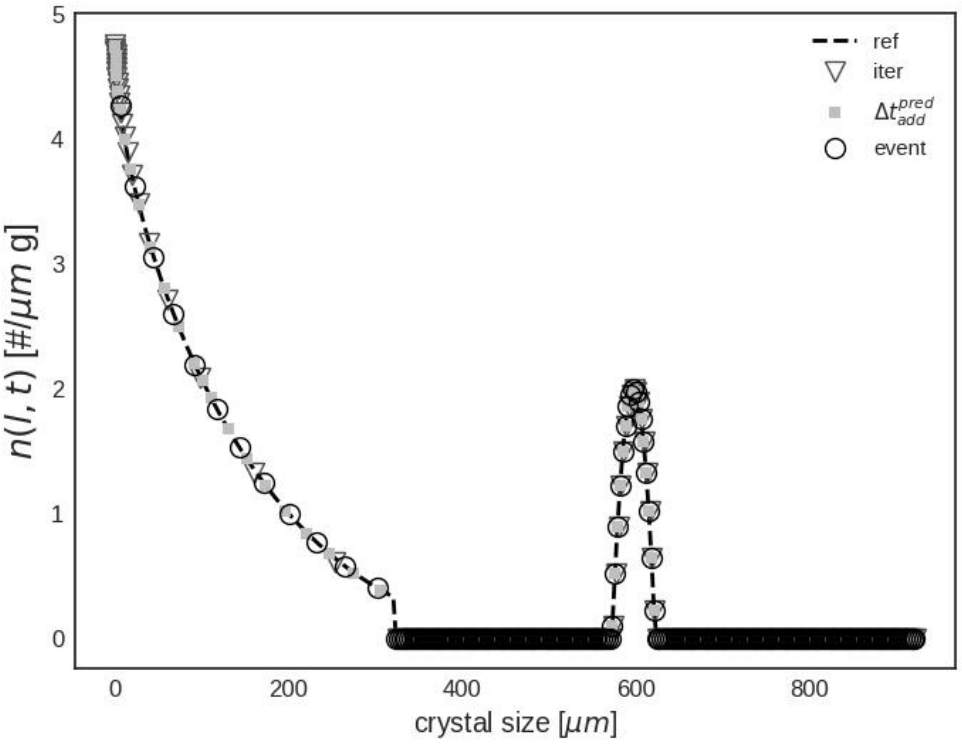

Figure 3.2: Particle size distribution for the mass balance numerical example comparing the bin addition schemes (ref: reference; iter: periodic addition; Δt_{add}^{pred}: estimated time interval; event: event based integrator).

$$B_0(t) = k_b S(t)^b \mu_3(t) \tag{3.55}$$

The size distribution at initial time is defined by a bimodal gaussian distribution Eq 3.56 with parameters: $\sigma_1 = 1.667{\cdot}10^{-4}$, $\bar{l}_1 = 8{\cdot}10^{-4}$, $\sigma_2 = 2.5{\cdot}10^{-4}$, $\bar{l}_2 = 1.6{\cdot}10^{-3}$ and $a_0 = 359895.88$. The seeds were discretized at initial time with 1000 bins and the nuclei size is $l_{min} = 1 \cdot 10^{-6}$ m.

$$n(l,0) = \frac{a_0}{\sqrt{2\pi}} \left[\frac{1}{\sqrt{\sigma_1}} \exp\left(-\frac{l - \bar{l}_1}{\sqrt{2}\sigma_1} \right) + \frac{1}{\sqrt{\sigma_2}} \exp\left(-\frac{l - \bar{l}_2}{\sqrt{2}\sigma_2} \right) \right] \tag{3.56}$$

The kinetic parameters are: $k_b = 3.42{\cdot}10^7$, $b = 2.624$, $k_g = 1.37{\cdot}10^{-5}$. The crystal density is $\rho_c = 1250\ kg/m^3$ and the volume shape factor is $k_v = 0.0288$. The process starts with a saturation concentration of $C_{sat,0} = 0.09881$ and at approximately $t = 4000$ min a drop in the saturation composition to $C_{sat,e} = 0.08$ is considered, which is numerically implemented by Eq. 3.57 (with $\xi = 0.005$).

$$C_{sat}(t) = C_{sat,0} + \frac{C_{sat,e} - C_{sat,0}}{2} \left[\tanh(\xi(t-1)) + 1 \right] \tag{3.57}$$

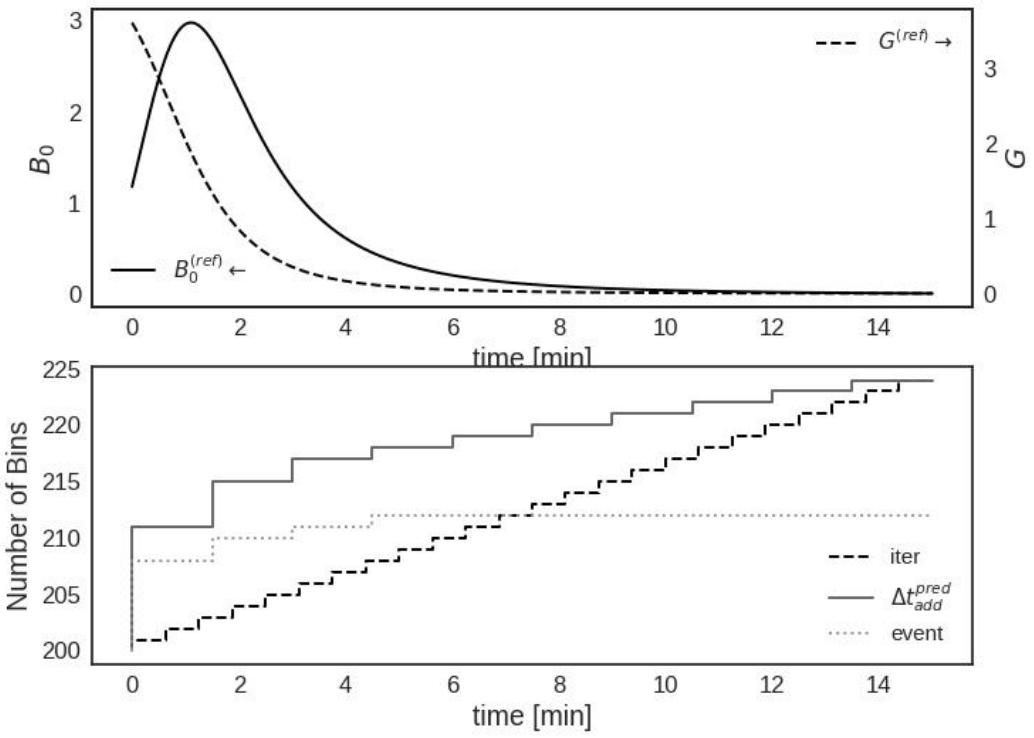

Figure 3.3: Number of added bins (bottom) and reference growth and nucleation rate (top) profiles for the mass balance numerical example comparing the bin addition schemes.

The described schemes for bin addition were used to simulate this test case up to $t = 6 \cdot 10^3$ min. As reference property for the first bin addition was chosen the mass of crystals with a maximum value of 10^{-5} g. The limiting time interval for the Sec. 3.3.1 strategy is 300 min.

Table 3.14 compares the *ref* as the reference case, in which 1000 bins are added to the system, the Δt_{add}^{pred} using the section 3.3.1 scheme and the *event* based approach. The periodic bin addition scheme (*iter*) was also included using the same number of added bins than the Δt_{add}^{pred} case, which were 33 new bins. It is compared the number of added bins, the zero order moment for the nucleated particles, the mass of nucleated crystals $m_c^{nucl} = \mu_3^{nucl} \rho_c k_v$ and the relative error for the zero and third order moments for the nucleated particles. All cases were solved with a Runge-Kutta method of order 5(4) (Jones et al., 2001).

The table shows that all cases provide relative small errors for the nucleated portion of the PSD, in which the range at final time is $10^{-6} \leq l < 2.5 \cdot 10^{-3} m$. Figure 3.4 presents the dynamic profile of the number of bins. The Δt_{add}^{pred} has the most bin addition occurring from time $4 \cdot 10^3$ to $5 \cdot 10^3$ min, which represents the time period with higher nucleation and growth rates, as depicted in the top chart.

Table 3.14: The number of added bins during simulation, the zero moment order, the mass and relative errors percentages for nucleated particles using the proposed bin addition schemes for the test case 2.

Scheme	**Added bins**	$\boldsymbol{\mu_0^{nucl}}$	$\boldsymbol{m_c^{nucl}}$(g)	$\boldsymbol{\mu_0^{nucl-rel}}$(%)	$\boldsymbol{\mu_3^{nucl-rel}}$ (%)
Reference	1000	23198.289	0.448	-	-
Periodic addition	33	23209.057	0.434	0.046	-3.095
Δt_{add}^{pred}	33	23201.346	0.445	0.013	-0.674
Event based	13	23199.825	0.446	0.007	-0.357

All added bins for the *event* scheme are within this size range. The *event* based case was able to provide smaller error with a shorter number of added bins (13), which indicates that the bins are efficiently added during the simulation using the reference maximum value for the first bin. Figure 3.5 reports the PSD for each scheme.

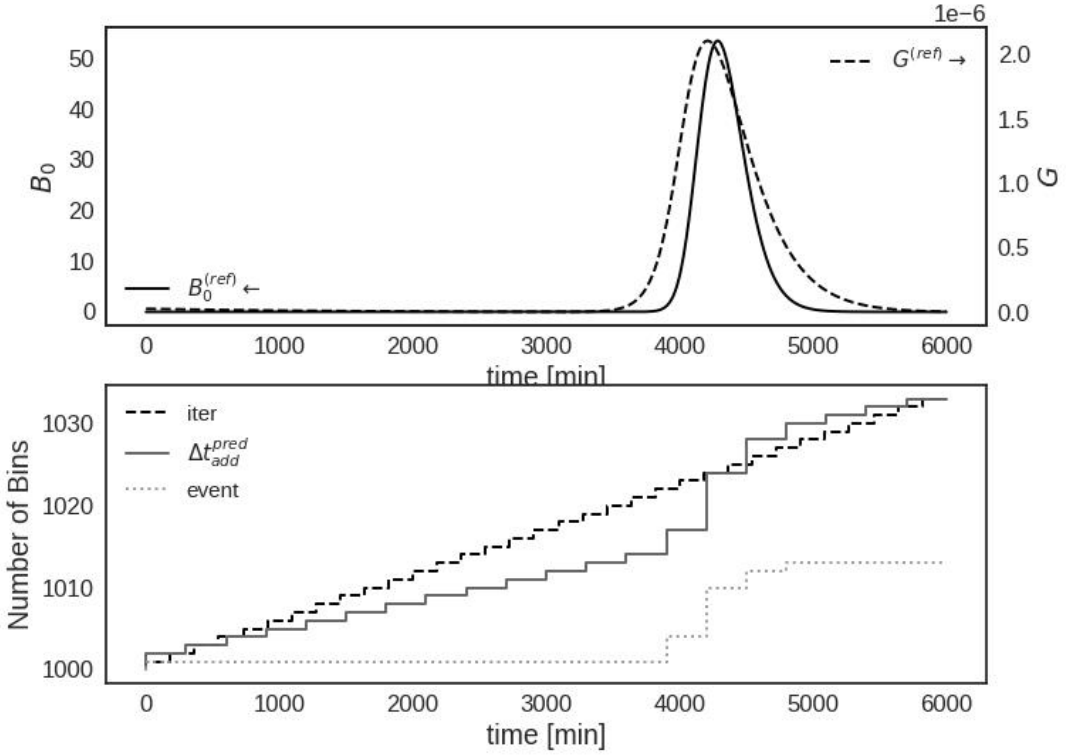

Figure 3.4: Number of added bins (bottom) and reference growth and nucleation rate (top) profiles for the test case 2 comparing the bin addition schemes.

3.4 Conclusion

In this section the MSM was evaluated in respect to the moment conservation in the presence of nucleation. The nucleation occurs at the critical size, but the MSM considers that the nucleated particles appear at the first pivot size, which

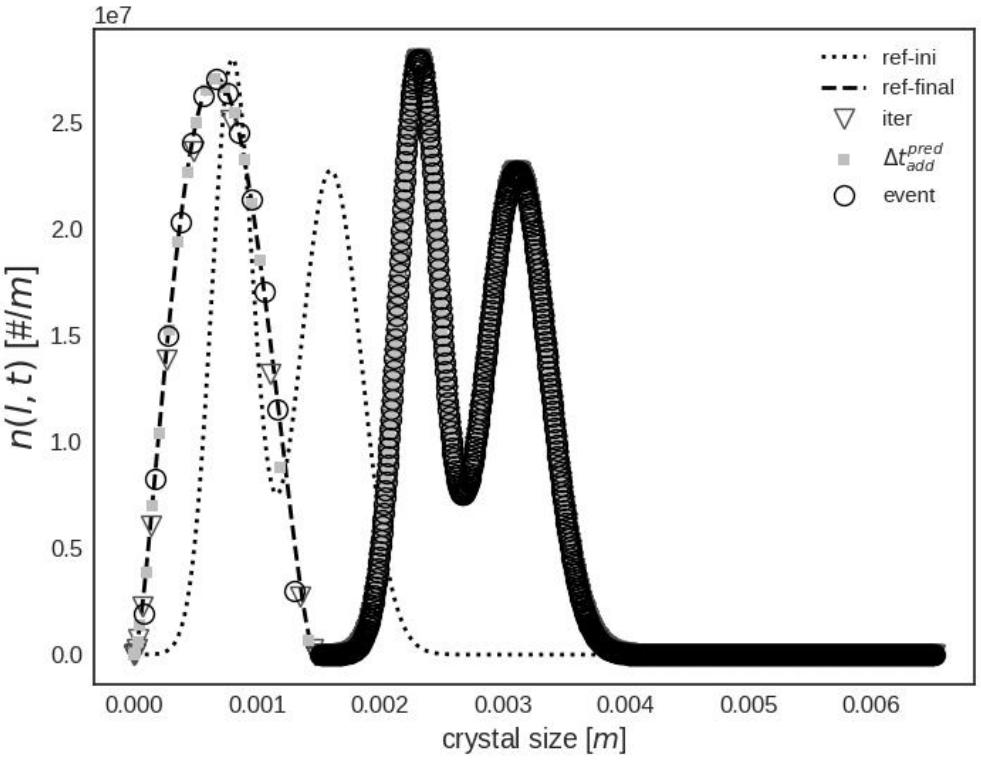

Figure 3.5: Particle size distribution for the test case 2 comparing the bin addition schemes. The initial PSD is denoted as *ref-ini*.

moves according to the growth rate, and this cause errors on the computed PSD properties.

The rate of change for the first bin moment with a defined order k using the MSM was compared with the expected moment rate of change. This provided the first bin growth rate as a function of the moment order to be preserved, nucleation rate, number of particles in the first bin, nuclei size, first pivot size, growth rate and also the expected moment $k-1$. When $k=1$, the first bin growth rate is independent of the expected moment computation. However, when $k>1$ in order to preserve the moment k the first bin growth rate is dependent on the expected moment. Thus it cannot be applied in a variety of application.

Furthermore, the cases with single bin addition and multiple bin addition were evaluated. Even if the calculation of the expected moment was made possible, when adding multiple bins the MSM using only the first bin with a specific growth rate calculation, while the others moving with the system growth rate, leads to moment errors. Moreover, it is usual to have the kinetic rates dependent on the PSD moments, thus errors on one of those moments lead to error on other moments, since the kinetics would be incorrectly computed.

In this sense, the frequent addition of new bins was necessary to mitigate moment

errors. There have been demonstrated two approaches for selectively add new bins to reduce moment errors, while avoiding unnecessary additions. The first was to consider the growth and nucleation rate constant at a certain time instant and estimate the time interval for a selected property of the first bin to reach certain predefined value. The second approach was to use root-finding methods during the temporal integration to find the time instants in which the first bin selected property reaches the reference value.

The controlled bin addition approach was evaluated for two test cases and it was shown that they were able to concentrate the bins addition at the most crucial time interval, which corresponds with the higher nucleation and growth rate. It should be noted that the periodic bin addition also provides relatively small errors and the time interval can be easyly adjusted by trial and error to achieve acceptable moment conservation. The bin addition based on the prediction using constant growth and nucleation was capable of automatically add bins when needed reducing errors, but requires the definition of a reference value for the fist bin. Also, because the prediction was made with *a priori* information at a given time, the kinetic rates may not be representative for the next time interval. The event based approach also requires the definition of a reference value to be reached, but it does not need the hypothesis of constant kinetic rates. Thus, it can efficiently add the required bins during the temporal integration. However, it depends on specialized methods, which can be time consuming for more intensive applications of the model predictions, such as in optimal control or parameter estimation.

Chapter 4

Inferring kinetic dissolution of NaCl in aqueous glycol solution using a low-cost apparatus and population balance model

This chapter presents the study performed on the dissolution of particles of NaCl in aqueous solutions of monoetilene glycol (MEG). The study uses data collected by Figueiredo (2016) using a low-cost apparatus and proposes a model to describe the PSD variation, which is correlated with the measured red-green-blue (RGB) color pattern.

The dissolution begins in a condition free of solute and progress to near equilibrium. Because of this, it was necessary to evaluate a more generic dissolution kinetics than if the dissolution occurred only near to equilibrium. The used model was able to represent the dissolution plateau (Lasaga, 1998) for far from equilibrium condition.

The methodology described in this chapter allows the use of a low cost equipment for determining particle kinetics. Although it is focused in the dissolution, analogous strategy can be performed by coupling the measurement apparatus with the population balance formulation to provide kinetic parameters for growth and nucleation.

4.1 Introduction

Different techniques are used to measure properties of the solid phase, varying from methods that provide mean properties to methods that can represent the whole particle size distribution (PSD) as, for instance, sieve analysis, laser diffraction,

laser backscattering, and image analysis. A detailed description of advantages and shortcomings of each method can be found in Chianese and Kramer (2012).

The online monitoring of the PSD is still a challenge and current techniques may not work for concentrated suspension, requiring additional equipment for dilution loops (Nagy et al., 2013). Moreover, those more sophisticated sensors are expensive for a broader range of applications.

In that sense, measurement of solid concentration is still an important issue for monitoring particulate systems. A technique to track suspended solid was introduced by Caciano de Sena et al. (2011). The authors proposed the use of a Charge Coupled Device (CCD) camera with image processing based on the RGB colors for the detection of low concentration of barium sulfate in suspension. Comparison with standard turbidimetric measurements showed higher sensitivity based on the limits of detection and quantification. This measurement technique was also employed to design a low-cost method for measuring solubility curves (Silva et al., 2013).

In this work, the dissolution rate of crystals is investigated using the image analysis method based on the RGB pattern using, for the first time, a dynamic population balance equation to track the size distribution variation. The system to be evaluated was the NaCl crystals in a solution of water and monoethylene glycol as co-solvent. This system is of crucial concern in the oil and gas industry, because MEG is injected at the wellhead to prevent hydrate formation during the fluid flow up to the topside. The experimental data was used to estimate parameters related with the RGB calibration and with the dissolution kinetics.

4.1.1 Importance of particle dissolution

Dissolution of solid particles is present in different fields of interest. In the pharmaceutical industry, for instance, the dissolution kinetics of the active pharmaceutical ingredient is related with the bioavailability and is considered in the quality control method (Nishinaga, 2014). In crystallization processes, a dissolution loop is employed as an additional manipulated variable to allow corrective action (as in uncontrolled nucleation) or to enhance crystal growth (Chianese and Kramer, 2012). Other examples may be found in the treatment of nuclear waste, cement hydration, corrosion, carbon sequestration and hydraulic fracturing of hydrocarbon reservoirs (Luttge et al., 2013).

The understanding of dissolution mechanism is also of fundamental importance in industries susceptible to scale deposition. The production of phosphoric acid in the fertilizer industry is an example; calcium sulphate can precipitate on the tube walls of heat exchangers. Thus, regular cleaning procedures using sulphuric acid are

required. Because the acid attacks the heater tubes and other pieces of equipment, replacements are often needed (Jamialahmadi and Müller-Steinhagen, 2007).

Scale deposition in reservoirs and oil platforms is a common problem in the oil and gas industry resulting in serious economic and operational problems. The formation of scale in producing wells is primarily due to temperature reduction and/or increase in salt concentration (Mackay, 2003). The most susceptible places to the formation of scale in the process of oil production are in the reservoir and in the surface equipment located on the platforms. In gas reservoirs, halite precipitation during production is observed, causing a significant decrease in the production rate (Kleinitz et al., 2003).

4.2 Methodology

4.2.1 Experimental apparatus and conditions

This section describe the experimental apparatus and methods used by Figueiredo (2016) to collect data for the NaCl dissolution using the *RGB* measurements.

Dissolution experiments were performed by Figueiredo (2016) using the experimental apparatus shown in Figure 4.1. It is a reaction vessel made of glass, with a total volume of 100 mL, whose temperature was controlled with a thermostatic bath. A propeller-type stirrer was used to continuously homogenize the solution. A camera with a CCD sensor configured to capture 24-bits digital images was coupled to the vessel. In order to avoid interferences by external light, the reactor was covered with aluminum foil during the measurements. A LED (Light Emitting Diode) was introduced into the system as a single source of light. Images were acquired in real time using a software called Masterview (Caciano de Sena et al., 2011) for processing and analyzing the digital images.

The software was developed by Caciano de Sena et al. (2011) to capture images from a computer webcam by evaluating changes in the *RGB* components. The software allows analysis of a specific area of the image captured by the camera and, with its stored coordinates, the average values of the *RGB* components are calculated. Changes in the values of these components are detected by the computer program (Silva et al., 2013). The variation in the grayscale (GS) can be obtained by calculating the average of the components red ($\langle R \rangle$), green ($\langle G \rangle$), and blue ($\langle B \rangle$), using Eq. 4.1 (Caciano de Sena et al., 2011).

$$GS = 0.298\langle R \rangle + 0.587\langle G \rangle + 0.114\langle B \rangle \tag{4.1}$$

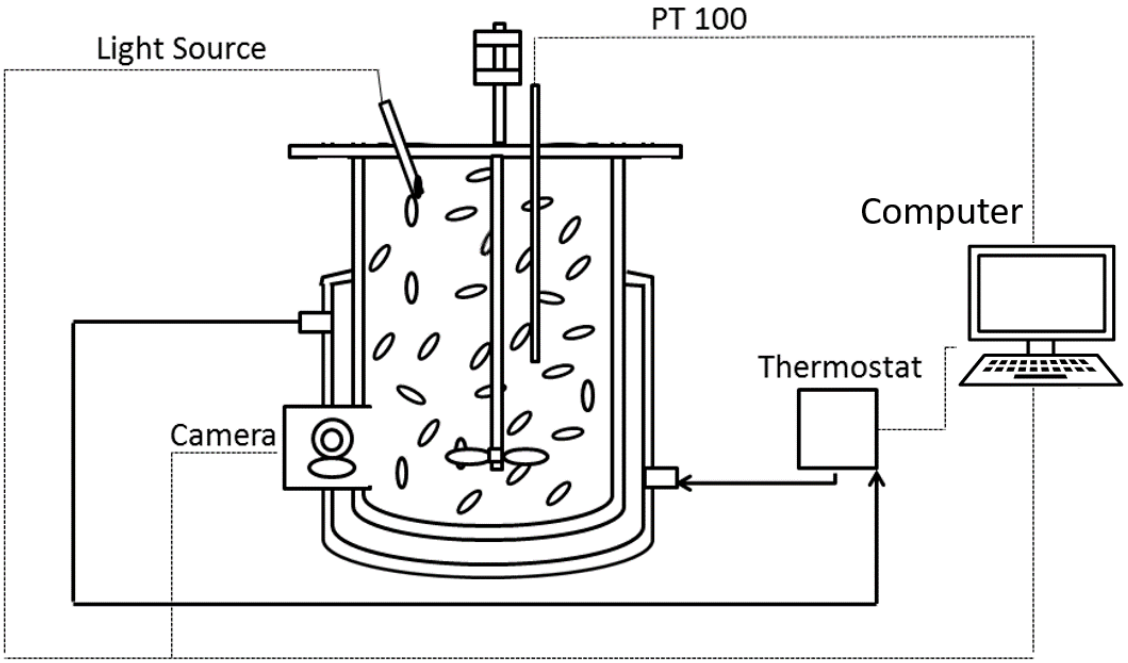

Figure 4.1: Experimental apparatus used in the experiments of dissolution, containing camera, light source, thermostat, stirrer, and a data acquisition system (Adapted from Figueiredo (2016)).

Masterview camera images and GS plot similar to the one issued by the program are shown in Figure 4.2. On Figure 4.2-a the stirrer and the CCD sensor can be observed in the clear MEG/water solution. The same view window of Figure 4.2-a, but after the first addition of NaCl particles, is shown in Figure 4.2-b. The GS profile after several additions of NaCl is presented in Figure 4.2-c. After each addition the GS value reached a peak and subsequently decreased because of the crystal dissolution, approximating the base line. Several additions were made and the GS profile during the experiment was analyzed by the software. It can be seen that after six additions (200 min) saturation was reached and the GS value no longer returns close to the base line. This strategy is used to study the dissolution kinetics.

Figueiredo (2016) prepared the solutions using Milli-Q^{TM} deionized water (Millipore, Bedford, MA, EUA), MEG Purity 99.5% (VETEC CHEMISTRY LTD) and NaCl Purity 99% (VETEC CHEMISTRY LTD). Three temperature levels at atmospheric pressure were studied: 20, 45, and 90°C. The author found a good homogenization, while avoiding excessive bubble formation, with a stirring rate of 300 rpm. Additionally, it was evaluated the MEG concentration of 10 and 50 wt% MEG. The experimental condition are summarized in Table 4.1, where the initial values of MEG and water masses, their temperature (T), and the MEG mass fraction w_{MEG} are listed.

Each experiment started after adjusting the solution concentration, temperature, and stirring rate. Figueiredo (2016) added specified masses of NaCl crystals ($m_{add,j}$)

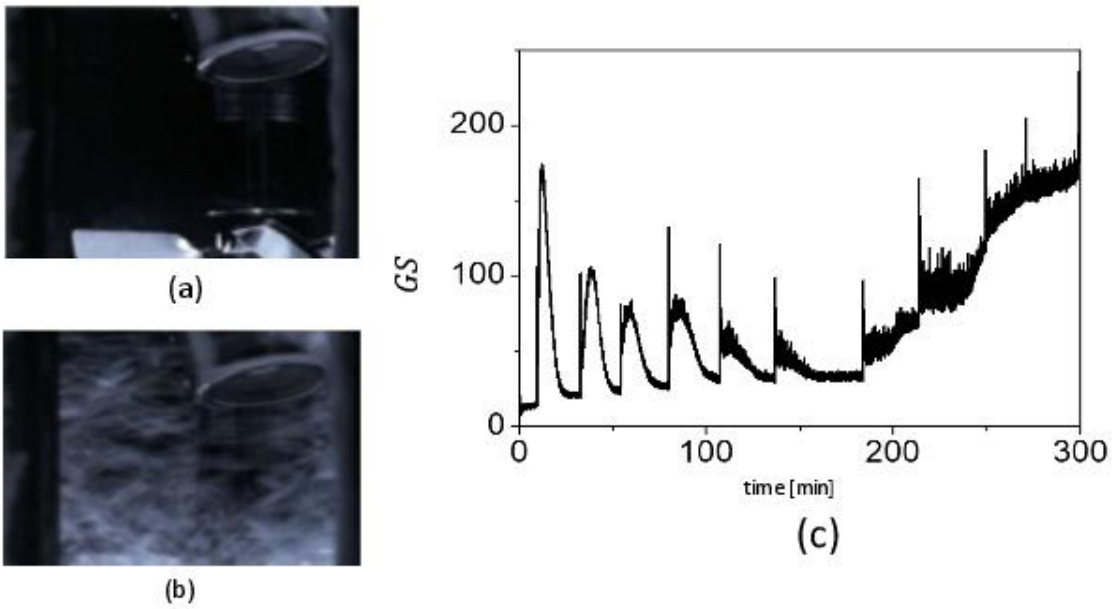

Figure 4.2: Masterview images: (a) Stirrer and a sensor in a clean MEG solution without salts (b) Stirrer and a sensor in a MEG solution after the first addition of NaCl (c) Typical GS plot issued during the experiments, showing several additions of salt (Figueiredo, 2016).

Table 4.1: Experimental conditions for NaCl dissolution.

Experiment	**MEG Mass** (g)	**Water Mass** (g)	**Temperature** (°C)	**MEG Mass Fraction**
exp1	10	70	20	0.125
exp2	50	36	20	0.581
exp3	50	36	45	0.581
exp4	50	36	45	0.581
exp5	50	36	90	0.581

to the vessel for each experiment according to Table 4.2 at different time instants $t_{add,j}$ for j-th addition. Each subsequent addition was performed after the GS value of the previous addition reached an approximate constant behavior, which indicates the end of dissolution. All experiments were performed up to 60 min and GS measurements were collected at constant intervals of 6 s. The number of additions for the experiment k is denoted as $r_{add,k}$.

4.2.2 Crystal dissolution dynamic model

The prediction of crystal dissolution was evaluated using a model based on the population balance equation (PBE), which is a well-established modeling approach to describe particulate systems. The PBE is a conservation law used to account

Table 4.2: Salt addition sequence with corresponding addition time instant $t_{add,j}$ (min) and added mass $m_{add,j}$ (g).

Experiment	1st Add.		2nd Add.		3rd Add.		4th Add.	
	$t_{add,j1}$	$m_{add,1}$	$t_{add,2}$	$m_{add,2}$	$t_{add,3}$	$m_{add,3}$	$t_{add,4}$	$m_{add,4}$
exp1	15.9	5.0	29.3	5.0	42.5	5.0	55.7	5.0
exp2	9.4	3.0	32.7	3.0	53.8	2.0	-	-
exp3	3.5	3.0	13.9	3.0	27.6	3.0	41.0	3.0
exp4	4.8	3.0	20.3	3.0	32.3	3.0	46.2	3.0
exp5	3.8	5.0	25.3	5.0	47.9	2.0	-	-

for the number of particles in a system and it has applications in several fields, such as polymerization and crystallization (Qamar, 2008). The PBE can account for different mechanisms capable of modifying the particles distribution, such as particle growth, dissolution, nucleation, agglomeration, and breakage.

Preliminary experiments under saturated solution were performed by Figueiredo (2016) with the presence of solid particles and no variation of the GS signal was perceived, indicating negligible aggregation or breakage. Therefore, only the dissolution is considered in the mathematical modelling. In this case, the PBE can be written as in Eq. 4.2. Moreover, $D(t)$ represents the rate in which a particle change its size. The term in the r.h.s. is due to the addition of NaCl crystals into the vessel, which is explained later in more detail. Eq. 4.2 is valid for the domain of $l \in (l_{min}, +\infty)$, thus, when particles reach the minimal stable size due to dissolution, they are disregarded from the PSD, see Section 4.2.3 for the details.

$$\frac{\partial n(l,t)}{\partial t} + \frac{\partial [D(t)n(l,t)]}{\partial l} = \dot{n}_{add}(l,t) \tag{4.2}$$

The mass of NaCl dissolved in the liquid phase ($m_{NaCl,L}$) varies along the experiment only due to the dissolution of particles as indicated by the mass balance in Eq. 4.3. In this equation ρ_c is the crystal apparent density (2165.00 kg/m^3), k_v is the crystal shape factor, which is equal to 1.0, since the NaCl particles are approximately cubic.

$$\frac{dm_{NaCl,L}}{dt} = -3\rho_c k_v \int_0^\infty [n(l,t) l^2 D(t) dl] \tag{4.3}$$

Dissolution Rate Calculation

The dissolution of NaCl is considered to follow the diffusion-reaction theory (Mullin, 2001), in which the dissociation of solute molecules through a surface reaction, followed by the diffusion of these molecules to the bulk liquid phase, is

involved. The approach assumed here is to consider the dissolution rate as an overall function of both reaction and diffusion processes as described by Eq. 4.4, which can be applied for both dissolution and particle growth (Lasaga, 1998). The dissolution rate is denoted as $D(t)$ and represents the variation of particle size with time $\left(\frac{dl}{dt}\right)$. It is written as a function of the change in molar free-energy of reaction ($\Delta\overline{G}$).

$$D(t) = k_d(T) f(\Delta\overline{G}) \prod_i a_i^{\zeta_i} \tag{4.4}$$

The dissolution rate (Eq 4.4) depends on the temperature, co-solvents, and undersaturation. The temperature dependence is in a greater extent described by the kinetic parameter $k_d(T)$, although it also has influence on the other terms. This parameter is considered to follow the Arrhenius equation (Eq. 4.5), in which $k_{d,0}$ is the pre-exponential factor and E_a is the activation energy. The term $\prod_i a_i^{\zeta_i}$ is associated with the co-solvents that modify physicochemical properties of the liquid, thus in this term $i = [MEG]$, a_i its activity and ζ_i is a parameter to be determined (Lasaga, 1998).

$$k_d(T) = k_{d,0} \exp\left[-\frac{E_a}{RT}\right] \tag{4.5}$$

The last term $f(\Delta\overline{G})$ is the dependence on the free-energy change for the dissolution reaction, $\Delta\overline{G}$, and has the constraint $\Delta\overline{G} = 0$ at equilibrium, which guarantees that the kinetics is in accordance with the thermodynamic limiting condition (Lasaga, 1998). A general formula to describe $f(\Delta\overline{G})$ (Eq. 4.6) is based on the transition state theory, but including the factor λ for cases with non elementary reaction.

$$f(\Delta\overline{G}) = \left[\exp\left(\frac{\lambda\Delta\overline{G}}{RT}\right) - 1\right] \tag{4.6}$$

For aqueous system, the Gibbs free-energy of the dissolution reaction is written as Eq. 4.7 (Prausnitz et al., 1998), in which a_i and ν_i are the activity and stoichiometric coefficient of the species i involved in the dissolution reaction ($i = [\mathrm{Na}^+, \mathrm{Cl}^-]$) and K_{eq} is the equilibrium constant.

$$\Delta\overline{G} = RT \ln\left(\frac{\prod_j a_j^{\nu_j}}{K_{eq}}\right) \tag{4.7}$$

Substituting Eq. 4.7 into Eq. 4.6, and the resulting equation into Eq. 4.4, the

dissolution rate given by Eq. 4.8 is obtained. Moreover, the term related with the co-solvent effects (MEG) is simplified by considering the MEG activity coefficient as unity. This term lumps all the MEG contribution to the system, such as change in viscosity and density, in a single factor.

$$D(t) = k_d(T)(w_{MEG})^{\zeta} \left[\left(\frac{\prod_j a_j^{\nu_j}}{K_{eq}} \right)^{\lambda} - 1 \right] \tag{4.8}$$

The equilibrium constant of the dissociation reaction NaCl(s) $\rightleftharpoons$ $Na^+_{(aq)}$ + $Cl^-{}_{(aq)}$, in pure water, which is only temperature dependent, is given by Eq. 4.9 (Kaasa, 1998) with T in Kelvin.

$$K_{eq} = -814.18 + 7.4685T - 2.3262 \cdot 10^{-2}T^2 + 3.0536 \cdot 10^{-5}T^3 - 1.4573 \cdot 10^{-8}T^4 \tag{4.9}$$

Ionic Activity Product Calculation

The ionic activity coefficient is defined based on the species molality c_{Na^+} and c_{Cl^-} (Eq. 4.10), which is defined as $c_i = \frac{\eta_i}{m_w}$ with η_i as the number of mols of a specie i in the liquid and m_w as the solvent mass (water and MEG). Since the stoichiometric in the NaCl dissociation is 1:1: c_{Na^+}=c_{Cl^-}=c_{NaCl}, the ionic activity product is rewritten as in Eq. 4.11.

$$\prod_j a_j^{\nu_j} = a_{Na^+} a_{Cl^-} = c_{Na^+} c_{Cl^-} \gamma_{Na^+} \gamma_{Cl^-} \tag{4.10}$$

$$\prod_j a_j^{\nu_j} = c_{NaCl}^2 \gamma_{Na^+} \gamma_{Cl^-} \tag{4.11}$$

The ionic activity product is dependent on the product $\gamma_{Na^+}\gamma_{Cl^-}$. Eq. 4.12 defines this product with two contributions: the ions in solution $\gamma_{\pm}$ and a correction factor τ due to the co-solvent presence.

$$\gamma_{Na^+}\gamma_{Cl^-} \equiv (\gamma_{\pm}\tau)^2 \tag{4.12}$$

The activity coefficient $\gamma_{\pm}$ is the mean activity coefficient of ions in solution due to electrostatic contribution, which is calculated here from the Pitzer model (Prausnitz et al., 1998). See Appendix G for the NaCl Pitzer model.

The correction factor (τ) is used to include the MEG effects and is empirically fitted from solubility data as function of MEG concentration (Sandengen, 2006).

Here Eq. 4.13 was used with w_{MEG} as the MEG mass fraction (free of solute). Thus, substituting Eq. 4.12 into 4.11 gives Eq. 4.14.

$$\tau = \exp\left[2.11 w_{MEG}\right] \tag{4.13}$$

$$\prod_j a_j^{\nu_j} = (\gamma_{\pm}\tau)^2 {c_{NaCl}}^2 \tag{4.14}$$

Grayscale correlation

The GS variation is mainly related with the amount of solids per volume in the suspension, since the presence of solid particles has a major impact on the color pattern collected by the CCD sensor (Silva et al., 2013). The light intensity is related to the turbidity and, thus, to the liquid solute concentration (Benavides et al., 2015). Moreover, because of uncontrolled illumination conditions, each experiment can start with a different GS value (clear solution).

Eq. 4.15 relates the calculated GS_{calc} to the solid concentration $C_{NaCl,S} = m_{NaCl,S}/V$ in g/cm^3, where $m_{NaCl,S}$ is the mass of solid NaCl in the suspension, and V is the mixture volume. The solid mass of NaCl is obtained from the PSD third order moment μ_3 (Eq. 4.16). The GS is also related to the liquid solute concentration $C_{NaCl,L} = m_{NaCl,L}/V$ (g/cm^3). The parameters β_1, β_2 and β_{clear} are to be determined for each experimental condition.

$$GS_{calc} = \beta_1 C_{NaCl,S} + \beta_2 C_{NaCl,L} + \beta_{clear} \tag{4.15}$$

$$m_{NaCl,S} = \mu_3 \rho_c k_v = \left[\int_0^{\infty} n(l,t) l^3 dl\right] \rho_c k_v \tag{4.16}$$

The volume V is obtained according to an experimentally fitted equation for the density of NaCl, MEG and water mixture (Eq. 4.17) (Figueiredo, 2016). In this equation, X_{NaCl} is a normalized variable based on the NaCl concentration: $X_{NaCl} = (m_{NaCl,L}/m_w - 0.01)/(0.26 - 0.01)$; X_T is the normalized temperature as $X_T = (T - 25)/(80 - 25)$ with T in °C. The regression parameters b_i are: [0.99651, -0.0297, 0.124599, 0.237546, -0.04193, -0.11162, 0.99651].

$$\rho_{mix} = b_0 + b_1 X_T + b_2 w_{MEG} + b_3 X_{NaCl} + b_4 X_{NaCl}^2 + b_5 w_{MEG} X_{NaCl} \tag{4.17}$$

Crystal addition

At each experiment, specified amount of NaCl crystals were added to the system to evaluate the dissolution behavior. The PSD of the added crystals were considered as an uniform distribution from size $l_{low,add}$ to $l_{up,add}$. Thus, for $m_{add,j}$ as the mass of added crystals in the j-th addition, its PSD $n_{add_j}(l)$ is defined as in Eq 4.18, see H for the details. A mean size of 0.25 mm for the added crystals was obtained from optical microscopy.

$$n_{add_j}(l) = \begin{cases} \dfrac{4m_{add,j}}{(l_{up,add}^4 - l_{low,add}^4)\rho_c k_v} & \text{if } l_{low,add} \leq l \leq l_{up,add} \\ 0 & \text{otherwise} \end{cases} \tag{4.18}$$

Even though the particles are added almost instantly, there is a damping effect on the GS values after each addition. The behavior from the solid mass addition instant to the subsequent GS value peak instant is mostly dependent on the hydrodynamics and wetting mechanism and its study is not the scope here. Thus, a simplification is assumed, which considers that the salt is continuously added during a time interval $\Delta t_{add,j}$ for each addition j and, hence, a rate of added salt can be defined. The GS profile behavior is further discussed in Section 4.3.1.

Both the addition starting time and the GS peak time (end of addition) were taken from visual inspection of the GS profiles for each experiment. The addition starting times are reported in Table 4.2, whereas the duration of each addition is reported in Table 4.3.

Table 4.3: Time interval from salt addition starting time to GS subsequent peak time.

Experiment	**1st Add.** $\Delta t_{add,1}$	**2nd Add.** $\Delta t_{add,2}$	**3rd Add.** $\Delta t_{add,3}$	**4th Add.** $\Delta t_{add,4}$
exp1	2.0	1.9	2.6	3.2
exp2	2.5	5.8	5.0	-
exp3	0.98	2.6	3.4	4.7
exp4	0.73	3.1	3.4	4.1
exp5	0.55	0.2	0.4	-

The salt addition was included in the numerical model using the additive term in Eq 4.2 ($\dot{n}_{add}(l,t)$), which represents the rate of added crystal number density along the dissolution experiments as a continuous function of time t. During each addition j, it is considered that $\dot{n}_{add}(l,t) = \dot{n}_{add,j}(l,t)$, which is obtained by Eq. 4.19 using $n_{add_j}(l)$ from Eq. 4.18, and it is zero otherwise. The added PSD rate $\dot{n}_{add}(l,t)$ has a dynamic profile of successive steps from zero to $\dot{n}_{add,j}(l,t)$ and is defined by Eq. 4.20.

$$\dot{n}_{add,j}(l,t) = \begin{cases} \dfrac{n_{add_j}(l)}{\Delta t_{add,j}} & \text{if } t_{add,j} \leq t \leq t_{add,j} + \Delta t_{add,j} \\ 0 & \text{otherwise} \end{cases} \tag{4.19}$$

$$\dot{n}_{add}(l,t) = \sum_{j=1}^{r_{add,k}} \dot{n}_{add,j}(l,t) \tag{4.20}$$

A regularization function (Eq. 4.21) is used to smooth the added PSD profile ($\dot{n}_{add}(l,t)$) in accordance with the ongoing solid addition. A vector of time events, which represents the discontinuities to be smoothed, is defined by Eq. 4.22, where $t_{add,end,j} = t_{add,j} + \Delta t_{add,j}$ is the end of addition j. The vector A indicates the successive values that $\dot{n}_{add}(l,t)$ takes along the experiment duration (Eq. 4.23).

$$\dot{n}_{add}(l,t) \approx A_0 + \sum_i \frac{(A_i - A_{i-1})}{2}[\tanh((t - t_{evnt,add_i})\xi) + 1] \tag{4.21}$$

$$t_{evnt,add} = [t_{add,1}\ t_{add,end,1}\ t_{add,2}\ t_{add,end,2}\ \ldots\ t_{add,r_{add,k}}\ t_{add,end,r_{add,k}}] \tag{4.22}$$

$$A = \left[0\ \dot{n}_{add,0}\ 0\ \dot{n}_{add,1}\ 0\ \dot{n}_{add,2}\ \ldots\ 0\ \dot{n}_{add,r_{add,j}}\ 0\right] \tag{4.23}$$

4.2.3 Numerical method for the dissolution process

The resulting model based on PBE consists of a set of coupled integro-differential equation (e.g. the mass balance) and a hyperbolic partial differential equation (the PBE), oftenly presenting sharp profiles. In order to deal with those features, several specialized numerical methods are needed, for a detailed review see Costa et al. (2007). The method of moment is widely used because it transforms the partial differential equations into a set of ordinary differential equations. The drawback is that it requires additional methods to reconstruct the PSD and it is not applicable in some situations, as in size dependent growth or the disappearance of particles at certain size.

When dissolution is considered, the particle sizes decrease towards the minimal stable size, here $l_{min} = 0$, when it is no longer stable and vanishes from the solid phase. Thus, it is taken from the particle distribution. The particle disappearance creates a discontinuity in the solution and thus causes instability in finite-difference numerical methods. Due to this phenomenum, the knowledge of the number density of particles at the minimal size is necessary during the dynamic integration, thus the method of moments requires special strategies for reconstructing the PSD (Massot et al., 2010).

The numerical method chosen for simulating the dissolution process was the *Moving Sectional Method* (MSM) (Kumar and Ramkrishna, 1997). In this approach the size domain is discretized in contiguous bins with boundaries given by l_i and l_{i+1} and with the number of particles in this bin as $N_i = \int_{l_i}^{l_{i+1}} n(l,t)dl$. Additionally, a representative size for each bin (x_i) is defined and the PSD is approximated as $n(l,t) = \sum_{i=0}^{M-1} N_i \delta(l - x_i)$, in which M is the total number of bins for a given time t. In each simulation run, a linearly spaced mesh with boundaries from $l_0 = l_{min} = 0$ to $l_{M_0} = 0.35$ mm were used, where M_0 is the number of bins at the initial time, which was set to 50. The pivots x_i were set as the mean value at each bin ($x_i = (l_i + l_{i+1})/2$) and the initial number of particles N_i is zero for all bins, since no seeds was used.

After applying the MSM to the proposed model, a set of ordinary differential equations (Eq. 4.24) is obtained, which can be integrated on time by suitable dynamic solvers. The initial conditions for number of particles and mass of NaCl were: $N_i = 0 \ \forall \, i$, since no seeds were used and $m_{NaCl,L} = 0$, because the experiments started without diluted NaCl.

$$\frac{dN_i(t)}{dt} = \dot{N}_{add,i}(t) \tag{4.24a}$$

$$\frac{dm_{NaCl,L}}{dt} = -3\rho_c k_v \sum_{j=0}^{M-1} [D(t) N_j(t) x_j^2] \tag{4.24b}$$

$$\frac{dx_i}{dt} = D(t) \tag{4.24c}$$

$$\frac{dl_i}{dt} = D(t) \tag{4.24d}$$

where $\dot{N}_{add,i}(t) = \int_{l_i}^{l_{i+1}} \dot{n}_{add}(l,t)dl$, $0 \leq i < M$ and $D(t)$ as shown in Eq. 4.8.

Eqs. 4.24 are valid only for $x_0 > l_{min}$. Hence, in order to incorporate the dissolution behavior to the model using the MSM, when the first bin (x_0) reaches the minimal size, its correspondent number of particles N_0 leaves the domain. Thus, during the simulation, a checking for $x_0 \leq l_{min}$ is performed at each solver iteration. The error on the removal of particles is minimized by the use of small time intervals.

The strategy used to solve the dissolution problem with the addition of particles using the MSM is with successive bin additions, one at time, at the maximum considered size. Adding bins at the maximum size ensure that new added particles to the system are represented. The new added bin has $l_{new} = x_{new} = l_{max}$ and $N_{new} = 0.0$. This scheme was used to perform the parameter estimation. The dynamic system was solved using an explicit third-order Runge-Kutta integration scheme.

4.2.4 Parameter estimation

The experiments described in Table 4.1 were used to evaluate the dissolution kinetics for the NaCl in water with MEG as co-solvent. The measurements used are the *RGB* temporal profile collected by the Masterview software.

The goal of the parameter estimation procedure is to obtain a model capable of representing all experiments from Table 4.1. The experimental conditions of temperature and MEG concentration are taken into account by the dissolution rate (Eq. 4.8). The temperature dependence is more related with the Arrhenius equation (Eq. 4.5), which requires the estimation of parameters $k_{d,0}$ and E_a. Since the MEG concentration influences the dissolution kinetics, being simplified by the term w_{MEG}^{ζ}, the estimation of the parameter ζ is required. From experimental observation, higher MEG concentration reduces the dissolution rate, thus $\zeta < 0$. A possible non-elementary surface reaction relating the system undersaturation with the dissolution rate is modelled by the parameter λ.

Because the *RGB* values depend on uncontrolled illumination conditions, an absolute value relating to the solid phase properties is not possible. Therefore, the parameters related with the *GS* correlation (Eq. 4.15) are estimated for each experiment.

The parameter estimation problem uses all five experiments in a single objective function to obtain the parameter set θ composed by the kinetic parameters: $k_{d,0}$, E_a/R, ζ, and λ and also the *GS* related parameters: $\beta_1^{(1)}$, $\beta_1^{(2)}$, $\beta_1^{(3)}$, $\beta_1^{(4)}$, $\beta_1^{(5)}$, $\beta_2^{(1)}$, $\beta_2^{(2)}$, $\beta_2^{(3)}$, $\beta_2^{(4)}$ and $\beta_2^{(5)}$. Additionally, since the measurement of the added PSD has considerable uncertainty, a new parameter Δl_{add} was introduced to be estimated. The lower and upper bounds of $n_{add_j}(l)$ are written as $l_{low,add} = l_{add,mean} - \Delta l_{add}$ and $l_{up,add} = l_{add,mean} + \Delta l_{add}$ with $l_{add,mean}$ as the mean size equal to 0.25 mm.

The parameters $\beta_{clear}^{(k)}$ are obtained directly from the corresponding *RGB* measurements using the mean value of the last 10 samples before the first addition time. Hence a total of 15 parameters are estimated. Note that each experiment contains 600 samples, summing up to a total of 3000 measurement points.

Eq. 4.25 states the parameter estimation problem with $GS^{(exp:k)}(t_i)$ as the measured values for experiment k at a sampling time t_i with a total number of samples $n_t = 600$. The calculated values $GS^{(calc:k)}(t_i)$ are obtained solving the model described in Section 4.2.2. The solution of Eq. 4.25 was obtained using the simplex Nelder-Mead method and further refined by a Levenberg-Marquardt method. The estimation was performed using the package LMFIT (Newville et al., 2014), which uses optimization routines from the SCIPY library (Jones et al., 2001).

$$\min_{\theta} \quad J(\theta) = \sum_{k=1}^{5} \sum_{i=1}^{n_t} \left[GS^{(exp:k)}(t_i) - GS^{(calc:k)}(t_i) \right]^2 \tag{4.25}$$

The adopted procedure for the parameter estimation is schematically showed in Figure 4.3. All experimental conditions (Tables 4.1 and 4.2) are used to obtain the $GS^{(exp:k)}$ measurements and also by the proposed dynamic model. The model provides the PSD and the solute solid and liquid concentration for each experiment using the kinetic parameters $k_{d,0}, E_a, \zeta$, and λ. The obtained PSD and solute concentrations are used by the correlation Eq. 4.15, yielding the calculated $GS^{(calc:k)}$ for each experiment. The estimation compares the experimental and calculated GS values according to Eq. 4.25 and interactively updates the kinetic parameters and Δl_{add} to the model and $\beta_1^{(k)}$ and $\beta_2^{(k)}$ to the correlation. When the estimation procedure converges, the final parameters set is obtained.

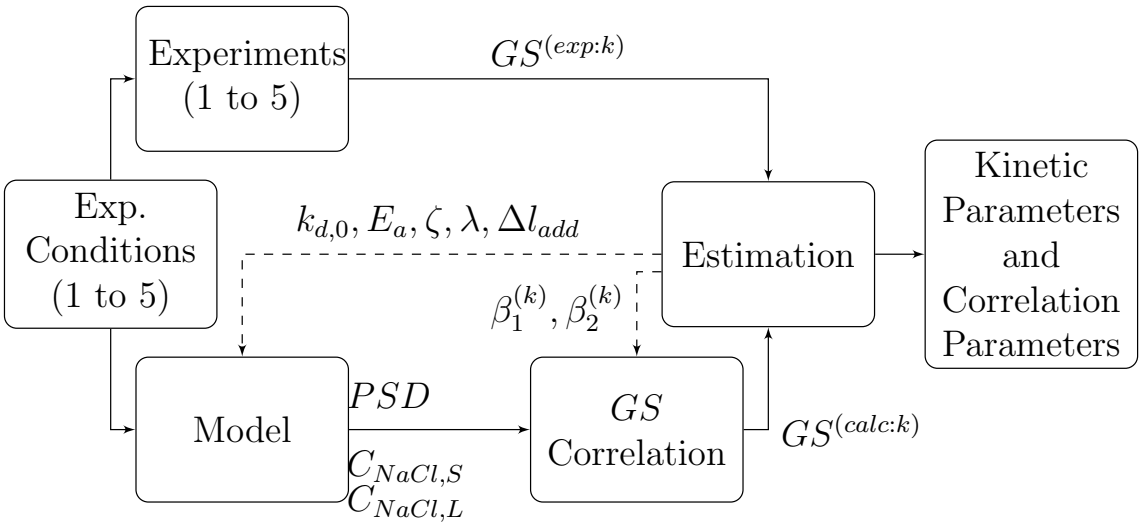

Figure 4.3: Procedure for the parameter estimation.

4.3 Results and Discussion

4.3.1 Qualitative discussion of the RGB measurements

The measured GS values depend on uncontrolled illumination conditions, thus their values can significantly vary for different experimental conditions. Therefore, in order to use them to infer the dissolution kinetics, calibrations are required for each experiment.

Figure 4.4 depicts two replicated experiments (exp3 and exp4 from Table 4.1). These experiments have four solid additions each and, even though at the same operating conditions, they have different addition time instants. For comparing the GS dynamic profile, in Figure 4.4 the addition time instant of the j-th addition of exp3 was matched with the corresponding j-th addition of exp4. On both experiments the GS measurement time is 0.1 min. It can be noted that the GS

absolute values were considerable different on each experiment, reaching a value of 230 for exp4 and 166 for exp3. However, the qualitative behavior of the GS are similar after each addition and it is possible to identify patterns occasioned by systematic effects of the underlying dissolution phenomena.

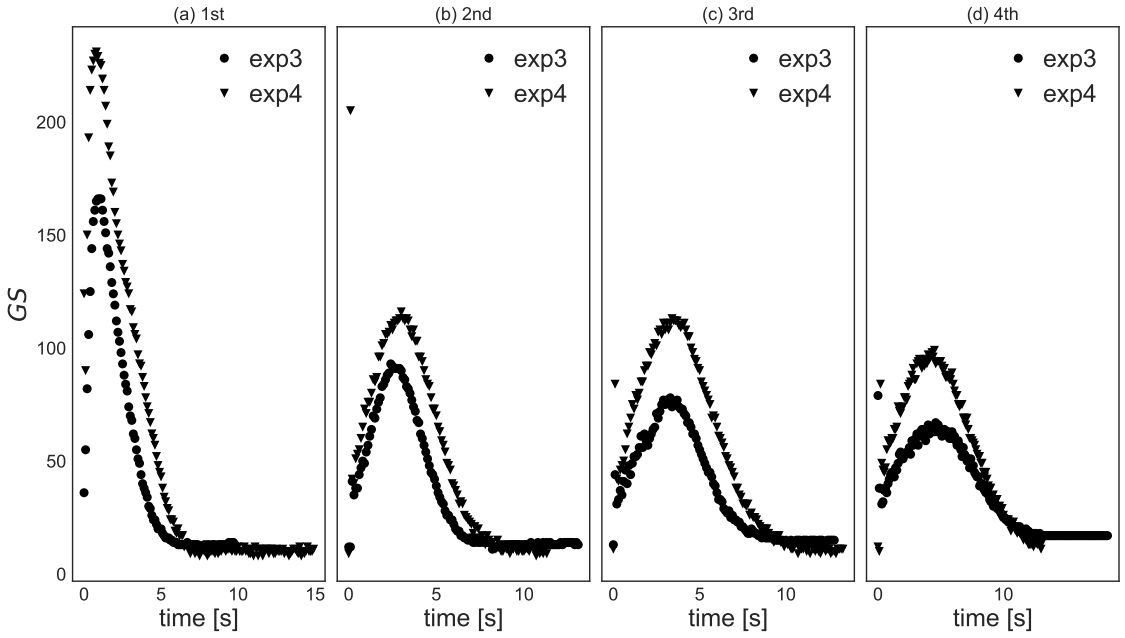

Figure 4.4: GS dynamic profile for replicate experiments 3 and 4 with matching addition time instants. Each addition correspond to a chart from (a), first addition, to (d), fourth addition. The plots share the y-axis and the x-axis indicates the time after j-th addition. Data from Figueiredo (2016).

The time interval for the GS value from the first addition to the peak is close to 1 min for both experiments. For the subsequent additions, the time intervals for exp3 and exp4 are: 2.7 and 3 min at second addition, 3.2 and 3.5 min at third addition and 4.2 and 4.6 min for the last addition.

The increase in the time intervals to reach the subsequent peak after successive addition has three main contributions: (i) the time for the experimenter to actually perform the addition of all the material; (ii) the time for the solution homogenization due to the hydrodynamics behavior as diffusion and stirring effect; and (iii) the surface wetting effect which is dependent on the concentration of ions in solution. The first contribution is negligible. During the dissolution there is an increase in Na^+ and Cl^- concentration that raises the fluid viscosity, thus it is expected a wider time interval for the suspension homogenization. Furthermore, higher ions concentration in the liquid phase decreases the water capacity to wetting the crystal's surface.

Along the successive additions, a decrease in the dissolution rate can be observed, e.g., after the forth addition the time interval after the peak for the GS value to reach a constant value is greater than for the previous additions (Figure 4.4). This

effect is due to the increase in the concentration of ions, which decreases the chemical affinity between the species and reduces the undersaturation.

Figure 4.5 shows the comparison for the first addition for two different values of MEG concentration (exp1 with 10wt% and exp2 with 50wt% MEG content). The experiments show that increasing the MEG mass fraction both the time interval from addition starting time to peak and the time interval from peak to a constant value increase. The former is due to the increase in the viscosity, which results in slower suspension homogenization. The later has two major contribution: the increase in the viscosity, which reduces the diffusion slowing down the dissolution, and also the higher MEG concentration increases the ionic activity product, thus decreasing the undersaturation by reducing the term $\left(\prod_j a_j^{\nu_j}/K_{eq} - 1\right)$ from Eq. 4.8.

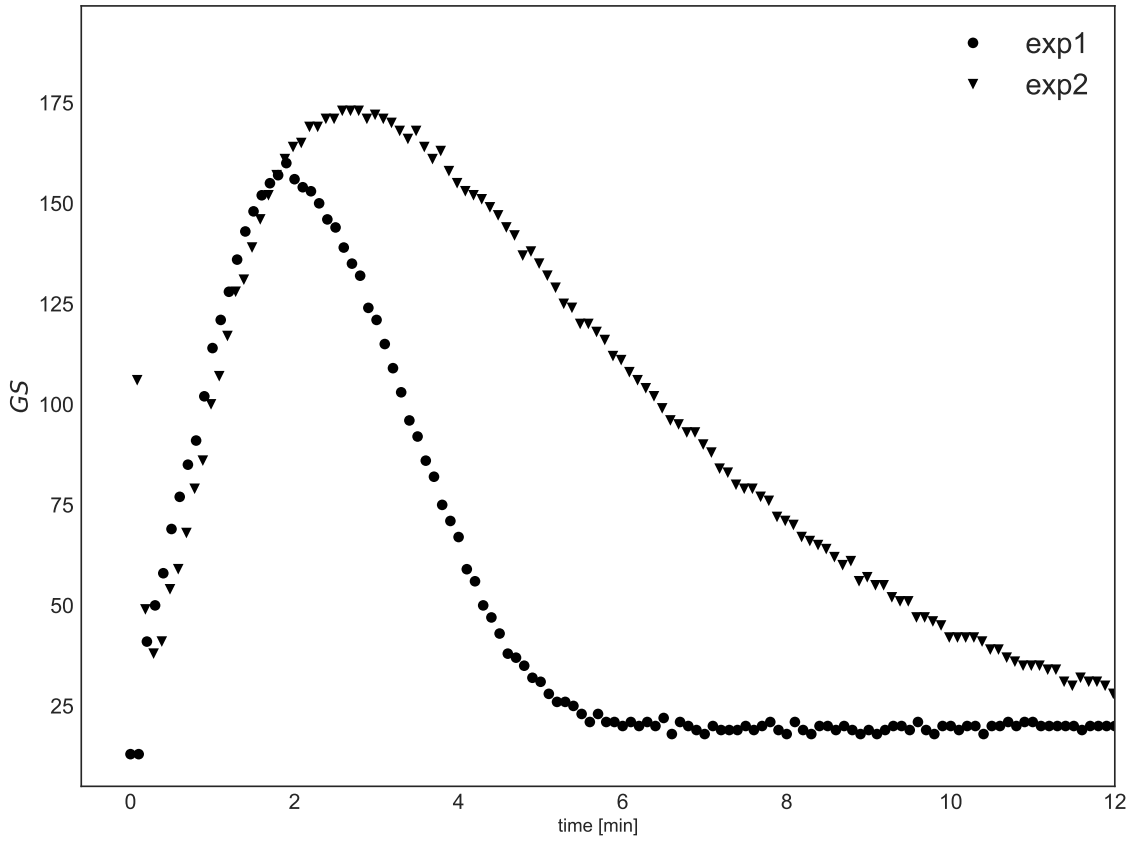

Figure 4.5: Comparison of the width to the peak after the first addition for experiments exp1 with 10wt% of MEG and exp2 with 50wt% of MEG. The time axes was shifted to match both addition times at zero. Data from Figueiredo (2016).

The temperature variation influences the dissolution profile changing both the time interval from addition starting time to peak, Δt_{add}, and the time from the peak to the complete solid dissolution. At higher temperature, the solution viscosity decreases and then the diffusion coefficient increases, which results in faster mixing and homogenization.

4.3.2 Parameter Estimation

Table 4.4 presents the estimated parameters and standard parameter errors. The standard errors are calculated from the estimated parameters covariance matrix (Newville et al., 2014). It should be noted that the parameter related with the liquid solute composition in the GS correlation, $\beta_2^{(4)}$, had a high standard error compared with the estimated value, which indicates parameter insignificance, thus it could be removed from the parameter set.

Table 4.4: Estimated parameters for each experiment.

Parameter	Value	Std. Error	Units
$k_{d,0}$	0.000777843	0.00018	m/s
$\frac{E_a}{R}$	-2459.16	73.89	K
ζ	-0.617508	0.017	–
λ	3.34659	0.22	–
Δl_{add}	0.09713	0.0071	mm
$\beta_1^{(1)}$	3659.62	53.32	cm^3/g
$\beta_2^{(1)}$	95.748	4.95	cm^3/g
$\beta_1^{(2)}$	5153.08	64.18	cm^3/g
$\beta_2^{(2)}$	34.2103	13.47	cm^3/g
$\beta_1^{(3)}$	3960.9	59.01	cm^3/g
$\beta_2^{(3)}$	11.0046	6.34	cm^3/g
$\beta_1^{(4)}$	6287.68	66.84	cm^3/g
$\beta_2^{(4)}$	0.0020226	8.67	cm^3/g
$\beta_1^{(5)}$	1714.44	110.28	cm^3/g
$\beta_2^{(5)}$	43.8066	5.87	cm^3/g

Figures 4.6-4.10 present at the top plot the comparison between the predicted values and experimental measurements of GS and, at the bottom plot, the dissolution rate ($D(t)$) temporal profile for each experiment from Table 4.1. Overall, reasonable predictions are obtained using the proposed methodology based on the used low-cost measurement apparatus. It can be noted that the decay dynamics after each addition peak value had good agreement with the experimental data. The main source of predictions errors are due to the damping effect after each addition, which was not modeled in this work.

Furthermore, those figures elucidate the effect of the operating conditions on the dissolution rate. It can be noted from the dissolution rate profile that, as the addition and dissolution occurs, the magnitude of the dissolution rate decreases, which is due to the higher NaCl liquid concentration that reduces the undersaturation level.

The MEG concentration contribution is evidenced comparing exp1 and exp2 dissolution rate values. At exp2 conditions the dissolution rate absolute values are smaller than at exp1, as discussed in Section 4.3.1. Experiments 3 and 4 occur at

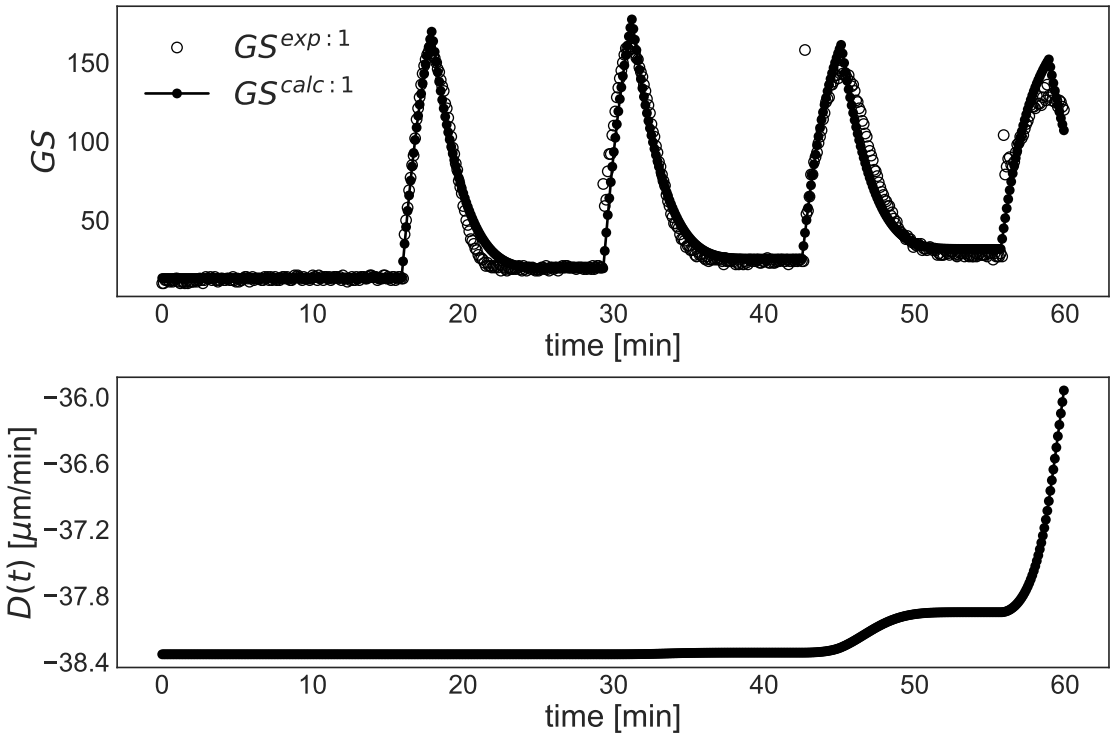

Figure 4.6: GS calculated values at experimental condition exp1 compared with GS measurements from Figueiredo (2016) ($T = 20$°C and $w_{MEG} = 0.125$) and the calculated dissolution rate profile (bottom plot).

the same operating conditions and Figures 4.8 and 4.9 indicate good reproducibility for the $D(t)$ values.

The temperature influence is observed by inspecting exp2 at 20°C, exp3 and 4 at 45°C and exp5 at 90°C, see Figures 4.7 to 4.10. At higher temperature a higher dissolution rate absolute value is obtained, as discussed in Section 4.3.1.

The experiments start free of solute at the initial time and after solid additions the undersaturation decreases. Thus the proposed model is required to fit a broader range of undersaturation. This was reflected in the relatively high estimated value of parameter λ, which decreases the magnitude of the term $\left(\prod_j a_j^{\nu_j}/K_{eq}\right)^{\lambda}$, thus making the dissolution rate less sensitive to the undersaturation. This behavior is shown in Figure 4.11 by plotting the dissolution rate against the Gibbs free-energy change ($\Delta\overline{G}/RT$) for each experiment. In this figure, the dotted lines are calculated using Eq. 4.4 with $f(\Delta\overline{G})$ from Eq. 4.6 for $\Delta\overline{G}/RT$ varying from -19.0 to zero for each experimental condition. Moreover, the dissolution values from the simulation with the estimated parameters are plotted for each experiment. Each addition time instant is represented by a circle maker (◯). The figure shows that the dissolution rate starts constant in respect to $\Delta\overline{G}/RT$ and then increases as $\Delta\overline{G}/RT$ goes to zero.

This behavior is in accordance with the dissolution plateau concept (Lasaga,

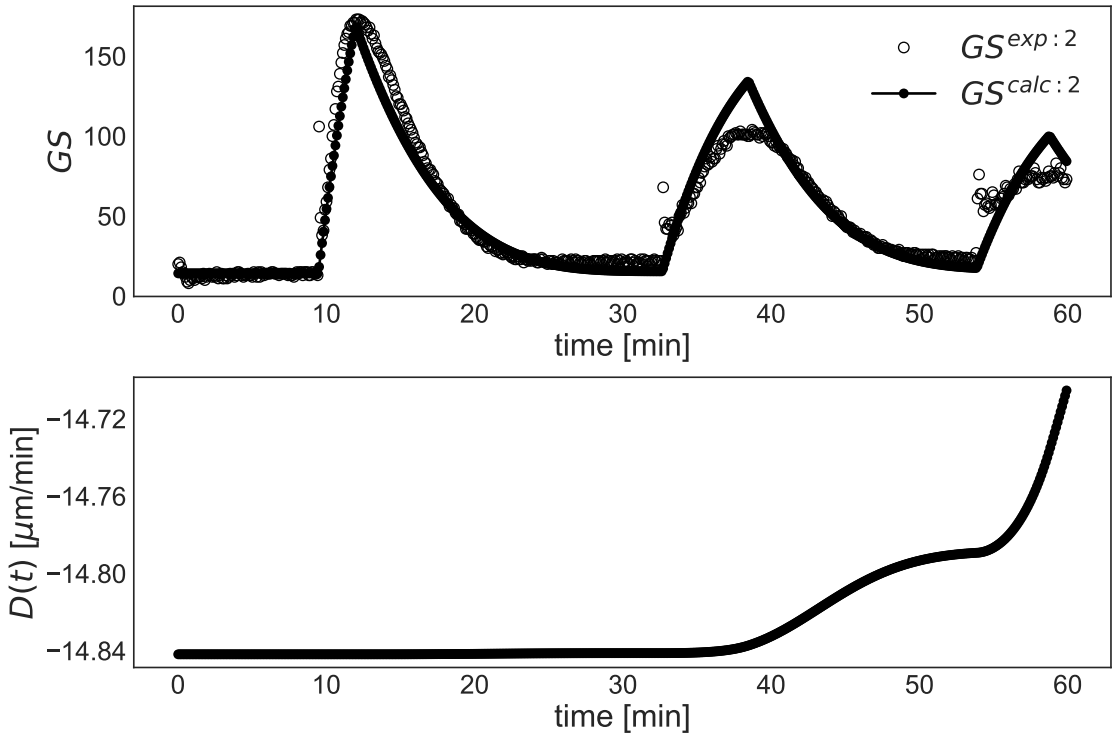

Figure 4.7: GS calculated values at experimental condition exp2 compared with GS measurements from Figueiredo (2016) ($T = 20$°C and $w_{MEG} = 0.581$) and the calculated dissolution rate profile (bottom plot).

1998). In conditions far from equilibrium, the dissolution rate of minerals become independent of the undersaturation, also denoted as zero order dynamics, and increases when closer to the equilibrium. Burch et al. (1993) indicated a limiting value for occuring the dissolution plateau as $\Delta\overline{G}/RT < -3$, which reasonably agrees with Figure 4.11. Quilaqueo and Aguilera (2015) evaluated the dissolution of single NaCl crystals in clear solute water and also found a zero order dynamics.

4.3.3 Process variables inference from the model

The proposed model provides detailed information of the dissolution dynamics, which after obtaining the model parameters can be used for further applications, such as PSD inference, process control, and optimal process design. In the following, experiment exp1 main dynamic variables are reported.

Figure 4.12 shows the liquid and solid NaCl mass profiles during the experiment. The solid mass is completely depleted after the three first additions and the experiment was halted during the dissolution of the fourth added solid mass. The liquid mass increases as the dissolution proceeds. The increase in the NaCl liquid concentration is responsible for the prediction of the base line jumps after each addition, since the mass of solids goes to zero.

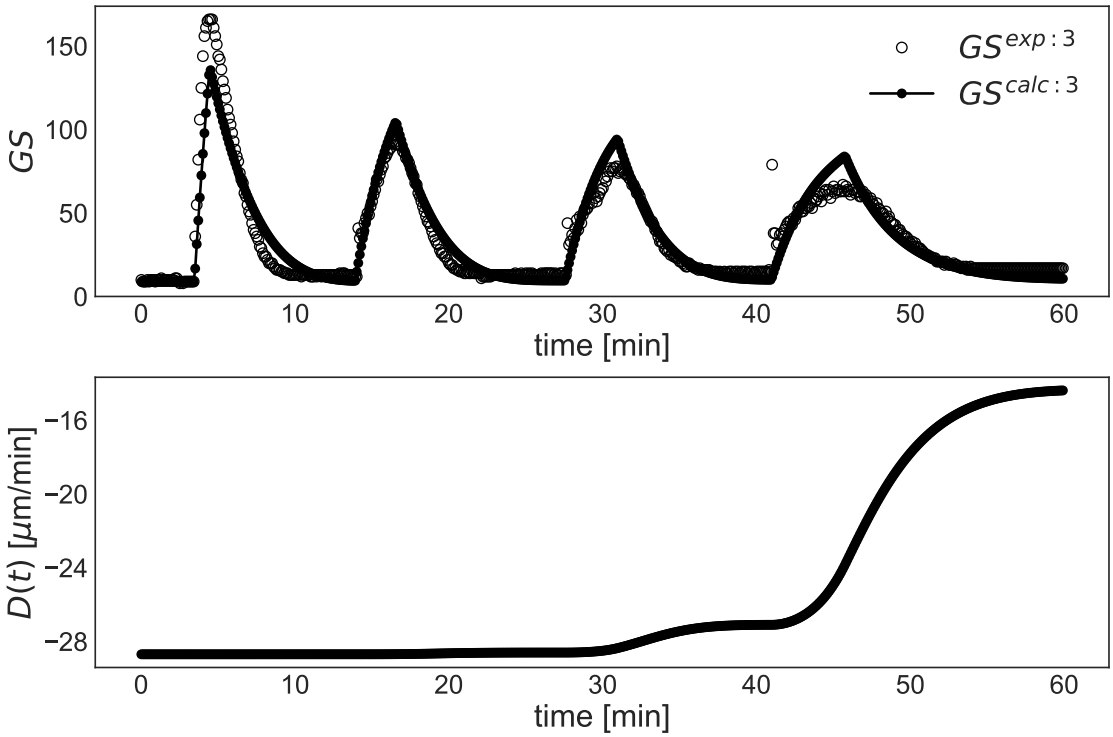

Figure 4.8: GS calculated values at experimental condition exp3 compared with GS measurements from Figueiredo (2016) ($T = 45$°C and $w_{MEG} = 0.581$) and the calculated dissolution rate profile (bottom plot).

The PSD for the first addition of exp1 is illustrated by Figure 4.13 using the number of particles per bin (N_i). The top plot shows the PSD during the addition of particles, which corresponds to the beginning of particle addition at $t \approx 16$ min to the GS peak value at $t \approx 18$ min. The bottom plot presents the PSD during the dissolution of the added particles from the GS peak value time instant to it reaching the base line. The former indicates that at early stages of the addition the PSD is similar to the added PSD (uniform distribution). However, particles are reducing their size while new particles are progressively being added to the system, hence, the PSD shape is modified along the addition. Moreover, in the bottom plot, after the GS peak, all particles decrease their size at the same rate, thus the PSD is translated maintaining the shape until the particles reach the critical size, when the disappearance of particles occurs. Compared to Figure 4.12, the top chart, representing particle's addition, is related to the first abrupt NaCl solid mass increase. Whereas the bottom chart is related to the decrease in solid mass and with the increase in NaCl liquid mass from $t \approx 18$ to 24 min.

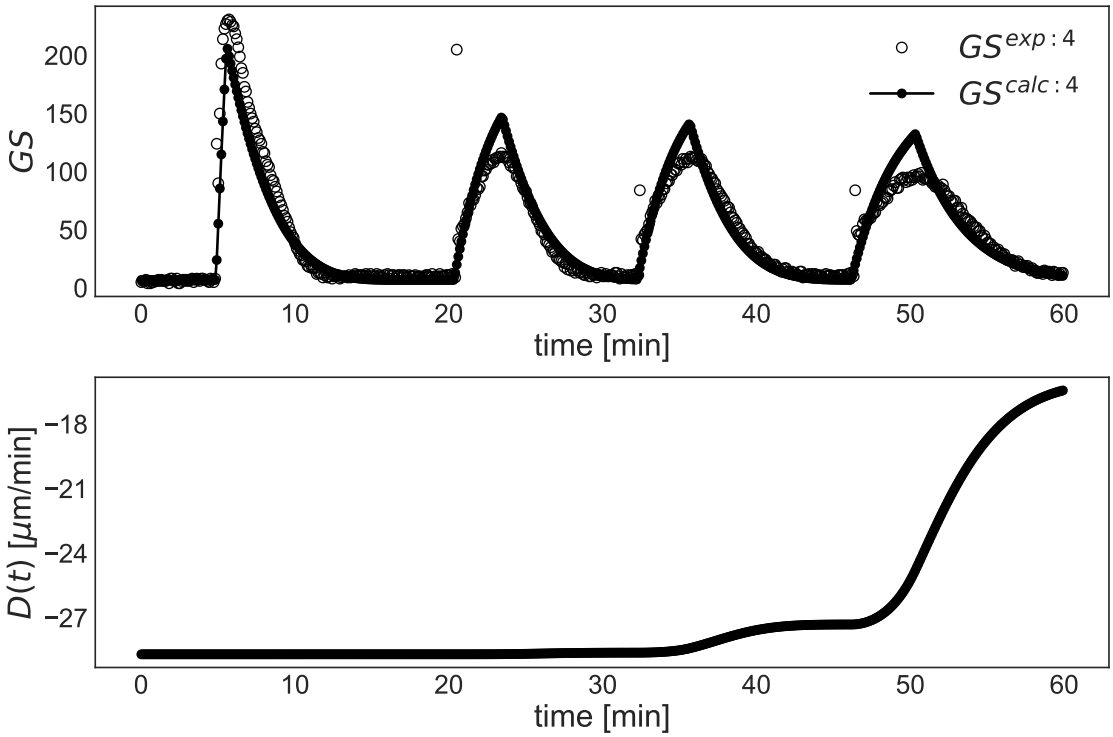

Figure 4.9: GS calculated values at experimental condition exp4 compared with GS measurements from Figueiredo (2016) ($T = 45$°C and $w_{MEG} = 0.581$) and the calculated dissolution rate profile (bottom plot).

4.4 Conclusions

In this work, available data from a low-cost measurement apparatus for the RGB color pattern was used to analyze the dissolution rate of NaCl in water/MEG mixture (Figueiredo, 2016). A dynamic model using the PBE was employed to predict the particle dissolution during successive solid mass additions. The used dissolution rate equation dependent on the temperature, MEG concentration and undersaturation was able to predict the behavior of all the experiments at different conditions. The model represented well the dissolution plateau far from equilibrium condition, as well as for condition closer to the saturation.

The GS profiles proved to be a suitable measurement to track the dissolution dynamics. Also, they provide information on how the operating condition (MEG concentration and temperature) affects the dissolution kinetics. It should be noted the limitation that calibrations for the GS parameters for each individual experiment are required.

The proposed dynamic model using the discretized PBE method was able to include the addition of classified particles during the simulation as well as representing the particle disappearance due to dissolution, which is a source of discontinuity and can cause instability in the solution.

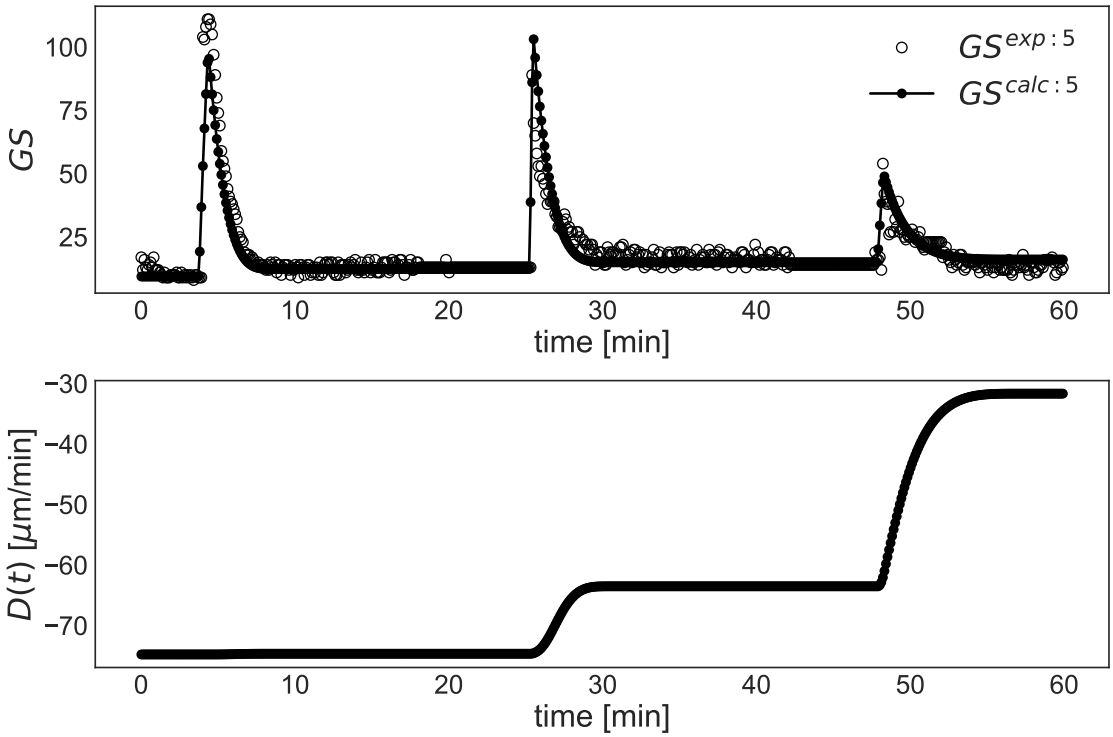

Figure 4.10: GS calculated values at experimental condition exp5 compared with GS measurements from Figueiredo (2016) ($T = 90$°C and $w_{MEG} = 0.581$) and the calculated dissolution rate profile (bottom plot).

Moreover, the proposed dynamic model can be used to infer other process variables, such as the particle distribution and the solid mass. Although the model was used only for dissolution it can be extended to include other particle interactions such as breakage or agglomeration and also to track the particle growth and nucleation.

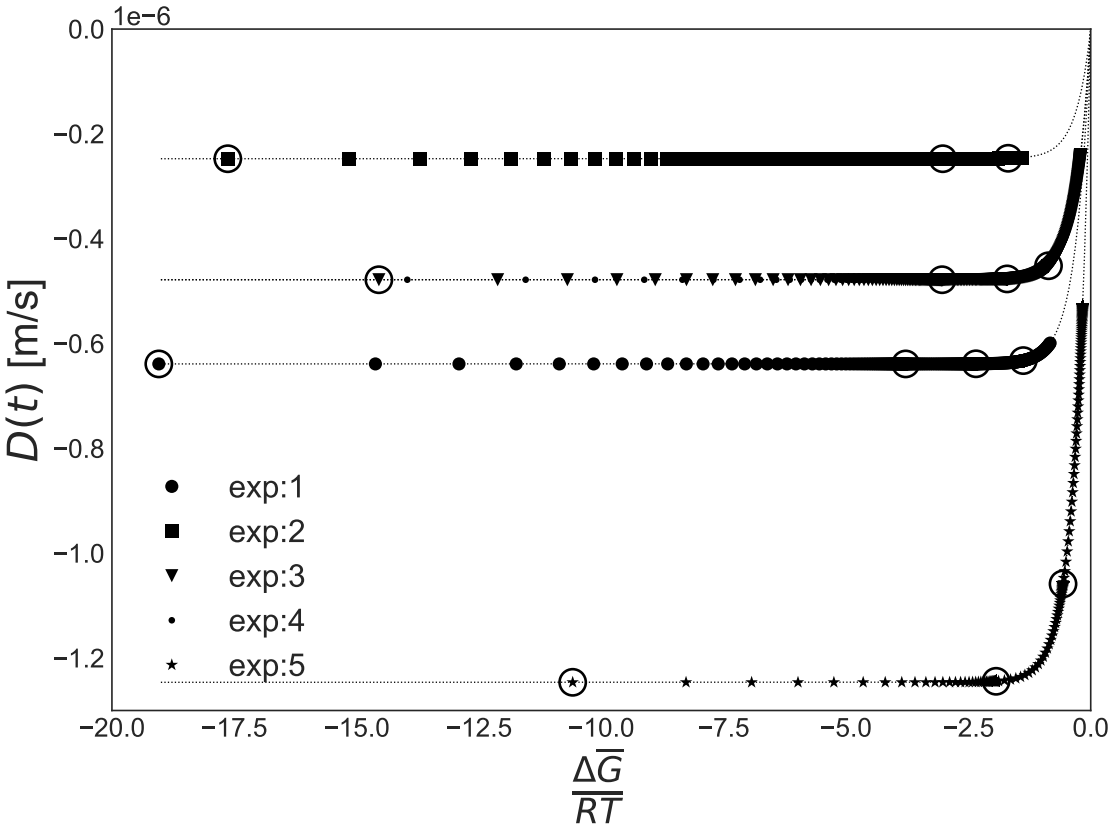

Figure 4.11: Gibbs free-energy change versus the dissolution rate for each experimental condition. The addition time instants for each experiment are shown by the circle makers ◯.

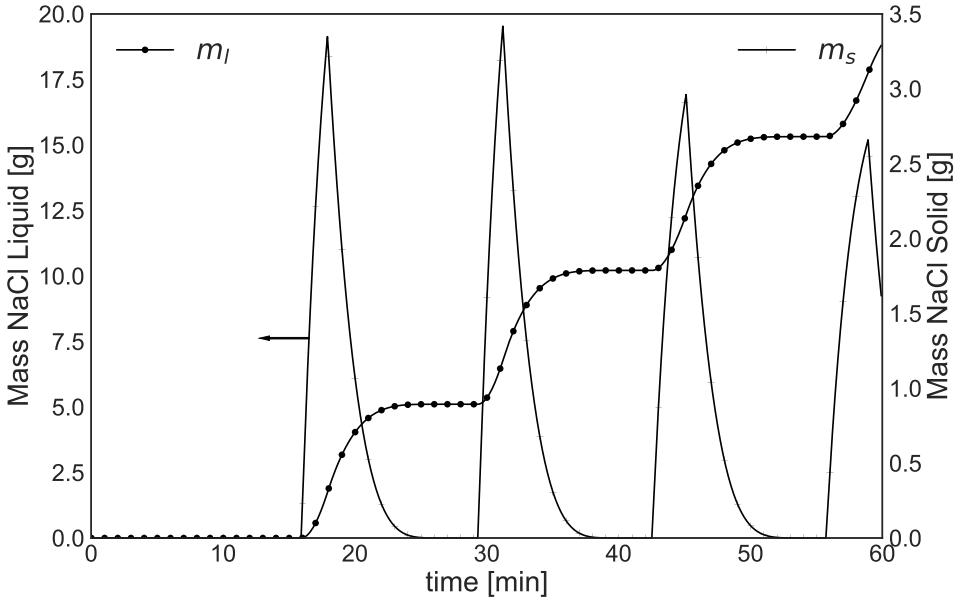

Figure 4.12: Dynamic profiles for the diluted (left y-axis) and solid (right y-axis) mass of NaCl for exp1.

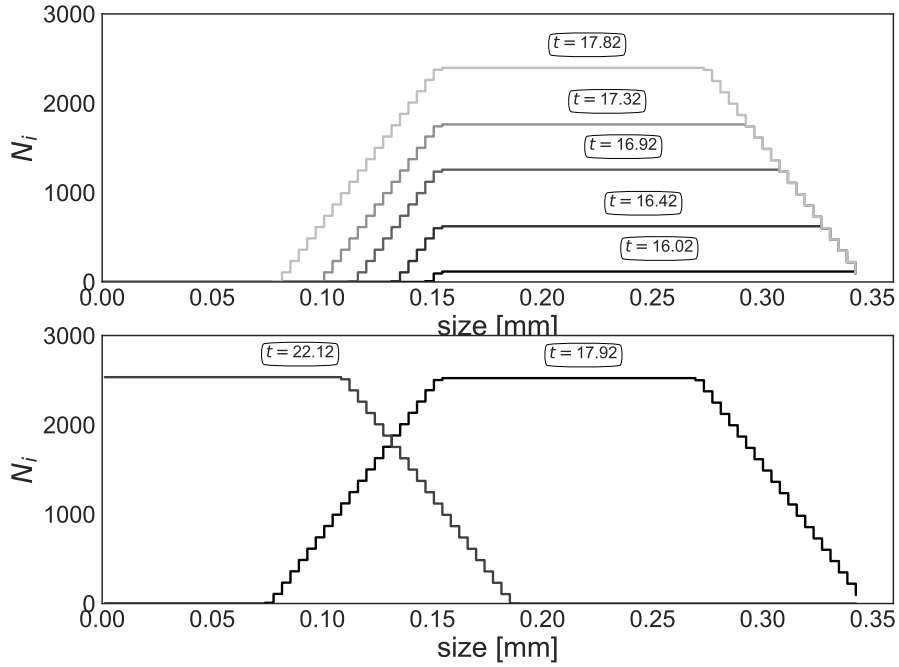

Figure 4.13: Particle size distribution after first addition of exp1 up to the peak GS value (top) and from the peak to dissolution (bottom) at different times instants (min).

Chapter 5

Optimal operation of batch enantiomer crystallization: From ternary diagrams to predictive control

This work consisted in the modeling and control of a batch crystallizer for the enantiomeric separation of racemic solid forming compounds with the development of a systematic methodology.

Specifically, the batch is considered pre-enriched with the enantiomer of interest so that the operation occurs in the region of pure preferred solid formation. For a detailed review on the ternary phase diagram for racemic compound forming system see Appendix A. A method for determining initial and final operating conditions was developed to facilitate process design and ensure maximum separation.

Then, information from the ternary diagram, as maximum yield reached, was incorporated into a predictive controller in which the objective function was to favor seed growth rather than nucleation. Scenarios with recycle and no recycling of fines were addressed.

These development were submitted to the following journal and conference proceedings:

- **Published in scientific journal:** Caio Felippe Curitiba Marcellos, Helen Durand, Joseph Sang II Kwon, Amaro Gomes Barreto, Paulo Laranjeira da Cunha Lage, Maurício Bezerra de Souza, Argimiro Resende Secchi, and Panagiotis D. Christofides. *"Optimal Operation of Batch Enantiomer Crystallization: From Ternary Diagrams to Predictive Control"*; AIChE Journal, 64 (5) 1618-1637 (2018); (Curitiba Marcellos et al., 2018).

- **Presented at the conference:** C. Curitiba Marcellos, H. Durand, J.

Kwon, A. Barreto Jr., P. Laranjeira da Cunha Lage, M. Bezerra de Souza Jr., A. Resende Secchi and P. D. Christofides; *"Optimal Operation of Batch Enantiomer Crystallization: From Ternary Diagrams to Predictive Control"*; AIChE Annual meeting, paper 597b, San Francisco, California, 2016

- **Presented at the conference:** C. Curitiba Marcellos, H. Durand, J. Kwon, A. Barreto Jr., P. Laranjeira da Cunha Lage, M. Bezerra de Souza Jr., A. Resende Secchi and P. D. Christofides; *"Model Predictive Control of Batch Enantiomer Crystallization Using Ternary Diagram Information"*; Proceedings of the American Control Conference, 5927-5933; Milwaukee, Wisconsin, 2018.

- **Presented at the conference:** C. Curitiba Marcellos, H. Durand, J. Kwon, A. Barreto Jr., P. Laranjeira da Cunha Lage, M. Bezerra de Souza Jr., A. Resende Secchi and P. D. Christofides; *"Optimal Enantiomer Crystallization Operation using Ternary Diagram Information"*; Proceedings of 13th International Symposium on Process Systems Engineering - PSE 2018; Computer-Aided Chemical Engineering, 44, 499-504; San Diego, California, 2018.

The following text was published in the AIChE journal (Curitiba Marcellos et al., 2018).

5.1 Introduction

A variety of useful molecules occur as chiral compounds, or compounds for which two non-superimposable chemical structures that are mirror images of one another (referred to as left- and right-handed enantiomers) exist though their chemical composition is the same. For example, the components of many drugs are chiral molecules (Rentsch, 2002). For many chiral compounds used in pharmaceuticals, the enantiomers of that compound have different biological activities (e.g., pharmacology, toxicology, pharmacokinetics and metabolism), despite having the same chemical composition (McConathy and Owens, 2003; Nguyen et al., 2006). Examples of substances in which these differences are well-known are described in Table 5.1. Therefore, the separation of enantiomers has great appeal as a topic in research and technology development (Karamertzanis et al., 2007; Nguyen et al., 2006; Pálovics et al., 2012; Yang et al., 2014).

Two major approaches for enantiomeric separation are asymmetric synthesis and chiral resolution. Though the former technology has progressed significantly, it still has limited application or may not meet certain purity requirements, or

Table 5.1: Enantiomers-based drugs with different biological effects.

Compound	**Active enantiomer effect**	**Counter enantiomer effect**
Ethambutol (Raymond, 2010)	Tuberculosis treatment	Causes blindness
Naproxen (Masterton and Hurley, 2006)	Treats arthritis pain	Liver damage
Methorphan (Brandenberger and Maes, 1997)	Cough suppressant	Narcotic analgesic
Methamphetamine (Newmeyer et al., 2015)	Nasal decongestant	Central nervous system stimulant
Praziquantel (Olliaro et al., 2014)	Treats schistosomiasis	Bitter taste

it may have a prohibitive cost (Lorenz and Seidel-Morgenstern, 2014; Mao et al., 2010; Subramanian, 2007). Thus, chiral resolution methods are in development to achieve cost-effective, reliable and flexible enantioselective separation processes (for a detailed review of both approaches see Lorenz and Seidel-Morgenstern (2014)). A technique for obtaining a pure enantiomer that falls within the chiral resolution category is crystallization, which is an important technological process for forming particles in the pharmaceutical industry and has a fundamental role in drug properties such as stability, processing, and toxicity, which can be affected by crystal properties such as the structure, particle size distribution, and purity (Myerson, 2002; Shekunov and York, 2000).

Enantiomers are commonly classified into three types based on the binary melting diagram for a solution of the enantiomers: (i) racemic compounds (in the solid phase, crystals are formed containing both enantiomers in the same unit cell); (ii) racemic conglomerates (in the solid phase, crystals of each pure enantiomer form and are mechanically mixed) and (iii) pseudoracemates (in the solid phase, crystals are formed containing both enantiomers but with a somewhat random order). Racemates, or racemic mixtures, contain equal amounts of left- and right-handed enantiomers. Further information and details on the types of enantiomers based on phase diagrams is provided by Busch and Busch (2006); Jacques et al. (1981).

It is estimated that about 90% of all enantiomeric systems belong to the racemic compound group (Busch and Busch, 2006). As a result, research on methods for enantioseparation for this group is of great interest. Several crystallization-based enantioseparation methods exist, including conversion of the enantiomers to diastereomers and crystallizing the diastereomers, and crystallization in the presence of an optically active solvent. However, such techniques require additional materials (e.g., resolving agents or optically active solvents) with specific features. The advantage of direct crystallization (without agents that promote optical changes) is the fact that it is a simple and economical technique performed with standard equipment (Lorenz and Seidel-Morgenstern, 2014).

For a racemic compound forming system at racemate liquid composition (equal mass fractions of both enantiomers), the solid phase formed upon cooling will be the racemic compound. To form the desired pure enantiomer solid, the liquid must be enantiomerically enriched in the desired enantiomer before cooling. Enrichment

can be obtained by separation operations such as simulated moving bed (SMB) chromatography, which in recent years has gained importance for the separation of enantiomers due to factors such as better characterization of design. The coupling of chromatography with direct crystallization can allow a pure enantiomer to be obtained in solid form by the crystallization process, while allowing the chromatography process to operate with high productivity without requiring high purities of the desired enantiomer in the effluent (Kaspereit, 2006; Lorenz and Seidel-Morgenstern, 2014). One of the pioneers of coupling a chromatographic method with crystallization was Lim et al. (1995) to obtain a single enantiomer of praziquantel.

Several studies have been performed in the analysis of the coupled simulated moving bed (SMB) chromatography-crystallization process for enantioseparation (e.g. Amanullah and Mazzotti (2006); Lorenz et al. (2001); Mao (2012); Ströhlein et al. (2003); Swernath (2013)). However, study of optimal control for a batch direct enantioselective crystallization process is scarce. Thus, this work focuses on analyzing the batch crystallization process using the ternary diagram, on modeling of the process with and without a fines dissolution loop and on the development of optimal control designs to achieve the highest pure enantiomer crystal yield possible while minimizing the ratio of the mass of crystals from nuclei to the mass of crystals from seeds. More specifically, the ternary diagram, a common chemical engineering tool for presenting solution thermodynamics information (e.g., Diab and Gerogiorgis (2017)), provides the information required to determine the batch operating conditions, controller constraints, and controller model (e.g., the saturation composition predictions required for nucleation and growth rate modeling throughout the batch) to determine optimal control actions with a model predictive control strategy when the solution thermodynamic data meets certain assumptions. The operation and control strategy is demonstrated throughout the work using the mandelic acid (MA) in water system since it is widely used in the literature as a model system and the kinetic and solid-liquid equilibrium data for this process is available in the literature.

5.2 Batch Crystallization Operation and Control Design for Racemic Compound Forming Systems Using the Ternary Diagram

This section presents a systematic method for controlling a batch crystallization process for a racemic compound forming system with model predictive control (MPC) to obtain crystals of a single desired enantiomer when the solution being

crystallized is assumed to be enriched in the desired enantiomer through a separation operation (e.g., SMB chromatography) prior to the batch crystallization. The process model utilized within the MPC and the operating strategy developed to be enforced by the MPC are based on solution thermodynamics information, visually displayed in a ternary diagram, in particular the saturation composition as a function of temperature and limitations on the crystallization process (yield and operating temperatures) based on thermodynamic limitations of crystallization of a single pure enantiomer. The next two sections build to the presentation of the systematic modeling, operation, and control strategy in the third section by introducing the framework necessary for assessing the saturation composition as a function of temperature and the theoretical crystallization/yield limitations that will be exploited within the control design.

5.2.1 Saturation Composition Equations Based on a Ternary Diagram

As noted in the "Introduction" section, it is desirable to obtain many useful chiral products as a single pure enantiomer, and therefore the batch crystallization operation and control strategy developed in this work will seek to produce crystals of a single desired enantiomer referred to as the R enantiomer or R in this manuscript (the counter will be referred to as the S enantiomer or S) from a mixture of both enantiomers and a solvent (which can also be a mixture). Solution thermodynamics indicates that this operating objective can only be achieved within a specific range of operating conditions (liquid-phase compositions and temperatures). Specifically, at a given temperature, depending on the composition of the mixture, a racemic compound forming system in a solvent may form one of six different phase combinations: a liquid solution, a liquid solution in equilibrium with pure enantiomer R, a liquid solution in equilibrium with pure enantiomer S, a liquid solution in equilibrium with a solid racemic compound, a liquid solution in equilibrium with the solid racemic compound and pure R, or a liquid solution in equilibrium with the solid racemic compound and pure S (Kaspereit, 2006). A ternary diagram (in right or equilateral triangle form (Jacques et al., 1981); details on converting between these forms can be found in Appendix B) provides a visual representation of the operating conditions which correspond to each of these six phases at a given temperature.

An example ternary diagram (in right triangle form) for a racemic compound forming system (in this case, MA in water) is presented in Figure 5.1. The x and y axes are labeled with the mass fractions w_R and w_S of the R and S enantiomers in the liquid phase solution. The bold line with a slope of -1 extending from $w_S = 1.0$

to $w_R = 1.0$ represents a line along which the mass fraction $w_W = 1 - w_S - w_R$ of solvent (water) in the liquid mixture is zero (a mixture of enantiomers only). The dashed line with a slope of 1 that passes through the origin corresponds to the racemic composition. Though this diagram could be partitioned into six regions reflecting the six possible phases of the racemic compound forming system, only the two-phase region in which the liquid solution is in equilibrium with solid R (the region of interest for the batch crystallization process) is delineated (for the full description of the ternary diagram for a racemic compound forming system, the reader is referred to Jacques et al. (1981); Lorenz and Seidel-Morgenstern (2002)). As the temperature changes, the boundaries of each of the six phase regions change within the ternary diagram. This is exemplified for the two-phase region of interest at three different temperatures in Figure 5.1. At temperature T_0, the two-phase region is represented by the region within triangle **BER**, at T_1 it is the region within triangle $\mathbf{B_1E_1R}$, and at T_2 it is the region within triangle $\mathbf{B_2E_2R}$. In Figure 5.1, **E**, $\mathbf{E_1}$, and $\mathbf{E_2}$ are the eutectic compositions at temperatures T_0, T_1, and T_2 respectively, with $T_2 < T_1 < T_0$ (the eutectic composition is the composition corresponding to coexistence of the racemic compound with pure R enantiomer and saturated liquid). **B**, $\mathbf{B_1}$, and $\mathbf{B_2}$ are the binary saturation compositions at temperatures T_0, T_1, and T_2 (the binary saturation composition refers to a mixture without the counter enantiomer, i.e., only R and solvent). The lines $\overline{\mathbf{EB}}$, $\overline{\mathbf{E_1B_1}}$, and $\overline{\mathbf{E_2B_2}}$ represent the solubility lines for the pure enantiomer R at temperatures T_0, T_1, and T_2, respectively.

When the composition of a liquid mixture falls within the two-phase region (for example, point **P** when the temperature is T_1 is within the two-phase region represented by the triangle $\mathbf{B_1E_1R}$), this liquid mixture is not at thermodynamic equilibrium and will separate into two phases (a saturated liquid in equilibrium with pure solid R) if allowed to come to thermodynamic equilibrium. For example, at T_1, a liquid mixture with initial composition **P** will separate into two phases with compositions on the line $\overline{\mathbf{RP}}$. The saturated liquid will have a composition corresponding to the intersection of line $\overline{\mathbf{RP}}$ with the solubility line at the given operating temperature ($\overline{\mathbf{E_1B_1}}$); this means that the saturated liquid will have the composition described by **Q**. When the temperature of the solution drops, the two-phase region changes, and a composition that used to be at thermodynamic equilibrium will fall within the two-phase region (e.g., a solution with composition **P** is at thermodynamic equilibrium at T_0 but is within the two-phase region if the temperature drops to T_1). Therefore, though the solution with composition **P** at T_0 is saturated and thus there is no driving force for crystallization, it is supersaturated at T_1 and can crystallize until it reaches the new solubility line $\overline{\mathbf{E_1B_1}}$. Upon cooling of a liquid mixture during the crystallization process, the saturation composition

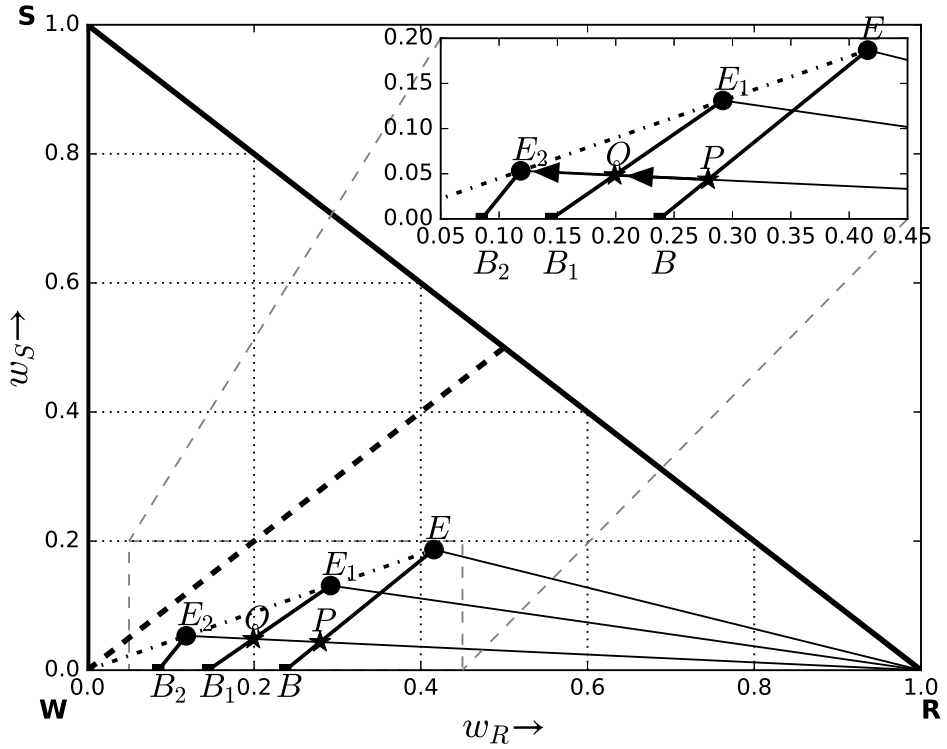

Figure 5.1: Ternary diagram in right triangle form for an example racemic compound forming system (mandelic acid in water). Only the two-phase region in which solid R is in equilibrium with a saturated solution is presented for three different temperatures. Points **R**, **S**, and **W** signify the compositions on the ternary diagram corresponding to pure R, S, and W, respectively. A zoomed-in version of several compositions on the diagram is presented in the upper right corner for better visualization. The dashed-dotted line represents a line of constant eutectic purity. The dashed line with a slope of 1 represents the racemic composition.

will move along the line $\overline{\mathbf{RP}}$.

We seek to utilize the ternary diagram to obtain an expression for the saturation composition as a function of temperature. The first step in this derivation for the systems that is considered in this work is to determine equations for line $\overline{\mathbf{RP}}$ and for the solubility curve at a given temperature; the second step is to determine the composition at which they intersect, which corresponds to the saturation composition at that temperature. The composition of R along line $\overline{\mathbf{RP}}$ (denoted by $w_R^{\overline{\mathbf{RP}}}$) can be represented in terms of the mass fractions of R and S corresponding to the initial composition at point **P** ($w_R^{\mathbf{P}}$ and $w_S^{\mathbf{P}}$, respectively) and the mass fraction of S along the line $\overline{\mathbf{RP}}$ (denoted by $w_S^{\overline{\mathbf{RP}}}$) as follows (the derivation of this relationship utilizing mass balances is provided in Appendix C):

$$w_R^{\overline{\mathbf{RP}}} = \frac{w_R^{\mathbf{P}} - 1}{w_S^{\mathbf{P}}} w_S^{\overline{\mathbf{RP}}} + 1 \tag{5.1}$$

When no experimental solubility data is available, approximations of the

solubility information may be obtained using the Schroeder-Van Laar equation (Jacques et al., 1981; Kaspereit, 2006; Worlitschek, 2003). Experimental solubility data can be used to indicate the shape of the solubility curves. For MA in water, experimental solubility data indicates that the solubility curve can be approximated by a straight line that extends from the binary saturation composition to the eutectic composition, which contributes to the triangular-shaped two-phase regions in Figure 5.1 (Kaspereit, 2006). At a given temperature, when the solubility curve can be represented by a line on the right triangle ternary diagram connecting the eutectic and binary saturation compositions at the given temperature, compositions $(w_R^{E_c}, w_S^{E_c})$ representing the mass fractions of R and S at the eutectic composition and $(w_R^{B_s}, w_S^{B_s})$ representing the mass fractions of R and S at the binary saturation composition for a given temperature T can be used to form the point-slope form of the equation for the mass fraction of R along the line connecting the binary saturation composition and eutectic composition at the given temperature. For example, the composition along the solubility line $\overline{\mathbf{E_1B_1}}$ at T_1 for MA in water is given by:

$$w_R^{\overline{\mathbf{E_1B_1}}} = \frac{w_R^{\mathbf{E_1}} - w_R^{\mathbf{B_1}}}{w_S^{\mathbf{E_1}} - w_S^{\mathbf{B_1}}} w_S^{\overline{\mathbf{E_1B_1}}} + \left[w_R^{\mathbf{B_1}} - \frac{w_R^{\mathbf{B_1}} - w_R^{\mathbf{E_1}}}{w_S^{\mathbf{B_1}} - w_S^{\mathbf{E_1}}} w_S^{\mathbf{B_1}} \right] \tag{5.2}$$

For the systems that it is considered in this work, when formulas for the solubility curve and the line including **R** and the initial composition **P** are determined at a given temperature (e.g., Eqs. 5.1-5.2 for T_1 in Figure 5.1), their intersection can be used to determine the composition (w_R^{sat}, w_S^{sat}, w_W^{sat}) of the liquid in equilibrium with pure R given the initial liquid composition at this temperature (the equations can be further simplified by setting $w_S^{\mathbf{B_1}} = 0$ by definition of the binary saturation composition). Furthermore, if relations have been obtained from experimental data for the R and S enantiomer binary saturation ($w_R^{B_s}$ and $w_S^{B_s}$) and eutectic compositions ($w_R^{E_c}$ and $w_S^{E_c}$) as functions of temperature (T) only, then the saturation compositions at any temperature T may be determined by finding $w_R^{B_s}(T)$, $w_R^{E_c}(T)$, $w_S^{B_s}(T) = 0$, and $w_S^{E_c}(T)$ and then setting $w_R^{sat} = w_R^{\overline{\mathbf{RP}}} = w_R^{\overline{\mathbf{E_c(T)B_s(T)}}}$ and $w_S^{sat} = w_S^{\overline{\mathbf{RP}}} = w_S^{\overline{\mathbf{E_c(T)B_s(T)}}}$, where $\mathbf{E_c(T)}$ and $\mathbf{B_s(T)}$ signify the points on the right triangle ternary diagram corresponding to compositions $(w_R^{E_c}(T), w_S^{E_c}(T))$ and $(w_R^{B_s}(T), w_S^{B_s}(T))$, respectively, to give the following:

$$w_R^{sat} = \frac{\dfrac{w_S^{\mathbf{P}}}{w_R^{\mathbf{P}} - 1} + \dfrac{w_R^{B_s} w_S^{E_c}}{w_R^{B_s} - w_R^{E_c}}}{\dfrac{w_S^{\mathbf{P}}}{w_R^{\mathbf{P}} - 1} + \dfrac{w_S^{E_c}}{w_R^{B_s} - w_R^{E_c}}} \tag{5.3}$$

$$w_S^{sat} = \frac{w_S^{E_c} w_S^{\mathbf{P}} (1 - w_R^{B_s})}{w_S^{E_c} - w_R^{B_s} w_S^{\mathbf{P}} + w_R^{E_c} w_S^{\mathbf{P}} - w_R^{\mathbf{P}} w_S^{E_c}} \tag{5.4}$$

where w_R^{sat} and w_S^{sat} in Eqs. 5.3-5.4 are now functions only of the initial composition and of temperature, and the explicit temperature dependence of $w_R^{B_s}$, $w_R^{E_c}$, and $w_S^{E_c}$ in the right-hand side of Eqs. 5.3-5.4 was not denoted for simplicity of notation. These equations can be further simplified in the special case of MA because for MA in water, the eutectic composition varies with temperature in such a way that the purity at the eutectic composition (P^e) can be modeled as a constant (independent of the temperature), where the purity is defined as

$$P = \frac{w_R}{w_R + w_S} \tag{5.5}$$

Therefore, given a function $w_R^{E_c}(T)$ from data, it is not necessary to also determine the function $w_S^{E_c}(T)$ from data because one can instead solve Eq. 5.5 for w_S at the eutectic composition to give $w_S^{E_c}(T) = \frac{1-P^e}{P^e} w_R^{E_c}(T)$ for use in Eqs. 5.3-5.4.

To demonstrate the use of Eqs. 5.3-5.4 for the MA case, correlations developed by Kaspereit (2006) are presented to correlate the R enantiomer binary saturation (w_R^B) and eutectic composition (w_R^E) with the temperature (T) in the range of $0°C$ to $40°C$ based on experimental solubility data for the MA system in water solvent from Lorenz et al. (2003). Polynomial equations were considered and the coefficients were determined by minimization of the sum of the absolute values of the relative errors. The obtained relations are as follows for T in $°C$:

$$w_R^{E_c}(T) = \sum_{i=0}^{4} c_{E,i}^{sat} T^i \tag{5.6}$$

$$w_R^{B_s}(T) = \sum_{i=0}^{5} c_{B,i}^{sat} T^i \tag{5.7}$$

with the estimated coefficients $c_E^{sat} = [c_{E,0}^{sat}\ c_{E,1}^{sat}\ c_{E,2}^{sat}\ c_{E,3}^{sat}\ c_{E,4}^{sat}]^T = [5.6939 \cdot 10^{-2}, 2.6283 \cdot 10^{-3}, -2.4289 \cdot 10^{-4}, 1.6516 \cdot 10^{-5}, -1.6197 \cdot 10^{-7}]^T$ and $c_B^{sat} = [c_{B,0}^{sat}\ c_{B,1}^{sat}\ c_{B,2}^{sat}\ c_{B,3}^{sat}\ c_{B,4}^{sat}\ c_{B,5}^{sat}]^T = [4.4892 \cdot 10^{-2}, 2.2451 \cdot 10^{-3}, -1.3164 \cdot 10^{-4}, 1.3519 \cdot 10^{-5}, -5.3634 \cdot 10^{-7}, 8.0205 \cdot 10^{-9}]^T$. Thus, at any T, the coupling of Eqs. 5.6-5.7 with Eqs. 5.3-5.4 allows the saturation composition to be calculated for any temperature (in the $0°C - 40°C$ range for consistency with the experimental data) and initial composition $\mathbf{P}$.

5.2.2 Crystallization Limitations for Batch Operation

As a solution of enantiomers of a racemic compound in a solvent with the properties that were described in this work is cooled, the intersection of line $\overline{\mathbf{RP}}$ with the solubility curve at the solution temperature can eventually reach the eutectic composition. Therefore, it is possible to recover more pure crystals of R from a given initial composition if the temperature is dropped until the saturation composition

is reduced to the eutectic composition on the line $\overline{\mathbf{RP}}$, which is the limit for pure R crystallization (for initial composition **P** in Figure 5.1, for example, this limit occurs at $\mathbf{E_2}$).

For the MA system in water, the eutectic purity is $P^e = 0.69$ (Lorenz and Seidel-Morgenstern, 2002), and the line with purity P^e through the eutectic compositions at all temperatures is represented by line $\overline{\mathbf{WE}}$ in the ternary diagram of Figure 5.1 due to the form of Eq. 5.5, which has no dependence on the solvent mass fraction. A line of constant purity P can be represented in Figure 5.1 as a line extending from the origin to the point with $w_R = P$ on the bold line of slope -1 connecting $w_S = 1$ and $w_R = 1$ in Figure 5.1 (because this bold line represents a solution of only w_R and w_S, so the denominator of Eq. 5.5 is 1 along this line, and the purity is equal to the value of w_R at each point along this line). At a given temperature, pure R will crystallize only if the purity of the initial solution is higher than P^e within the two-phase region (Kaspereit, 2006). When the eutectic purity of an enantiomeric solution can be modeled as constant regardless of temperature as for mandelic acid in water (Kaspereit, 2006), the eutectic composition representing the limit for pure R crystallization for a given initial composition **P** can be determined from the intersection of line $\overline{\mathbf{RP}}$ with the line of purity P^e ($\overline{\mathbf{WE}}$).

The thermodynamic limitations on crystallization impact the crystal yield Y_c, defined as the ratio of the mass of solid R that is crystallized during batch operation to the mass of R initially present in the liquid phase, that can be obtained from a solution with a given initial purity and is given by:

$$Y_c = \frac{P^i - P^f}{P^i(1 - P^f)} \tag{5.8}$$

Eq. 5.8 provides the yield at the end of a batch operation as a function of initial and final purities P^i and P^f, respectively (i.e., the initial purity from the pre-enrichment process is defined as $P^i = \frac{w_R^i}{w_R^i + w_S^i}$, where w_R^i and w_S^i represent the mass fractions of R and S in the feed to the crystallizer (which may be different than their values in the outlet of the pre-enrichment process if solvent was added or removed before the pre-enrichment process outlet entered the crystallizer; such addition or removal of solvent, however, would not affect the purity of the liquid), and P^f is defined analogously). The relation in Eq. 5.8 is obtained using mass balances in a manner analogous to that presented for a continuous crystallization process in Kaspereit (2006) and is derived in Appendix D.

Furthermore, the mass fraction of R at the end of the batch (w_R^f) depends only on the initial mass fraction of R and the initial and final purities as follows:

$$w_R^f = \frac{(P^f P^i - P^f) w_R^i}{(P^i - P^f) w_R^i + P^f P^i - P^i} \tag{5.9}$$

5.2.3 Batch Crystallization Operation and Controller Design Using Ternary Diagram Data

In this section, the results of the last two sections are combined to develop a systematic procedure for modeling, operation, and control of a batch crystallization process for a racemic compound forming system that has been pre-enriched in the desired enantiomer. The first step in the operating procedure is the determination of the initial operating temperature and composition. The choice of these conditions relies on the initial purity from the pre-enrichment process and the desired working temperature range.

For a given P^i, Eq. 5.5 shows that the ratio of w_R to w_S is fixed, but that the actual values of w_R and w_S can vary because the purity does not specify the solvent mass fraction. Replacing $w_R + w_S$ with $1 - w_W$ in Eq. 5.5, the mass fraction of the desired enantiomer is a function of the solvent mass fraction for a given purity P as follows: $w_R = P(1 - w_W)$. Thus, when the initial purity is fixed by the pre-enrichment process, the initial composition can be readily adjusted by solvent evaporation or diluting with additional solvent before starting the batch; however, the exact value to which to adjust the initial composition depends on the desired operating temperature range.

The lower bound on the desired operating temperature range is fixed by solution thermodynamics. In particular, Eq. 5.8 implies that for a given P^i, the greatest yield of crystals of pure R will be obtained when P^f is as low as it can be without crystallization of S, which occurs when $P^f = P^e$ due to thermodynamic restrictions for the systems considered in this work. The temperature at which the eutectic purity P^e is reached is fixed thermodynamically by the initial mixture composition. This temperature (referred to as T_{min} in the following) can be obtained by solving:

$$w_R^f - w_R^{sat}(T) = 0 \tag{5.10}$$

with w_R^f given by Eq. 5.9 (which gives w_R^f as a function only of the final purity and initial liquid composition) and $w_R^{sat}(T)$ given by a relationship such as that developed in Eq. 5.3 for MA in water with relations such as those in Eqs. 5.6-5.7 that describe how the eutectic and binary saturation compositions change with temperature (with $w_S^{\mathbf{P}} = w_S^i$ and $w_R^{\mathbf{P}} = w_R^i$). Eq. 5.10 can be solved through an iterative method when no analytic solution exists. From the dependence of w_R^f and $w_R^{sat}(T)$ in Eq. 5.10

on the initial mixture composition, it is seen that the initial mixture composition directly affects the temperature T_{min} that the batch crystallizer must achieve at the end of process operation to achieve the desired yield at P^e.

When the initial mixture composition falls within the two-phase region at a given temperature, some of the mixture will crystallize unless the initial mixture composition is on the solubility line at the given temperature. Thus, it can be beneficial to initiate the batch at the saturation condition since that may avoid undesired nucleation and help the seeding control. It will also have no negative effect on the yield when P^f is fixed because according to Eq. 5.8, any initial composition on the line of constant purity P^i will have the same crystal yield. If it is assumed that the batch should initiate at a saturated condition, the initial mixture composition thermodynamically sets the temperature required at the beginning of batch operation according to the following equation:

$$w_R^i - w_R^{sat}(T) = 0 \tag{5.11}$$

where $w_R^{sat}(T)$ is obtained in a similar manner as in Eq. 5.10. Thus, by fixing the final purity to a value that maximizes the yield and by initiating the batch at the saturation composition based on equilibrium considerations, the initial composition defines both the initial temperature of operation as well as the final temperature of operation. Based on the desired working temperature range, the desired initial composition can be determined for a given P^i. Considerations in selecting a working temperature range may include that all temperatures in the range can be reached in a cost-effective manner with the proposed equipment and cooling capabilities. The operating temperature range may also be chosen by considering its effect on enantiomeric system characteristics (e.g., choosing an operating temperature range that avoids undesired polymorphism or solvate configurations or is one in which the crystal kinetics behavior or crystal stability have been previously characterized, allowing effective process modeling).

To exemplify the choice of the initial mixture composition based on the operating temperature range, the MA case is re-examined. Figure 5.2 shows the eutectic purity line for $P^e = 0.69$ and the line for an initial purity of $P^i = 0.80$. Figure 5.2 was constructed using Eqs. 5.10 and 5.11 with Eqs. 5.6-5.7 for a variety of initial compositions with purity $P^i = 0.80$. In the bottom plot in this figure, a number of circles representing various initial compositions for which $P^i = 0.80$ are plotted, as well as a number of squares representing various final compositions for which $P^e = 0.69$. The arrow signifies that a given circle corresponds to a given square in the sense that if an initial mixture with the composition signified by a circle is cooled to the eutectic point, it will reach the composition signified by the corresponding square at

the eutectic point (the leftmost circle corresponds to the leftmost square, the second circle from the left corresponds to the second square from the left, and so forth). The top plot of the figure shows temperatures corresponding to each circle and square in the bottom plot, assuming that each circle in the bottom plot represents an initial mixture composition on the saturation curve (the leftmost circle in the top figure corresponds to the leftmost circle in the bottom plot, the second circle from the left in the top plot corresponds to the second circle from the left in the bottom plot, and so forth). The temperatures are plotted against $w_{R,start}$, the initial composition of the liquid mixture (assumed to be at the saturation condition). For each value of $w_{R,start}$, the temperature corresponding to saturation for the given $w_{R,start}$ is represented as a circle, and the temperature corresponding to the eutectic composition given $w_{R,start}$ is represented as a square. As in the bottom plot, the arrow indicates that a circle on a line of constant $w_{R,start}$ corresponds to a square on this same line. The top plot, then, shows the change in temperature required to go from an initial saturated solution with purity P^i to the eutectic composition representing the limit of the region of pure R crystallization associated with the initial mixture composition. The arrow shown in the top plot of Figure 5.2 specifically shows the temperature decrease required to crystallize a saturated solution with an initial temperature $T_{start} = 40°C$ to the eutectic point. When $T_{start} = 40°C$, Eq. 5.11 can be solved to find the starting composition $w_{R,start}$ by solving $w_{R,start} - w_R^{sat}(T_{start}) = 0$ (and a similar equation for w_S based on Eq. 5.4), where $w_R^{sat}(T_{start})$ is from Eq. 5.3, giving $w_{R,start} = 0.31$. A final composition at $w_R^f = 0.20$ is calculated using Eq. 5.9 with $P^f = P^e$, which occurs at a temperature of $28.05°C$ from Eq. 5.10. Figure 5.2 gives a clear indication of the operating temperature range required for a variety of initial mixture compositions with the same initial purity and allows the appropriate operating temperature range to be chosen based on the plot, which then fixes the appropriate initial composition.

MPC is proposed for operating the batch crystallization process within the desired operating temperature range because it is an optimization-based control methodology that incorporates a process model and constraints when determining control actions to apply to the process, and crystallizing a single enantiomer from a solution of two enantiomers is a thermodynamically constrained procedure (e.g., there are limitations on the range of temperatures and compositions for which crystals of a pure enantiomer will form). Composition or temperature-dependent properties in the process model used in MPC, such as the saturation composition, can be based on ternary diagram information (e.g., Eq. 5.3) to appropriately reflect the process thermodynamics. In addition, MPC is a flexible control design in the sense that it computes control actions that allow constraints to be met while an objective function (e.g., a function of desired crystal size properties) is optimized,

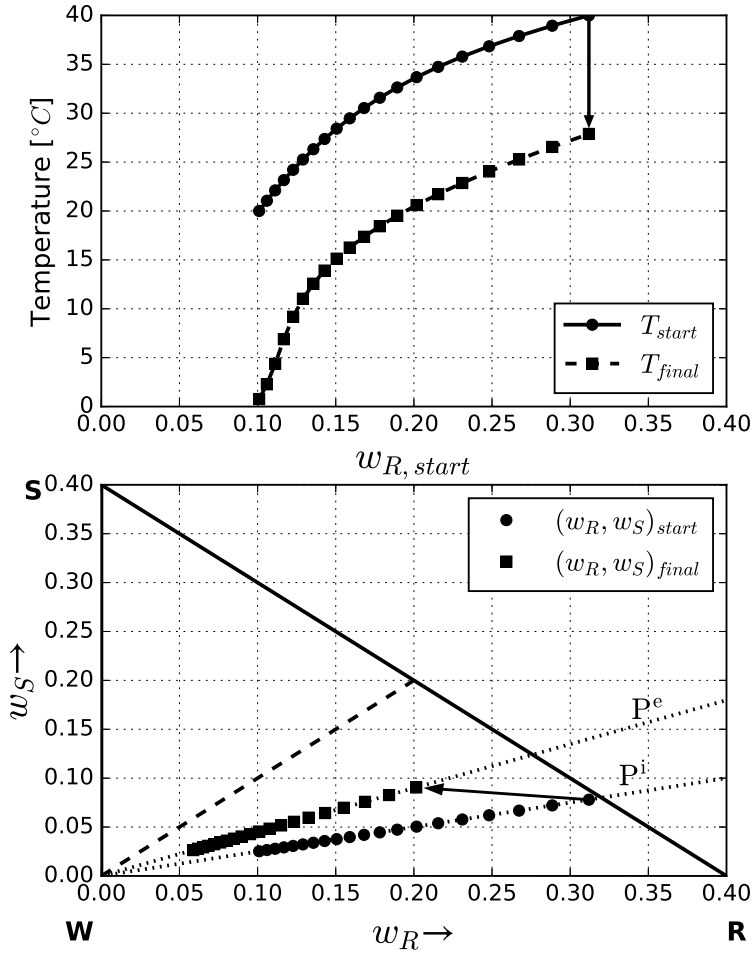

Figure 5.2: MA batch crystallization operation for different starting compositions $w_{R,start}$. The bottom figure shows the starting composition (•) associated with the final composition (■) in the ternary diagram and an arrow shows that each starting temperature and initial purity ($P^i = 0.80$) corresponds to a final temperature and eutectic purity ($P^e = 0.69$; for better visualization, only one arrow is presented). The top figure depicts the starting temperature (•) and the final temperature (■) for each starting composition considered in the bottom figure. It is noted that in the bottom figure, the bold line with a slope of -1 represents a line of constant solvent composition $w_W = 0.6$ (since only a subset of the ternary diagram data from Figure 5.1 is shown in this figure, the bold line with a slope of -1 does not have the same meaning in this figure as in Figure 5.1). The dashed line with a slope of 1 represents the racemic composition.

resulting in a cooling trajectory for the crystallizer that, perhaps, results in higher profits or greater effectiveness of the crystals in their intended application than would be achieved by performing the crystallization with a pre-determined temperature profile in the crystallizer like a linear cooling strategy. Furthermore, constraints can also be added to aid in improving the efficiency of the crystallization process, such as adding constraints on the desired yield (e.g., for the mandelic acid in water process, a constraint could be added that requires the yield at the end of the batch to reach

its theoretical maximum value of Eq. 5.8). Furthermore, as a feedback control law, it provides a degree of robustness to disturbances and plant/model mismatch.

Because MPC calculates optimal control actions, and requires that a process model be available, it allows for closed-loop simulations to be performed to determine the most preferable final batch time for maximizing a desired objective function. MPC allows flexibility in both the constraints as well as the objective function, with the result that one or both may depend on the final batch time (e.g., requiring a desired yield to be obtained at the end of the batch). In this case, it is necessary to perform closed-loop simulations to understand the effect of the final batch time on optimizing the objective function. This is an advantage of MPC for control of enantiomeric crystallization compared to a pre-set cooling strategy such as linear cooling because pre-set strategies do not allow for optimization, feedback, or accounting for constraints, so it would be more difficult to obtain the best operating parameters for operation under such controllers.

Based on the discussion of this section, the operation and control procedure proposed in this work for batch crystallization of a racemic compound forming system is now summarized by the steps (also by Figure 5.3):

Step 1. Obtain thermodynamic phase information for the racemic compound forming system (including a ternary phase diagram) and receive information on the initial purity from the pre-enrichment process.

Step 2. Develop equations for the saturation composition as a function of only the initial composition and $w_R^{E_c}(T)$ and $w_R^{B_s}(T)$ (e.g., Eqs. 5.3-5.4), and $w_S^{E_c}(T)$ if required.

Step 3. Setting both the initial and final compositions to be at saturated conditions, develop a plot like that in Figure 5.2 showing the various operating temperature ranges possible by varying the initial solvent composition for the given initial purity.

Step 4. Determine the desired operating temperature range and initial composition based on the plot developed in Step 3.

Step 5. Develop a batch crystallization process model to be used in an MPC formulation. The process model may depend on thermodynamic relations derived based on the ternary diagram analysis.

Step 6. Develop the constraints to be used in the MPC based on considerations for racemic compound forming systems as derived from the ternary diagram such as the desired yield (e.g., maximum yield thermodynamically possible with $P^f = P^e$ from Eq. 5.8 at the end of the batch) and crystallizer temperature limits.

Step 7. Run closed-loop simulations of the crystallization process under MPC with different batch times to determine the minimum batch time necessary to achieve the desired crystallization results.

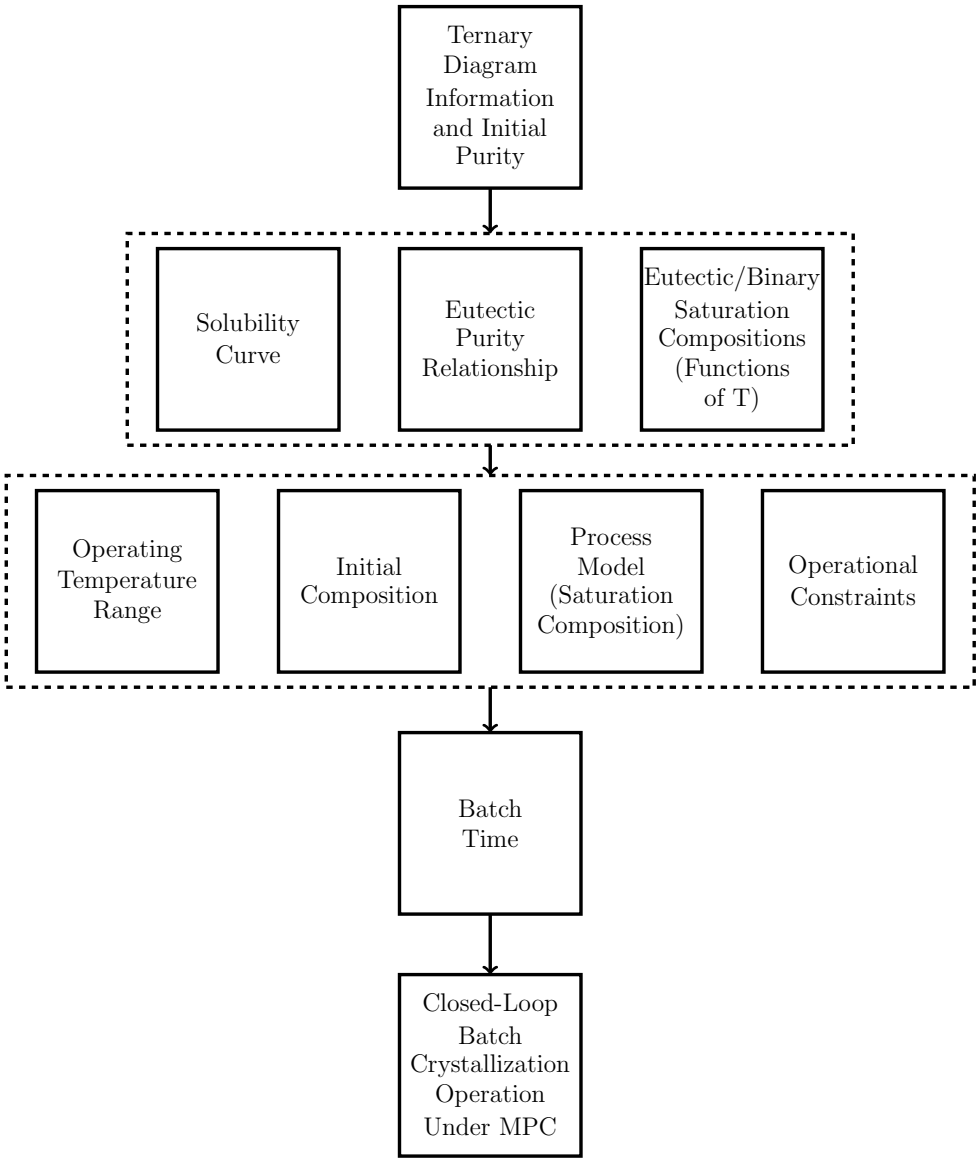

Figure 5.3: Schematic depicting the proposed batch modeling, operation, and control procedure. Solution thermodynamic data including a ternary diagram and the initial purity of the solution are provided, which are then used to develop important relationships for the procedure, including equations related to the solubility curve as a function of temperature, the relationship describing the eutectic purity (e.g., $P^e = 0.69$ for mandelic acid in water), and information on the eutectic and binary saturation compositions as functions of temperature. This information is subsequently used to determine the operating conditions of the crystallizer, including the operating temperature range and initial condition, it is used in the development of the process model (e.g., by developing a relationship for the saturation composition as a function of temperature), and the development of other operational constraints such as yield constraints. This is incorporated within a model predictive control design. The length of the batch run is selected and the crystallization process is operated under the MPC with the constraints based on solution thermodynamics.

Step 8. Operate the process under the proposed control strategy and adjust operating parameters or controller constraints and the model as necessary to achieve the desired yield and enantioseparation.

Several assumptions were considered to hold during the development of this operating/control procedure as follows:

Assumption 1 *The mixture under consideration is a racemic compound forming system that was pre-enriched in the desired enantiomer and for which phase equilibrium data is available at various temperatures and has the properties considered in this work (e.g., the intersection of a line through the initial composition and pure R and the solubility curve at a given temperature determines the saturation composition in the ternary diagram, and the limit of pure R crystallization occurs when this initial composition line intersects the eutectic composition at a given temperature).*

Assumption 2 *Relations for* $w_R^{E_c}(T)$ *and* $w_R^{B_s}(T)$ *(and* $w_S^{E_c}(T)$ *as applicable) are available.*

Assumption 3 *The initial purity* P^i *is fixed.*

Assumption 4 *Thermodynamic equilibrium is reached at the beginning and end of the batch.*

A key component of the proposed method is MPC for the control of direct crystallization of a racemic compound forming system, and the use of MPC in general does not depend on the assumptions but only on the availability of a process model. The required thermodynamic data for Assumptions 1 and 2 can be experimentally obtained if unavailable for a specific system. The final batch time can be adjusted to allow Assumption 4 to be met at the end of the batch (closed-loop simulations under MPC can be performed to determine a final batch time that will allow the assumption to hold). In the event that the pre-enrichment process is also being designed such that P^i is not yet fixed, the yield and operating temperature range at a variety of purities can be compared with the cost of changing the purity of the material exiting the pre-enrichment process to optimize the operating conditions of the entire process instead of only the crystallization unit. Small variations in P^i due to process disturbances between batch runs may be handled by the MPC because it incorporates feedback to provide some robustness to disturbances and plant/model mismatch, and safety factors can be used in the constraint design to prevent the cooling procedure from causing the temperature to drop to a level that would result in crystallization of the S enantiomer even in the presence of expected disturbances that cause P^i to vary.

Remark 1 *Figs. 5.1-5.2 were constructed using the mathematical developments of this section (Eqs. 5.1-5.11), rather than plotting experimental data points.*

Remark 2 *There may be uncertainties or possible errors or disturbances for a given batch process that make it desirable to operate the batch crystallization until a final purity $P^f > P^e$ (despite that the greatest theoretical yield for a given P^i occurs when $P^f = P^e$ in Eq. 5.8) to avoid crystallization of the opposite enantiomer. In such a case, the analysis surrounding Eqs. 5.10-5.11 can still be performed, but with P^f set to the desired final purity in Eqs. 5.3 and 5.9 used to solve Eq. 5.10 for the temperature at the end of the batch. A purity $P^f > P^e$ may also be selected if cooling until $P^f = P^e$ requires the batch temperature to drop lower than can be achieved in a cost-effective and safe manner with the process equipment.*

Remark 3 *The equations examined in the above sections for thermodynamic properties such as yield have focused on the MA in water process for which the solubility curve can be approximated as a straight line and the eutectic purity is independent of temperature. Linear approximations of solubility curves could be investigated for various enantiomeric systems for which the solubility curves in the equilateral ternary diagrams presented appear to be approximately linear (e.g., Tröger's base/ethanol (Worlitschek, 2003) and bicalutamide/methanol (Kaemmerer et al., 2010)) and, as demonstrated in Ap. B, a linear solubility curve on a standard equilateral triangle ternary diagram, with pure enantiomers R and S on the base of the diagram, will result in a linear solubility curve in a right triangular representation. In the event that a nonlinear solubility curve provides a better representation of the thermodynamic data and Assumption 1 is met, Eq. 5.2 can be replaced with equations that approximate the phase boundaries through nonlinear functions of $w_R^{\mathbf{E_1}}$, $w_R^{\mathbf{B_1}}$, and $w_S^{\mathbf{E_1}}$, and the procedure of finding the point of intersection of the modified solubility curve with line $w_R^{\overline{\mathbf{RP}}}$ will give different equations for the saturation composition in Eqs. 5.3-5.4. Eqs. 5.10-5.11 would use the modified equations to extend to this case. Furthermore, when the eutectic purity is not independent of temperature and Assumption 1 is met, a potential method for extending the results of this work to that case would be to examine whether the constraints of the MPC (e.g., constraints on the yield and minimum crystallizer temperature) should reflect the value of P^f according to Eq. 5.5 that causes P^f to equal the value of P^e that is achieved at the temperature at which $w_R^{\overline{\mathbf{RP}}}$ intersects both the curve for $w_R^{sat}(T)$ and the curve for $w_R^{E_c}(T)$. A correlation for $w_S^{E_c}(T)$ would also be required in this case (in addition to the correlations in Eqs. 5.6-5.7). It should also be verified that the resulting constraints do not require any safety factor (i.e., P^f greater than the determined value of P^e) to prevent the S enantiomer from crystallizing throughout the cooling process given the manner in which the eutectic*

purity varies throughout the cooling procedure.

Remark 4 *The flexibility of MPC in the constraints and the objective function enables it to be used for control of batch enantiomer crystallization. Classical stabilizing control designs for chemical processes, such as PID control, seek to drive the process state to an operating steady-state; however, for a batch process there is no steady-state, and as a result these classical control designs cannot be applied to the batch process under consideration in this work (other stabilizing control designs, such as geometric control and Lyapunov-based control, are also not applicable in this case for the same reason). Not only is MPC a viable control method for operation of batch processes, but it also offers benefits compared to other potential approaches (e.g., a pre-specified temperature trajectory within the crystallizer) because it has the ability to optimize an objective function which can be related to desired production goals which may be motivated by, for example, process economics, while simultaneously accounting for process thermodynamic limitations through constraints, and accounting for disturbances/plant-model mismatch through feedback.*

5.3 Batch Crystallizer Model with Fines Dissolution Loop

The operation of a batch crystallizer for a racemic compound forming system using operating conditions and a controller design based on the ternary solid-liquid equilibrium data is exemplified through a chemical process example for mandelic acid in water. In this section, the batch crystallizer design considered for this example and the model of the crystallization process for this crystallizer design are discussed. The system is composed of a crystallizer with a jacket for temperature control and a fines dissolution tank, as depicted in Figure 5.4. The stream sent to the fines dissolution tank is liquid from the crystallizer that has been passed through a fines trap to filter out larger crystals of the desired enantiomer (and leave primarily fines in the stream). The fines trap in this process is not modeled as having a physical volume, and therefore, its behavior for the purposes of process modeling is like the behavior of a filter between the crystallizer volume and the stream leaving the crystallizer. The fines dissolution loop scheme was considered since it is a widely used strategy to enhance crystal growth while reducing the total number of particles in the system (Kwon et al., 2014a). Though material is exchanged between the crystallizer and the fines dissolution tank, the overall system comprised of both of these tanks is closed, so the operation is a batch operation.

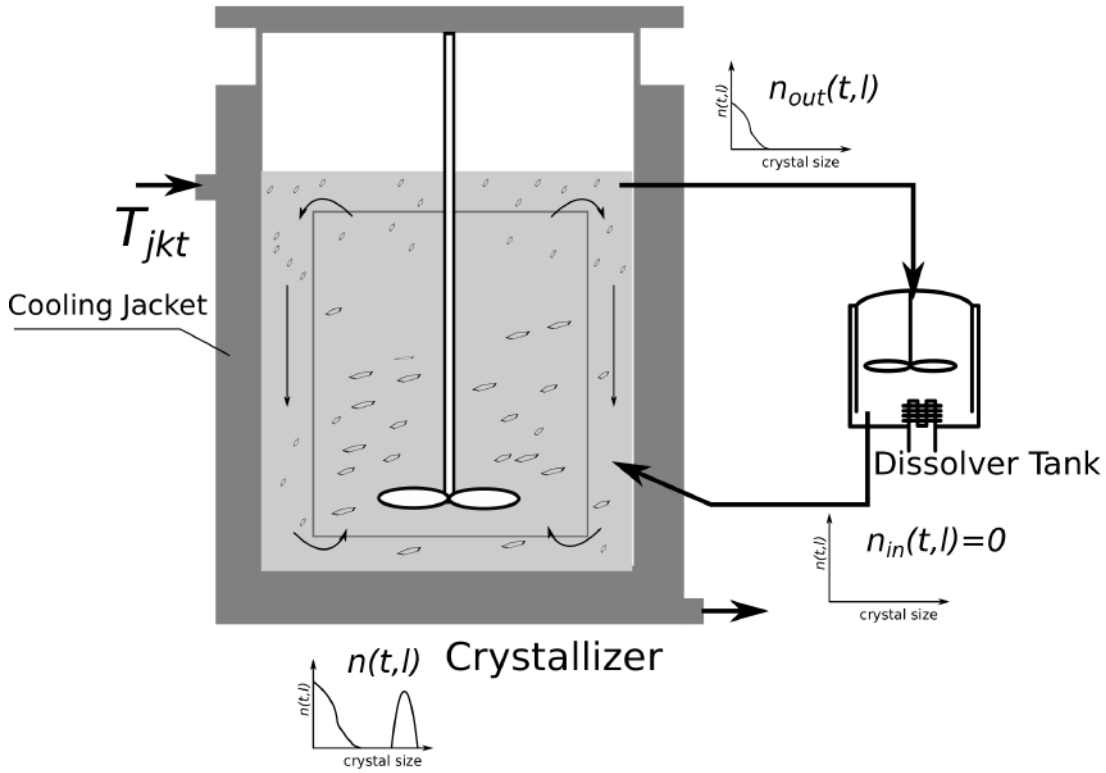

Figure 5.4: Batch crystallizer with fines dissolution loop scheme. To illustrate the typical particle size distributions for the various streams in the crystallizer, example distributions are shown for the solution in the crystallizer (showing a large number of particles at the larger crystal sizes as desired), stream entering the fines dissolution tank (showing that primarily small particles make it through the fines trap), and stream exiting the fines dissolution tank (showing that all crystals have been dissolved).

The following modeling assumptions are made in the development of mass, energy, and population balances for the crystallization process:

- The internal coordinates of the crystal particles can be represented only by the crystal characteristic size l;
- Both the crystallizer and fines dissolution tank are assumed to be well-mixed;
- Both the liquid (solvent with dissolved S and R enantiomers) and solid crystal R in the crystallizer and fines dissolution tank are assumed to have constant densities;
- The liquid in the crystallizer is assumed to have a constant heat capacity;
- Crystal breakage and aggregation is neglected;

- The crystal nucleation and growth kinetics can be expressed by empirical correlations;
- Only pure R enantiomer is crystallized (no S enantiomer or solvent takes a crystal form).

These assumptions are consistent with standard chemical engineering and crystallization modeling practices in the literature (Angelov et al., 2008; Chianese and Kramer, 2012; Chiu and Christofides, 2000; Randolph and Larson, 1988; Shi et al., 2006).

The crystal size distribution can be described by the well-established population balance equation, which for a batch process with fines removal takes the form:

$$\frac{\partial n}{\partial t} = -\frac{\partial}{\partial l}(Gn) + B_0\delta(l - l_{min}) - n\frac{d}{dt}\ln m_W + \frac{1}{m_W}\left[n_{in}\dot{m}_{W,in} - n_{out}\dot{m}_{W,out}\right] \tag{5.12}$$

where l_{min} is the minimum stable characteristic crystal size (here considered to be zero), B_0 represents the nucleation rate, G is the growth rate and $n = n(t, l)$ is the particle size distribution (PSD) dependent on characteristic size l and time t. $\delta(l - l_{min})$ is the Dirac delta function centered at l_{min}. The crystal size distribution is defined based on solvent mass m_W in the crystallizer (i.e., $n(t, l)$ represents the number of crystals at time t with size l per unit mass of solvent in the crystallizer and has units of $(kg_W \cdot m)^{-1}$, with kg_W standing for kilogram of water).

For the chemical process example under consideration, the initial PSD was based on the reference seeded distribution $n_0^{REF}(l)$ (Zhang et al., 2010) defined by Eq. 5.13. The initial PSD is given by Eq. 5.14, in which a_0 is a factor chosen based on the mass of crystals ($m_c(t)$) at initial time in the crystallizer (Eq. 5.15). Also, ρ_c is the crystal density and k_V is the crystal shape factor.

$$n_0^{REF} = \begin{cases} (3 \cdot 10^{-4} - l)(l - 2.12 \cdot 10^{-4}) & \text{if } 2.12 \cdot 10^{-4} \leq l \leq 3 \cdot 10^{-4} m \\ 0 & \text{otherwise} \end{cases} \tag{5.13}$$

$$n(t_0, l) = a_0 n_0^{REF}(l) \tag{5.14}$$

$$a_0 = \frac{m_c(t_0)}{m_w k_v \rho_c \int_0^\infty l^3 n_0^{REF}(l) dl} \tag{5.15}$$

The term $n\frac{d}{dt}\ln m_W$ in Eq. 5.12 accounts for possible variation of mass of solvent in the crystallizer during batch operation due to its possible accumulation in the fines

dissolution tank (Randolph and Larson, 1988), while the last term includes the effect of input and output streams related to the fines dissolution loop. Specifically, $\dot{m}_{W,in}$ and $\dot{m}_{W,out}$ represent the mass flow rates of solvent into and out of the crystallizer from the fines dissolution tank, and n_{in} and n_{out} are the particle size distributions in the streams entering and leaving the crystallizer from the fines dissolution tank.

In order to track the supersaturation during batch operation, the mass balance on species i (where $i = R, S, W$, corresponding to the desired enantiomer, the undesired enantiomer, and the solvent water, respectively) in the liquid phase in the crystallizer can be written as:

$$\frac{dm_i}{dt} = -\dot{m}_{cryst,i} + w_{in,i}\rho_l \dot{V}_{l,in} - w_{out,i}\rho_l \dot{V}_{l,out} \tag{5.16}$$

In this equation, $\dot{m}_{cryst,i}$ represents the rate (mass/time) at which component i is crystallized (enters the solid phase), and thus it is zero for $i = S$ and $i = W$, but for the desired enantiomer R it is given by:

$$\dot{m}_{cryst,R} = 3m_W \rho_c k_V \int_0^\infty l^2 Gn(t,l)dl \tag{5.17}$$

where ρ_l is the liquid density (the derivation of this equation is discussed in Appendix E). Moreover, in Eq. 5.16, the mass fraction of species i in the liquid phase in the inlet stream to the crystallizer ($w_{in,i}$) is equal to the mass fraction of species i in the liquid phase in the fines dissolution tank, and the mass fraction of species i in the liquid phase in the stream out of the crystallizer ($w_{out,i}$) is the same as the mass fraction of species i in the liquid phase in the crystallizer. $\dot{V}_{l,in}$ and $\dot{V}_{l,out}$ refer to the liquid volumetric flow rate of the inlet and outlet streams of the crystallizer, respectively.

The energy balance in the crystallizer was taken to be:

$$M_{tot} c_p \frac{dT}{dt} = -UA(T - T_{jkt}) \tag{5.18}$$

where M_{tot} is the total mass in the crystallizer (assumed to be constant), c_p is the specific heat capacity of the suspension in the crystallizer (assumed to be a constant), T is the temperature of the suspension in the crystallizer, U is the overall heat transfer coefficient of the crystallizer surface in contact with the jacket, A is the heat exchange area, and T_{jkt} is the jacket temperature. It is noted that the energy balance only accounts for temperature changes in the crystallizer due to the jacket; any heating/cooling effects due to the streams entering and leaving the fines dissolution tank were considered to be negligible because it was considered that

there is perfect temperature control of the stream returning to the crystallizer from the fines dissolution tank such that the energy flows out of and into the crystallizer are equal and opposite at all times and thus do not contribute to the energy balance (Kwon et al., 2014a). In addition, it was assumed that the time required for heating of the crystals was shorter than the time required for heating of the liquid such that the temperature of the crystals was assumed to be equal to that of the liquid at all times, and the enthalpy of crystallization was assumed to be negligible.

In this work, the contents of the dissolution tank were assumed to be perfectly mixed and to consist only of liquid (i.e., it is assumed that all crystals are dissolved into the mother liquor when they enter the fines dissolution tank so that $n_{in} = 0$ in Eq. 5.12). Thus, the mass balance for each component i in the fines dissolution tank is:

$$\frac{dm_{diss,i}}{dt} = \dot{m}_{diss,i} + w_{out,i}\rho_l \dot{V}_{l,out} - w_{in,i}\rho_l \dot{V}_{l,in} \tag{5.19}$$

where $m_{diss,i}$ is the mass of species i in the fines dissolution tank, and $\dot{m}_{diss,i}$ represents the rate at which crystal mass is dissolved to liquid mass. Thus, $\dot{m}_{diss,i} = 0$ for $i = S, W$ and $\dot{m}_{diss,R}$ is the rate at which fines crystal mass leaves the crystallizer. If C_{fines} is the fines concentration (in mass of fines crystals per mass of solvent) in the removal stream, the rate of dissolved crystals of R can be given by $C_{fines}\dot{m}_{W,out}$. The fines concentration can be calculated with the following equation:

$$C_{fines} = k_V \rho_c \int_0^\infty n_{out}(t,l) l^3 dl \tag{5.20}$$

The volumetric flow rate of the fines removal stream ($\dot{V}_{sp,out}$) is taken to be a constant operational parameter. To keep a constant mass in the crystallizer, the volumetric flow rate ($\dot{V}_{sp,in}$) for the returning stream is given by:

$$\dot{V}_{sp,in} = \dot{V}_{sp,out} + C_{fines}\dot{m}_{W,out}\left(\frac{1}{\rho_l} - \frac{1}{\rho_c}\right) \tag{5.21}$$

It is noted that if the removal stream is sufficiently diluted, the approximation $\dot{V}_{sp,in} = \dot{V}_{sp,out}$ is valid. With Eq. 5.20 it is possible to get the liquid volumetric flow rate appearing in the mass balances: $\dot{V}_{l,out} = \dot{V}_{sp,out} - \dot{m}_{W,out}\frac{C_{fines}}{\rho_c}$. Also, as all fines are dissolved, $\dot{V}_{l,in} = \dot{V}_{sp,in}$.

The fines dissolution tank receives a stream from the crystallizer that is enriched in fines crystals. This enrichment is modeled by setting the crystal number density of the stream leaving the crystallizer to $n_{out} = h(l)n(t,l)$, where $h(l)$ is calculated

from the following equation (Qamar et al., 2009):

$$h(l) = n_{max} \exp\left[-\left(\frac{l}{2\sigma_l}\right)^2\right] \tag{5.22}$$

with $n_{max} = 0.6$ and $\sigma_l = 0.15$.

To numerically simulate the process described by Eqs. 5.12-5.22, a numerical method capable of capturing the features of interest of the particle size distribution must be chosen. In the crystallization literature, it is common to apply the method of moments to transform the population balance equation into a system of first-order ordinary differential equations that describe the variations in the moments of the particle size distribution in time. When the flow to the fines dissolution tank is halted (i.e., $\dot{m}_{W,in} = \dot{m}_{W,out} = 0$ in Eq. 5.12), the method of moments can be readily applied to simulate the resulting population balance model, with the j-th order moment of the distribution defined by Eq. 5.23 ($j = 0, 1, \ldots$), and the derivatives of the moments described in Eq. 5.24 (Randolph and Larson, 1988):

$$\mu_j = \int_0^\infty l^j n(t,l) dl \tag{5.23}$$

$$\frac{d\mu_j}{dt} = \begin{cases} B_0 & \text{if } j = 0 \\ \int_0^\infty nGjl^{j-1}dl + l_{min}^j B_0 & \text{if } j > 0 \end{cases} \tag{5.24}$$

with $l_{min} = 0$ m in Eq. 5.24.

However, because the integration required to define the moments removes the dependence of the particle size distribution characteristics on the characteristic size l by integrating over all particle sizes, the method of moments cannot be applied to numerically simulate the population balance of Eq. 5.12 when the fines dissolution process is used. This is because the ability of the fines trap to separate larger and smaller crystals is modeled using the function $h(l)$ (Eq. 5.22) which has an explicit dependence on the particle length, and a numerical method that removes the dependence of the particle size distribution characteristics on the characteristic length of the particles would be unsuitable for representing the batch crystallization process with fines dissolution described above. Instead, the moving sectional method, to be described in the next section, is utilized to simulate the particle size distribution of the crystallization process with fines dissolution throughout the batch simulation.

5.3.1 Moving Sectional Method for Crystal Nucleation and Growth

The moving sectional method (Kumar and Ramkrishna, 1997) (with only nucleation and growth mechanisms of crystal variation) considers the PSD to be divided into M contiguous sections (bins) with lower and upper boundaries given by l_i and l_{i+1} and with the number of particles per mass of solvent in each bin i defined as in Eq. 2.63.

The method considers that l_i and l_{i+1}, as well as the pivot for each bin (x_i, which is a representative size for the $i-th$ bin) change with time according to the crystal growth rate. After discretization and derivation based on the method of characteristics, the population balance equation (Eq. 5.12) is expressed for each bin as:

$$\frac{dN_i(t)}{dt} = \begin{cases} B_0(t) - N_i \dfrac{d}{dt}\ln m_W + \mathcal{Q}_{I/O,i}(t) \text{ if } i = 1 \\ -N_i \dfrac{d}{dt}\ln m_W + \mathcal{Q}_{I/O,i}(t) \text{ if } i = 2, \ldots, M \end{cases} \tag{5.25a}$$

$$\frac{dx_i}{dt} = \begin{cases} \dfrac{1}{2}\left(\dfrac{dl_1}{dt} + \dfrac{dl_2}{dt}\right) \text{ if } i = 1, \\ G(t) \text{ if } i = 2, \ldots, M \end{cases} \tag{5.25b}$$

$$\mathcal{Q}_{I/O,i}(t) = \frac{1}{m_W}\left[N_{i,in}(t)\dot{m}_{W,in} - N_{i,out}(t)\dot{m}_{W,out}\right] \tag{5.25c}$$

where $N_{i,in}(t) \equiv 0$ (because $n_{in} \equiv 0$) and $N_{i,out}$ are the number of particles per mass of solvent in each bin i for the input and output streams. The discretization of n_{out} for the i-th bin was taken to be $N_{i,out} = \sum_{i=1}^{M} h(x_i)N_i$, where $h(x_i)$ is given by Eq. 5.27. The particle size distribution can be approximated from the states in Eq. 5.25 using the expression for the i-th bin shown by Eq. 5.28:

$$N_{i,out}(t) = \sum_{i=1}^{M} h(x_i)N_i \tag{5.26}$$

$$h(x_i) := n_{max}\exp\left[-\left(\frac{x_i}{2\sigma_l}\right)^2\right] \tag{5.27}$$

$$n(t, x_i) = \frac{N_i}{l_{i+1} - l_i} \tag{5.28}$$

In this discretization scheme, the bin boundaries l_i at the initial time can be uniformly spaced in a size range that covers the entire initial PSD. The pivots x_i at the initial time are defined at the centers of each bin (i.e., $x_i = \frac{1}{2}(l_i + l_{i+1})$). The number of particles per bin N_i is obtained by the integral defined by Eq. 2.63 using

the initial PSD (Eq. 5.14).

To model growth of the smallest crystals, their corresponding pivots (Eq. 5.25b) increase with time, with the result that the smallest crystals become characterized by larger average sizes. As particles are nucleated, they must be added to a specific bin, but as the pivots increase, it can happen that the smallest pivot becomes significantly larger than the size at which particles nucleate such that nucleation can no longer be represented properly. The growth of the bins and pivots is also problematic for the selection behavior of the fines trap because it causes the particle size distribution to lack the number of bins required at lower particle sizes that are required to achieve the desired separation behavior described by $h(l)$ (Eq. 5.22).

To overcome these difficulties, Kumar and Ramkrishna (1997) proposed that new bins are added to Eq. 5.25 at intervals separated by time length Δt_{bin} sufficiently small to track the nucleation dynamics and to simulate the fines trap with adequate resolution. Each new bin is added at the minimum crystal size (zero in this work; thus, $x_1 = l_1 = l_2 = 0$ at each bin addition). Also, it is considered that each new bin contains no crystals when it is initialized ($N_1 = 0$ at each bin addition). An efficient numerical scheme of the moving sectional method was implemented for the bin additions that utilizes a constant Δt_{bin} during the simulation for adding new bins. This strategy takes advantage of the fact that once the bins are added in constant intervals Δt_{bin} at the intermediate time steps (not including the initial and final times), at the end of the simulation the total number of bins will be $M_f = M_0 + N_t - 2$, where N_t can be obtained from the initial and final times as $N_t = \lfloor \frac{t_f - t_0}{\Delta t_{bin}} + 0.5 \rfloor + 1$, where $\lfloor \cdot \rfloor$ is an operator that returns the largest integer smaller than its argument. Thus, an augmented state sequence $\widetilde{y}$ capable of accommodating all the states at the final time can be created before starting the numerical integration, which avoids the need to create new states and renumber the older bins when a new bin is added. Hence, the total number of elements in the sequence $\widetilde{y}$ will be $v_{\widetilde{y}} = 2M_f + v_{\overline{y}}$, where $v_{\overline{y}}$ is the number of elements in the state sequence $\overline{y}$ that contains the extra states required to close the dynamic system, which in this case are the mass of each component in the crystallizer and fines dissolution tank and the crystallizer temperature. N_i and p_i must be integrated for each bin. Further details on the implementation of the moving sectional method in this work are provided in Appendix F.

In this work, the derivatives for the optimization schemes were obtained using automatic differentiation methods, which involves a substantial amount of data to calculate the derivatives (Walther and Griewank, 2012). Thus it is desired to minimize the computer memory usage for the function evaluations. At each simulation time step, the dynamic system was integrated using a low memory Runge-Kutta method. The two storage register third-order Runge-Kutta method

defined by Carpenter and Kennedy (1994) was chosen, which used Williamson (1980) derivations.

Though the moving sectional method involves the calculation of an approximation of the particle size distribution in time, instead of the moments of the distribution as would be undertaken if the method of moments were used, the moments of the particle size distribution can be obtained from the moving sectional method as follows:

$$\mu_j = \sum_{i=1}^{M} \left[N_i x_i^j \right], \; j = 0, 1, \ldots \tag{5.29}$$

5.3.2 Parameter Estimation

Obtaining crystal nucleation and growth rates is considered to be a challenging task because of the difficulty of measuring particle sizes and their distributions, especially for small crystal sizes. Even when crystal data is available that can be used for estimating the parameters of nucleation and growth rate models, the experimental conditions under which that data was obtained may be different from the conditions for which a nucleation and growth rate model is desirable (one approach to deal with this issue is the use of Kinetic Monte Carlo simulation (Kwon et al., 2014b)). In the particular case of mandelic acid, an additional difficulty for determining crystal nucleation and growth rates is that the presence of the opposite enantiomer in the mother liquor can affect the nucleation and growth kinetics of the desired enantiomer (Zhang et al., 2010).

There are few studies in the literature addressing the estimation of kinetic parameters for enantiomeric system crystallization. For example, for the *R*-MA case, Mao et al. (2010) study the unseeded cooling batch crystallizer to evaluate the growth and nucleation. A growth-only kinetics evaluation of *S*-mandelic acid and the opposite enantiomer effects were investigated by Codan et al. (2013).

Zhang et al. (2010) experimentally evaluates the direct crystallization of a partially resolved system of *R*-MA enantiomer in water solution during batch operation (on lab-scale and without fines dissolution). They study the influence of various operating condition changes and the presence of the opposite enantiomer (*S*-MA) on the nucleation and growth of *R*-MA. They propose the use of the nucleation rate model $B_0 = k_{b0} \exp\left(-\frac{E_b}{R_g T}\right) \Delta c_R^b M_T$ and the growth rate model $G = k_{g0} \exp\left(-\frac{E_g}{R_g T}\right) \Delta c_R^g$, where $b, k_{b0}, E_b, g, k_{g0}$ and E_g are model parameters, R_g is the gas constant, and M_T is the suspension density (ratio of crystal mass to solvent mass). The term $\Delta c_R := c_R - x_R c_{sol}^{eq}$, where c_R is the *R*-MA concentration (g *R*-MA $/g$ of water) and x_R is given by $\frac{c_R}{c_R + c_S}$, represents the supersaturation of *R* in the presence of the *S* enantiomer with concentration c_S. The term c_{sol}^{eq} is the

solubility of the mixture solution, which is given by a fitted polynomial function of both temperature and composition. To estimate the parameters k_{b0}, E_b, k_{g0} and E_g, data was gathered from batch crystallization experiments performed for controlled linear cooling with different operating conditions. Then, a constrained least-squares estimation was performed to determine the model parameters by minimizing the difference between the measurements of the *R*-MA concentration in the system (g *R*-MA $/g$ of water) and the values of the *R*-MA concentration calculated based on population balance equations with the growth and nucleation rate expressions.

In this work, the crystal nucleation and growth rate expressions are similar to those from Zhang et al. (2010), but replacing the term c_{sol}^{eq} with the term $(S_{sup} - 1)$ (Mullin, 2001), where S_{sup} is the supersaturation defined with respect to the solubility of R in the liquid phase. This expression for supersaturation, where $S_{sup} = \frac{w_R}{w_{R,sat}}$, is consistent with the literature (Kaspereit, 2006) and eliminates the need for the experimentally developed fit for the solubility data utilized by Zhang et al. (2010) and instead allows for use of solubility data derived from the ternary diagram in determining the crystal growth and nucleation rates. Specifically, using w_R^{sat} computed from Eq. 5.3, it is use the following expressions for the nucleation and growth rates:

$$B_0 = k_{b0} \exp\left(-\frac{E_b}{R_g T}\right) (S_{sup} - 1)^b M_T \tag{5.30}$$

$$G = k_{g0} \exp\left(-\frac{E_g}{R_g T}\right) (S_{sup} - 1)^g \tag{5.31}$$

Because of the difference between the growth rate expressions used in this work and those determined by Zhang et al. (2010), the parameters of the nucleation and growth rate expressions in Eqs. 5.30 and 5.31 are estimated using the data available in Zhang et al. (2010) (run 2) with the operating conditions listed in Table 5.2.

For consistency with Zhang et al. (2010), the parameter estimation is performed for batch operation without fines dissolution by determining the values of the growth rate parameters that minimize a constrained least-squares problem that penalizes in the objective function the difference between calculated and experimental values of the concentration of the R enantiomer in the crystallizer. The moment equations (Eq. 5.24) were used to calculate the values of the R concentration used in the least-squares estimation. The first five moment equations were used to capture the dominant dynamics of the system (Christofides, 2002b), along with a mass balance

Table 5.2: Operating parameters used for parameter estimation (run 2 from Zhang et al. (2010)).

Parameter	Notation	Value	Unit
Initial temperature	$T(t_0)$	23.0	$^{\circ}C$
Final temperature	$T(t_f)$	19.0	$^{\circ}C$
Batch time	t_f	200.0	min
Solvent mass	m_W	200.0	g
Initial R liquid mass	$m_R(t_0)$	0.0275	kg
Initial purity	P^i	0.82	(-)
Seed mass	$m_c(t_0)$	0.34	g
Initial zero moment	$\mu_0(t_0)$	$6.110 \cdot 10^5$	$1/kg_W$
Initial first moment	$\mu_1(t_0)$	156.4296	m/kg_W
Initial second moment	$\mu_2(t_0)$	0.04028	m^2/kg_W
Initial third moment	$\mu_3(t_0)$	$1.0435 \cdot 10^{-5}$	m^3/kg_W
Initial fourth moment	$\mu_4(t_0)$	$2.7184 \cdot 10^{-9}$	m^4/kg_W
R crystal density	ρ_c	1349.0	kg/m^3
Crystal shape factor	k_V	0.12	(-)
Eutectic purity	P^e	0.69	(-)
Kinetic nucleation order	b	1.5	(-)
Kinetic growth order	g	1.0	(-)
Seed coefficient	a_0	$5.38 \cdot 10^{18}$	$1/(kg_W \cdot m^3)$

on R, as follows:

$$\frac{dm_R}{dt} = -3m_W\rho_c k_V \mu_2 G(t) \tag{5.32a}$$

$$\frac{d\mu_j}{dt} = \begin{cases} B_0, \ j = 0 \\ jG(t)\mu_{j-1}, \ j = 1,2,3,4 \end{cases} \tag{5.32b}$$

where B_0 and $G(t)$ are defined in Eqs. 5.30-5.31, and $m_R(t)$ represents the mass of enantiomer R in the liquid phase in the crystallizer at time t. The initial moments (reported in Table 5.2) were obtained using the initial PSD (Eq. 5.14) and the definition in Eq. 5.23. The seed mass is calculated based on the third order moment as: $m_c(t_0) = m_W\rho_c k_V \mu_3(t_0)$. No energy balance was required in this simulation for consistency with Zhang et al. (2010), which assumed that the temperature in the crystallizer followed a linear cooling profile from $23^{\circ}C$ to $19^{\circ}C$. During the simulation, the crystal yield can be obtained using: $Y_c = \frac{m_c(t_f) - m_c(t_0)}{m_R(t_0)}$, in which $m_c(t)$ is the mass of crystals at time t and is given by $m_c(t) = m_W\rho_c k_V \mu_3(t)$, where t_f is defined as the final time and t_0 as the initial time of the batch. Moreover, as the crystallization process without a fines dissolution loop is a closed system, all the formed crystal mass is from the liquid phase (i.e., $m_c(t_f) - m_c(t_0) = m_R(t_0) - m_R(t_f)$), such that the yield can be written as: $Y_c = 1.0 - \frac{m_R(t_f)}{m_R(t_0)}$.

As suggested by Zhang et al. (2010), the parameters k_{b0}, E_b, k_{g0} and E_g were estimated using a least-squares minimization between the predicted (i.e., from Eqs. 5.30-5.32) and experimental values of the concentration of R in the liquid phase throughout the batch. In the predictions, the coefficients b and g in the growth and nucleation rate expressions were set to 1.5 and 1.0, respectively, for consistency with Zhang et al. (2010). Also for consistency with Zhang et al. (2010), a constraint on the ratio $L_{43} = \frac{\mu_4}{\mu_3}$ (volume-weighted mean size) at the end of the batch was included to account for experimental results on the size distribution. An additional constraint was added for the present work on the process yield to take advantage of additional information reported in Zhang et al. (2010) for the experimental crystal yield (Y_c).

The parameter estimation problem with $\theta = [k_{b0}, k_{g0}, E_b, E_g]$ is stated as:

$$\begin{aligned} \underset{\theta}{\text{minimize}} \quad & J(\theta) = \sum_{i=1}^{n_t} \left[c_R(t_i)^{exp} - c_R(t_i)^{calc} \right]^2 \\ \text{subject to} \quad & 0.9 {L_{43}}^{exp} \leq \frac{\mu_4}{\mu_3} \leq 1.1 {L_{43}}^{exp} \\ & 0.95 {Y_c}^{exp} \leq \left[1.0 - \frac{m_R(t_f)}{m_R(t_0)} \right] \leq 1.05 {Y_c}^{exp} \end{aligned} \tag{5.33}$$

The calculated concentration of R at time t_i, $c_R(t_i)^{calc}$, is given by $\frac{m_R(t_i)}{m_W}$ based on Eqs. 5.30-5.32, with the temperature set to the linear cooling strategy for run 2 in Zhang et al. (2010) (i.e., perfect temperature control was assumed, and Eq. 5.18 was not solved), $c_R(t_i)^{exp}$ is the experimental concentration at time t_i and n_t is the number of experimental samples used (50 data points, which were extracted from the plots for run 2 in Zhang et al. (2010)). The experimental values of the mean size and yield used were $L_{43}^{exp} = 440.1\ \mu m$ and $Y_c^{exp} = 8.5\%$, respectively, as reported in Zhang et al. (2010) for run 2. The parameter estimation problem in Eq. 5.33 was solved using IPOPT (Wächter and Biegler, 2006) and ADOL-C (Walther and Griewank, 2012) for the gradient and Jacobian. The dynamic model of Eq. 5.32 was solved using the Explicit Euler numerical integration method with an integration step size of 1 s.

The parameter estimation problem of Eq. 5.33 resulted in the following estimated parameter values: $k_{b0} = 1.6416 \cdot 10^{12}\ \frac{1}{kg_W s}$, $k_{g0} = 54416.74\ \frac{m}{s}$, $E_b = 33297.23\ \frac{J}{mol}$ and $E_g = 63862.05\ \frac{J}{mol}$. The upper bounds for the L_{43} and Y_c constraints were active for this solution.

Figure 5.5 shows the comparison between the experimental (EXP-ZR in Figure 5.5) concentrations and calculated concentrations from the moment model (MOM in Figure 5.5) using these estimated parameter values. To verify the adequacy of the moment model of Eq. 5.32b for numerically simulating the crystallization

process, the moving sectional method of Eq. 5.25 for the case without a fines dissolution loop ($\dot{m}_{W,in} = \dot{m}_{W,out} = 0$) was also used to determine the predictions of the concentration of R in the liquid phase throughout the batch and was plotted for comparison in Figure 5.5 (labeled PBE in the figure). The trajectories calculated from the moving sectional method and the method of moments overlaid one another, verifying that the first five moments of the particle size distribution were sufficient for modeling the dominant process dynamics in this case. Though the predicted and experimental values of the concentration profiles show some offset, a number of factors may be responsible for this. Firstly, because Zhang et al. (2010) did not report the exact values of their experimental data points but only plotted the data, there may be some inaccuracy in the experimental values used for the parameter estimation in this work due to the need to extract the values from the plots.

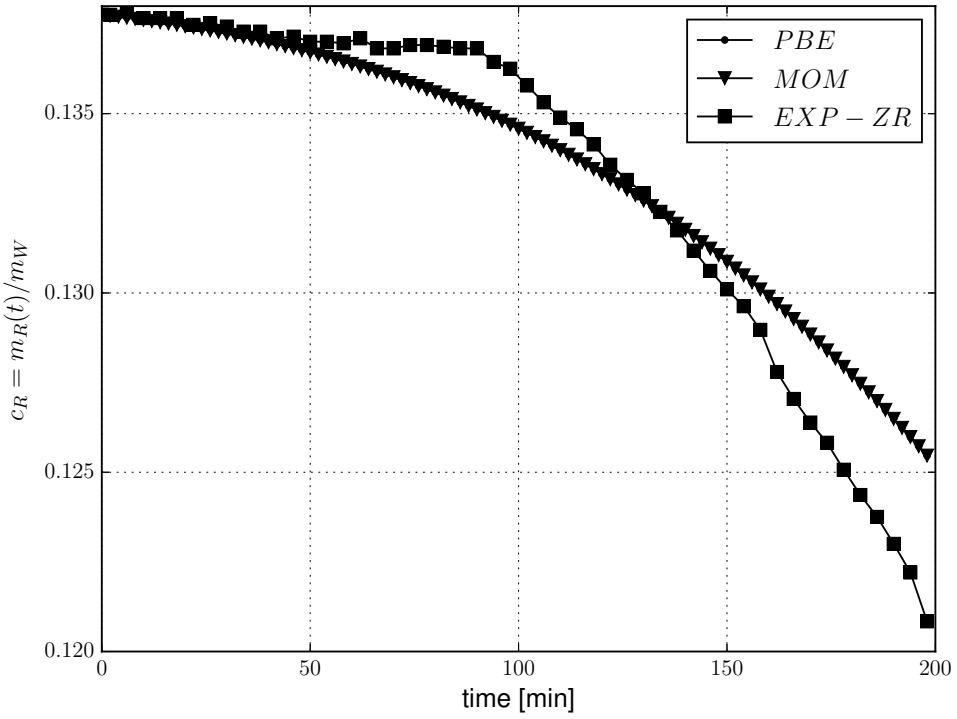

Figure 5.5: Experimental and calculated concentration profiles for parameter estimation based on Table 5.2. PBE: simulation with moving sectional method (Eq. 5.25); MOM: method of moments simulation (Eq. 5.32; overlays PBE); EXP-ZR is the experimental data extracted from Zhang et al. (2010).

In addition, errors may be introduced for the same reasons noted by Zhang et al. (2010) as causes for offset between the experimental and predicted R concentrations in their own work, namely limitations of the particle size measurement equipment and modeling approximations such as neglecting breakage and agglomeration and assuming a narrow seed initial particle size distribution. However, it is notable that the particle size distribution obtained by simulating the batch process with linear cooling with the parameter values estimated from Eq. 5.33 shows many

similarities to the predicted particle size distribution developed for run 2 by Zhang et al. (2010). This particle size distribution is shown in Figure 5.6, simulated using the moving sectional method with the growth and nucleation rates determined by solving Eq. 5.33. The evolution of the particle size distribution throughout the batch is plotted by showing the particle size distribution distribution at five different times (2 min, 50 min, 100 min, 150 min, and 198 min) after the batch was initiated.

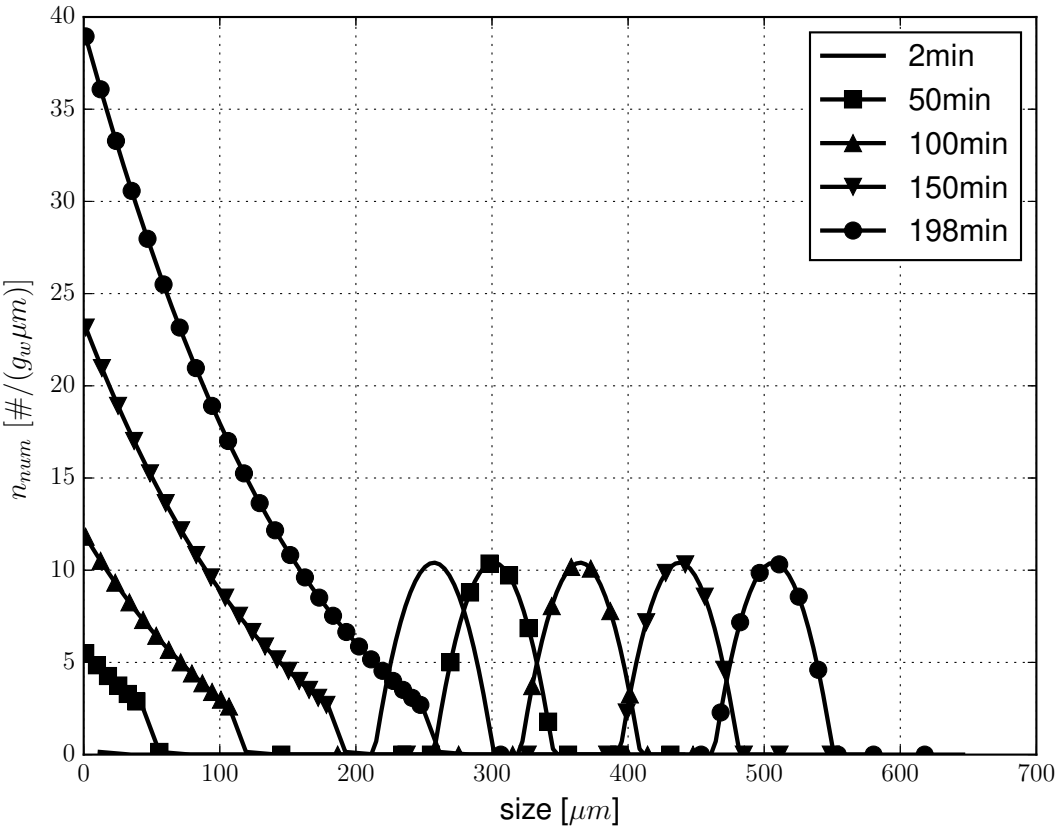

Figure 5.6: Calculated PSD (using Eq. 5.28 in number of particles per gram of solvent (g_W) and micrometer) at five times after the batch crystallization process was initiated (crystallization begins at 0 min) without fines dissolution under the linear cooling strategy with the parameters k_{b0}, k_{g0}, E_b, and E_g estimated from Eq. 5.33.

Remark 5 *Because the parameter estimation in Eq. 5.33 is a nonlinear program, the parameters obtained for the growth and nucleation rates do not necessarily correspond to a global optimum, but the good agreement of the experimental results with the results from the parameter estimation in Figure 5.5 indicates that the results are expected to be sufficient for simulating the growth and nucleation rates.*

5.4 Batch Crystallization Study

In the next two sections, the demonstration of the process operation, modeling, and control policy developed in the section "Batch Crystallization Operation and Control Design for Racemic Compound Forming Systems Using the Ternary Diagram" is completed by demonstrating the application of model predictive control to the batch crystallization process of the section "Batch Crystallizer Model with Fines Dissolution Loop". Specifically, for this mandelic acid in water example, Steps 1-4 of the proposed operation, modeling, and control strategy were demonstrated in the section "Batch Crystallization Operation and Control Design for Racemic Compound Forming Systems Using the Ternary Diagram" and Step 5 was demonstrated in the section "Batch Crystallizer Model with Fines Dissolution Loop". In the following two sections, it is demonstrated Steps 6-8. The closed-loop performance of the batch crystallization process, in both the case without the fines dissolution loop and the case with the fines dissolution loop, was investigate to demonstrate the applicability of MPC in controlling a batch enantioselective crystallization process for a racemic compound forming system.

5.4.1 Optimal Jacket Temperature Profile Without Fines Dissolution

In this section, the batch crystallization of R-MA enantiomer without the fines dissolution loop is considered. Because the experimental data for parameter estimation of nucleation and growth kinetics (Zhang et al., 2010) were available only within the temperature range of $23°C$ to $19°C$, an operating temperature range that deviated from this range by only a few degrees above and below was chosen for the batch crystallization process. Specifically, Figure 5.2 was analyzed to determine a reasonable operating temperature range, assuming that the initial purity P^i is fixed at 0.80, close to the purity used to obtain the growth and nucleation rate parameters, from the pre-enrichment process, and that it is desired to obtain the greatest yield possible during the crystallization process by crystallizing until the eutectic purity P^e is reached. The top figure in Figure 5.2 was analyzed, and it was seen that cooling a solution with an initial R mass fraction of 0.1336 would allow a saturated solution at $26.0°C$ to be cooled to reach the eutectic composition at $12.13°C$. Thus, due to its closeness to the $23°C$ to $19°C$ operating temperature range from Zhang et al. (2010), the $26.0°C$ to $12.13°C$ operating temperature range was chosen for this example. Also, the batch process was scaled up compared to Zhang et al. (2010) (i.e., a total initial liquid mass of 20 kg was assumed) with $P^i = 0.80$ and seeding with 28.92 g of R to maintain approximately the same ratio of seeds to mass of

solvent as in Table 5.2. Table 5.3 lists the operational parameters used in this case study. The liquid density and heat capacity are assumed to be close to those of the solvent, and the thermal coefficient is on an order of magnitude consistent with the value in Shi et al. (2006).

Table 5.3: Operational parameters used in optimal control study without fines trap.

Parameter	Notation	Value	Unit
Initial temperature	$T(t_0)$	26.0	$^\circ C$
Final temperature	$T(t_f)$	12.13	$^\circ C$
Batch time	t_f	30	h
Solvent mass	m_W	16.658	kg
Initial R liquid mass	$m_R(t_0)$	2.673	kg
S liquid mass	m_S	0.668	kg
Initial purity	P^i	0.80	(-)
Seed mass	$m_c(t_0)$	28.92	g
Initial zero moment	$\mu_0(t_0)$	$6.281 \cdot 10^5$	$1/kg_W$
Initial first moment	$\mu_1(t_0)$	160.7909	m/kg_W
Initial second moment	$\mu_2(t_0)$	0.04140	m^2/kg_W
Initial third moment	$\mu_3(t_0)$	$1.0724 \cdot 10^{-5}$	m^3/kg_W
Initial fourth moment	$\mu_4(t_0)$	$2.7935 \cdot 10^{-9}$	m^4/kg_W
R Crystal density	ρ_c	1349.0	kg/m^3
Liquid density	ρ_l	1000.0	kg/m^3
Crystal shape factor	k_V	0.12	(-)
Seed coefficient	a_0	$5.53 \cdot 10^{18}$	$1/(kg_W \cdot m^3)$
Thermal coefficient	UA	250	W/K
Heat capacity	c_p	$3.8 \cdot 10^3$	$J/(K \cdot kg)$

A model predictive controller was used to control the batch crystallization process to minimize the ratio of the mass of crystals grown from nuclei to the mass of crystals grown from the seeds. The model developed for use within the MPC tracked the population balance characteristics using the method of moments. To accomplish the control objective of maximizing the mass of crystals obtained from seeds while reducing the mass of crystals obtained from nucleation, the model used two sets of five moment equations, one for crystals growing from seeds and one for crystals growing from nuclei (Shi et al., 2006). Applying this scheme, the differential equations for mass, energy and moments for the model used within the MPC are:

$$\frac{dm_R}{dt} = -3m_W\rho_c k_V(\mu_2^n + \mu_2^s)G(t) \tag{5.34a}$$

$$M_{tot}c_p\frac{dT}{dt} = -UA(T - T_{jkt}) \tag{5.34b}$$

$$\frac{d\mu_0^\nu}{dt} = B_0^\nu,\ \nu = n, s \tag{5.34c}$$

$$\frac{d\mu_j^\nu}{dt} = jG(t)\mu_{j-1}^\nu,\ j = 1, 2, 3, 4,\ \nu = n, s \tag{5.34d}$$

where ν designates the seeds (s) or nucleation (n) moments. No breakage or agglomeration is considered, and $B_0^s = 0$. The growth rate $G(t)$ is given by Eq. 5.31 and B_0^n by Eq. 5.30 with the parameters obtained from Eq. 5.33. The initial values of μ_j^n, $j = 0, 1, 2, 3, 4$, are zero. Initial values for m_R, T, and μ_j^s, $j = 0, 1, 2, 3, 4$, are reported in Table 5.3.

The MPC optimization problem at each sampling time can be stated as:

$$\underset{\Delta T_{jkt,k}}{\text{minimize}} \quad J(T_{jkt,k}) \coloneqq \frac{\mu_3^n(t_f)}{\mu_3^s(t_f)} \tag{5.35a}$$

$$\text{subject to:} \quad \text{Model: Eq. 5.34} \tag{5.35b}$$

$$\Delta T_{jkt,k} \leq 0, k = k_{it}, \ldots, k_{N_t-1} \tag{5.35c}$$

$$T_{min} \leq T(t_f) \leq T_{max} \tag{5.35d}$$

$$Y_c(t_f) = \frac{P^i - P^e}{P^i(1 - P^e)} \tag{5.35e}$$

in which the decision variables are $\Delta T_{jkt,k} = T_{jkt,k} - T_{jkt,k-1}$, where $k = k_{it}, \ldots, k_{N_t-1}$, with k_{it} at the current sampling time $t_{k_{it}}$ and N_t as the total number of sampling times between t_0 and t_f, and with each value of t_k separated by a sampling period of length Δ. $T(t_k)$ is the temperature within the crystallizer at time t_k. A shrinking prediction horizon was used for the optimization problem that was initially set to $N_t - 1$ and decreased by one at each subsequent sampling time in the simulation so that the remainder of the batch was included in the prediction horizon at all times. The constraint $\Delta T_{jkt,k} \leq 0$ indicates that no heating was allowed (cooling was enforced to enable crystallization). $Y_c(t_f)$ is the crystal yield at the end of the batch, defined by Eq. 5.8, which is forced to the maximum value 0.4435 obtained by setting $P^f = P^e$ in Eq. 5.8. No feasibility issues were encountered during the dynamic simulations with this terminal constraint on the yield, indicating that the batch time was sufficiently long to allow this constraint, which essentially requires thermodynamic equilibrium at the end of the batch, to be met. The minimum temperature T_{min} was set to the temperature required to achieve the eutectic composition ($T_{min} = 12.13°C$ from Eq. 5.10). For consistency with standard MPC formulations, a maximum temperature $T_{max} = 30°C$ was also included, though due to the cooling constraint of Eq. 5.35c, it was never approached. The sampling period Δ was set to 360 s and the ordinary differential equations (Eq. 5.34) were solved using the low memory Runge-Kutta scheme RK33 from Carpenter and Kennedy (1994). The gradient of the objective function and Jacobian of the constraints were obtained using ADOL-C. The optimization problem was solved

with the interior point optimization software package IPOPT.

To simulate the closed-loop crystallization process, Eq. 5.12 (with $\dot{m}_{W,in} = \dot{m}_{W,out} = 0$) was discretized and solved using the moving sectional method (Eq. 5.25) of Kumar and Ramkrishna (1997). A new bin was added every sampling time ($\Delta t_{bin} = \Delta = 360\ s$). Thus, at the initial time there are $M_0 = 50$ active bins, so at the final time the number of active bins is $M_f = M_0 + N_t - 2$ (bins added only at the intermediate steps, i.e., not at the initial or final times). The $(M_f - M_0)$ bins initially are considered to contain zero crystals and are activated according to the methodology described in the section "Moving Sectional Method for Crystal Nucleation and Growth" and Appendix F.

To enable feedback to the MPC when the plant dynamics are assumed to follow Eqs. 5.34a-5.34b and the population balance equation is solved using the moving sectional method, the values of m_R, T, and also of the moments of the particle size distribution must be measured and fed back to the MPC at each sampling time so that the model of Eq. 5.35b can be integrated at the new sampling time. The values of m_R and T can be obtained in a straightforward manner from numerical integration of Eqs. 5.34a-5.34b. The moments μ_j^s, $j = 0, 1, 2, 3, 4$ can be obtained from the last M_0 bins while the moments μ_j^n, $j = 0, 1, 2, 3, 4$, can be obtained from the first $M_f - M_0$ bins at a given time when the moving sectional method is used with bin additions, as follows:

$$\mu_j^s = \sum_{i=M_f-M_0+1}^{M_f} \left[N_i x_i^j\right],\ j = 0, 1, 2, 3, 4 \tag{5.36a}$$

$$\mu_j^n = \sum_{i=1}^{M_f-M_0} \left[N_i x_i^j\right],\ j = 0, 1, 2, 3, 4. \tag{5.36b}$$

The closed-loop simulation results for the batch crystallization process without fines dissolution under the model predictive control strategy of Eq. 5.35 are shown in Figure 5.7. These closed-loop profiles under MPC are compared with the closed-loop trajectories under the linear cooling strategy from 26 to 12.13°C during the 30 h operation. Specifically, the dynamic behavior of the mass of crystals from the seeds and the mass of crystals from nucleation are compared for the closed-loop crystallizer under MPC and under the linear cooling strategy.

Figure 5.7 shows that the crystal mass from the seeds is 9.65% greater for the process operated under the MPC than under the linear cooling strategy, and there is also less total crystal mass due to nucleation. On the same plot, the jacket profile computed by the MPC of Eq. 5.35 is shown ($T_{jkt,otm}$ in Figure 5.7), and the temperature in the crystallizer when a linear cooling profile from 26°C to 12.13°C is used (denoted by T_{lin} in the figure) is shown. The flattening of the

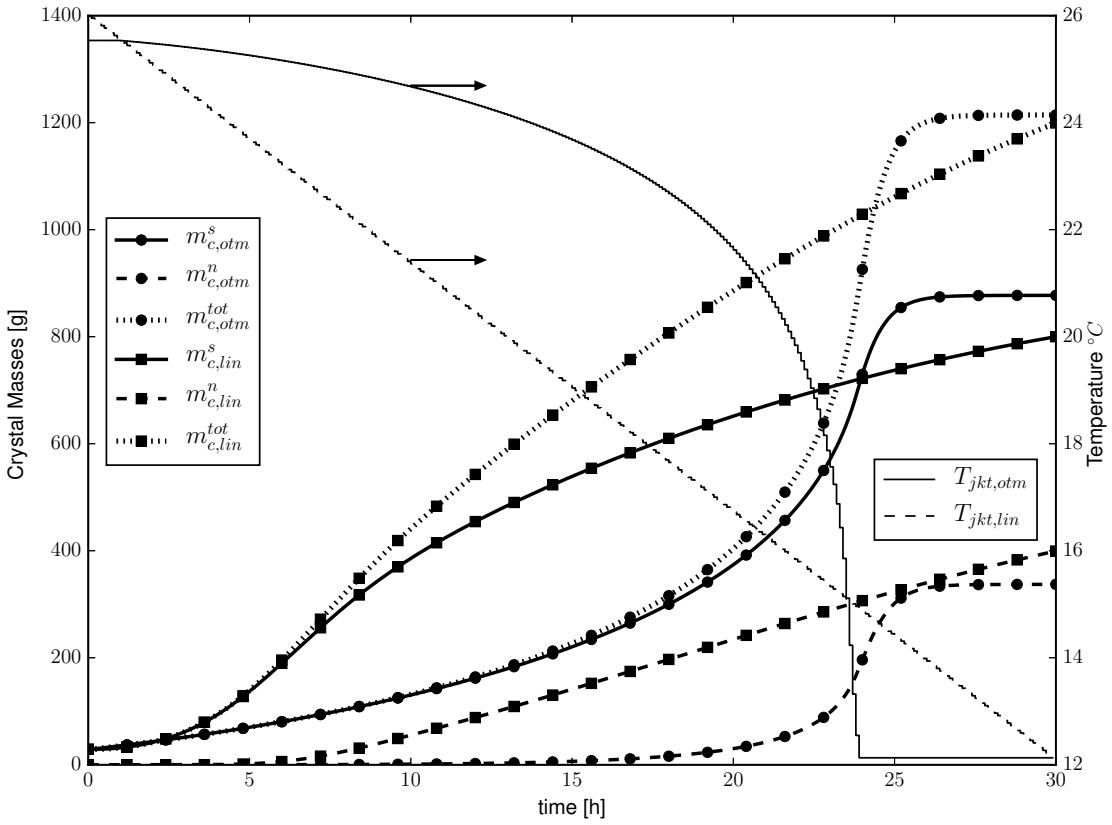

Figure 5.7: Crystal mass using linear cooling (*lin*) and optimized profile under MPC (*otm*) in batch crystallization. The optimized case has jacket temperature $T_{jkt,otm}$, crystal mass from seeds $m^s_{c,otm}$, nuclei mass $m^n_{c,otm}$ and total crystal mass $m^{tot}_{c,otm}$. The linear cooling case has crystallizer temperature T_{lin}, crystal mass from seeds $m^s_{c,lin}$, nuclei mass $m^n_{c,lin}$ and total crystal mass $m^{tot}_{c,lin}$. The two arrows pointing to the right indicate that the y-axis for the temperature trajectories is on the right of the plot, whereas it is on the left for the mass profiles.

jacket temperature profile occurs under the control actions calculated by the MPC to optimize the objective function subject to the constraints in the MPC. Because the yield constraint essentially requires that thermodynamic equilibrium be reached at the end of the batch, it is reasonable to expect that the jacket temperature will need to remain constant at the eutectic temperature for some time at the end of the batch to allow thermodynamic equilibrium to be reached.

Under MPC, the temperature is slowly decreased at the beginning of the batch to suppress nucleation, which is consistent with previous studies on batch crystallization (Chianese and Kramer, 2012; Miller and Rawlings, 1994). As the order of dependence of nucleation rate on supersaturation is greater than the order of dependence of the growth rate on supersaturation ($b > g$), the optimal profile induces a small supersaturation magnitude during most of the operation. However, at approximately 24 h of operation there is a supersaturation peak that quickly enhances the crystal growth and leads to a burst of new crystals. The

supersaturation peak timing is optimized in a way to maintain a relatively low rate of solute mass transfer to the new generated crystals (Miller and Rawlings, 1994). This behavior is shown in Figure 5.8, which compares the supersaturation profile for the optimized operation ($S_{sup,otm}$) and the linear run ($S_{sup,lin}$).

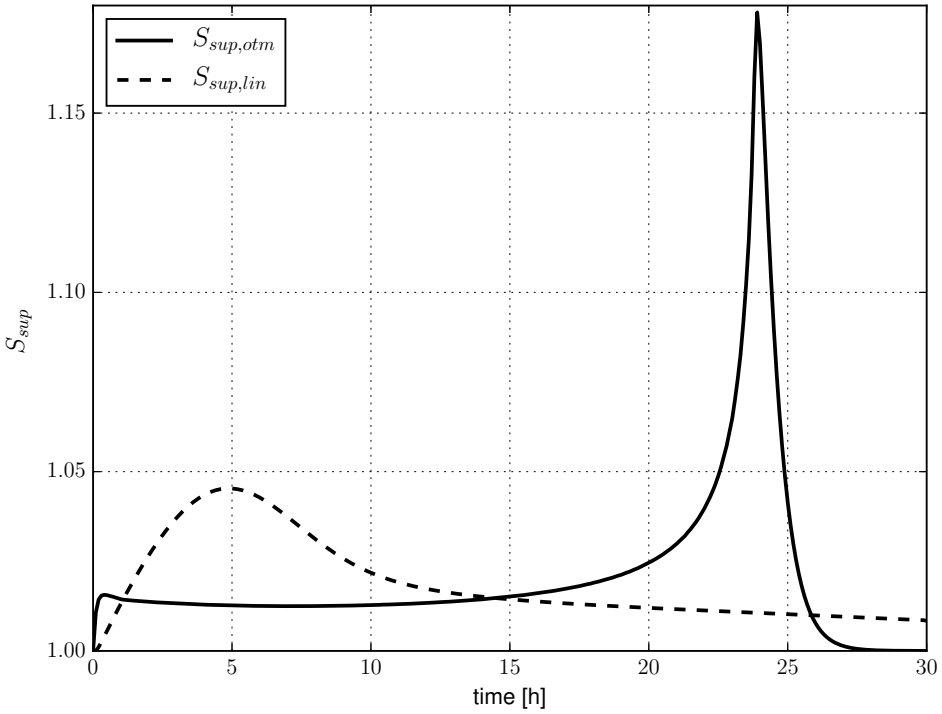

Figure 5.8: Supersaturation profiles for linear cooling (*lin*) and optimized operation under MPC (*otm*).

Figure 5.9 depicts the mass fraction trajectory in the ternary diagram during the batch crystallization. At the initial time the solution in the crystallizer has a composition represented by point **P** and, as it is being cooled, the R enantiomer in the liquid phase is crystallizing. Because of the yield constraint in Eq. 5.35e, the solution in the crystallizer is forced to achieve the eutectic purity P^e at the final time. Note that the non-equilibrium points were used in the ternary diagram to allow a visualization of the process with respect to the solid-liquid equilibrium.

Figure 5.10 shows the particle size distribution at the end of the batch for the process under both MPC and the linear cooling strategy. The bottom plot shows that the optimal policy was able to produce larger crystals originated from the seeds by the final time. The linear cooling approach gives a lower total number of crystals at the final time than the MPC approach (though the total mass of the crystals from seeds is less for the MPC approach than the linear cooling approach). This is due to the way the MPC objective function was formulated (Eq. 5.35a), since it seeks to minimize the mass of fines crystals compared to the mass from seeds, instead of the number. This fact motivates the investigation of including the fines dissolution

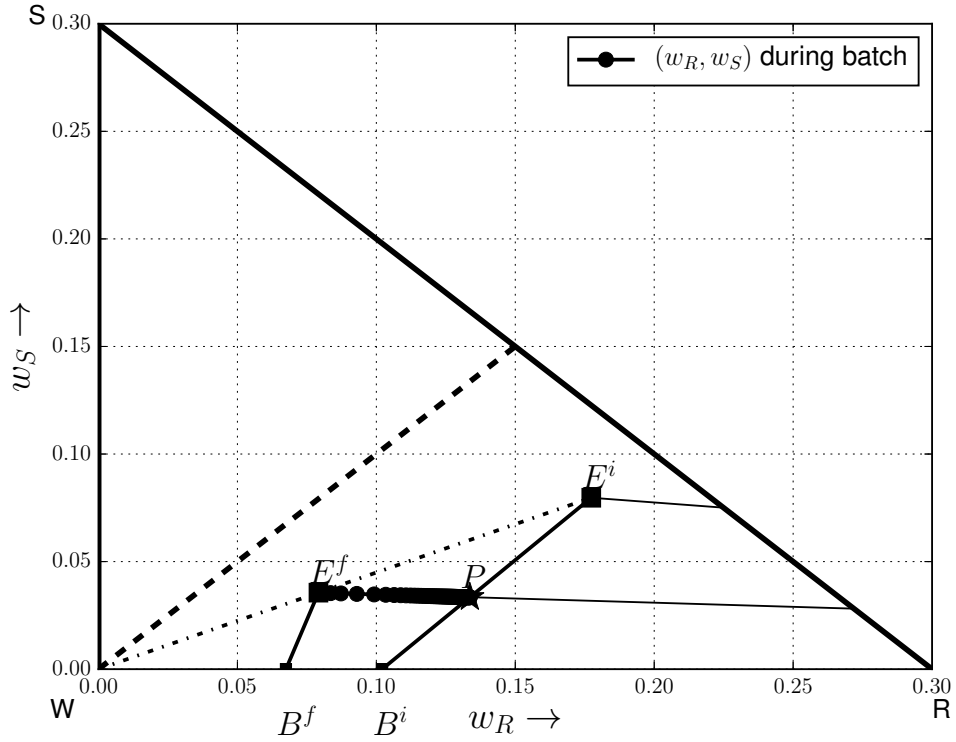

Figure 5.9: Batch crystallization trajectory in the ternary diagram starting at point **P** and ending at the eutectic composition $\mathbf{E^f}$. Each • represents the composition of the liquid in the crystallizer, with 24 *min* time intervals between successive points. Note that the diagram was zoomed in around the solvent corner for a better visualization. The dashed line with a slope of 1 represents the racemic composition. The dashed-dotted line through E^f and E^i represents a line of constant eutectic purity. The bold line with a slope of -1 in this figure represents a line of constant solvent composition $w_W = 0.7$ (only the portion of the ternary diagram to the left of this line is plotted in the figure).

loop, which will be discussed in the next section.

As noted in the section "Batch Crystallization Operation and Controller Design Using Ternary Diagram Data," the MPC of Eq. 5.35 will compute different control actions for different t_f because the objective function (Eq. 5.35a) and the constraints (Eqs. 5.35d-5.35e) depend on the final batch time. Thus, as in Step 7 of the operation, modeling, and control procedure developed in the section "Batch Crystallization Operation and Controller Design Using Ternary Diagram Data," closed-loop simulations of the crystallization process with different final batch times can be evaluated to determine the desired final batch time. To investigate this for the batch crystallization process without fines dissolution under the MPC of Eq. 5.35, closed-loop simulations were performed with t_f ranging from 20 h to 130 h in 5 h increments. The mass of crystals from nuclei and seeds at the end of each batch is plotted in Figure 5.11. This figure shows that there is a trade-off between maximizing the crystal mass from seeds and reducing the final batch time (i.e.,

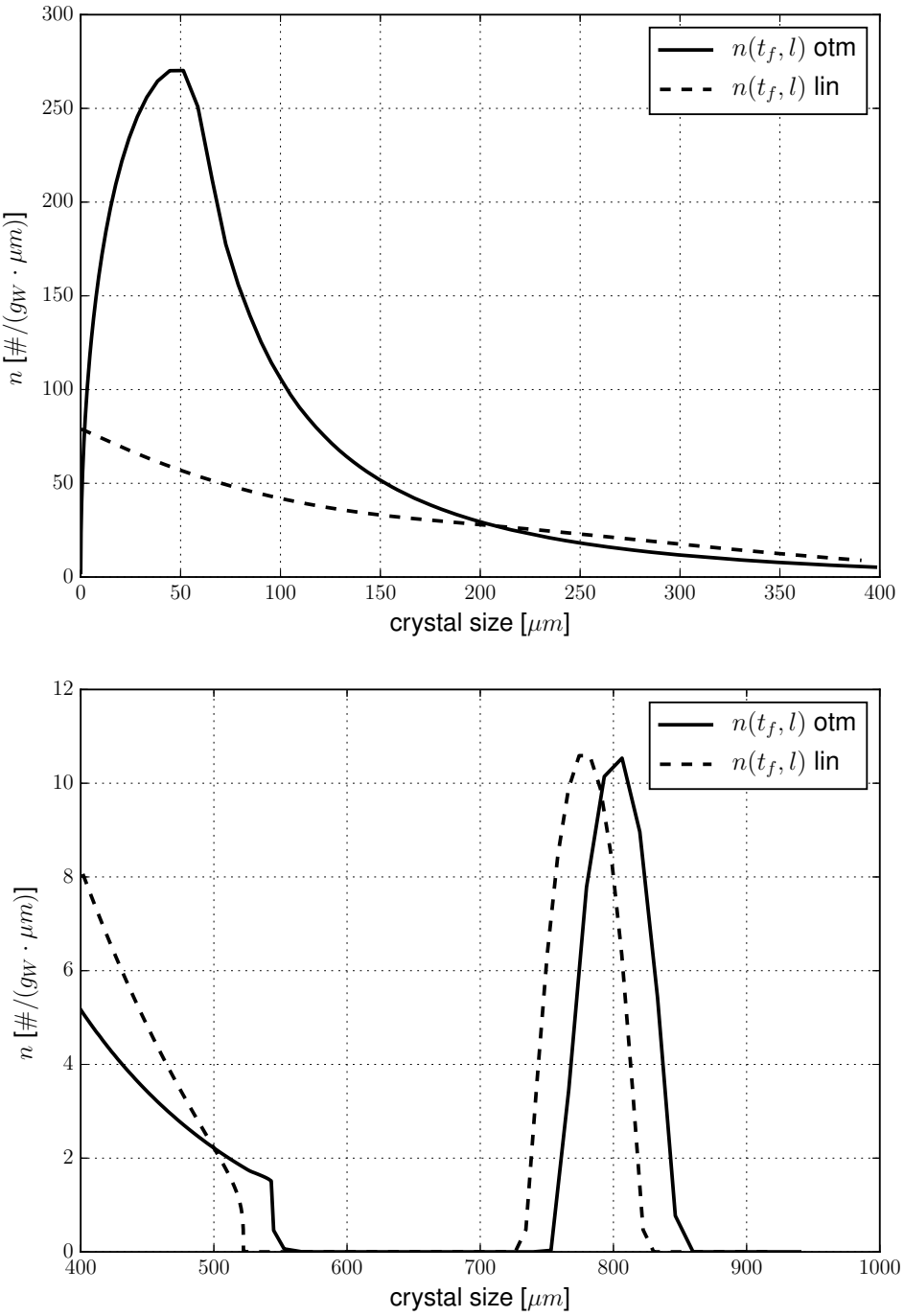

Figure 5.10: PSD at the end of the batch crystallization process without a fines dissolution loop for linear (lin) and optimal (otm) jacket temperature profiles. Top: PSD for 0 to 400 μm and Bottom: 400 to 1000 μm. The plots have independent x and y scales.

increases in final batch time correspond to production of more crystals from seeds and less from nuclei), which is because increasing the batch time allows the system to operate with a lower cooling rate, and thus a smaller supersaturation. This plot can be used to understand the trade-off and choose a batch time with a reasonable length that gives reasonably high production of crystals from seeds. Alternatively,

if none of the combinations of batch time with crystal production from seeds is acceptable, another operating strategy can be proposed for the batch crystallization process. One strategy for enhancing the crystal mass formed from seeds and hence attenuating long batch times is the use of a fines dissolution loop (Chianese and Kramer, 2012). Thus, in the following the operation of the batch crystallization process with the fines dissolution scheme is evaluated.

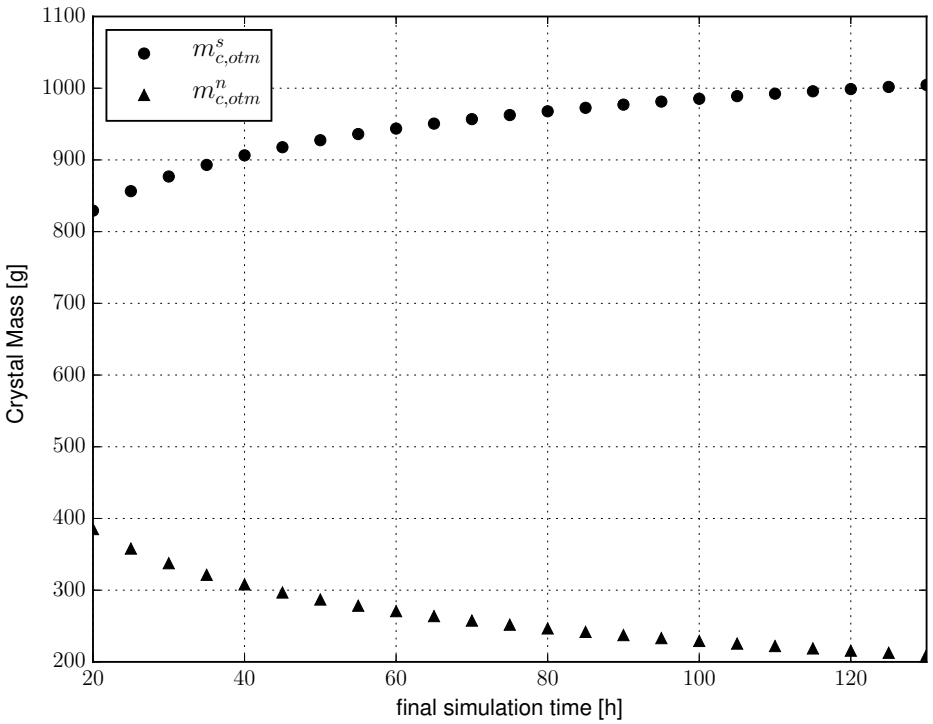

Figure 5.11: Optimal crystal mass from seeds $m^s_{c,otm}$ and nucleation $m^n_{c,otm}$ using different batch final times.

Remark 6 *The parameters of the growth and nucleation rate equations were obtained from experiments using a linear cooling strategy. Zhang et al. (2010) indicates that different cooling rates may impact the growth and nucleation rates. The impact of the non-linear cooling rate for the crystallizer under MPC on the growth and nucleation rates in the model utilized by the MPC could be analyzed when developing the MPC model for an industrial application.*

5.4.2 Inclusion of Fines Dissolution Loop

To simulate the crystallization process with the fines dissolution loop, the same total liquid mass of each component as in the case without the fines dissolution loop was considered; however, that mass was divided between the crystallizer and the fines dissolution tank. The total mass in the fines dissolution tank was 4.3236 kg, and thus the crystallizer liquid mass was 15.6764 kg (giving the same total liquid mass of

20 kg as in the previous case without the fines dissolution tank). Additionally, the same initial composition was used for each component ($w_R = 0.13364$, $w_S = 0.03341$ and $w_W = 0.83294$) as in the case without the fines trap for both the crystallizer and fines dissolution tank. Using these considerations, the initial masses of all components in the crystallizer and dissolution tank are depicted in Table 5.4, in addition to other operating parameter values.

Table 5.4: Operational parameters used in optimal control study with fines trap.

Parameter	Notation	Value	Unit
Initial temperature	$T(t_0)$	26.0	$°C$
Final temperature	$T(t_f)$	12.13	$°C$
Batch time	t_f	30	h
Crystallizer initial solvent mass	$m_{cryst,W}(t_0)$	13.057	kg
Crystallizer initial R liquid mass	$m_{cryst,R}(t_0)$	2.095	kg
Crystallizer initial S liquid mass	$m_{cryst,S}(t_0)$	0.5237	kg
Dissolver initial solvent mass	$m_{diss,W}(t_0)$	3.601	kg
Dissolver initial R liquid mass	$m_{diss,R}(t_0)$	0.5778	kg
Dissolver initial S liquid mass	$m_{diss,S}(t_0)$	0.1444	kg
Initial purity	P^i	0.80	(-)
Seed mass	$m_c(t_0)$	28.92	g
R crystal density	ρ_c	1349.0	kg/m^3
Liquid density	ρ_l	1000.0	kg/m^3
Crystal shape factor	k_V	0.12	(-)
Seed coefficient	a_0	$7.0552{\cdot}10^{18}$	$1/(kg_W \cdot m^3)$
Thermal coefficient	UA	250	W/K
Heat capacity	c_p	$3.8{\cdot}10^3$	$J/(K \cdot kg)$
Dissolver tank total mass	$m_{diss,L}$	4.3236	kg

To obtain the same initial seed mass in the crystallizer as in the case without fines dissolution, the parameter a_0 in Eq. 5.14 was adjusted as: $a_0 = a_0^{ref} \frac{m_W^{ref}}{m_{cryst,W}}$, in which the superscript ref indicates the case without the fines dissolution tank. As there is less mass of solvent in the crystallizer for the case with the fines dissolution tank, $a_0 > a_0^{ref}$, which means that there are more crystals of each size in the initial PSD for the case with the fines dissolution tank than without it to obtain the same initial seed mass in the crystallizer.

The death function of Eq. 5.22 can be defined using the pivots as in Eq. 5.27 and the number of crystals leaving the crystallizer for each bin ($N_{i,out}$) was defined by Eq. 5.26. The fines concentration (Eq. 5.20) is approximated by $C_{fines} = k_V \rho_c \sum_{i=1}^{M} [N_{i,out} {x_i}^3]$. Additionally, the rate of crystallization of the R enantiomer is approximated by $\dot{m}_{cryst,R} = -3\rho_c k_V m_W \sum_{i=1}^{M} [N_i x_i^2 G(t)]$.

The proposed MPC formulation from Eq. 5.35 was used, but the controller model was changed to the moving sectional method, instead of the moment model, in order

to include the fines removal effect in the particle size distribution. The discretized model was solved using the augmented state approach described in the section 5.3.1 with $M_0 = 30$ and uniformly spaced bins covering the initial PSD for setting the initial number of crystals in each bin and the initial pivots. The same sampling period and final batch time were used as in the section 5.4.1. Because of the higher model complexity, a higher computational time is required for solving the MPC at each sampling time than is required when using the moment model. To circumvent this issue in a practical implementation, one could implement the second control action in the prediction horizon from the MPC solution at the previous sampling time.

Figs. 5.12 to 5.14 show input and state profiles obtained by controlling the batch crystallization process under MPC for three values of $\dot{V}_{sp,out}$ (0, 5 and 10 $\frac{mL}{s}$). The case with $\dot{V}_{sp,out}$=0 does not include the fines dissolution tank and is simulated according to Table 5.3. The optimal jacket temperature profiles computed by the MPC for the three different values of $\dot{V}_{sp,out}$ are shown in Figure 5.12. The MPC computes that the jacket profile that optimizes the objective function subject to the constraints should reach its final value earlier in the batch for the two cases that $\dot{V}_{sp,out}$ is nonzero than when it is zero. Under these manipulated input profiles, the dynamic profiles for the seed, nuclei and total crystal mass depicted in Figure 5.13 are obtained. Though the total mass from crystals is approximately the same for the three different values of $\dot{V}_{sp,out}$, operation for the cases with larger values of $\dot{V}_{sp,out}$ is associated with more crystal mass from seeds and less from nuclei in this figure. For example, the crystallizer under MPC with a fines dissolution loop with $\dot{V}_{sp,out} = 10\ \frac{mL}{s}$ gives a 21.3% increase in the crystal mass from the seeds compared to the crystallizer under MPC without a fines dissolution loop ($\dot{V}_{sp,out} = 0\ \frac{mL}{s}$).

Figure 5.14 presents the PSD at the final batch time for all three values of $\dot{V}_{sp,out}$. To allow for better visualization of the results, the PSD has been split into two ranges corresponding to the top (the PSD from 0 to 400 μm crystal size) and bottom (the PSD from 400 to 1000 μm) plots in the figure. The initial PSD is also shown for the fines dissolution cases for comparison (the initial PSD for the case with $\dot{V}_{sp,out} = 0\ \frac{mL}{s}$ is slightly different than that for the fines dissolution case but takes a similar shape, with seed crystals in a limited size range, and is omitted). The figures indicate that the crystallizer with a fines dissolution loop under optimal control has less crystals from nucleation at the end of the batch, with enhanced seed growth. For example, the average crystal size resulting from the seeds in the case that the fines dissolution loop is used with $\dot{V}_{sp,out} = 10\frac{mL}{s}$ is approximately 6.8% larger than in the case without the fines dissolution loop. These results indicate that MPC can be an effective controller for a batch crystallization process for a racemic compound forming system, for various crystallizer designs, and can allow

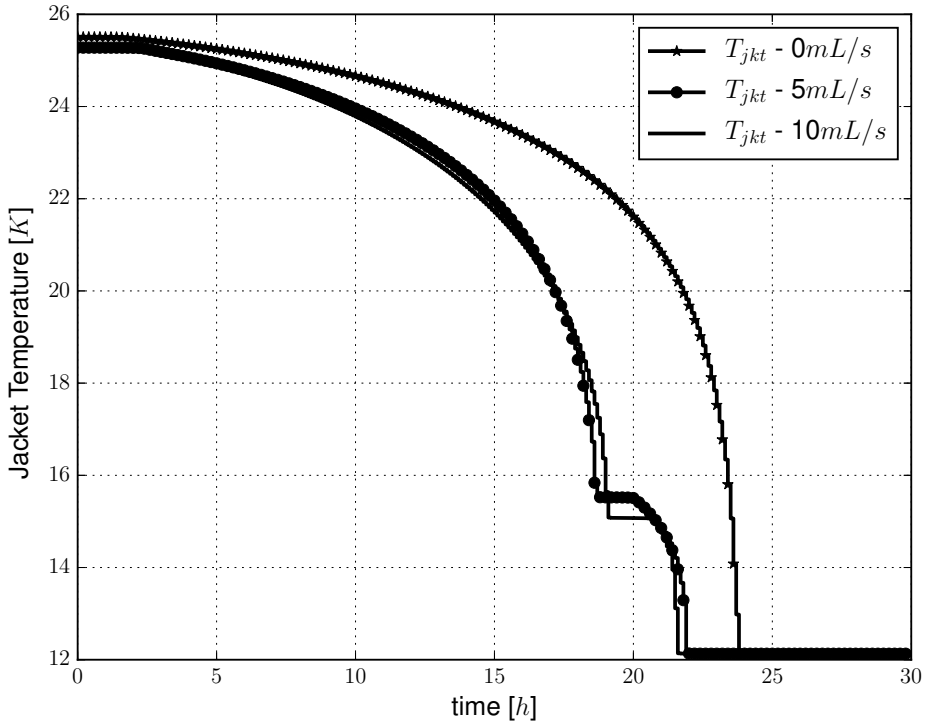

Figure 5.12: Optimal jacket temperature profiles for $\dot{V}_{sp,out}$ equal to 0 (starred trajectory), 5 (dotted trajectory) and 10 $\frac{mL}{s}$ (solid trajectory).

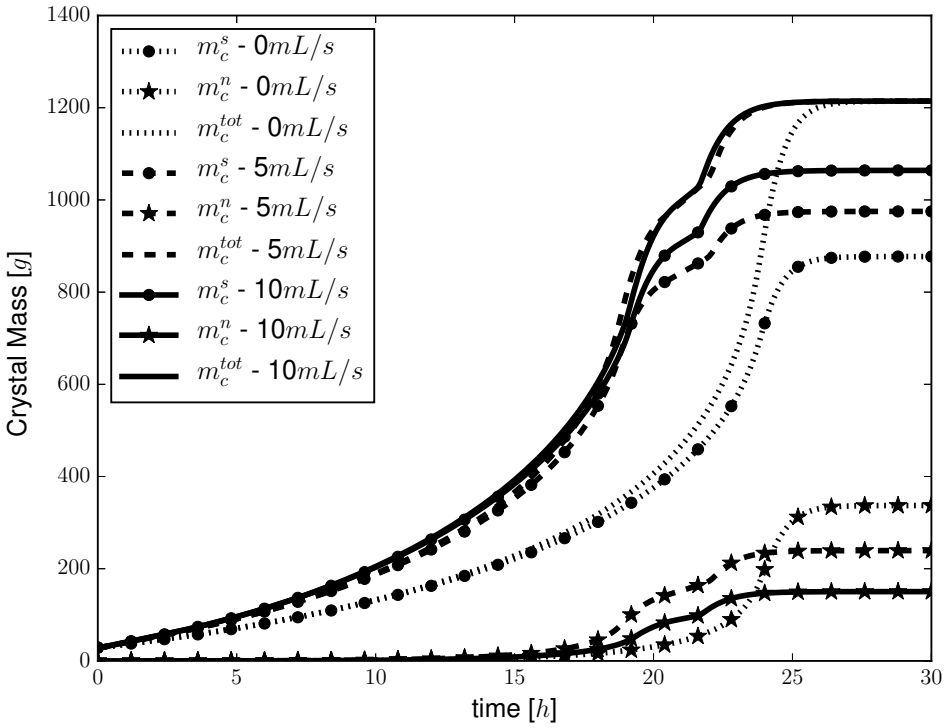

Figure 5.13: Crystal masses using $\dot{V}_{sp,out}$ equal to 0, 5 and 10 $\frac{mL}{s}$ and applying optimal jacket temperatures profiles. In this figure, m_c^s signifies the crystal mass from seeds, m_c^n signifies the crystal mass from nuclei, and m_c^{tot} signifies the total crystal mass from both seeds and nuclei.

thermodynamic constraints, as well as constraints related to profit like yield, to be satisfied while an objective function related to crystal properties is optimized.

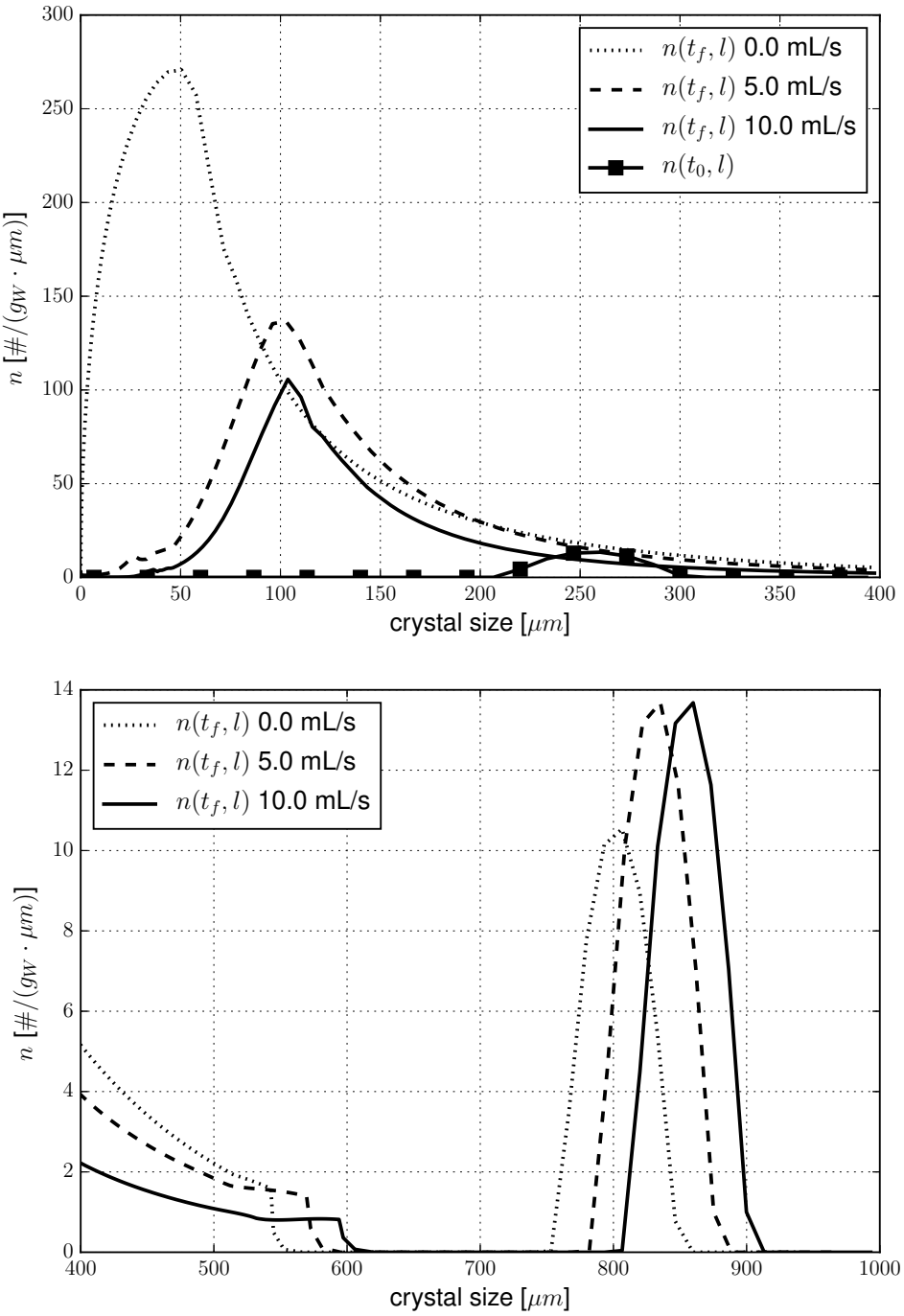

Figure 5.14: Comparison of crystal number density at final batch time with $\dot{V}_{sp,out}$ equal to 0, 5 and 10 $\frac{mL}{s}$. Top: PSD for 0 to 400 μm and Bottom: 400 to 1000 μm. The initial PSD for the fines dissolution case is also plotted for comparison. The plots have independent x and y scales.

Remark 7 *While a number of researchers have looked at MPC for crystallization, the novelty of this work is the focus on enantiomer systems and specifically on*

using thermodynamic data for a racemic compound forming system to develop constraints and an operating procedure for MPC that is based on solution thermodynamics. The two enantiomers of a racemic compound forming system have many identical properties and thus crystallizing a single enantiomer, as is often desirable in industry, poses challenges that are not observed for other types of systems (e.g., non-enantiomeric). Firstly, the solution must be pre-enriched in the desired enantiomer, and secondly, the solution thermodynamics must be carefully understood and exploited during the batch operation to prevent crystals of the counter enantiomer from forming by maintaining the temperature and composition within a required range (which changes as the temperature changes). This work develops a methodology for achieving the desired enantioseparation while allowing product properties related to process economics to be optimized by exploiting ternary diagrams and solution thermodynamic data in the design of a controller for the batch process. The focus is not on the specific trajectories obtained during the crystallization operation, but rather on examining the use of MPC for a very different system thermodynamically than has been considered in other works on crystallization (e.g., Kwon et al. (2015); Patience et al. (2004); Tseng and Ward (2017)). Furthermore, to the knowledge of the authors, MPC has not been examined for racemic compound forming systems in the literature, so the results of this work are also novel in showcasing the possible benefits of MPC compared to traditional cooling strategies in the literature for racemic compound forming systems such as linear cooling.

5.5 Conclusions

In this work, a batch crystallization process for enantioseparation of racemic compound forming systems was considered. An operation and control strategy based on MPC for the crystallization process was developed that uses equations and information developed from a ternary diagram, and it was exemplified for the mandelic acid in water system. The MPC can optimize an objective function related to desired product characteristics while satisfying thermodynamic constraints (e.g., constraints on the minimum crystallizer temperature and yield) subject to a process model based on the solution thermodynamics data to allow for crystals of a single enantiomer to be obtained. The temperature profile in the crystallizer for the mandelic acid example was shown to be different under MPC than under a pre-defined linear cooling profile. A fines dissolution loop was shown to be effective at decreasing the number of crystals from nuclei for the process under MPC.

Chapter 6

Conclusions

In this thesis the Population Balance Equation was used in the design and optimal control of the enantioselective crystallizers of racemic compound forming system. For such, a detailed evaluation of the Moving Sectional Method for nucleation and growth was given. Also, a methodology for estimating kinetic parameters was presented based on the low-cost apparatus of Caciano de Sena et al. (2011) and using dissolution data from Figueiredo (2016) for NaCl in glycol solutions.

The first bin analysis for the MSM discussed the definition of a first bin growth rate for the preservation of selected moment order in the presence of both nucleation and growth. The main simplification hypotheses were discussed and simple test cases were shown such that the main definitions of the first bin growth rate found in the literature were obtained. The issue on the preservation of moment of orders higher than one was elucidated. Efficient schemes for controlled bin addition were proposed such that more bins are added when the system is under higher growth and nucleation rate. Crystallization numerical examples were performed showing that such controlled bin addition schemes can reduce errors on the moment conservation.

The dissolution study evaluated different operational conditions of temperature and MEG composition using data collected by Figueiredo (2016). This work provided a methodology for the determination of dissolution kinetics using the population balance and a dissolution rate capable of describing a broad range of undersaturation.

In the enantioselective crystallizer study, a method for the definition of proper initial condition operation and final obtained yield and compositions and the working temperature range was presented. Based on these definitions, the equilibrium conditions elucidated in the ternary diagram were employed in the design of an optimal control structure. The controller was implemented to maximize the growth of seeds in detriment to the particle nucleation. The ternary diagram information was used to ensure maximum thermodynamic yield of the enantiomer separation as an optimization constraint. The cases with and without fine dissolution loop

were evaluated in closed-loop control. The former was solved using the standard method of moments. The latter required a distributed method to treat the classified removal of particles. Because a distributed model was used in the controller model, an efficient implementation of both time integration and optimization was required. For that, an efficient bin addition scheme was adopted, a low memory Runge-Kutta method was used and the objective jacobian and constraint gradient were obtained using automatic differentiation methods.

6.1 Suggestions for future works

As suggestion for future work on the optimal operation of enantioselective crystallization can be the development of robust optimal control approaches to account for parameter uncertainties. Moreover, the case of preferential crystallization, with both enantiomers crystallizing, can be addressed.

The methodology presented for crystallization separation could be applied for other enantiomeric system of importance, as the praziquantel. The developments of Chapter 3 provide enhanced strategies for the bins addition when using the MSM for nucleation and growth. The proposed methodology for parameter estimation on Chapter 4 can be adjusted for the estimation of growth and nucleation kinetics. Finally, Chapter 5 structured methodology can be used to analyze the operation yield and working temperature range. Also, it allows the study of optimal control operation integrated with the enantiomeric system ternary diagram.

Bibliography

Aamir, E., 2010. Population balance model-based optimal control of batch crystallisation processes for systematic crystal size distribution design. Ph.D. thesis. Erum Aamir.

Ajinkya, M., Ray, W., 1974. On the optimal operation of crystallization processes. Chemical Engineering Communications 1, 181–186.

Amanullah, M., Mazzotti, M., 2006. Optimization of a hybrid chromatography-crystallization process for the separation of Tröger's base enantiomers. Journal of Chromatography A 1107, 36–45.

Angelov, I., Raisch, J., Elsner, M., Seidel-Morgenstern, A., 2008. Optimal operation of enantioseparation by batch-wise preferential crystallization. Chemical Engineering Science 63, 1282–1292.

Benavides, M., Mailier, J., Hantson, A.L., Muñoz, G., Vargas, A., Van Impe, J., Vande Wouwer, A., 2015. Design and test of a low-cost RGB sensor for online measurement of microalgae concentration within a photo-bioreactor. Sensors 15, 4766–4780. URL: https://doi.org/10.3390/s150304766, doi:10.3390/s150304766.

Brandenberger, H., Maes, R.A.A. (Eds.), 1997. Analytical Toxicology for Clinical, Forensic and Pharmaceutical Chemists. Walter de Gruyter, Berlin, Germany.

Burch, T., Nagy, K., Lasaga, A., 1993. Free energy dependence of albite dissolution kinetics at 80°C and pH 8.8. Chem. Geol. 105, 137–162. URL: https://doi.org/10.1016/0009-2541(93)90123-z, doi:10.1016/0009-2541(93)90123-z.

Busch, K.W., Busch, M.A. (Eds.), 2006. Chiral Analysis. Elsevier, Amsterdam, The Netherlands.

Carpenter, M.H., Kennedy, C.A., 1994. Fourth-order 2N-storage Runge-Kutta schemes. Technical Report. NASA, Technical Memorandum 109112.

Chang, C., Epstein, M.A., 1982. Identification of Batch Crystallization Control Strategies Using Characterietic Curves. volume 78. Wiley Online Library.

Chianese, A., Kramer, H.J., 2012. Industrial Crystallization Process Monitoring and Control. Wiley-VCH Verlag GmbH & Co. KGaA. URL: https://doi.org/10.1002/9783527645206, doi:10.1002/9783527645206.

Chiu, T.Y., Christofides, P.D., 2000. Robust control of particulate processes using uncertain population balances. AIChE Journal 46, 266–280.

Christofides, P.D., 2002a. Model-based control of particulate processes. volume 14. Springer.

Christofides, P.D., 2002b. Model-Based Control of Particulate Processes. Kluwer Academic Publishers, Dordrecht, The Netherlands.

Christofides, P.D., Li, M., Mädler, L., 2007. Control of particulate processes: recent results and future challenges. Powder technology 175, 1–7.

Codan, L., Eckstein, C.F., Mazzotti, M., 2013. Growth kinetics of S-mandelic acid in aqueous solutions in the presence of R-mandelic acid. Crystal Growth & Design 13, 652–663.

Costa, C.B.B., Maciel, M.R.W., Filho, R.M., 2007. Considerations on the crystallization modeling: Population balance solution. Computers & Chemical Engineering 31, 206–218. URL: https://doi.org/10.1016/j.compchemeng.2006.06.005, doi:10.1016/j.compchemeng.2006.06.005.

Curitiba Marcellos, C.F., Durand, H., Kwon, J.S.I., Gomes Barreto Jr, A., Laranjeira da Cunha Lage, P., Bezerra de Souza Jr, M., Secchi, A.R., Christofides, P.D., 2018. Optimal operation of batch enantiomer crystallization: From ternary diagrams to predictive control. AIChE Journal 64, 1618–1637.

Diab, S., Gerogiorgis, D.I., 2017. Process modeling, simulation, and technoeconomic evaluation of separation solvents for the continuous pharmaceutical manufacturing (CPM) of diphenhydramine. Organic Process Research & Development in press.

Eaton, J.W., Rawlings, J.B., 1990. Feedback control of chemical processes using on-line optimization techniques. Computers & chemical engineering 14, 469–479.

Eek, R.A., 1995. Control and dynamic modelling of industrial suspension crystallizers. Technische Universiteit Delft.

Elsner, M.P., Menendez, D.F., Muslera, E.A., Seidel-Morgenstern, A., 2005. Experimental study and simplified mathematical description of preferential crystallization. Chirality 17, S183–S195.

Figueiredo, C.S., 2016. Cinética de Crescimento de Siderita(FeCO3) e dissolução de Halita(NaCl) em Soluções de Água e MEG. Ph.D. thesis. Universidade Federal do Rio de Janeiro.

Gamez-Garci, V., Flores-Mejia, H., Ramirez-Muñz, J., Puebla, H., 2012. Dynamic optimization and robust control of batch crystallization. Procedia Engineering 42, 471–481.

Gedicke, K., Beckmann, W., Brandt, A., Sapoundjiev, D., Lorenz, H., Budde, U., Seidel-Morgenstern, A., 2005. Coupling chromatography and crystallization for efficient separations of isomers. Adsorption 11, 591–596.

Hindmarsh, A.C., Brown, P.N., Grant, K.E., Lee, S.L., Serban, R., Shumaker, D.E., Woodward, C.S., 2005. Sundials: Suite of nonlinear and differential/algebraic equation solvers. ACM Transactions on Mathematical Software (TOMS) 31, 363–396.

Hounslow, M., Reynolds, G., 2006. Product engineering for crystal size distribution. AIChE journal 52, 2507–2517.

Jacques, J., Collet, A., Wilen, S.H., 1981. Enantiomers, Racemates, and Resolutions. John Wiley & Sons, Inc., New York.

Jamialahmadi, M., Müller-Steinhagen, H., 2007. Heat exchanger fouling and cleaning in the dihydrate process for the production of phosphoric acid. Chem. Eng. Res. Des. 85, 245–255. URL: `https://doi.org/10.1205/cherd06050`, doi:`10.1205/cherd06050`.

Jones, A., 1974. Optimal operation of a batch cooling crystallizer. Chemical Engineering Science 29, 1075–1087.

Jones, A., Chianese, A., Mullin, J., 1984. Effect of fines destruction on batch cooling crystallization of potassium sulphate solutions. .

Jones, A.G., 2002. Crystallization process systems. Butterworth-Heinemann.

Jones, E., Oliphant, T., Peterson, P., et al., 2001. SciPy: Open source scientific tools for Python. URL: `http://www.scipy.org/`.

Kaasa, B., 1998. Prediction of pH, mineral precipitation and multiphase equilibria during oil recovery. Ph.D. thesis. Institutt for unorganisk kjemi, Norges teknisk-naturvitenskapelige universitet (NTNU).

Kaemmerer, H., Jones, M.J., Lorenz, H., Seidel-Morgenstern, A., 2010. Selective crystallisation of a chiral compound-forming system - Solvent screening, SLE determination and process design. Fluid Phase Equilibria 296, 192–205.

Kahaner, D., Lawkins, W., Thompson, S., 1989. On the use of rootfinding ode software for the solution of a common problem in nonlinear dynamical systems. Journal of computational and applied mathematics 28, 219–230.

Kail, N., Briesen, H., Marquardt, W., 2007. Advanced geometrical modeling of focused beam reflectance measurements (fbrm). Particle & Particle Systems Characterization 24, 184–192.

Karamertzanis, P.G., Anandamanoharan, P.R., Fernandes, P., Cains, P.W., Vickers, M., Tocher, D.A., Florence, A.J., Price, S.L., 2007. Toward the computational design of diastereomeric resolving agents: An experimental and computational study of 1-phenylethylammonium-2-phenylacetate derivatives. The Journal of Physical Chemistry B 111, 5326–5336.

Kaspereit, M., 2006. Separation of Enantiomers by a Process Combination of Chromatography and Crystallisation. Ph.D. thesis. Otto-von-Guericke-Universität Magdeburg.

Kleinitz, W., Dietzsch, G., Köhler, M., 2003. Halite scale formation in gas-producing wells. Chem. Eng. Res. Des. 81, 352–358. URL: https://doi.org/10.1205/02638760360596900, doi:10.1205/02638760360596900.

Koren, B., 1993. A robust upwind discretization method for advection, diffusion and source terms. Centrum voor Wiskunde en Informatica Amsterdam.

Kumar, S., Ramkrishna, D., 1996a. On the solution of population balance equations by discretization—i. a fixed pivot technique. Chemical Engineering Science 51, 1311–1332.

Kumar, S., Ramkrishna, D., 1996b. On the solution of population balance equations by discretization—ii. a moving pivot technique. Chemical Engineering Science 51, 1333–1342.

Kumar, S., Ramkrishna, D., 1997. On the solution of population balance equations by discretization—III. nucleation, growth and aggregation of particles. Chem. Eng. Sci. 52, 4659–4679. URL: https://doi.org/10.1016/s0009-2509(97)00307-2, doi:10.1016/s0009-2509(97)00307-2.

Kwon, J.S.I., Nayhouse, M., Christofides, P.D., Orkoulas, G., 2013. Protein crystal shape and size control in batch crystallization: comparing model predictive control with conventional operating policies. Industrial & Engineering Chemistry Research 53, 5002–5014.

Kwon, J.S.I., Nayhouse, M., Christofides, P.D., Orkoulas, G., 2014a. Modeling and control of crystal shape in continuous protein crystallization. Chemical Engineering Science 107, 47–57.

Kwon, J.S.I., Nayhouse, M., Orkoulas, G., Christofides, P.D., 2014b. Crystal shape and size control using a plug flow crystallization configuration. Chemical Engineering Science 119, 30–39.

Kwon, J.S.I., Nayhouse, M., Orkoulas, G., Ni, D., Christofides, P.D., 2015. Run-to-run-based model predictive control of protein crystal shape in batch crystallization. Industrial & Engineering Chemistry Research 54, 4293–4302.

Lasaga, A.C., 1998. Kinetic Theory in the Earth Sciences. Princeton University Press. URL: https://doi.org/10.1515/9781400864874, doi:10.1515/9781400864874.

Lee, G., Yoon, E.S., Lim, Y.I., Le Lann, J.M., Meyer, X.M., Joulia, X., 2001. Adaptive mesh method for the simulation of crystallization processes including agglomeration and breakage: the potassium sulfate system. Industrial & engineering chemistry research 40, 6228–6235.

Lemos, E., Secchi, A., Biscaia Jr, E., 2014. Implementation of galerkin and moments methods by gaussian quadrature in advection–diffusion problems with chemical reactions. Computers & Chemical Engineering 61, 156–174.

Lim, B.G., Ching, C.B., Tan, R.B., Ng, S.C., 1995. Recovery of (-)-praziquantel from racemic mixtures by continuous chromatography and crystallisation. Chemical engineering science 50, 2289–2298.

Liotta, V., Sabesan, V., 2004. Monitoring and feedback control of supersaturation using atr-ftir to produce an active pharmaceutical ingredient of a desired crystal size. Organic process research & development 8, 488–494.

Liu, Y., Wang, X., Wang, J.K., Ching, C.B., 2006. Investigation of the phase diagrams of chiral praziquantel. Chirality 18, 259–264.

Lorenz, H., Perlberg, A., Sapoundjiev, D., Elsner, M.P., Seidel-Morgenstern, A., 2006a. Crystallization of enantiomers. Chemical Engineering and Processing: Process Intensification 45, 863–873.

Lorenz, H., Polenske, D., Seidel-Morgenstern, A., 2006b. Application of preferential crystallization to resolve racemic compounds in a hybrid process. Chirality 18, 828–840.

Lorenz, H., Sapoundjiev, D., Seidel-Morgenstern, A., 2003. Solubility equilibria in chiral systems and their importance for enantioseparation. Engineering in Life Sciences 3, 132–136.

Lorenz, H., Seidel-Morgenstern, A., 2002. Binary and ternary phase diagrams of two enantiomers in solvent systems. Thermochimica Acta 382, 129–142.

Lorenz, H., Seidel-Morgenstern, A., 2014. Processes to separate enantiomers. Angewandte Chemie International Edition 53, 1218–1250.

Lorenz, H., Sheehan, P., Seidel-Morgenstern, A., 2001. Coupling of simulated moving bed chromatography and fractional crystallisation for efficient enantioseparation. Journal of Chromatography A 908, 201–214.

Luttge, A., Arvidson, R.S., Fischer, C., 2013. A stochastic treatment of crystal dissolution kinetics. Elements 9, 183–188. URL: `https://doi.org/10.2113/gselements.9.3.183`, doi:`10.2113/gselements.9.3.183`.

Mackay, E., 2003. Predicting in situ sulphate scale deposition and the impact on produced ion concentrations. Chem. Eng. Res. Des. 81, 326–332. URL: `https://doi.org/10.1205/02638760360596874`, doi:`10.1205/02638760360596874`.

Mao, S., 2012. Chiral Separation of Racemic Mandelic Acid by the Coupling Crystallization Process and Simulated Moving Bed Technology. Ph.D. thesis. The University of Western Ontario.

Mao, S., Zhang, Y., Rohani, S., Ray, A.K., 2010. Kinetics of (R, S)-and (R)-mandelic acid in an unseeded cooling batch crystallizer. Journal of Crystal Growth 312, 3340–3348.

Marchal, P., David, R., Klein, J., Villermaux, J., 1988. Crystallization and precipitation engineering—i. an efficient method for solving population

balance in crystallization with agglomeration. Chemical Engineering Science 43, 59–67.

Massot, M., Laurent, F., Kah, D., de Chaisemartin, S., 2010. A robust moment method for evaluation of the disappearance rate of evaporating sprays. SIAM J. Appl. Math. 70, 3203–3234. URL: https://doi.org/10.1137/080740027, doi:10.1137/080740027.

Masterton, W.L., Hurley, C.N., 2006. Chemistry: Principles and Reactions. fifth ed., Thomson Brooks/Cole, Belmont, California.

McConathy, J., Owens, M.J., 2003. Stereochemistry in drug action. The Primary Care Companion to the Journal of Clinical Psychiatry 5, 70–73.

Mesbah, A., Nagy, Z.K., Huesman, A.E., Kramer, H.J., Van den Hof, P.M., 2012. Nonlinear model-based control of a semi-industrial batch crystallizer using a population balance modeling framework. Control Systems Technology, IEEE Transactions on 20, 1188–1201.

Miller, S.M., Rawlings, J.B., 1994. Model identification and control strategies for batch cooling crystallizers. AIChE Journal 40, 1312–1327.

de Moraes, M.G., de Souza Jr, M.B., Secchi, A.R., 2018. Dynamics and MPC of an evaporative continuous crystallization process, in: Computer Aided Chemical Engineering. Elsevier. volume 43, pp. 997–1002.

Mullin, J., Nỳvlt, J., 1971. Programmed cooling of batch crystallizers. Chemical Engineering Science 26, 369–377.

Mullin, J.W., 2001. Crystallization. fourth ed., Butterworth-Heinemann, Woburn, Massachusetts.

Myerson, A., 2002. Handbook of industrial crystallization. Butterworth-Heinemann.

Nagy, Z., Aamir, E., Rielly, C., 2011. Internal fines removal using population balance model based control of crystal size distribution under dissolution, growth and nucleation mechanisms. Crystal growth & design 11, 2205–2219.

Nagy, Z.K., Braatz, R.D., 2012. Advances and new directions in crystallization control. Annual review of chemical and biomolecular engineering 3, 55–75.

Nagy, Z.K., Fevotte, G., Kramer, H., Simon, L.L., 2013. Recent advances in the monitoring, modelling and control of crystallization systems. Chemical Engineering Research and Design 91, 1903–1922.

Newmeyer, M.N., Concheiro, M., da Costa, J.L., Flegel, R., Gorelick, D.A., Huestis, M.A., 2015. Oral fluid with three modes of collection and plasma methamphetamine and amphetamine enantiomer concentrations after controlled intranasal l-methamphetamine administration. Drug Testing and Analysis 7, 877–883.

Newville, M., Stensitzki, T., Allen, D.B., Ingargiola, A., 2014. LMFIT: Non-linear Least-Square Minimization and Curve-Fitting for Python. URL: `https://doi.org/10.5281/zenodo.11813`, doi:`10.5281/zenodo.11813`.

Nguyen, L.A., He, H., Pham-Huy, C., 2006. Chiral drugs: an overview. International journal of biomedical science: IJBS 2, 85.

Nishinaga, T., 2014. Handbook of Crystal Growth: Fundamentals. Elsevier.

Nopens, I., Beheydt, D., Vanrolleghem, P.A., 2005. Comparison and pitfalls of different discretised solution methods for population balance models: a simulation study. Computers & chemical engineering 29, 367–377.

Novaes, M., Souza, J., Araújo, H., 1999. Síntese do anti-helmíntico praziquantel, a partir da glicina. Quim. Nova 22, 5–10.

Olliaro, P., Delgado-Romero, P., Keiser, J., 2014. The little we know about the pharmacokinetics and pharmacodynamics of praziquantel (racemate and R-enantiomer). Journal of Antimicrobial Chemotherapy 69, 863–870.

Pálovics, E., Faigl, F., Fogassy, E., 2012. Separation of the mixtures of chiral compounds by crystallization, in: Mastai, Y. (Ed.), Advances in Crystallization Processes. InTech.

Patience, D.B., Dell'Orco, P.C., Rawlings, J.B., 2004. Optimal operation of a seeded pharmaceutical crystallization with growth-dependent dispersion. Organic Process Research & Development 8, 609–615.

Prausnitz, J.M., Lichtenthaler, R.N., de Azevedo, E.G., 1998. Molecular thermodynamics of fluid-phase equilibria. Pearson Education.

Qamar, S., 2008. Modeling and simulation of population balances for particulate processes. Ph.D. thesis. Otto-von-Guericke-Universität Magdeburg, Universitätsbibliothek.

Qamar, S., Ashfaq, A., Angelov, I., Elsner, M., Warnecke, G., Seidel-Morgenstern, A., 2008. Numerical solutions of population balance models in preferential crystallization. Chemical Engineering Science 63, 1342–1352.

Qamar, S., Mukhtar, S., Seidel-Morgenstern, A., Elsner, M.P., 2009. An efficient numerical technique for solving one-dimensional batch crystallization models with size-dependent growth rates. Chemical Engineering Science 64, 3659–3667.

Quilaqueo, M., Aguilera, J.M., 2015. Dissolution of NaCl crystals in artificial saliva and water by video-microscopy. Food Res. Int. 69, 373–380. URL: https://doi.org/10.1016/j.foodres.2015.01.020, doi:10.1016/j.foodres.2015.01.020.

Ramkrishna, D., 2000. Population balances: Theory and applications to particulate systems in engineering. Academic press.

Randolph, A., Larson, M., 1988. Theory of Particulate Processes: Analysis and Techniques of Continuous Crystallization. Academic Press, San Diego.

Rawlings, J.B., Miller, S.M., Witkowski, W.R., 1993. Model identification and control of solution crystallization processes: a review. Industrial & Engineering Chemistry Research 32, 1275–1296.

Raymond, K.W., 2010. General Organic and Biological Chemistry: An Integrated Approach. third ed., John Wiley & Sons, Inc., Hoboken, New Jersey.

Rentsch, K.M., 2002. The importance of stereoselective determination of drugs in the clinical laboratory. Journal of biochemical and biophysical methods 54, 1–9.

Rohani, S., Haeri, M., Wood, H., 1999. Modeling and control of a continuous crystallization process part 2. model predictive control. Computers & chemical engineering 23, 279–286.

Sandengen, K., 2006. Prediction of mineral scale formation in wet gas condensate pipelines and in MEG (Mono Ethylene Glycol) regeneration plants. Ph.D. thesis. Norwegian University of Science and Technology.

Caciano de Sena, R., Soares, M., Pereira, M.L.O., Cruz Domingues da Silva, R., Ferreira do Rosário, F., Cajaiba da Silva, J.F., 2011. A simple method based on the application of a CCD camera as a sensor to detect low concentrations of barium sulfate in suspension. Sensors 11, 864–875. URL: https://doi.org/10.3390/s110100864, doi:10.3390/s110100864.

Shampine, L., Thompson, S., 2000. Event location for ordinary differential equations. Computers & Mathematics with Applications 39, 43–54.

Shekunov, B.Y., York, P., 2000. Crystallization processes in pharmaceutical technology and drug delivery design. Journal of Crystal Growth 211, 122–136.

Shen, J.X., Chiu, M.S., Wang, Q.G., 1999. A comparative study of model-based control techniques for batch crystallization process. Journal of chemical engineering of Japan 32, 456–464.

Shi, D., El-Farra, N.H., Li, M., Mhaskar, P., Christofides, P.D., 2006. Predictive control of particle size distribution in particulate processes. Chemical Engineering Science 61, 268–281.

Shi, D., Mhaskar, P., El-Farra, N.H., Christofides, P.D., 2005. Predictive control of particle size distribution in protein crystallization, in: American Control Conference, 2005. Proceedings of the 2005, IEEE. pp. 943–948.

Silva, A.d.P.d., de Oliveira, P.B., Bandini, T.B., Barreto Junior, A.G., de Sena, R.C., Silva, J.F.C.d., 2013. Low-cost system based on image analysis to determine solubility curves. Sens. Actuators, B 177, 1071–1074. URL: `https://doi.org/10.1016/j.snb.2012.11.097`, doi:`10.1016/j.snb.2012.11.097`.

Silva, L., Rodrigues, R., Mitre, J., Lage, P., 2010. Comparison of the accuracy and performance of quadrature-based methods for population balance problems with simultaneous breakage and aggregation. Computers & chemical engineering 34, 286–297.

Solsvik, J., Jakobsen, H.A., 2013. Evaluation of weighted residual methods for the solution of a population balance model describing bubbly flows: The least-squares, galerkin, tau, and orthogonal collocation methods. Industrial & Engineering Chemistry Research 52, 15988–16013.

Spicer, P.T., Chaoul, O., Tsantilis, S., Pratsinis, S.E., 2002. Titania formation by ticl 4 gas phase oxidation, surface growth and coagulation. Journal of Aerosol Science 33, 17–34.

Stoller, M., Orlandi, P., Leonardi, S., Chianese, A., 2008. Modelling of the fine crystals dissolution in an externally heated tube, in: Proceedings of 18th Symposium on Industrial Crystallization, Industrial Crystallization. pp. 14–17.

Ströhlein, G., Schulte, M., Strube, J., 2003. Hybrid processes: Design method for optimal coupling of chromatography and crystallization units. Separation Science and Technology 38, 3353–3383.

Subramanian, G. (Ed.), 2007. Chiral Separation Techniques: A Practical Approach. third ed., Wiley-VCH, Weinheim, Germany.

Swernath, S., 2013. Design and Control of Combined Chemical Processes for the Production of Pure Enantiomers. Ph.D. thesis. Otto-von-Guericke-Universität Magdeburg.

Tseng, Y.T., Ward, J.D., 2017. Comparison of objective functions for batch crystallization using a simple process model and Pontryagin's minimum principle. Computers & Chemical Engineering 99, 271–279.

Tung, H.H., Paul, E.L., Midler, M., McCauley, J.A., 2009. Crystallization of organic compounds: an industrial perspective. John Wiley & Sons.

Wächter, A., Biegler, L.T., 2006. On the implementation of an interior-point filter line-search algorithm for large-scale nonlinear programming. Mathematical Programming 106, 25–57.

Walther, A., Griewank, A., 2012. Getting started with ADOL-C., in: Naumann, U., Schenk, O. (Eds.), Combinatorial Scientific Computing, CRC Press, Boca Raton, Florida. pp. 181–202.

Williamson, J.H., 1980. Low-storage Runge-Kutta schemes. Journal of Computational Physics 35, 48–56.

Witkowski, W., Rawlings, J., 1987. Modelling and control of crystallizers, in: American Control Conference, 1987, IEEE. pp. 1400–1405.

Worlitschek, J., Mazzotti, M., 2004. Model-based optimization of particle size distribution in batch-cooling crystallization of paracetamol. Crystal Growth & Design 4, 891–903.

Worlitschek, J.R.G., 2003. Monitoring, modeling and optimization of batch cooling crystallization. Ph.D. thesis. Diss., Eidgenössische Technische Hochschule ETH Zürich, Nr. 15189, 2004.

Yang, X., Wong, S.Y., Bwambok, D.K., Atkinson, M.B.J., Zhang, X., Whitesides, G.M., Myerson, A.S., 2014. Separation and enrichment of enantiopure from racemic compounds using magnetic levitation. Chemical Communications 50, 7548–7551.

Yinghong, L., 2009. Application of preferential crystallization for racemic compound integrating thermodynamics, kinetics and optimization. Ph.D. thesis.

Zemaitis, J.F., Clark, D.M., Rafal, M., Scrivner, N.C., 1986. Handbook of Aqueous Electrolyte Thermodynamics. John Wiley & Sons, Inc. URL: `https://doi.org/10.1002/9780470938416`, doi:`10.1002/9780470938416`.

Zhang, G., Rohani, S., 2003. On-line optimal control of a seeded batch cooling crystallizer. Chemical Engineering Science 58, 1887–1896.

Zhang, Y., Mao, S., Ray, A.K., Rohani, S., 2010. Nucleation and growth kinetics of (R)-mandelic acid from aqueous solution in the presence of the opposite enantiomer. Crystal Growth & Design 10, 2879–2887.

Appendix A

Crystallization of Enantiomeric Systems

Enantiomers are stereoisomers with mirror images that do not overlap. Pairs of enantiomers have identical physicochemical properties, except the ability to rotate the plane of polarized light, which are the same, but with opposite direction (Lorenz et al., 2006a).

The enantiomer that rotates the polarized light clockwise is classified by (+) or dextrorotatory (d), by the other hand, the one that rotates anticlockwise is referred to as (-) or levorotatory (l). The D/L classification is often applied to amino acids and sugars, where L have the hydroxyl group on the left side of the asymmetric carbon furthest from the carbonyl group, whereas the D are those with the hydroxyl grouping on the right side (Lorenz et al., 2006a).

Another classification is using R (or *rectus*) and S (or *sinister*). The enantiomers in this case are defined from a group prioritization procedure (Tung et al., 2009). It is also customary to distinguish the enantiomers simply according to the purpose, the one of interest being referred to as *preferential* and the other as unwanted (counter).

Enantiomers are commonly classified into three types in relation to the type of crystal formed:

- Racemic compounds (heterochiral): correspond of about 90 to 95% of all enantiomeric systems. The crystal formed consists of the homogeneously distributed mixture of both enantiomers in equal ratio (1:1);
- Racemic conglomerates (homochiral): refers to the physical mixing of the pure crystals of each enantiomer, which crystallize independently
- Pseudoracemates (solid solution): such systems are unusual and occur when the enantiomers crystallize in any ratio between them in the solid structure.

Lorenz et al. (2001) studied the coupling of the enantiomeric enrichment via SMB with the fractional crystallization. The (+) and (-) mandelic acid system was evaluated in the aqueous solvent in order to obtain simplified models capable of providing the relationship between productivity and purity.

Lorenz et al. (2006b) have empirically demonstrated the application of the preferential crystallization to the separation of crystals from the enantiomer of interest. Cyclic steps are exemplified from mandelic acid to effect preferential crystallization in the region of two solid phases. The experiments carried out showed for the first time the viability of the preferential crystallization for the resolution of racemic solid systems.

Yinghong (2009) evaluated the crystallization of two systems: mandelic acid and ketoprofen. The study included the evaluation of solubility, metastable zone limit, crystallization kinetics and supersaturation control. They used simplified models and polynomial adjustments to follow the process. Cyclic preferential crystallization was not implemented. They evaluated isolated batches of the system operating in the region of pure solid with possible entrances in the region of two solids when the final temperature reduced.

Crystallization of Racemic Compound Forming System

The racemic compounds forming systems have thermodynamic constraints relative to the compositions and system temperature to define the amount and types of solid phases generated. One approach that allows the understanding and evaluation of this behavior is by the use of phase diagram, generally represented in a ternary diagram, since the systems usually are formed by the enantiomer pair and a solvent, which can also be a mixture.

The figure A.1 confronts the ternary diagram of the two enantiomeric systems: conglomerate and racemic solid. In the first, there are two regions in which occur the formation of pure crystals and a saturated solution (***a*** e ***a'***); a region of three phases contemplating the mixture of pure crystals of each enantiomer and a solution with eutectic concentration (***b***); and the region ***c*** where there is no formation of solids (can occur dissolution if solids are present). The point ***E*** refers to the eutectic composition.

The second diagram of Figure A.1 shows that racemic compound forming system have a more complex phase diagram behavior. In this case, there are three regions with two phases, two three-phase regions and a single-phase region. Regions ***a*** and ***a'*** originate pure solids and saturated solution, whereas the region *c* provides racemic solid (*rac*) and saturated solution. The regions of ***b*** and ***b'*** generate two solid phases: pure solid and racemic solid. This region also form a saturated solution

of eutectic composition. The point ***M*** corresponds to the saturation composition with the maximum fraction of the solvent for a given temperature.

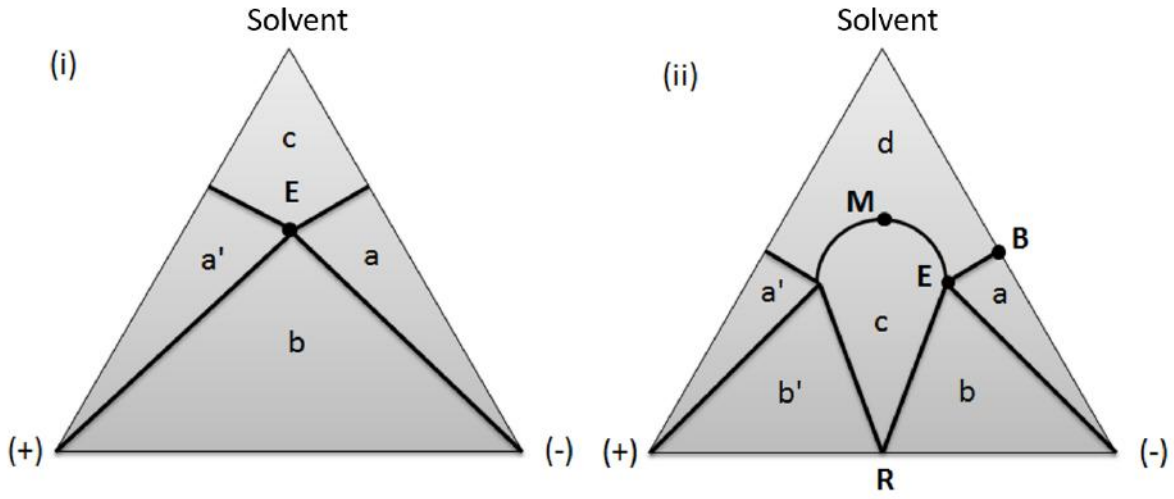

Figure A.1: Ternary diagram for enantiomeric system with formation of conglomerate (i) and racemic solid (ii).

The formation of crystals for racemic compound forming system can be exemplified by Figure A.2, with the (-) enantiomer as the preferential and the (+) enantiomer being the counter. In the region ***a***, the saturation of the system depends on the point of operation ***P***, on the temperature (which defines the eutectic point ***E*** and on a curve that describe the solubility from the eutectic composition to point ***B***, which is the solubility for a solution free of the undesirable enantiomer. The saturation, represented by $\mathbf{S_a^p}$, can be obtained by the intersection of the line $\overline{(-)\mathbf{P}}$ with the solubility curve from from ***E*** to ***B***. This solubility curve is described by the Schröder van Laar equation (present in next section). For racemic solids having a high enantiomeric ratio eutectic point, such a curve can be approximated by the straight line $\overline{\mathbf{EB}}$.

Figure A.2 also illustrates the crystallization operating in region ***b***. As there are two stable solids in this situation, starting in a composition ***P'***, the system is supersaturated with respect to the pure solid of (-) and racemic solid (*rac*). The saturation for the racemic solid ($\mathbf{S_b^{rac}}$) is determined by the intersection of the straight line $\overline{\mathbf{RP'}}$ with the dividing line between the regions ***a*** and ***b***: line $\overline{(-)\mathbf{E}}$. Furthermore, the saturation for the pure solid ($\mathbf{S_b^p}$) is obtained by the intersection of the line $\overline{(-)\mathbf{P'}}$ with the line $\overline{\mathbf{RE}}$. The region ***c*** generates racemic solid and liquid solution given by the intersection of the line connecting the operating composition with the point ***R*** and the solubility curve given by the equation of Prigogine-Defay.

Another definition obtained by the ternary diagram of racemic solids refers to the fraction obtained of pure solid and of racemic solid when operating in the three-phase

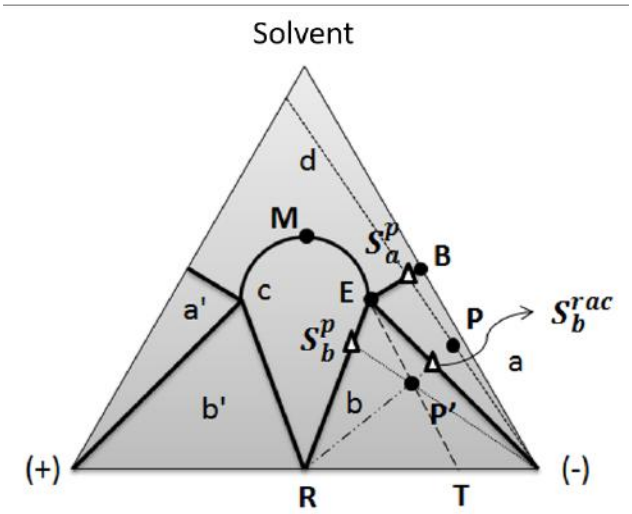

Figure A.2: Saturation compositions based on the ternary diagram for enantiomeric system with formation of racemic solid.

region ***b***. The tie line given by the straight line $\overline{\mathbf{EP}'}$ gives the relationship between the solid phases formed when equilibrium is reached. Denominating the difference of composition of the preferential enantiomer between the points ***R*** and ***T*** of $dist_{RT}$ and the difference of composition for the preferential from points ***R*** to **(-)** as $dist_{R(-)}$, the fraction of pure solid (-) obtained ($w_{TIE}^{(p)}$) is given by Eq. A.1.

$$w_{TIE}^{(p)} = \frac{dist_{RT}}{dist_{R(-)}} \tag{A.1}$$

In the region ***b***, the path to the equilibrium composition varies according to the initial composition, to the degree of supersaturation imposed, to the form of seeding, and to the crystals growth and nucleation kinetics. Generally, when seeding the system with a certain type of solid, there is an initial selectivity in crystal formation. Thus, the trajectory in the ternary diagram will tend to reduce in a higher rate the composition of the component forming such a solid.

Figure A.3 illustrates two cases of seeding with pure crystals of (-) and with racemic solid (*rac*). For the first, there is a tendency to reduce the (-) component in the liquid phase, but there is an instant in which nucleus occurs followed by the nuclei growth. This leads the system to the eutectic point. Similarly, when seeding with racemic crystals in the condition at point P there is initially a favored formation of *rac* solid, but after reduction of its supersaturation, there is an instant at which the pure crystal of (-) begins its formation leading to the eutectic point ***E***.

The preferred racemic solid crystallization addressed by Lorenz et al. (2006b) is illustrated in Figure A.4. Starting at the eutectic composition for a given temperature T_0 and cooling the system to reach a temperature T_c, being $T_0 - T_c$

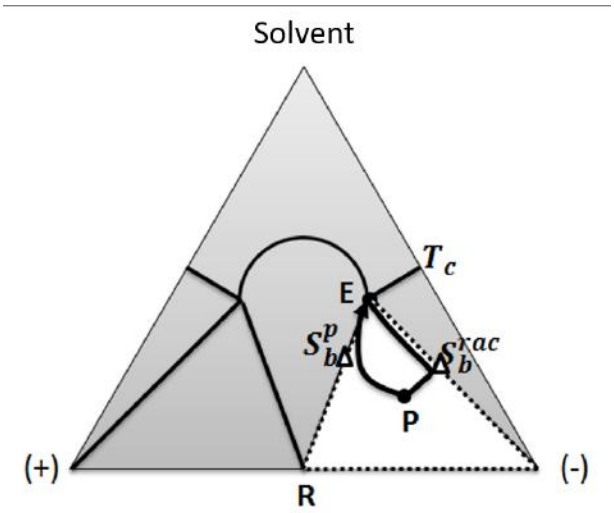

Figure A.3: Preferential pathways of crystallization dependent on crystal seeding.

smaller than the metastable limit of spontaneous nucleation of the solids, the system is in the region of three phases ***b*** (Figure A.4-i).

Applying pure (-) seeds the system tends to form only crystals of the preferred, so that the composition of the liquid phase makes the path represented by Figure A.4-ii. Before nucleation of the racemic solid occurs, crystallization is discontinued and the solid is collected. This is followed by the addition of eutectic composition solution. Thus, the system follows the trajectory represented in the condition (iii) of the figure. The next step is the seeding of pure (*rac*), which forces its own crystallization to the detriment of forming solid (-), as presented in condition (iv). Finally, the crystals of *rac* are collected and a solution of eutectic composition is added again, bringing the system back (or approximately) to the initial point *A*.

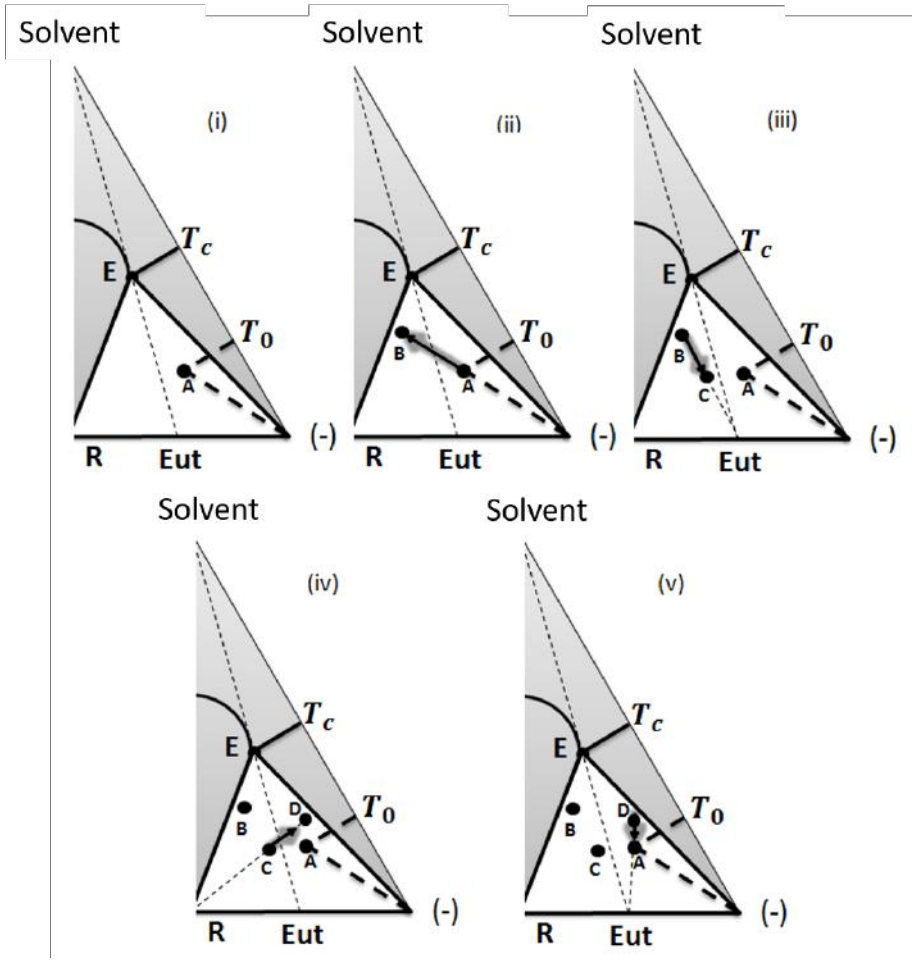

Figure A.4: Preferential crystallization of racemic solids.

Solid-liquid Equilibrium for the Racemic Compound Forming System

As discussed, the enantiomers of racemic solids can crystallize in two ways: pure crystals of the richest enantiomer in the solution and the crystallization of the racemic solid (crystal mixing). For the first case, the equation of Schröder van Laar (Eq. A.2) is used, which relates the saturation composition to the system temperature.

$$\ln \mathrm{x}_i \gamma_i = \frac{\Delta_{fus} h_i}{R} \left(\frac{1}{T_{m,i}} - \frac{1}{T} \right) \tag{A.2}$$

wherein $\Delta_{fus} h_i$ and $T_{m,i}$ are the enthalpy per mol and the melting temperature of an enantiomer i. Such parameters are usually evaluated with the use of Differential Scanning Calorimetry (DSC) (Liu et al., 2006).

In the case of crystallization of racemic solids the phase equilibrium can be represented by the Prigogine-Defay equation (Eq. A.3).

$$\ln\left(4\mathrm{x}_i\gamma_i\mathrm{x}_2\gamma_2\right) = \frac{2\Delta_{fus}h_{rac}}{R}\left(\frac{1}{T_{m,rac}} - \frac{1}{T}\right) \tag{A.3}$$

where $\Delta_{fus}h_{rac}$ and $T_{m,rac}$ are the enthalpy per mol and the melting temperature of the racemic solid.

Such equations are originally formulated for the description of binary system, however, considering optically inactive solvent, they can be applied to the formulation of the ternary diagram Lorenz and Seidel-Morgenstern (2002).

The coefficient of activity can be obtained via the non-random two liquids approach (NRTL) neglecting terms of interactions higher than the second order. The equation of the NRTL for system with m components is in the form of Eq. A.4 (Worlitschek, 2003).

$$\ln\gamma_i = \frac{\sum_{j=1}^{m}\tau_{ji}G_{ji}\mathrm{x}_j}{\sum_{l=1}^{m}G_{li}\mathrm{x}_l} + \sum_{j=1}^{m}\frac{\mathrm{x}_jG_{ij}}{\sum_{l=1}^{m}G_{lj}\mathrm{x}_l}\left(\tau_{ij} - \frac{\sum_{r=1}^{m}\tau_{rj}G_{rj}\mathrm{x}'_r}{\sum_{l=1}^{m}G_{lj}\mathrm{x}_l}\right) \tag{A.4}$$

$$G_{ji} = \exp(-\alpha_{ji}\tau_{ji}) \tag{A.5}$$

$$\tau_{ji} = \frac{g_{ji} - g_{ii}}{RT} \tag{A.6}$$

In a general sense, the NRTL considers: $\tau_{ii} = 0$, $G_{ii} = 1$, $\alpha_{ji} = \alpha_{ij}$ and $\Delta g_{ji} = g_{ji} - g_{ii}$ independent of temperature. According to Worlitschek (2003), for the ternary enantiomeric systems, in a general approach, further simplifications can be applied (Eq. A.7). Eq. A.7a to A.7c consider that the non-linearities between the solvent ($i = 3$) and each enantiomer ($i = 1, 2$) are equal; those considerations results in Eq. A.7d and A.7e; Eq. A.7f and A.7g are consequence of considering ideal liquid solution behavior of the enantiomers interactions.

$$\tau_{13} = \tau_{23} \tag{A.7a}$$

$$\tau_{31} = \tau_{32} \tag{A.7b}$$

$$\alpha_{13} = \alpha_{23} = \alpha_{31} = \alpha_{32} = \alpha \tag{A.7c}$$

$$G_{13} = G_{23} \tag{A.7d}$$

$$G_{31} = G_{32} \tag{A.7e}$$

$$\tau_{12} = \tau_{21} = 0 \tag{A.7f}$$

$$G_{12} = G_{21} = 1 \tag{A.7g}$$

In view of such considerations, one must specify three parameters for the solution

of the NRTL equation: α, ($\Delta g_{13} = \Delta g_{23}$) e ($\Delta g_{31} = \Delta g_{32}$). These simplifications provide an equal activity coefficient for the pair of enantiomers in solution.

Obtaining the ternary diagram depends on the knowledge of the eutectic composition. This can be determined by the intersection between the solubility curve of the racemic solid and the solubility curve for the pure solid of the preferred enantiomer. Given the parameters of the NRTL (or other method for calculating activity coefficient), the enthalpy and the melting temperature of the involved solids, the eutectic point can be calculated by the equation system (Eq. A.8) obtained from Eqs. A.2 and A.3 with γ_i given from Eq. A.4.

$$\begin{cases} 4\mathrm{x}_1\gamma_1\mathrm{x}_2\gamma_2 - \exp\left[\dfrac{2\Delta_{fus}h_{rac}}{R}\left(\dfrac{1}{T_{m,rac}} - \dfrac{1}{T}\right)\right] = 0 \\ \mathrm{x}_1 - 1/\gamma_1 \exp\left[\dfrac{\Delta_{fus}h_1}{R}\left(\dfrac{1}{T_{m,1}} - \dfrac{1}{T}\right)\right] = 0 \end{cases} \tag{A.8}$$

Appendix B

Rectangular and equilateral Ternary diagram

The literature for enantiomer mixtures generally uses equilateral triangle ternary diagrams to describe the solution thermodynamics. The mixture composition axes in such a diagram are along each side of the triangle, rather than on a Cartesian scale. The right triangle representation, on the other hand, uses Cartesian coordinates, with the mass fraction of two different components of the ternary mixture increasing along the x and y axes respectively, and the origin representing 100% of the third component. Converting an equilateral triangle ternary diagram to a right triangle form is straightforward, as it only involves obtaining the compositions of the two enantiomers and solvent from the equilateral triangle ternary diagram and then plotting the compositions on the Cartesian coordinate axes described above, and drawing appropriate phase boundaries through the compositions in the right triangle form that correspond to phase boundaries in the equilateral triangle form. In this section of the Appendix, the geometric relationships for ternary diagrams are reviewed, which allow ready transformation between the points on an equilateral triangle ternary diagram (in Cartesian coordinates) and the points on a right triangle form ternary diagram (in Cartesian coordinates). This relationship facilitates conclusions regarding the form of the phase boundaries in a right triangle ternary diagram by looking at the more commonly published equilateral triangle ternary diagram data.

We first note that if an equilateral triangle ternary diagram is presented on Cartesian coordinate axes, it takes the form given in Figure B.1. A point P' has mass fractions $w_R = w_R^{P'}$, $w_S = w_S^{P'}$, and $w_W = w_W^{P'}$ from reading the ternary diagram. This same point P' also has a representation in (x, y) coordinates on the Cartesian coordinate axes that the plot is on. This Cartesian representation is obtained by using the fact that this ternary diagram is equilateral and that the lines of constant composition are parallel to the side opposite the corner giving 100% of

the component, so that any point P' on the ternary diagram can be represented as shown in Figure B.2 (where P' is represented by point **C**). Taking advantage of the fact that Figure B.2 contains an equilateral triangle **FCE** adjoining an isosceles trapezoid **ABCF**, the geometry of the triangle **ABE** can be represented as shown in Figure B.3.

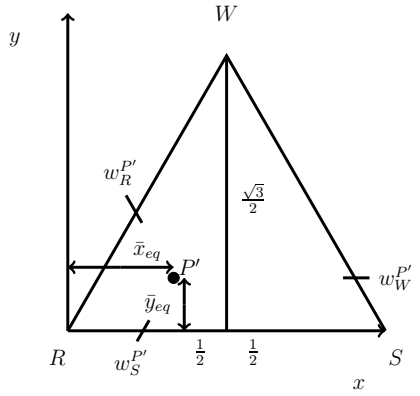

Figure B.1: Point P' in an equilateral triangle ternary diagram displayed on Cartesian coordinate axes.

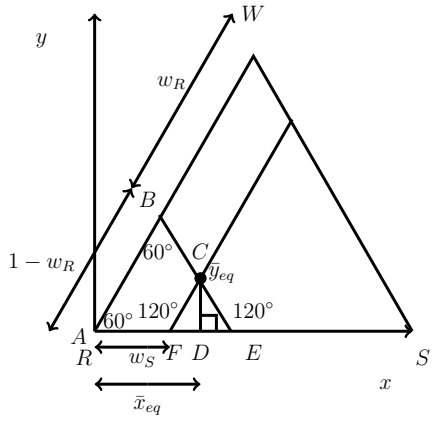

Figure B.2: Geometric relationships applied to the equilateral ternary diagram from Figure B.1.

From standard geometric relationships for the triangle in Figure B.3, the following relationships are obtained:

$$cos(60°) = \frac{\bar{x}_{eq} - w_S}{h_1} \tag{B.1}$$

$$sin(60°) = \frac{\bar{y}_{eq}}{h_1} \tag{B.2}$$

$$cos(60°) = \frac{a_1}{w_S} \tag{B.3}$$

$$2a_1 + h_1 = 1 - w_R \tag{B.4}$$

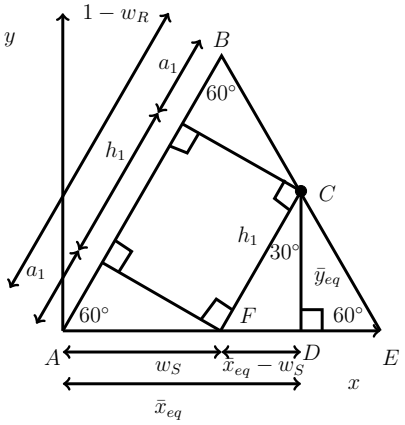

Figure B.3: Geometric relationships applied to triangle **ABE** from Figure B.2.

Solving for $\bar{x}_{eq}$ and $\bar{y}_{eq}$ in terms of w_S and w_R then gives the following transformation:

$$\hat{x}_{eq} = \begin{bmatrix} \bar{x}_{eq} \\ \bar{y}_{eq} \end{bmatrix} = \underbrace{\begin{bmatrix} -\frac{1}{2} & \frac{1}{2} \\ -\frac{\sqrt{3}}{2} & -\frac{\sqrt{3}}{2} \end{bmatrix}}_{A} \underbrace{\begin{bmatrix} w_R \\ w_S \end{bmatrix}}_{\overline{w}} + \underbrace{\begin{bmatrix} \frac{1}{2} \\ \frac{\sqrt{3}}{2} \end{bmatrix}}_{b_{eq}} \tag{B.5}$$

which can be written as $\hat{x}_{eq} = A\overline{w} + b_{eq}$. The coordinates $(\bar{x}_{eq}, \bar{y}_{eq})$ represent the Cartesian coordinates of a point on the equilateral triangle ternary diagram. On the alternative ternary diagram representation, the right triangle ternary diagram, $(\bar{x}_{rt}, \bar{y}_{rt})$ represent the Cartesian coordinates. As shown in Figure B.4, the values of $(\bar{x}_{rt}, \bar{y}_{rt}) = (w_R, w_S)$ in this representation. This means that when (w_R, w_S) data is known for a given system, it can be readily plotted on Cartesian coordinate axes using either Eq. B.5 to obtain an equilateral triangle form or $(\bar{x}_{rt}, \bar{y}_{rt}) = (w_R, w_S)$ for a right triangle form. Furthermore, given $\hat{x}_{eq} = A\overline{w} + b_{eq}$, $\hat{x}_{rt} = [\bar{x}_{rt}, \bar{y}_{rt}]^T$ can be determined from $[\bar{x}_{rt}, \bar{y}_{rt}]^T = [w_R, w_S]^T = A^{-1}(\hat{x}_{eq} - b_{eq})$. The implication of the relationship between $(\bar{x}_{eq}, \bar{y}_{eq})$ and $(\bar{x}_{rt}, \bar{y}_{rt})$ is that if a phase boundary in the equilateral triangle ternary diagram is a straight line (i.e., along this boundary, $\bar{y}_{eq}$ is linearly related to $\bar{x}_{eq}$), then $\bar{y}_{rt}$ will be linearly dependent on $\bar{x}_{rt}$ along the phase diagram in the right triangle ternary diagram. This shows that some important features of a right triangle ternary diagram may be inferred from an equilateral triangle ternary diagram without the need to plot all points, which can be used to determine the shapes of curves like the solubility curve used in this paper in a right triangle ternary diagram, given data in equilateral triangle form as it is commonly reported in the literature.

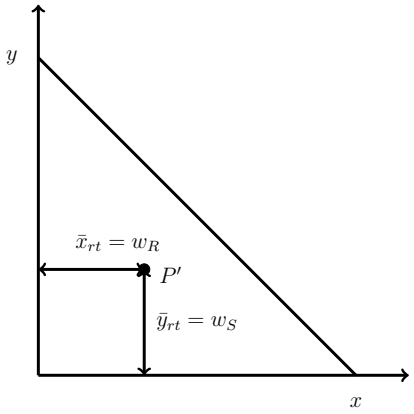

Figure B.4: Right triangle ternary diagram representation of point P' from Figure B.1.

Appendix C

Mixing Rule in ternary diagram

Eq. 5.1 is developed from mass conservation principles. Specifically, the mass fraction of species j in a mixture (w_j^{mix}) of a mass p at a given composition w_j^p with another mass q at composition w_j^q in a mass ratio $k = \frac{q}{p}$ has the mass fraction calculated by:

$$w_j^{mix} = \frac{w_j^p + k w_j^q}{1 + k} \tag{C.1}$$

This relationship can be used to express every initial composition within the two-phase region at a given temperature as a weighted sum of the mass fraction of pure R ($w_R = 1$) and the mass fraction of R in the saturated liquid in equilibrium with solid R at the given temperature given the initial composition. This does not imply that the original point in the two-phase region is a mixture of pure R and a saturated solution; at thermodynamic equilibrium, only the two separate phases would be observed. However, the initial composition (the mixture composition in Eq. C.1) represents the composition of the liquid mixture that would be obtained if the temperature of the mixture was changed in a way that brought the initial composition in the two-phase region to be only a liquid phase.

To demonstrate the use of the mixing rule for Figure 5.1, it is noted that at T_0, the composition $w_R^{\overline{\mathbf{RP}}}$ (defined to be an initial composition within the two-phase region on the line $\overline{\mathbf{RP}}$) can be represented as a mixture with a mass ratio k of pure R with a liquid of composition $\mathbf{P}$:

$$w_R^{\overline{\mathbf{RP}}} = \frac{w_R^{\mathbf{P}} + k}{1 + k} \tag{C.2}$$

where $w_R^{\mathbf{P}}$ represents the mass fraction of R at $\mathbf{P}$ and the equation follows from Eq. C.1 since the mass fraction of R at point $\mathbf{R}$ ($w_R^{\mathbf{R}}$) is 1. Similarly, the composition of S on line $\overline{\mathbf{RP}}$ ($w_S^{\overline{\mathbf{RP}}}$) can be represented by:

$$w_S^{\overline{\mathbf{RP}}} = \frac{w_S^{\mathbf{P}}}{1 + k} \tag{C.3}$$

since the mass fraction of S at point $\mathbf{R}$ ($w_S^{\mathbf{R}}$) is zero. Solving Eqs. C.2-C.3 for k, setting the two expressions for k equal, and solving the resulting expression for $w_R^{\overline{\mathbf{RP}}}$ gives Eq. 5.1.

We can examine the principle of conservation of mass within the ternary diagram as compositions change along the line $\overline{\mathbf{RP}}$ during cooling of a mixture through a numerical example. If there is a starting composition $\mathbf{P}$ at T_0 with 279.1 g of R, 43.5 g of S and a total mass of 1 kg ($w_R = 0.279$, $w_S = 0.0435$, and $w_W = 0.678$) and considering that this solution is cooled to T_1 and as a result loses 100 g of R due to crystallization of pure R with constant S and solvent mass in the liquid phase, the composition of the saturated liquid phase in equilibrium with solid R at T_1 is given in Figure 5.1 by $\mathbf{Q}$ ($w_R = 0.20$, $w_S = 0.048$, and $w_W = 0.752$).

Appendix D

Derivation of yield for Racemic Compound Forming System

In the following, Eqs. 5.8 and 5.9 are derived with mass balances defined using the total liquid mass L, the total solid mass C, the liquid mass fraction of species j (w_j) and the solid mass fraction of species j (v_j) for $j = R,\ S,\ W$ representing the R enantiomer, S enantiomer and solvent, respectively. Also, the superscripts i and f on these quantities designate the values of these quantities at the initial and final batch times. Assuming that there is no transformation of one species to another, the following species and total mass balances can be written:

$$L^i w_R^i + C^i v_R^i = L^f w_R^f + C^f v_R^f \tag{D.1}$$

$$L^i w_S^i + C^i v_S^i = L^f w_S^f + C^f v_S^f \tag{D.2}$$

$$L^i + C^i = L^f + C^f \tag{D.3}$$

Multiplying Eq. D.3 by w_R^f and substituting $L^f w_R^f$ from Eq. D.1, the following expression for C^f is obtained:

$$C^f = \frac{(C^i v_R^i - C^i w_R^f - L^i w_R^f + L^i w_R^i)}{(v_R^f - w_R^f)} \tag{D.4}$$

If it is considered that all solid mass is only R enantiomer ($v_R^i = v_R^f = 1$ and $v_S^i = v_S^f = 0$), Eq. D.4 becomes:

$$C^f = C^i + L^i \frac{(w_R^i - w_R^f)}{1 - w_R^f} \tag{D.5}$$

The mass of solid crystallized during the crystallization process is $C_{form} = C^f -$

C^i. Hence, with $L_R^i = w_R^i L^i$ and Eq. D.5, the crystal yield will be:

$$Y_c = \frac{C_{form}}{L_R^i} = \frac{1}{w_R^i} \frac{(w_R^i - w_R^f)}{1 - w_R^f} \tag{D.6}$$

During the batch crystallization, with only pure R crystals being formed, mass balances on R and S provide the following relations:

$$w_R^f = \frac{w_R^i L^i - C_{form}}{L^f} \tag{D.7}$$

$$w_S^f = \frac{w_S^i L^i}{L^f} \tag{D.8}$$

Solving these equations for L^f and setting them equal gives:

$$\frac{w_R^i L^i - C_{form}}{w_R^f} = \frac{w_S^i L^i}{w_S^f} \tag{D.9}$$

By dividing both sides of Eq. D.9 by $w_R^i L^i$, the definition of the yield Y_c (Eq. D.6) appears in the equation, and the resulting equation can be solved for Y_c to give:

$$Y_c = \frac{w_S^f w_R^i - w_R^f w_S^i}{w_S^f w_R^i} \tag{D.10}$$

From Eq. 5.5, $P^i = \frac{w_R^i}{w_R^i + w_S^i}$ and $P^f = \frac{w_R^f}{w_R^f + w_S^f}$, so these equations can be solved for w_S^i and w_S^f and the resulting expressions substituted into Eq. D.10 to give Eq. 5.8. To obtain Eq. 5.9, Eq. D.6 and Eq. 5.8 are equated.

Appendix E

Mass balance Equation for the enantioselective crystallizer

This derivation is also discussed in Section 2.2.1. In this section, an alternative approach is presented. Eq. 5.17 is derived by considering the volume of a single crystal of size l ($V_{1c}(l)$), given by:

$$V_{1c}(l) = k_V l^3 \tag{E.1}$$

The mass of a single particle of size l will be:

$$m_{1c}(l) = \rho_c V_{1c}(l) = \rho_c k_V l^3 \tag{E.2}$$

The total mass of all crystals in the crystallizer at time t is $m_c(t)$:

$$m_c(t) = \int_0^\infty m_{1c}(l) m_W(t) n(t,l) dl \tag{E.3}$$

The change in the total crystal mass with time is:

$$\frac{dm_c}{dt} = \int_0^\infty \rho_c k_V l^3 \frac{\partial (m_W(t) n(t,l))}{\partial t} dl \tag{E.4a}$$

$$= \int_0^\infty \rho_c k_V l^3 \left[m_W \frac{\partial n}{\partial t} + n \frac{dm_W}{dt} \right] dl \tag{E.4b}$$

Substituting Eq. 5.12 into Eq. E.4b gives:

$$\begin{aligned}
&\frac{dm_c}{dt} = \int_0^\infty \rho_c k_V l^3 \left[m_W \left(-\frac{\partial(Gn)}{\partial l} + B_0 \delta(l - l_{min}) - n \frac{d}{dt} \ln m_W + \right.\right. \\
&\left.\left. \frac{1}{m_W} [n_{in} \dot{m}_{W,in} - n_{out} \dot{m}_{W,out}] \right) + n \frac{dm_W}{dt} \right] dl \\
&= \rho_c k_V \int_0^\infty \left[-l^3 m_W \frac{\partial(Gn)}{\partial l} + l^3 m_W B_0 \delta(l - l_{min}) - n l^3 m_W \frac{d}{dt} \ln m_W + \right. \\
&\left. l^3 n_{in} \dot{m}_{W,in} - l^3 n_{out} \dot{m}_{W,out} + l^3 n \frac{dm_W}{dt} \right] dl
\end{aligned} \tag{E.5}$$

Simplifying by canceling terms, performing the integral for the term containing B_0, and using $n_{in} = 0$ gives:

$$\frac{dm_c}{dt} = \rho_c k_V \int_0^\infty \left[-l^3 m_W \frac{\partial(Gn)}{\partial l} - l^3 n_{out} \dot{m}_{W,out} \right] dl \tag{E.6}$$

When there is no fines dissolution loop (i.e., $\dot{m}_{W,out} = 0$), integrating Eq. E.6 by parts gives that the change in the total mass of crystals in the crystallizer with time, which is equal to the rate at which mass is entering the crystal phase, is the result of Eq. 5.17. When the fines dissolution loop is included, Eq. E.6 represents the change in the total mass of crystals in the crystallizer due to both the growth of the crystals (corresponding to the first term on the right-hand side) and the exit of fines through the fines trap (corresponding to the second term on the right-hand side). Because Eq. 5.17 represents only the rate at which mass exits the liquid phase to grow the crystals, integrating the first term on the right-hand side of Eq. E.6 again results in Eq. 5.17.

Appendix F

State vector definition for the Moving Sectional Method bin addition

In Kumar and Ramkrishna (1997) it is suggested the bins addition scheme for taking the nucleation into account when using the MSM and indicates the need of renumbering of old bins as an increasing sequence of integers. In this section an efficient numerical strategy to apply the bins addition is demonstrated that is suitable for computational implementation.

The dynamic simulation using Eq. 2.66 uses at initial time a mesh grid with a total of $r_{x,0}$ bins in which the initial values for x_i, l_i and N_i are defined. During the simulation new bins are added to the grid at the critical size to include the nucleation mechanism. Moreover, new bins can also be needed to be added at larger sizes depending on the process, such as with classified larger particle feeding. Another scenario is a process with particle disappearing due to dissolution, in that case it is convenient to remove bins smaller than the critical size, since they are not stable and should be discounted from the overall PSD. Thus, at a given simulation time the grid will contain a defined number of active bins denoted as r_x.

In order to consider the cases with bins addition both at smallest and at largest sizes, as well as the possible removal of particles due to dissolution a strategy using an augmented state sequence $\tilde{y}$ is demonstrated. In this approach it is defined active states associated with the active bins used at a given simulation time and also nonactive states that are not being used by the dynamic model. Both set of states are contained in the augmented state sequence. The strategy adopted consists in the selection the active states at certain t based on the process condition that should be used in the dynamic integration. An approach to accomplish this is demonstrated as follows.

It is considered that the augmented state sequence $\tilde{y}$ is defined using all the initial condition states and also states related to bins to be included along the simulation. The initial condition states are the discretized bins states $x_i(t_0)$, $l_i(t_0)$ and $N_i(t_0)$ and states that are related with differential equations not derived from Eq. 5.12, such as mass balances and energy balance, denoted as y_{ex}. The nonactive states are defined based on a given number of additional bins $r_{e,l}$ at smallest size and $r_{e,u}$ at largest size that can potentially be added to the active set during the simulation. In case the bins addition are performed in regular time intervals, those values can be adjusted accordingly such that at final time all values from $\tilde{y}$ are used. However, when the addition is dependent on process variables, $r_{e,l}$ and $r_{e,u}$ should be defined conservatively using a sufficient larger number. Eq. F.1 defines $\tilde{y}$ using the augmented pivot, boundaries and number of particles sequences $\tilde{x}$, $\tilde{l}$ and $\tilde{N}$, respectively, and also y_{ex}. The bin boundaries $\tilde{l}$ can be removed if not needed.

$$\tilde{y} = [\tilde{x}\ \tilde{l}\ \tilde{N}\ y_{ex}] \tag{F.1}$$

The augmented state $\tilde{x}$ at initial time is defined as in Eq. F.2, in which states $x_i^{*,l}$ and $x_i^{*,u}$ are nonactive states at smallest and largest sizes. The remaining values composes the active pivots, which at t_0 are the values from position $r_{e,l}$ up to $r_{e,l} + r_x - 1$. The position of the first active pivot is denoted as $\eta_{x,s} = r_{e,l}$ and for the last active pivot is $\eta_{x,f} = r_{e,l} + r_x - 1$. The augmented states $\tilde{l}$ and $\tilde{N}$ at initial time are defined analogously, except that $\tilde{l}$ contains $r_x + 1$ in the active set. In that sense, the first active boundary for $\tilde{l}$ is $\eta_{l,s} = r_{e,l}$ and the last active position is $\eta_{l,f} = r_{e,l} + r_x$. For $\tilde{N}$ the first and last active state position are $\eta_{N,s} = r_{e,l}$ and $\eta_{N,f} = r_{e,l} + r_x - 1$. All the states $x_i^{*,l}$ and $l_i^{*,l}$ are set to the critical size l_0, whereas all states $x_i^{*,u}$ and $l_i^{*,u}$ assume the value of the largest considered size l_{max}. The number of particles at nonactive bins $N_i^{*,l}$ and $N_i^{*,u}$ are set to zero.

$$x = [x_0^{*,l}\ x_1^{*,l}\ \ldots\ x_{r_{e,l}-1}^{*,l}\ x_{r_{e,l}}\ x_{r_{e,l}+1}\ \ldots\ x_{r_{e,l}+r_x-1}\ x_{r_{e,l}+r_x}^{*,u}\ \ldots\ x_{r_{e,l}+r_x+r_{e,u}-1}^{*,u}] \tag{F.2}$$

The addition of a new bin at the smallest size is represented decreasing by one the position of the first active position $\eta_{\nu,s}$, in which ν stands for x, l or N. Whereas, the removal of a bin at smallest size is performed by increment by one the first active position. In a similar manner, at largest size the addition of a bin is done by increasing by one the position of $\eta_{\nu,f}$ and the removal is performed by decreasing it by one.

Based on those definitions, a generic procedure is established to allow the use of the MSM for different applications. The events of adding or removing a bin are summarized by adjusting the positions of the active states based on $\eta_{\nu,s}$ and $\eta_{\nu,f}$.

Those events can be triggered based on regular time intervals as in (Kumar and Ramkrishna, 1997), or accordingly with the dynamic behavior of the process.

Appendix G

Pitzer Model for NaCl

The Pitzer Model is used to calculate the activity coefficient for the NaCl dissociation (Zemaitis et al., 1986):

$$\ln \gamma_{NaCl} = |z_{Na^+} z_{Cl^-}| f^\gamma + b_{NaCl} \left[2(\nu_{Na^+}\nu_{Cl^-})^{\frac{3}{2}}\right] C^\gamma \tag{G.1}$$

$$f^\gamma = -A_\phi \left[\frac{I^{\frac{1}{2}}}{1 + b^\gamma I^{\frac{1}{2}}} + \frac{2}{b^\gamma} \ln\left(1 + b^\gamma I^{\frac{1}{2}}\right)\right] \tag{G.2}$$

$$A_\phi = \frac{1}{3}\left(\frac{e}{\sqrt{D k_b T}}\right)^3 \sqrt{\frac{2\pi d_0 N_A}{1000}} \tag{G.3}$$

$$D = 305.7 \exp\left[-\exp\left(-12.741 + 0.01875T\right) - \frac{T}{219.0}\right] \tag{G.4}$$

$$B^\gamma = 2\beta^{(0)} + \frac{2\beta^{(1)}}{\alpha^2 I}\left[1 - \left(1 + \alpha I^{\frac{1}{2}} - \frac{\alpha^2 I}{2}\right)\exp\left(-\alpha I^{\frac{1}{2}}\right)\right] \tag{G.5}$$

$$C^\gamma = \frac{3}{2} C^\phi \tag{G.6}$$

$$B^\phi = \beta^{(0)} + \beta^{(1)} \exp\left(-\alpha I^{\frac{1}{2}}\right) \tag{G.7}$$

$$I = \frac{1}{2}\sum c_i z_i^2 \tag{G.8}$$

Where z_i is the charge of ion i, e is the electronic charge (e=1.60218$\cdot 10^{-19} C$), k_b is Boltzmann's constant, D is the dieletric constant, T is the temperature in Kelvin, N_A is Avogadro's constant, ρ is solvent density, b^γ is a universal parameter equal to 1.2 $kg^{1/2}mol^{-1/2}$; α is a parameter equal to 2.0 $kg^{1/2}mol^{-1/2}$ for NaCl (Prausnitz et al., 1998). Adjustable binary parameters $\beta^{(0)}$, $\beta^{(1)}$ and C^ϕ are specific for each salt and dependent on temperature (Zemaitis et al., 1986). Those are defined by

Table G.1: Pitzer q_j parameters

q_1 = 0.0765	q_2 = -777.03	q_3 = -4.4706
q_4 = 0.008946	q_5 = -3.3158·10^{-6}	q_6 = 0.2664
q_9 = 6.1608·10^{-5}	q_{10} = 1.0715·10^{-6}	q_{11} = 0.00127
q_{12} = 33.317	q_{13} = 0.09421	q_{14} = -4.655·10^{-5}

Eqs. G.9, G.10 and G.11 with T in Kelvin and parameters q_j are shown on Table G.1. T_{ref} is a reference temperature equal to $298.15K$.

$$\beta^{(0)} = q_1 + q_2\left(\frac{1}{T} - \frac{1}{T_{ref}}\right) + q_3 \ln\left(\frac{T}{T_{ref}}\right) + q_4(T - T_{ref}) + q_5(T^2 - T_{ref}^2) \quad \text{(G.9)}$$

$$\beta^{(1)} = q_6 + q_9(T - T_{ref}) + q_{10}(T^2 - T_{ref}^2) \quad \text{(G.10)}$$

$$C^{\phi} = q_{11} + q_{12}\left(\frac{1}{T} - \frac{1}{T_{ref}}\right) + q_{13} \ln\left(\frac{T}{T_{ref}}\right) + q_{14}(T - T_{ref}) \quad \text{(G.11)}$$

Appendix H

Added PSD as function of added mass

The added particle size distribution is considered as uniform in the size range from $l_{low,add}$ to $l_{up,add}$ with a constant value of $c_{psd,add}$:

$$n_{add_j}(l) = \begin{cases} c_{psd,add} & \text{if } l_{low,add} \leq l \leq l_{up,add} \\ 0 & \text{otherwise} \end{cases} \tag{H.1}$$

The constant PSD value $c_{psd,add}$ can be obtained based on the added solid mass using the third order moment, since the mass of solid for a given PSD is defined as Eq. H.2. The definition for the third order moment is as Eq. H.3, which after integration for an uniform distribution yields Eq. H.4.

$$m_{add} = \mu_3 \rho_c k_v \tag{H.2}$$

$$\mu_3 = \int_0^\infty n(l,t) l^3 dl \tag{H.3}$$

$$\mu_3 = \int_{l_{low,add}}^{l_{up,add}} c_{psd,add} l^3 dl = \frac{c_{psd,add}}{4} (l_{up,add}^4 - l_{low,add}^4) \tag{H.4}$$

The substitution of Eq. H.4 into Eq. H.2 and after rearranging provides the constant PSD value $c_{psd,add}$:

$$c_{psd,add} = \frac{4 m_{add_j}}{(l_{up,add}^4 - l_{low,add}^4) \rho_c k_v} \tag{H.5}$$